Octyl-Decorated Fréchet-Type Dendrons: A General Motif for Visualisation of Static and Dynamic Behaviour Using Scanning Tunnelling Microscopy

Inauguraldissertation
zur
Erlangung der Würde eines Doktors der Philosophie
vorgelegt der
Philosophisch-Naturwissenschaftlichen Fakultät
der Universität Basel

von
Lukas J. Scherer

aus Adligenswil (Luzern)

Basel, 2006

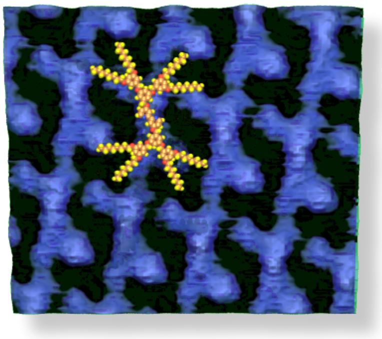

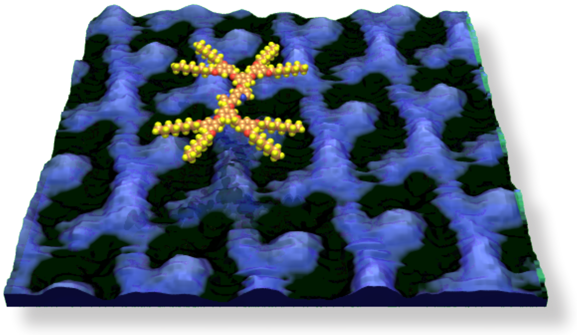

Genehmigt von der Philosophisch-Naturwissenschaftlichen Fakultät
auf Antrag von

Prof. Dr. E. C. Constable　　Prof. Dr. W. P. Meier　　Prof. Dr. B. A. Hermann

Basel, den 4. April 2006

Dekan
Prof. Dr. H.-J. Wirz

Acknowledgements

In acknowledging my debts I must begin with Ed Constable. I have had the benefit of his advice and experience. He managed to give me back the interest for the appealing world of chemistry. It has always been a great honour for me to work for him in an environment of scientific freedom, which was very beneficial for the creativity of such an interdisciplinary project. In these last three years, he has stimulated me in a fascinating way not only how to solve chemical problems but also how to make chemistry beautiful. Sometimes, I felt more as an artist or a designer than as a scientist. His last minute corrections around half the globe arrived on time, thanks!

To have not only Ed, but also Catherine Housecroft as the second supervisor, has made the working environment even more attractive. Catherine has always been able to motivate me, even in harder times. Her smile in the morning has always been a great help to improve my daily mood. Her knowledge of the principles of chemistry have always been helpful. The thesis was most ably maintained and revised by Catherine who has been unfailingly helpful and generous to me.

I am indebted to Bianca Hermann for leading the project very well. In spite of the distance, she has always taken good care of me and has been very reliable. It has also been a big honour that Bianca helped me with the incertainties concerning the STM part of the thesis. Furthermore, I would like to thank the National Research Project NFP47 for the financial support of this thesis.

Since Bianca Hermann was in Munich, I was really lucky to have with Leo Merz an expert in STM who introduced me this machine. He did not only explain me the technique, he also helped me at the beginning with a lot of measurements and participated in the discussions concerning the observed results. I have to mention, that without his help, Chapters 3 and 5 would never have been realised, parts of preliminary results are discussed in his PhD thesis.

A very close collaboration was done with the crystallography laboratory of the University of Basel. Markus Neuburger was able to get even from the smallest single crystals enough reflections to resolve the structures. He also showed me the insights in X-ray crystallography. Silvia Schaffner resolved most of the X-ray data. Her patience and preciseness were responsible for the quality of the final structures.

Most NMR spectroscopy experiments on the 500 MHz apparatus were conducted by Valérie Jullien. These data were a big help for the full assignement of the signals. Special NMR spectroscopy experiments, as ^{195}Pt NMR spectroscopy or temperature experiments were conducted by Klaus Kullicke. Michael Malarek was responsible for the last minute experiments I needed from the 500 MHz NMR machine. Daniel Häussingers expertise was very helpful whenever problems concerning the NMR measurements or the interpretations of the spectra occurred.

Most ESI-MS experiments were carried out on the mass spectrometer of the group of Wolf-Dietrich Woggon. Christian Grütter, Dominik Meyer, Alain Schlatter, and Axel Buss had performed them before Dominik introduced me in how to use the machine. Thanks a lot, not only for that but also for the Friday's after-work beer. Ellie Shardlow and Hoi Shan Chow conducted some other ESI-MS experiments. As responsible person for the MALDI-TOF spectrometer, Sandra Thöni was a very reliable colleague whenever problems during the measurements occurred. FAB and EI mass spectroscopy experiments were performed by Peter Nadig. Wolfgang Kirsch measured the elemental composition of the compounds. The assistance of Andreas Taubert was necessary for the interpretation of the DSC data.

I would like to offer particular thanks to Stefan Graber as a labmate fixing all computer problems, even when the problem occurred late in the night. I am grateful to Stefan not only therefore, but also for the work he has done during his Wahlpraktikum for me (which is not included in this thesis). He has been a very pleasant person to work with. Nora Kristen started in her Wahlpraktikum the work presented in Section 8.2 and we had a very enjoyable time sharing the fume hood. Damaris Ammann was involved in some measurements of the platinum(II) complexes of Chapter 6 and on measurements of compound **8**. I was supervising Björn Gschwend during his diploma work. The results are not presented in this thesis but the informations from his results were helpful for the formation of some bis(tpy) complexes discussed in the thesis.

The help and the support of the people in the lab has always been very splended. The three years I could spend in the lab were unforgettable and the mixture of people of different cultures enhanced my social experience. Dan Malarek has not only been a colleague in the lab but also a funny flatmate during one year. Special thanks are due to all labmates: Valérie Chaurin for lively atmosphere she has brought into the lab, Ellie Shardlow for being President of the Swiss Young Chemists Association, Stefan Graber for his positive way of thinking, Ljumni (sorry, Lumni) Ademi, the future minister of Macedonia, Conor Brennan and Kevin Doyle, the best beer drinkers I have ever met (I look forward to tonights St. Patrick's day cellebration with you), Frank (or Hein?) Schaper, the always fascinated chemist, and all other actual and former group members: Ana Hernandez (gracias por la camiseta de los txuri urdin que trajístes a Nicolas), Hoi Shan Chow, Barbara Brisig, Deborah Gusmeroli, Emma Dunphy, Yaqui Tao, Valérie Jullien, Annette Hougen, Ayton Sezen, Kate Harris, Jonathon Beves, Azad Mahmood, Michael Malarek, Sébastien Reymann, Amar Boudebous, Marc Häussler, Christopher Smith, Egbert Figgemeier and William Kylberg; thanks a lot!!!

Special thanks go to Beatrice Erismann, the most humane secretary I have ever met. How she managed to solve administrative problems in a non-bureaucratic way was impressive. I also want to thank Markus Hauri for the orderings and for managing the Schalter and to Franz Stählin for fixing all the problems concerning machines etc.

I am also very thankful to Wolfgang Meier for being the co-reference in my viva.

A special thank goes to my brother Matthias, the thesis would never have been in this form if he had not convinced me to write it with InDesign. It was also very advantageous to phone him whenever a problem with InDesign or Photoshop occurred or I needed competent advise concerning the layout or the design.

It is customary on these occasions to thank one's family, and mine here are more than formal. I have received during all the years a lot of support; without your backup and motivation I would never have achieved all that. The lic.phil.I influence I got from my family has been used for writing this thesis in English. My sister Miriam (or however you write it now) enriched my life tremendously with the birth of Nicolas, his contagious smile and his unconventional locomotion are just great.

El apoyo y el amor que recibí de Lola me motivaron muchísimo durante este tiempo. Mientras que he estado escribiendo, me ayudaste muchísimo. Sin las inolvidables habichuelas, lentejas, tortillas, ensaladas etc. que me preparastes no hubiese tenido la fuerza de escribir tan intensamente. Muchas gracias por tus correcciones tan exactas que me hicistes al final.

Lukas Scherer, Basel, 18.03.2005

Contents

Acknowledgements I
Abbreviations IX
Abstract XIII

Chapter 1 Introduction 1

1.1 Supramolecular chemistry 1
1.1.1 History and terminology 1
1.1.2 Weak chemical bonds 2
1.1.2.1 Hydrogen bonding 3
1.1.2.2 π–π Interactions 4
1.1.3 Supramolecular synthons 5
1.1.4 Self-assembly 6
1.1.5 Functional materials and molecular machines 18
1.2 Dendrimers 20
1.2.1 History and terminology 20
1.2.2 Construction of dendrimers 21
1.2.3 Fréchet-type dendrimers 24
1.3 References 25

Chapter 2 Methods and Instruments 31

2.1 General experimental 31
2.2 Scanning probe microscopy 32
2.2.1 Overview 32
2.2.2 Scanning tunnelling microscopy 34
2.2.2.1 Mode of operation 35
2.2.2.2 Substrates used for STM measurements 38
2.2.2.3 Sample preparation 39
2.2.2.4 Artefacts and peculiarities of the graphite surface 40
2.3 Data processing 42
2.3.1 Using X-ray data to prepare figures for overlay on STM images 42

2.3.2 STM data 42

2.4 HOMO, LUMO calculations 45

2.5 References 46

Chapter 3 Studying Self-Organised Monolayers of Bpy Decorated with Fréchet-type Dendritic Wedges using Scanning Tunnelling Microscopy 49

3.1 Compound synthesis and discussion of single crystal structure of **8** 50

3.1.1 Synthesis of compounds **3**, $[\mathbf{Pd(3)Cl_2}]$ and $[\mathbf{Pd(3)_2}]_2[\mathbf{PF_6}]_2$ 50

3.1.2 Synthesis of second generation compounds **4** and **6** 55

3.1.3 Synthesis and single crystal structure of compound **8** 56

3.2 Conformational analysis of self-organised monolayers of the first and second generation dendrons **3** and **6** 58

3.3 Data analysis and discussion of the monolayers of **3** and **6** 61

3.4 Switching molecular conformation 64

3.5 Studies of self-assembled monolayers obtained from Langmuir-Blodget films 65

3.6 Data analysis and discussion of the monolayers containing **8** 67

3.7 Experimental part 68

3.8 References 73

Chapter 4 STM Studies and Synthesis of Tpy-Decorated with Fréchet-Type Dendritic Wedges 77

4.1 Compound synthesis and discussion of single crystal structures 77

4.1.1 Synthesis and crystal structure analysis of 2,2':6',2''-terpyridine-4'(1'*H*)-thione **9** 77

4.1.2 Synthesis of compound 10 and 11 and crystal structure analysis of **10** 82

4.1.3 Synthesis and crystal structure analysis of compound **12** 85

4.2 Comparison of the 3D crystal structure with the self-assembled monolayer of **10** 87

4.3 Conformational analysis of self-organised monolayers of the second generation dendrons **11** 91

4.4 Comparing the self-assembled monolayers of **12** and **13** 93

4.5 Experimental part 95

4.6 References 98

Chapter 5 STM Studies and Synthesis of Octyl-decorated Fréchet-Type Dendrons 101

5.1 Compound Synthesis of Compounds **14** and Single Crystal Structure of Compounds **4** and **14** 101
5.2 Self-organised monolayers of compounds **4**, **14** and **15** 106
5.2.1 The trimeric pattern of the monolayer formed by compounds **4**, **14** and **15** .. 106
5.2.2 Delayed conversion of the trimeric pattern resulting in a supramolecular arrangement 111
5.3 Exchanging the *seventh molecule* of the trimeric pattern of **4** by a metal complex . 118
5.4 Experimental part 123
5.5 References 124

Chapter 6 STM Studies of Self-assembled Monolayers of Metal Complexes Decorated with Fréchet-type Dendrimers 127

6.1 Compound synthesis 128
6.1.1 Synthesis and analysis of compounds **16–21** 128
6.1.2 Synthesis and analysis of bis(tpy) metal complexes 134
6.1.2.1 Synthesis and analysis of bis(tpy) iron(II) complexes 134
6.1.2.2 Synthesis and analysis of bis(tpy) cobalt(II) and cobalt (III) complexes 139
6.1.2.3 Synthesis and analysis of bis(tpy) ruthenium(II) complexes 142
6.2 Study of self-assembled monolayers of metal complexes 145
6.2.1 Self-assembled monolayers of bis(tpy) metal complexes 145
6.2.2 Self-assembled monolayers of bis(alkyne) platinum complexes 156
6.3 Experimental part 160
6.4 References 167

Chapter 7 Octyl-decorated Fréchet-type Dendrons: what have we learnt? 171

7.1 Investigating intermolecular forces: STM versus X-ray diffraction 171
7.2 Special features of octyl-decorated Fréchet-type dendrimers for STM studies....... 173
7.3 References 179

Chapter 8 Formation of metallomacrocycles with tpy metal-binding domains 183

8.1 Synthesis and solid-state characterisation of pre-organised homoditopic disulfide **22** and a metallomacrocycle out of 22 183
8.1.1 Synthesis and crystal structure analysis of compound **22** 183
8.1.2 Formation of a metallomacrocycle from preorganised homoditopic ligand **22** 186
8.2 Studies of macrocycles containing homoditopic tpy ligands with alkyl-chain linkers 190
8.2.1 Synthesis, crystal structure and monolayer analysis of compound **23** 190
8.2.2 Ligand lability in Fe(II) complexes of tpy 195
8.2.3 Formation of metallomacrocycles using **23** and Fe(II), Co(II) and Ru(II) salts 198
8.2.4 Metalomacrocycles containing **23** and ruthenium(II) metal centres 198
8.2.5 Metallomacrocycles containing **23** and iron(II) metal centres 204
8.2.6 Metalomacrocycles containing **23** and cobalt(II) metal centres 206
8.3 Experimental part 208
8.4 References 212

Chapter 9 Additional and Further Work 215

9.1 Building of [Ru(tpy)$_2$] arrays with pendant octyl-decorated Fréchet-type dendrons 215
9.2 Synthesis of a Fujita-square with peripheral octyl-decorated Fréchet-type dendrons 219
9.3 Study of the effect of apolar anions for the formation of self-assembled monolayers 221
9.4 Related work by other group members 222
9.5 References 223

Appendix 225

Publications 225
Curriculum Vitae 227

Abbreviations

General

2D	two-dimensional
3D	three-dimensional
HOMO	highest occupied molecular orbital
LUMO	lowest unoccupied molecular orbital

Chemical

L	ligand
M	metal
R	rest
Ar	aromate
sat.	saturated
aq.	aqueous
PCC	pyridinium chlorochromate
tpy	2,2':6',2''-terpyridine
bpy	2,2'-bipyridine
phen	1,10-phenanthroline
TMA	1,3,5-benzenetricarboxylic acid (trimesic acid)
TPPSA	5, 10, 15, 20-tetraphenyl-21*H*, 23*H*-porphine-*p,p',p'',p'''*-tetrasulfonate
DMF	*N, N*-dimethylformamide
THF	tetrahydrofuran
DMSO	dimethylsulfoxide
TLC	thin layer chromatography

Chemical Analysis

NMR	**nuclear magnetic resonance spectroscopy**
COSY	correlated spectroscopy
DEPT	distortionless enhancement by polarisation transfer
NOESY	nuclear overhauser effect spectroscopy

s	singlet
d	doublet
t	triplet
q	quartet
m	multiplet
dd	doublet of doublets
ddd	double doublet of doublets
dt	doublet of triplets
td	triplet of doublets
m	multiplet
br	broad
HMQC	heteronuclear multiple quantum correlation
HMBC	heteronuclear multiple bond correlation
δ	chemical shift
J	coupling constant
MS	**mass spectrometry**
ESI	electrospray ionisation
EI	electron impact
FAB	fast-atom bombardment
MALDI	matrix assisted laser desorption ionisation
TOF	time of flight
m/z	mass:charge ratio
M	molecular (parent) ion
X	counter anion
IR	**infrared spectroscopy**
w	weak
m	medium
s	strong
$\tilde{\nu}$	wavenumber
UV-vis	**ultra-violet visible spectroscopy**
MLCT	metal-to-ligand charge transfer
λ	wavelength
ε	extinction coefficient
DSC	**differential scanning calorimetry**

elemental analysis

Calcd	calculated

Scanning Probe Microscopy

SPM	scanning probe microscopy
STM	scanning tunnelling microscopy
AFM	atomic force microscopy
SFM	scanning force microscopy
HOPG	highly oriented pyrolytic graphite
UHV	ultra high vacuum
PZT	lead zirconium titanate

Abstract

Firstly, a short overview on supramolecular chemistry including definitions, basic principles and examples taken from the literature of 2D and 3D self-assembly processes is given in Chapter 1. The introduction is completed by some general ideas of dendrimer chemistry.

In the second Chapter the techniques used in this thesis are introduced with a special focus on scanning tunnelling microscopy (STM). Besides the mode of operation and the data processing, the historical background is briefly described.

The following four Chapters present STM studies of monolayers formed by different types of compounds, all functionalised with Fréchet-type dendrons. Not only static features of monolayers such as conformational analysis of single molecules have been investigated, but also dynamic processes such as delayed conversion of a whole domain and conformational changes by protonation have been examined. The 2D properties of monolayers on a graphite surface have been compared with the X-ray data of 3D single crystals. For two compounds, the same molecular arrangement has been detected in monolayers on graphite and in single crystals.

Together with organic molecules, the self-assembly of metal complexes possessing tpy ligands and organometallic species with platinum(II) bis(alkynyl) units has been examined. Not all of these metal complexes were stable under the scanning conditions used in STM.

A synthetic programme leading to dendrimer-functionalised organic and organometallic compounds has been developed. Discussions of synthetic routes are given at the beginning of each Chapter.

Chapter 7 compares X-ray diffraction methods with STM, the two main analysis tools used for investigation of self-organised assemblies in the solid state in this thesis. In the second part of Chapter 7, the results presented in the previous Chapters are discussed with some general reflections on the self-assembling properties of Fréchet-type dendrimers with pendant octyl groups.

Additional to the studies of self-assembled monolayers, the formation of metallomacrocycles has been investigated using two novel homoditopic tpy ligands. This work is presented in Chapter 8. It was demonstrated that the ring-size depends on the metal used for the cyclisation. Furthermore, some of the macrocycles formed self-assembled monolayers on graphite, which have been examined using STM. One homoditopic ligand formed a molecular square by complexation with an iron(II) salt which was analysed using single crystal X-ray diffraction.

This thesis has brought together the realms of chemical design with studies of the physical behaviour of the envisioned molecules on the surface. It has been demonstrated that Fréchet-type dendrimers with octyl end-groups are a general motif for visualisation of static and dynamic behaviour using STM.

Supramolecular chemistry is what supramolecular chemists do.

E. C. Constable

1 Introduction

1.1 Supramolecular chemistry

1.1.1 History and terminology

For more than 170 years, since the synthesis of urea by F. Wöhler,[1] molecular chemistry has developed a vast array of powerful methods for the construction of ever more complex molecular structures in a controlled and precise fashion. Organic synthesis grew rapidly and masterfully, leading to a whole series of brilliant achievements. Major developments have been made in understanding the roots of complexity in synthetic problems and the specific forms which that complexity takes.[2, 3]

Beyond molecular chemistry based on the covalent bond, lies the field of *supramolecular chemistry*, whose goal it is to gain control over the intermolecular bond.[4] The meaning of *supramolecular* is *beyond the molecule*. The adjective *supramolecular* can be traced back at least to 1925.[5] The basis of *molecular recognition* was laid in 1894 by E. Fischer with his "lock and key" image of steric fit.[6] P. Ehrlich recognised at the beginning of the last century that molecules do not act if they do not bind, thus introducing the concept of *receptor*.[7] The idea of the *coordination bond* as one affinity between partners was initiated by A. Werner.[8] Molecular associations have been recognised and studied for a long time describing the interaction between macromelcules,[9, 10] and the organisation of enzyme and membrane system.[11, 12] The term *Übermoleküle* was used in the mid-1930's to describe entities of higher organisation (such as the dimer of acetic acid) resulting from the association of coordinately saturated species.[13-15]

The field of supramolecular chemistry, as we know it, started with the selective binding of alkali metal cations by crown ethers[16] and cryptands.[17-19] The field broadened leading to the emergence and identification of *molecular recognition*[20] as a novel domain of chemical research that, by extension to intermolecular interactions and processes in general and by broadly expanding over other areas, grew into supramolecular chemistry. The chemistry of molecular recognition is also at the core of *host–guest chemistry*.[21]

The concept and term of supramolecular chemistry were introduced in 1978 by J.-M. Lehn[22] and was defined with the words:

"Just as there is a field of *molecular chemistry* based on the covalent bond, there is a field of *supramolecular chemistry*, the chemistry of molecular assemblies and of the intermolecular bond."

The definition has been reformulated several times. In his Nobel Lecture in 1988, J.-M. Lehn writes:[23]

"Supramolecular chemistry may be defined as *chemistry beyond the molecule*, bearing on the organized entities of higher complexity that result from the association of two or more chemical species held together by intermolecular forces, not by covalent bonds."

The use of *covalent bonds* to describe interactions is unhelpful because it mixes interactions that are energetically different.[24] Furthermore, metal ligand bonds or hydrogen bonds can be substantial and strong.

A grander view of supramolecular chemistry focuses on the controlled assembly of multiple chemical components. The assembly can involve standard intermolecular interactions, and/or metal coordination. For a multi-component assembly to be feasible, timely, and controlled, exchanges of individual entities must be fast in order to achieve the required thermodynamic control of the system. Covalent bonds may be reversibly formed and can therefore act as intermolecular forces between different chemical species. Reversible covalent bonds (e. g. disulfide exchange, exchange of oximes and hydrazones) are also often used in the concept of dynamic combinatorial libraries introduced by J. K. M. Sanders,[25] which is considered as part of supramolecular chemistry.

Since the current terminology is imprecise, *supramolecular* currently has three different meanings:[24]

(a) intermolecular interactions;
(b) applied coordination chemistry;
(c) a strategy of controlled organisation of multiple separate components.

To disentangle this confusion, I. Dance recommended using *intermolecular* as the adjective for the well-known weak and long interactions between molecules, and describing elaborate coordination complexes and polymers under the terminology of coordination chemistry. He suggested restricting the use of *supramolecular* to "the philosophies and strategies of grand assembly".[24]

1.1.2 Weak chemical bonds

As seen above, supramolecular chemists often use the terminology of chemical bonds. But what is a chemical bond?

In 1939, L. Pauling defined a chemical bond as follows: "We shall say that there is a chemical bond between two atoms or two groups of atoms in case that forces acting between them are such as to lead to the formation of an aggregate with sufficient stability to make it convenient for the chemist to consider it as an independent chemical species."[26] Pauling explained that this definition was meant to include not only the directed valence bond of the organic chemist but also such bonds as those between sodium cations and chloride anions in the sodium chloride crystal or even the weak bond which holds together the two O_2 molecules in O_4. He did not consider the weak van der Waals forces between molecules as leading to chemical bonding. L. Pauling's definition is more than 65 years old. It was written at a time when only very few crystal structures of organic compounds were known. In the meantime, a vast and still expanding library of organic crystal structures has been accumulated and we now possess the theoretical and computational ability to estimate intermolecular forces and energies by different methods at a variety of levels. With the help of the 3×10^5 organic and organometallic crystal structures in the Cambridge Structural Database[27] and the 2.5 x 10^4 structures of biological macromolecules in the Protein Data Bank[28] one can find examples of just about any proposed intermolecular interaction involving peripheral atoms. From these databases, the evidence for weak bonds is easy to find. With the help of chemical intuition or theoretical calculations, such bonding interactions can be associated with energies extending all the way from strong hydrogen bonds to weak interactions that are barely above thermal noise level (RT = 2.5 kJ mol^{-1} at 300K). In supramolecular chemistry, multiple ligands on one entity bind simultaneously to multiple receptors on another, therefore the understanding of the concept of *multivalency*[29-33] is important. Multivalent interactions tend to be much stronger than the corresponding monovalent ones. The binding of two molecules, both having multiple recognition sites, may occur with an affinity greater than the sum of the corresponding monovalent interactions, a phenomenon that has been defined as the *cluster effect*.[34] In the following two Sections two interactions playing a major role in supramolecular chemistry are briefly explained, the hydrogen bond and π–π stacking interactions.

1.1.2.1 Hydrogen bonding

The hydrogen bond is the most important of all directional intermolecular interactions.[35] It is operative in determining molecular conformation, molecular aggregation, and the function of a vast number of chemical systems ranging from inorganic to biological. The question of distinguishing intermolecular atom–atom bonds from more delocalised types of interaction are not problematic in "normal" or "classical" X−H···Y (X, Y = O, N) hydrogen bond, with energies of 20−40 kJ mol^{-1}, or "strong" charge-assisted or resonance-assisted X−H···Y hydrogen bonds, with energies up to 150 kJ mol^{-1}.[36] Such bonds have considerable covalent character and are, when present, the principal driving force in intermolecular recognition.[37] Nevertheless, the concept of weak C−H···O and C−H···N interactions as structure-defining, hydrogen-bonding entities still enjoys widespread popularity in the chemical literature.[35, 38] Since the peripheral and protruding atoms in typical organic molecules tend to be H or otherwise F, Cl, O, N and π-electron systems are also often easily accessible molecular regions, it is hardly surprising that C−H···F, C−H···Cl, C−H···O, C−H···N, and C−H···π contacts have been identified. The interpretation of such contacts as extensions or extrapolations of hydrogen bonds is natural and has been followed by many researchers of intermolecular interactions in terms of "weak" or "unconventional" hydrogen bonds or hydrogen "bridges", as expressed in a crystal engineering context.[39] One can not deny that these weak intermolecular atom–atom bonds can be neatly categorised on the basis of geometrical, spectroscopic, and even energetic criteria and are thus according to these criteria existent rather than non-existent, provided one is prepared to accept a continuum of energies all the way to nearly zero. The question is not whether weak hydrogen bonds exist, but to what extend they are relevant in distinguishing one possible crystal structure from another.[37] One example of an "unconventional" hydrogen bond, where the proton acceptor[35] is a π-system, is shown in Figure 1.1.

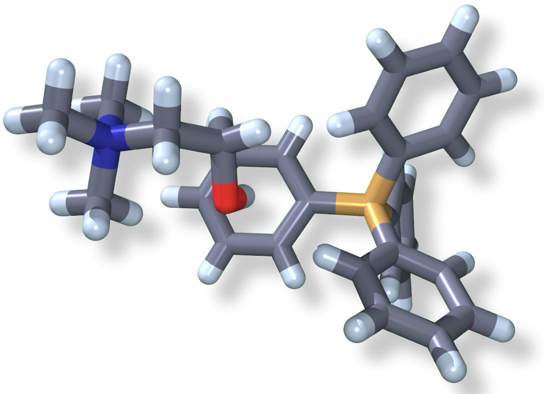

Figure 1.1 X-ray crystal structure of choline tetraphenylborate.[40] The proton is positioned almost over the aromatic midpoint *M*; the six H…C distances are in the range 2.49–2.70 Å; H···*M* is much shorter, 2.17 Å, and the O-H···*M* angle is 160°.

1.1.2.2 π–π Interactions

Strong attractive interactions between π-systems have been known for over half a century. They control such diverse phenomena as the vertical base–base interactions which stabilise the double helical structure of DNA, the intercalation of drugs into DNA, the packing of aromatic molecules in crystals, the tertiary structures of proteins, and complexation in many host–guest systems. Two different geometries of π–π stacking are observed (Scheme 1.1). Full *ab initio* calculations were carried out 20 years ago for a limited number of small systems which reproduced the experimental results well;[41, 42] an explanation of the basic mechanisms of π–π interactions was done some years later by C. A. Hunter *et al.*[43] This model indicates that the geometries of π–π interactions are controlled by electrostatic interactions but that the major energetic contribution occurs when the attractive interactions between π-electrons and the σ-framework outweigh unfavourable contributions such as π-electron repulsion. It is therefore a π–σ attraction rather than a π–π electronic interaction which leads to favourable interactions. These electrostatic effects determine the geometry of interaction, while van der Waals interactions (and solvophobic effects) make the major contribution to the magnitude of the observed interaction. Both T-shaped and face-to-face, offset geometries often observed in crystal structures with aromates can be explained in that way (Figure 1.2). Figure 1.3 shows a crystal structure with both geometries for π-stacking.[44]

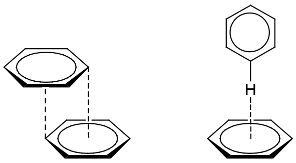

Scheme 1.1 The two different possibilities of π–π stacking. Left, the face-to-face geometry, and right the edge-on or T-shaped geometry.

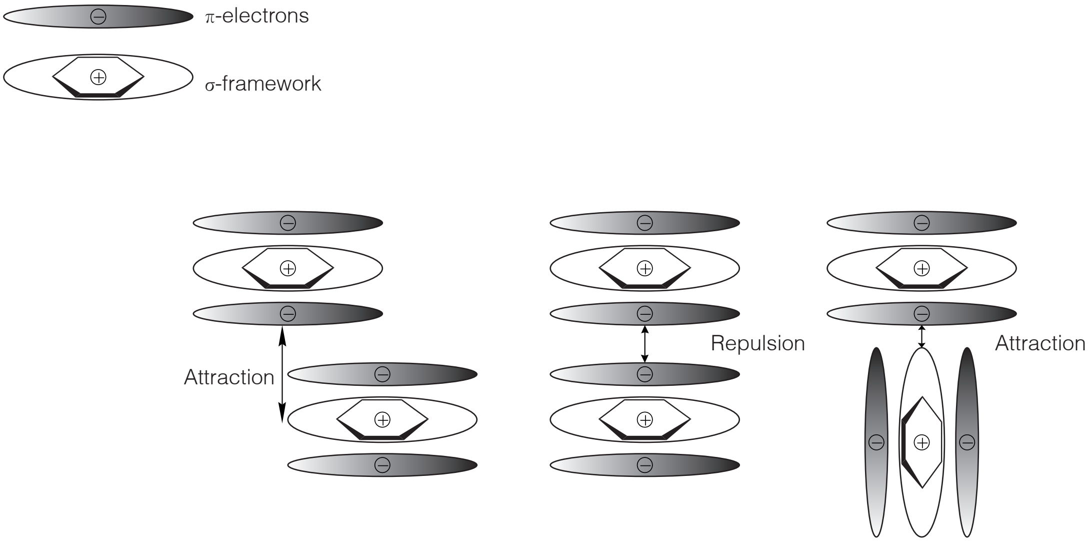

Figure 1.2 The origin of π-stacking.[43] In this model, the π–σ attractions determine the geometry.

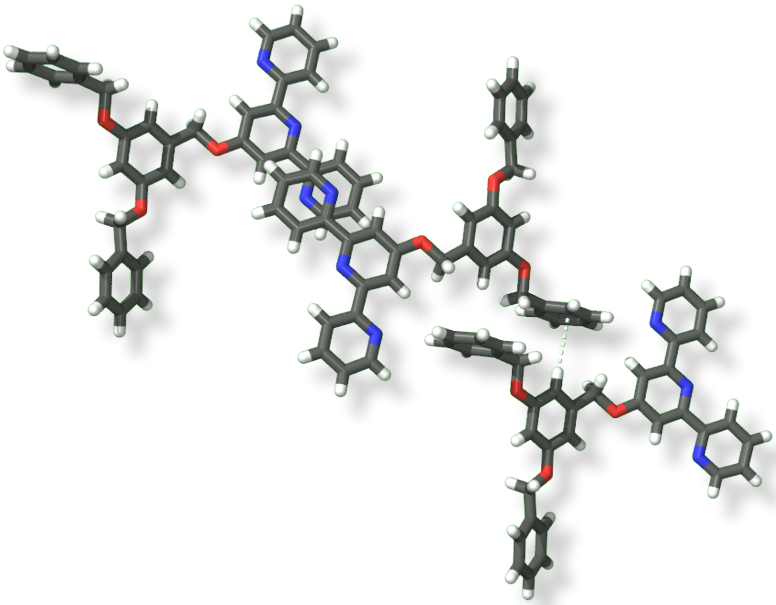

Figure 1.3 X-ray crystal structure of a terpyridine with a first generation Fréchet-type dendrimers attached at the 4'-position.[44] Both geometries introduced for π–π stacking interactions are observed in this crystal structure. The face-to-face π-stacking of terminal pyridine rings in adjacent molecules, is indicated, the T-shaped aryl(C–H)···π-phenyl interaction.

1.1.3 Supramolecular synthons

Since in supramolecular chemistry not just one interaction between one atom and another but normally multiple interactions between structural units take place, it is often confusing and misleading speaking about intermolecular bonds. Therefore, G. R. Desiraju introduced the term *supramolecular synthon*,[45] based on the term synthon used in the context of retrosynthetic analysis in organic chemistry.[2] He describes *supramolecular synthon* as “structural units within supermolecules which can be formed and/or assembled by known or conceivable synthetic operations involving intermolecular interactions”.[45]

Supramolecular synthons are spatial arrangements of intermolecular interactions. With this terminology a simplification of the crystal structures is obtained and therefore it should be easier to anticipate one-, two-, and three-dimensional patterns formed with intermolecular interactions. In this approach to classify intermolecular interaction, the origin of the approach is not relevant; it is more a collection of observed interactions (e. g. from the Cambridge Structural Database), followed by categorising them.

Some representative supramolecular synthons are shown in Scheme 1.2.

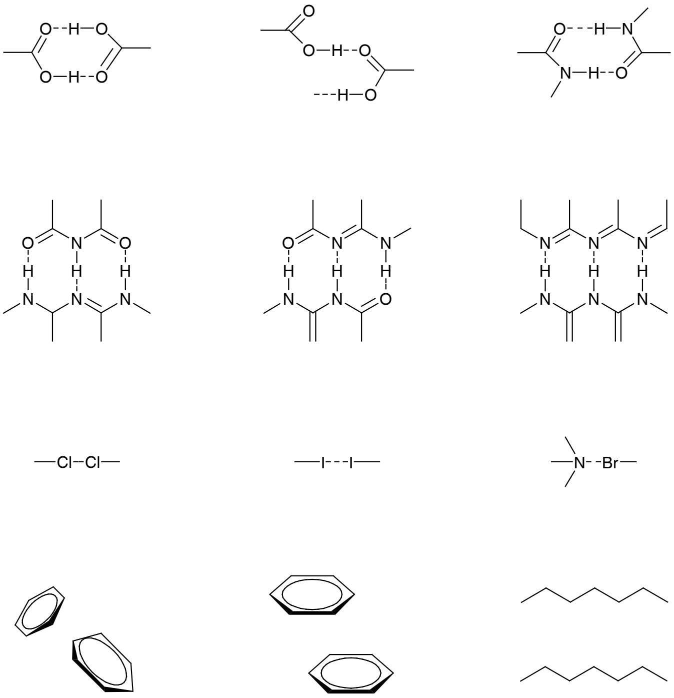

Scheme 1.2 Some representative supramolecular synthons.[45]

1.1.4 Self-assembly

In supramolecular chemistry, the build up from their components to the supramolecule occurs through self-processes. Such a preorganisation of supramolecular structures from diverse entities is called *self-assembly* process. The term *self-assembly* can not just be used in the supramolecular level; it is used generally to “designate the evolution towards spatial confinement through spontaneous connection of a few/many components, resulting in the formation of discrete/extended entities at either the molecular, covalent or the supramolecular, non-covalent level”. [4] J.-M. Lehn defines *supramolecular self-assembly* as “the spontaneous association of either a few or many components resulting in the generation of either discrete or oligomolecular supermolecules or of extended polymolecular assemblies such as molecular layers, films, membranes, etc. The formation of supermolecules results from the recognition-directed spontaneous association of a well-defined and limited number of molecular components under the intermolecular control of the non-covalent interactions that hold them together".[4]

Self-assembly of a supramolecular architecture is a multistep process implying information and instructed components of one or several types. They require kinetic lability of the connecting events. This reversibility is necessary in order to allow the full exploration of the energy hypersurface of the system.

In the following, the formation of different helicates is shown as an example of inorganic self-assembly process. Coordination complexes displaying helicate motifs have been obtained by treating a semiflexible linear polydentate ligand with a kinetically labile metal ion which is too small for the binding cavity that would be present if the ligand were in a planar conformation.[46] The resulting mismatch between the geometry of the ligand binding site and the preferred geometry of the metal ion destabilises the monomeric complex,[47] so that twisted bi- or polymetallic compounds having the characteristic helicate secondary structure are instead favoured.

An example of such a reaction is shown in Figure 1.4, which depicts the spontaneous formation of the trisilver(I) helicate $[Ag_3(\mathbf{L1})_2]^{3+}$ from three Ag(I) ions and two tris(bipyridyl) ligands **L1** having semiflexible linkers.[48]

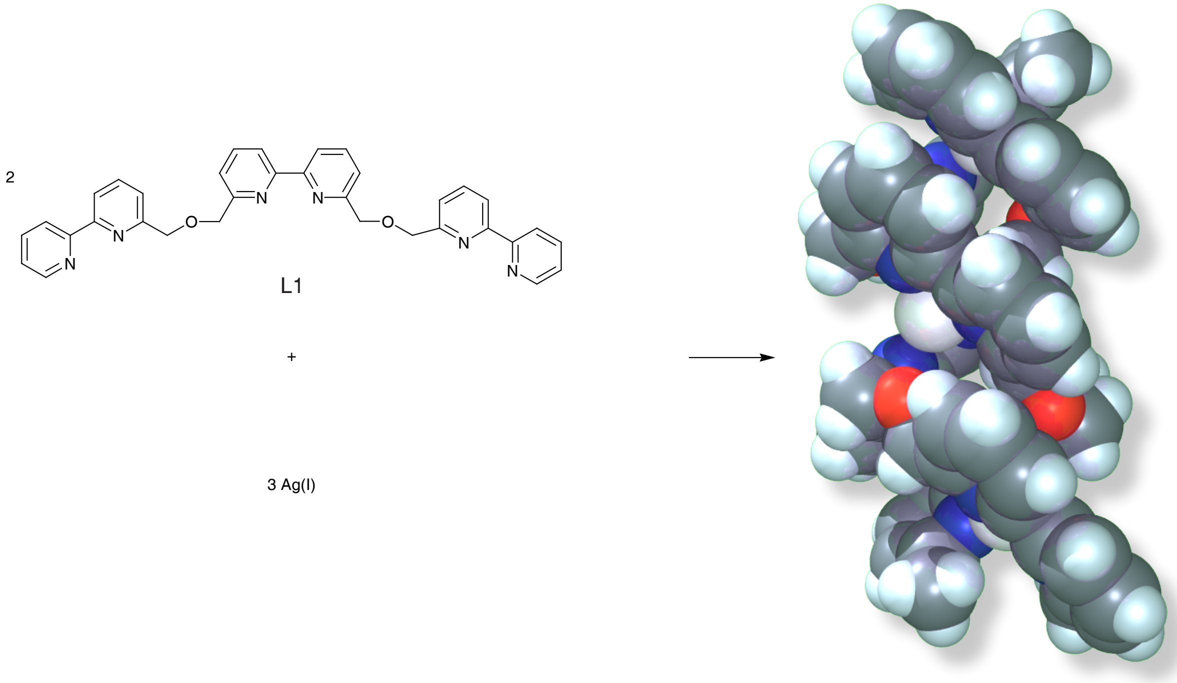

Figure 1.4 The formation of a double-stranded, trimetallic helicate of Ag(I) with a tris(bipyridine) ligand **L1**.[48] The solvents and counter-ions in the crystal structure are omitted for clarity.

Helicates could also be obtained by reacting metals with coordination numbers other than 4. One example is shown in Figure 1.5, where a helicate was formed from two sexipyrdine ligands **L2** and two cadmium(II) cations with a octahedral coordination geometry.[49]

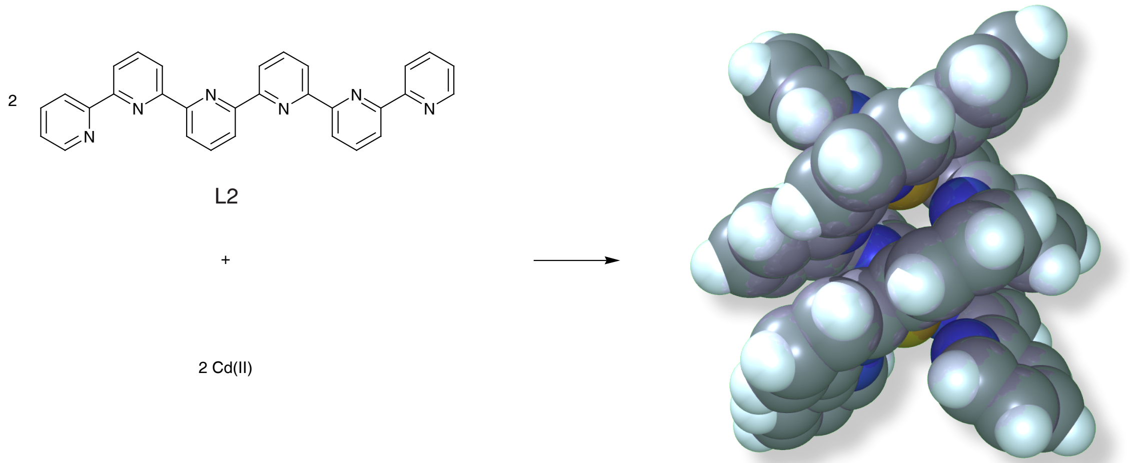

Figure 1.5 The formation of a dimetallic helicate of Cd(II) with two sexipyridine ligands **L2**.[49] The double helix is probably stabilised by π–π stacking interactions between superimposed pyridine rings. The solvents and counter-ions in the crystal structure are omitted for clarity.

However, it is very hard to predict if a helicate is going to form. By attempting of forming linear helicates, circular helicates are sometimes obtained. An example in which helicates and circular helicates simultaneously existed in a mixture as apparent thermodynamic products was the reaction of Cu(I) with the quaterpyridine ligand **L3** in which an ethyl spacer was used to split the binding domain into two bipyridine binding sites (Figure 1.6). ESI-MS revealed the existence of a library of compounds which included the [3+3], as well as the [4+4] and the [5+5] macrocycles, in addition to the expected diastereomeric *P* and *M* double helicates. An X-ray crystal structure determination of the [3+3] macrocycle, which could be selectively isolated, revealed a diastereomeric pair of *P* and *M* circular helicate products. Additionally, the structural determination of another single crystal was possible containing equal amounts of the diastereomeric *P* and *M* double helicates (Figure 1.6).

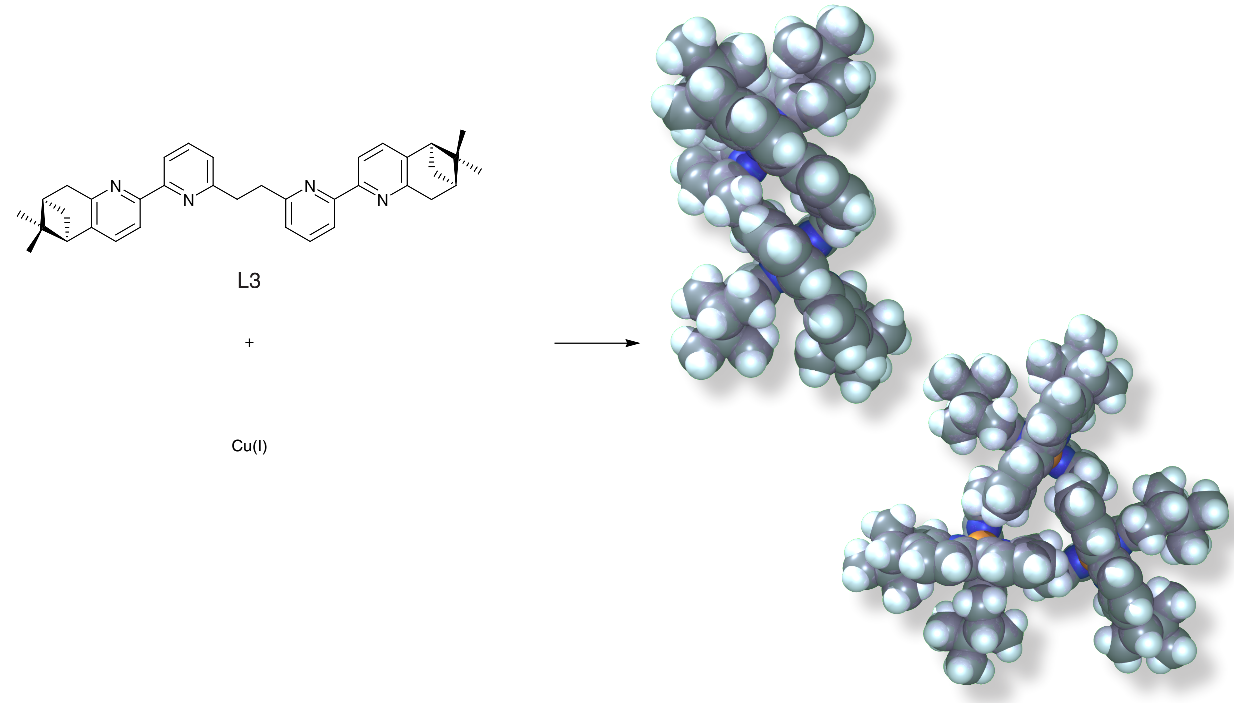

Figure 1.6 By mixing ligand **L3** with copper(I), a library of helicates and different macrocycles was obtained. For the helicate and the [3+3] macrocycle, both diasteromers *P* and *M* were obtained in the crystal structure. The solvents and counter-ions in the crystal structure are omitted for clarity.

Concentration of the mixture resulted in an increase in the higher nuclearity species, suggesting that the formation of the circular helicates in the solution was strongly influenced by entropic factor. At concentrations below 10^{-4} M, only the binuclear helicates were present.

Several other self-assembled circular helicates have been reported. O. Mamula *et al*. have prepared the single stranded [6+6] macrocycle by the complete stereoselective reaction of Ag(I) with the bis(bipyridyl) ligand **L4** having a spacer incorporating two chiral pinene groups (Figure 1.7).[50] In the reaction with the ligand prepared from (−)-α-pinene, a circular helicate of *P*-handedness was obtained. The corresponding reaction with the ligand prepared from (+)-α-pinene delivered the *M* analogue.

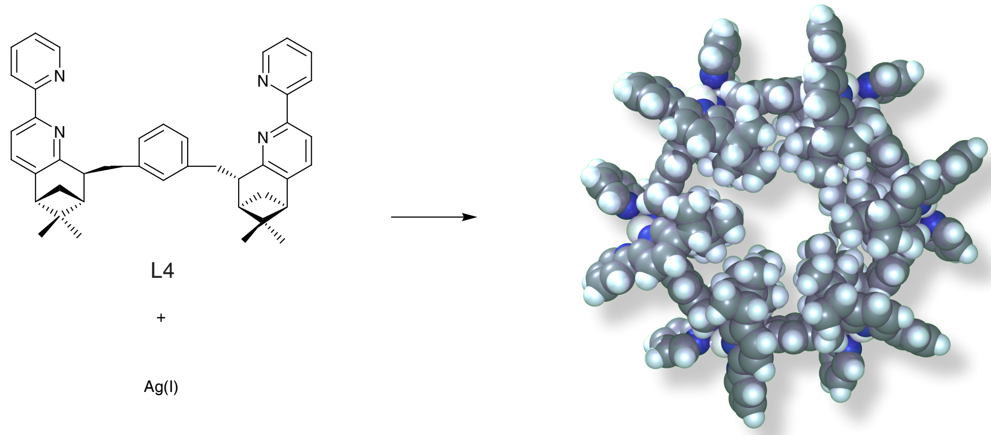

Figure 1.7 A [6+6] macrocycle of a circular helicate obtained by reacting **L4** with Ag(I). The solvents and counter-anions in the crystal structure are omitted for clarity.

As shown in Figure 1.6, the mixing of a multidentate ligand with a metal cation results often in a mixture of products. The specific formation of just one product can sometimes be achieved by using an appropriate *template*. In Figure 1.8, such an example is shown, where 4,4'-bypyridine acted as a template.[51] ^{1}H NMR studies on equimolar mixtures of **L5** with each of the acceptor porphyrins **L6** prior to addition of 4,4'-bypyridine showed the formation of dynamic combinatorial libraries containing numerous complexes. By adding one equivalent of 4,4'-bypyridine to the NMR-solution, just one species was detected, which could additionally be analysed by single crystal X-ray diffraction technique.

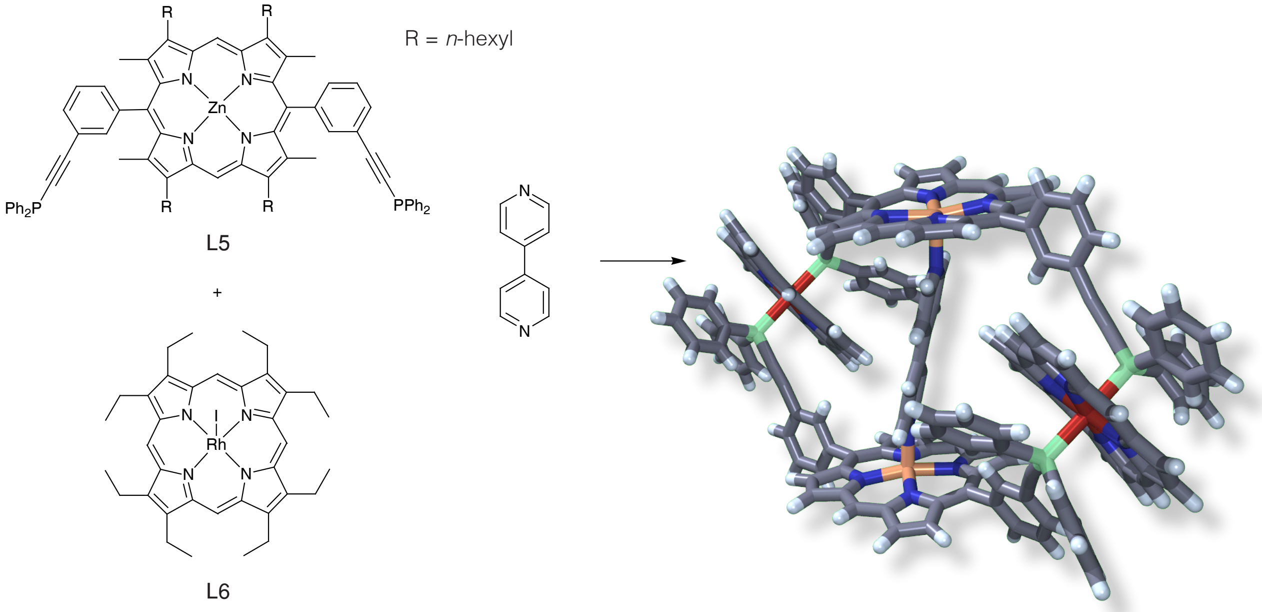

Figure 1.8 To selectively form the macrocyle with four porphyrin units, 4,4'-bypyridine had to be added to the reaction mixture which then acted as template. The solvents and alkyl-chains in the crystal structure are omitted for clarity.

One of the most intriguing examples of self-assembly is the construction of the Borromean rings (see Figure 1.9).[52, 53] In the Borromean rings, three rings are linked, but no two rings are linked (as e. g. in the catenane), yet all three remain, as a whole inseparable.

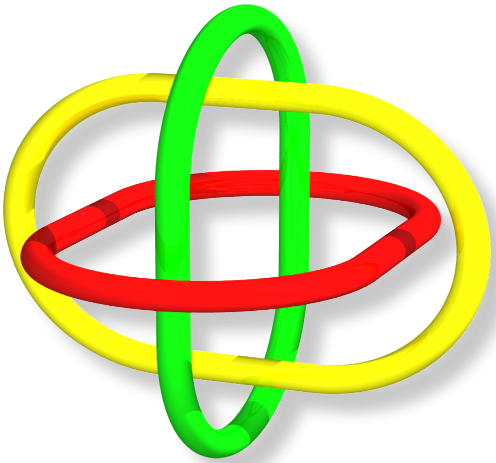

Figure 1.9 One possible representation of the Borromean rings.

The construction of the molecular Borromean rings was achieved in one single step from 18 components by the template-directed formation of 12 imine and 30 dative bonds, associated with the coordination of three interlocked macrocycles, each tetranucleating and decadentate overall, to a total of six zinc(II) ions.[52] Imines and the dative zinc(II)−N bonds are kinetically labile bonds and therefore all the reactions occurring during this self-assembly process are reversible. In Figure 1.10, a schematic representation of the one-pot synthesis is shown.

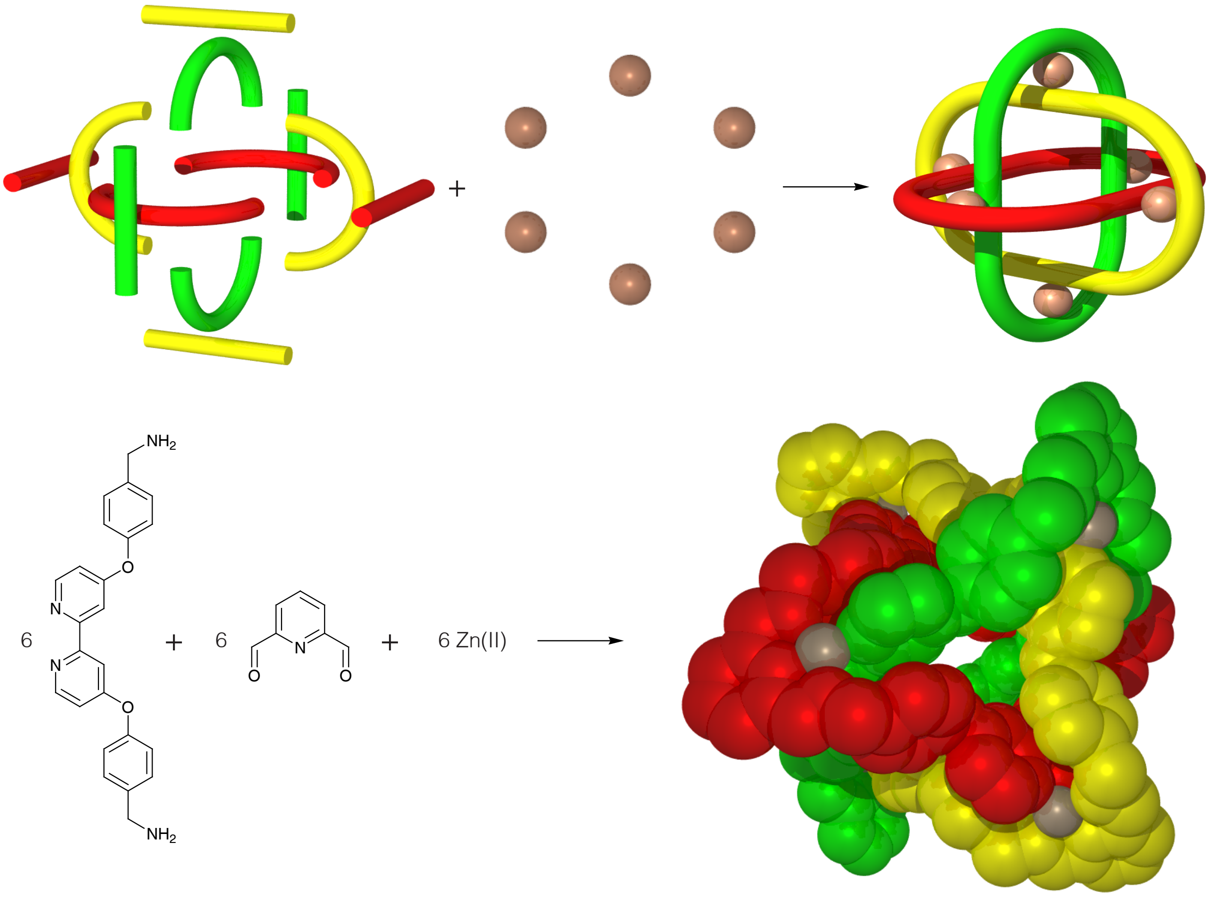

Figure 1.10 Schematic representation of the one-pot synthesis of the Borromean rings. The solvents and counter-anions and hydrogens in the crystal structure are omitted for clarity.

Among the variety of framework-forming building blocks employed in the synthesis of organic supramolecular solids, the three-armed trimesic acid (TMA) is of special interest, as its rigidity and triangular geometry can lead to formation of frameworks enclosing large cavities (Scheme 1.3).

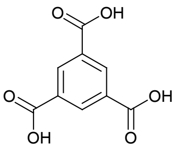

Scheme 1.3 1,3,5-Benzenetricarboxylic acid (trimesic acid)

In solid state, TMA forms a “chicken-wire” pattern with an approximately 14 Å diameter hole, but has a high tendency for self-inclusion, leading to 4-fold interpenetrating networks, thus filling the cavities and preventing clathrate formation (Figure 1.11).[54]

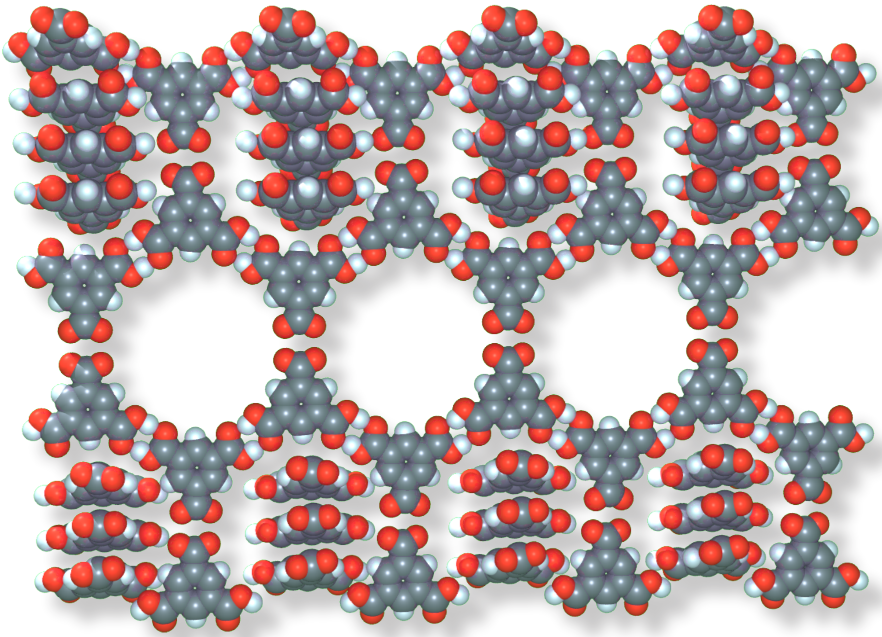

Figure 1.11 One layer of the X-ray crystal structure of trimesic acid (TMA).[54] The structure has high tendency to interpenetrate.

An effective strategy to for suppressing interpenetration is to cocrystallise TMA with suitable *guests*. In Figure 1.12 such an example is shown, where two pyrene molecules were encapsulated per cavity.[55]

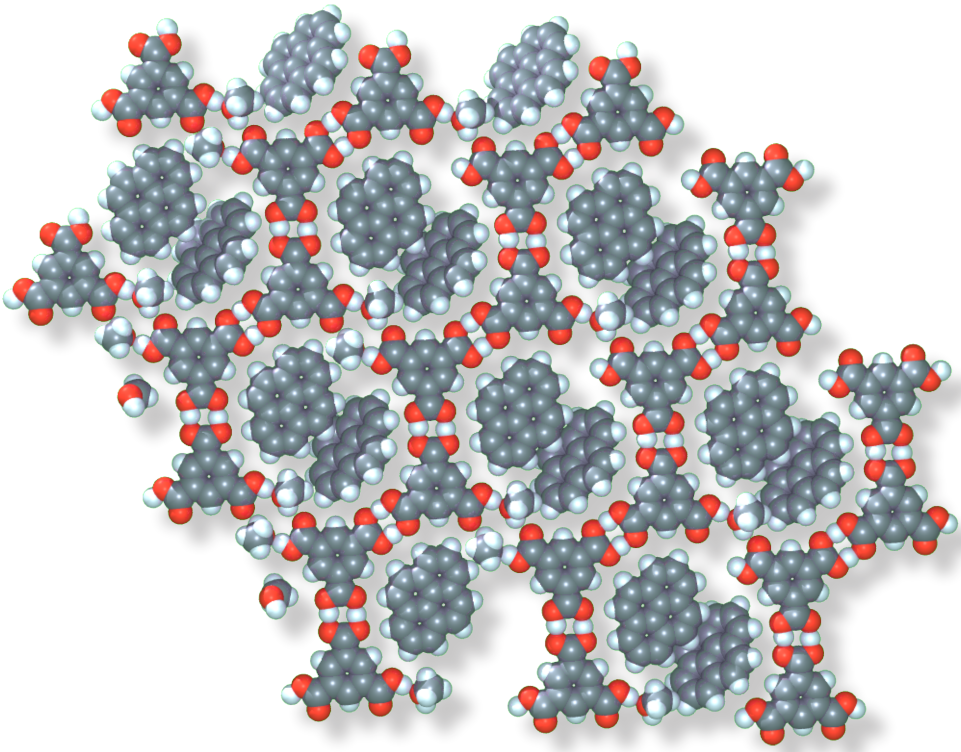

Figure 1.12 Two pyrene molecules act as host molecules in the "chicken-wire" framework formed of TMA molecules.

The "chicken-wire" framework was extended by cocrystalline the TMA and the pyrene with 1,3,5-tri(4-pyridyl)-2,4,6.triazine.[56] This enlarged the cavity size to give internal dimensions of 18 Å (Figure 1.13). Thus, three pyrene molecules were placed into the cavity.

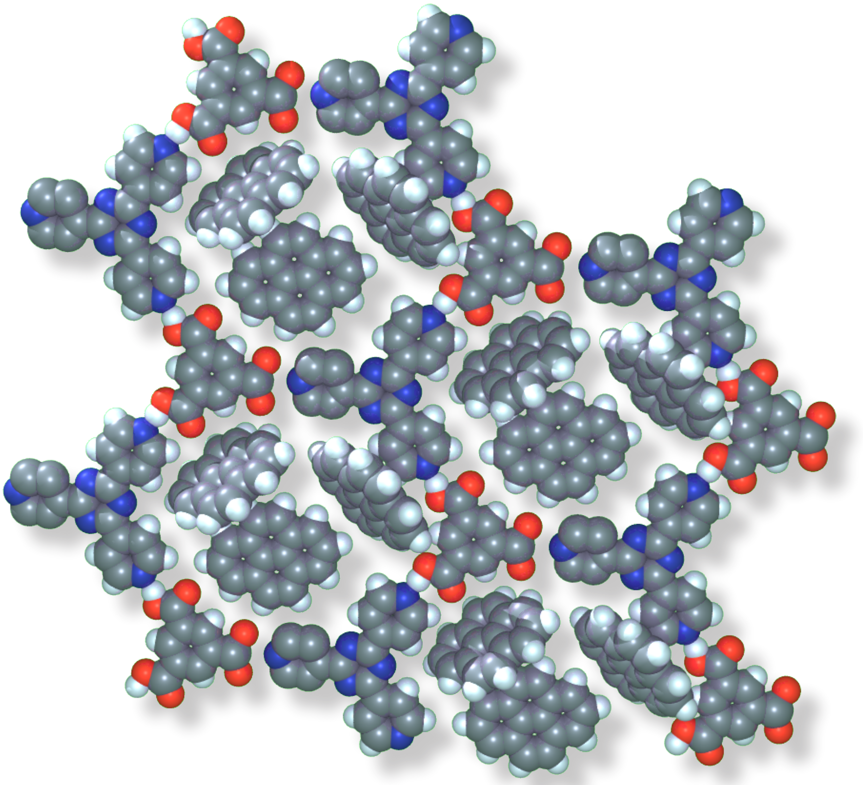

Figure 1.13 Three pyridine molecules are placed into each cavity of the "chicken-wire" framework consisting of three TMA and three 1,3,5-tri(4-pyridyl)-2,4,6-triazine units.[56]

In all these examples of *host–guest chemistry* of TMA, just one layer of the crystal structure was discussed. Another method to follow monolayered self-assembly processes is by using scanning tunneling microscopy (STM) techniques (see Chapter 2). Therefore, the monolayer has to be formed on a conductive substrate, e.g. graphite or gold. Recently, self-assembled monolayers of TMA have been extensively studied using STM techniques.[57-61] The "chicken-wire" structure with similar dimensions to those in the single crystal was also observed in the monolayer (Figure 1.14).[57, 61] Since interpenetration is not a problem in a monolayer, no guest molecules were necessary to stabilise this structure; occasionally, an encapsulated TMA molecule was observed (Figure 1.14(a)). Additionally to the "chicken-wire" pattern, a "flower" pattern was observed (Figure 1.14(b)). The pattern depended highly on the solvent used for the measurements in solid–liquid interface. By using solvents with longer alkyl-chains (octanoic acid and solvents with longer alkyl chains) the "chicken-wire" pattern was formed and by using solvents with shorter alkyl-chains (hexanoic acid and shorter chains alkylic acids) only the "flower" pattern was found.[61]

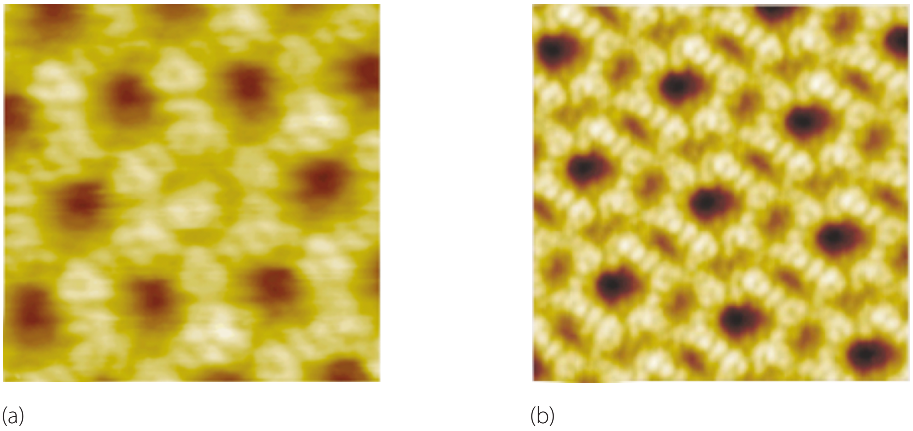

Figure 1.14 Two observed pattern of self-assembled monolayers of TMA.[57] (a) "chicken-wire" pattern with one encapsulated TMA molecule; (b) "flower" structure. Image sizes: (a) 5.4 nm x 5.4 nm; (b) 8.2 nm x 8.2 nm.

Host–guest properties of self-assembled monolayers could also be studied using the "chicken-wire" skeleton.[58, 60] Coronene was found to be an ideal guest molecule (Figure 1.15).

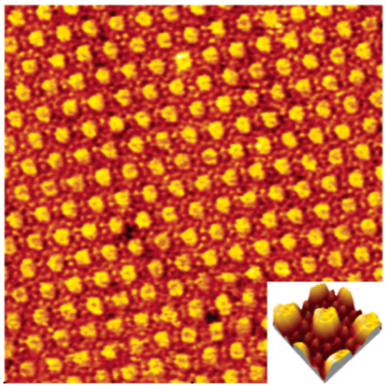

Figure 1.15 A 20 nm x 20 nm STM image of coronene molecules inserted into the TMA host structure.[60]

Calix[8]arene are able to include guest molecules into its cavity. Scheme 1.4 illustrates the chemical insertion of a fullerene molecule into the calix structure.[62] Well-ordered arrays of Calix[8]arene and of the C_{60}/Calix[8]arene complex could be constructed on a Au(111) surface and observed by STM (Figure 1.16).[63] The host–guest structure was very stable.

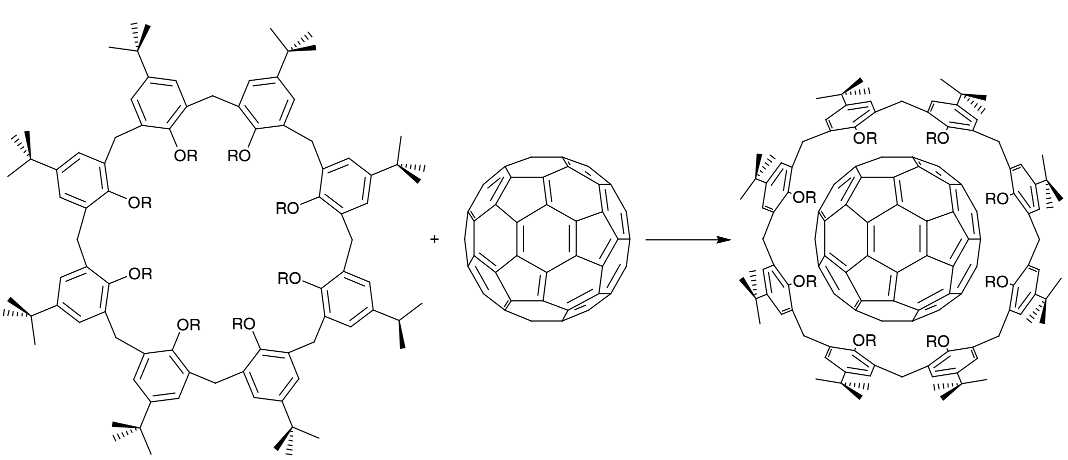

Scheme 1.4 The formation of a C_{60}/Calix[8]arene complex.[62]

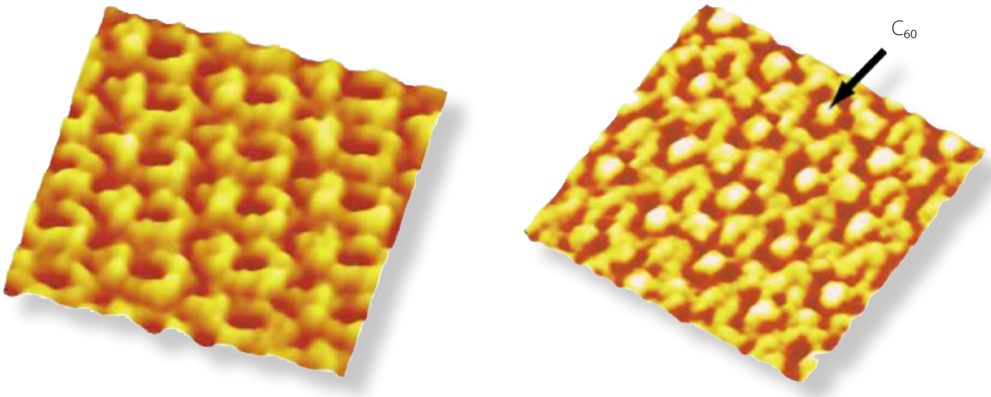

(a)

(b)

Figure 1.16 Two 6 nm x 6 nm STM images of self-assembled monolayers of (a) a calyx[8]arene derivative, and (b) of the C_{60}/Calix[8]arene complex.[63]

In the past 15 years a whole variety of self-assembled monolayers could be imaged by STM.[64-66] The first experiments on molecular adlayers were carried out under ultrahigh vacuum (UHV) conditions on metal surfaces.[67] To overcome the problem of molecular mobility for those systems with too weak adsorbate-substrate interactions, two approaches have been followed. Either the temperature was decreased under UHV conditions, or 2D adlayers were formed. In addition, the presence of certain functional groups can help in stabilising the monolayer via intermolecular interactions (e.g. hydrogen bonding as seen in the example of self-assembled monolayers of TMA) or adsorbate-substrate interactions (e.g. alkyl-chains on graphite). An example which combines intermolecular hydrogen bonding interaction and adsorbate-substrate interactions is the self-assembled monolayer of compound **L7** (Scheme 1.5).[68]

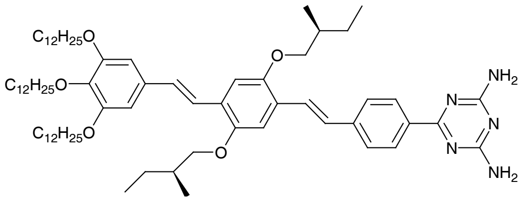

Scheme 1.5 Molecular structure of compound **L7**.

The self-assembled monolayer of **L7** showed an arrangement of the molecules in individual rosettes (Figure 1.17). The driving force for this hexameric pattern was the formation of hydrogen-bonded hexameric structure of six diamino triazine moieties. The rosette appeared exclusively to rotate clockwise. Molecular chirality was transferred to the rosette structures which in turn formed chiral 2D crystalline patterns.

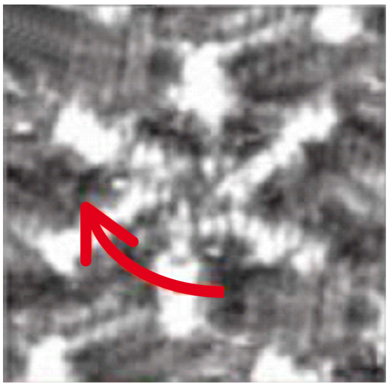

Figure 1.17 STM image of a self-assembled monolayer of compound **L7**.[68] The π-conjugated system of six molecules appeared with highest contrast as a rosette rotating clockwise. The interdigitating alkyl-chains are also visible.

1.1.5 Functional materials and molecular machines

The use of molecules for building nanoscale motors or machines is an increasing field in chemistry, particularly during the past 15 years. The construction of molecular machineries is closely coupled with supramolecular chemistry. The motivation of supramolecular chemistry lies not only in the fundamental understanding of self-assembly and molecular recognition processes relevant to the origin of life, but also toward the designing of a new class of materials and devices for future technologies.[33] The idea of making machines out of molecule is not new, R. Feynman came along with this idea 1959 in his famous talk entitled "There's a Plenty of Room at the Bottom": [69]

"Ultimately, we can do chemical synthesis… The chemist does a mysterious thing when he wants to make a molecule. He sees that it has got that ring, so he mixes this and that, and he takes it, and he fiddles around. And, at the end of a difficult process, he usually does succeed in synthesizing what he wants."

The motivation in the past for such machineries lies in the fact that the miniaturising of electronic and mechanical devices by the conventional *top–down* lithiographic techniques is not suited for the fabrication of nanoscale components. Thus, the *bottom–up* approach,[70] centered upon the design and manipulation of molecular assemblies has emerged as a potential tool for the development of nanomechanical systems.[71] The most current investigations have focused upon the transduction of chemical, electrical, or photochemical energy into controllable molecular action and hold potential for producing controllable nanoscale mechanical systems driven by molecular machinery. Two examples of transduction of electrical energy into molecular motion will now be shown.

Y. Liu *et al.* presented recently a "linear artificial molecular muscle".[71] In this work a palindromic [3]rotaxane **L8**$\cdot 8PF_6$ was created in order to mimic the contraction and extension motion of skeletal muscles (Scheme 1.6). The recognition system occured between the π-electron-deficient ring system (cyclobis(paraquat-*p*-phenylene)) and the redox-active electron-rich tetrathiofulvalene unit. Upon one- or two-electron oxidation of the tetrathiofulvalene unit, the macrocycle was electrostatically repelled and moved to the naphthalene unit. ^1H NMR spectroscopic and UV-vis spectroelectrochemical experiments showed that the voltage addressable oxidation/reduction cycle of tetrathiafulvalene units could control the locations of the two ring components.

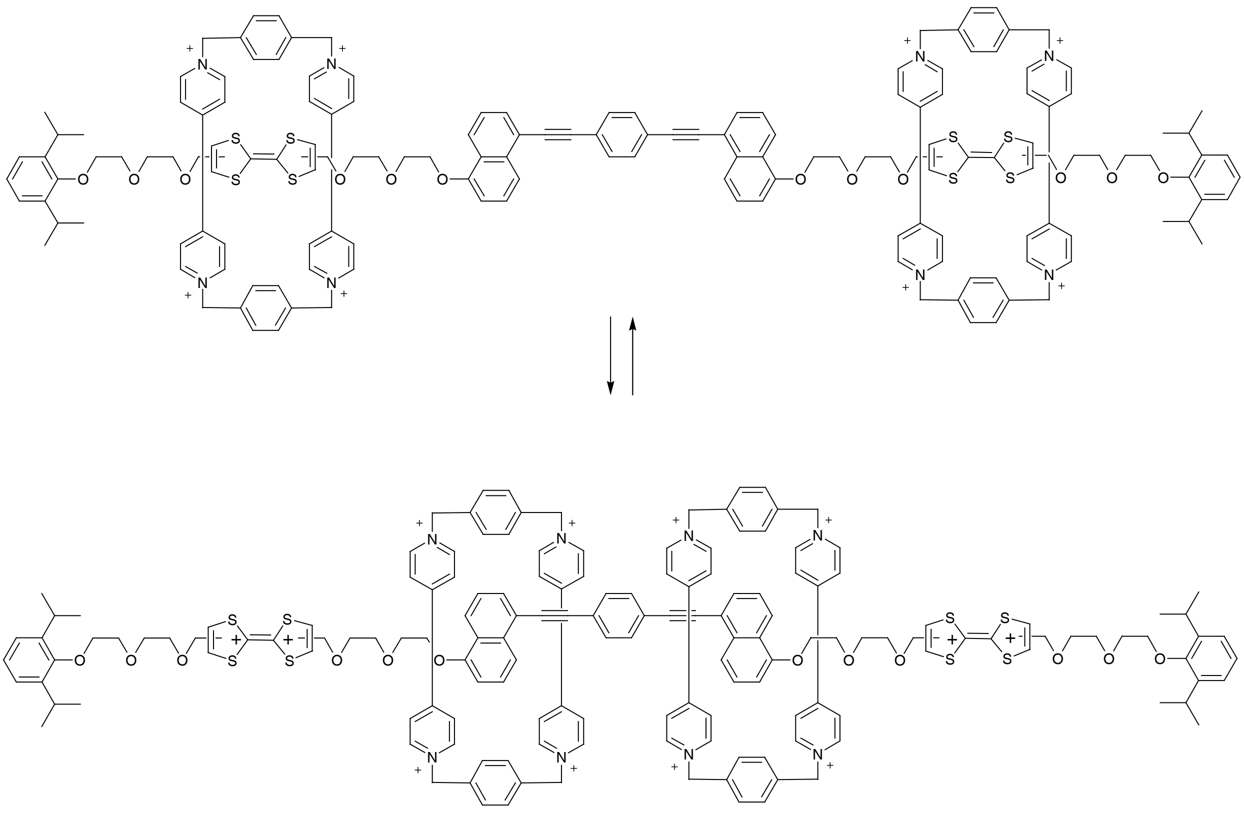

Scheme 1.6 Structural formulas of contracted **L8**·8PF$_6^{8+}$ and extended **L8**·8PF$_6^{12+}$ states of the molecular muscle. The distance between the adjacent recognition units was around 1.4 nm.

By attaching disulfide ethers to the rings, enabled them to anchor to gold surfaces. By formation of a self-assembled monolayer on a gold surface, controllable and reversible bending of the gold beam by oxidation/reduction could be observed, due to the contraction and extension of the surface-bound molecular muscle.[71]

One of the first examples of molecular machines was based on transition-metal complexes in a [2]catenane and is also electrochemically driven.[72] The organic backbone consisted of two interlocked coordination rings. One ring encloses a 1,10-phenanthroline and a 2,2':6',2''-terpyridine subunit. The principle of the process is explained in Scheme 1.7. Essential was the difference of preferred coordination number for the two redox states of copper: copper(I) has a coordination number of 4, and copper(II) has a coordination number of 5 (in oligopyridine systems). Depending upon the mutual arrangement of both interlocked rings, the central copper atom can be tetrahedrally complexed (two phenantroline ligands) or 5-coordinate (phenantroline + terpyridine ligands). Interconversion between these two complexing modes resulted from a complete pirouetting of the two-site ring. This process was reversible.

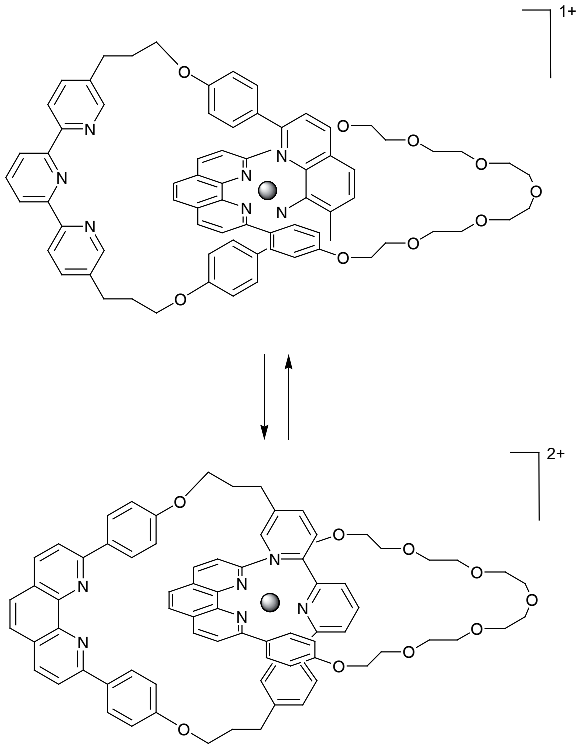

Scheme 1.7 A two-geometry [2]-catenane constructed around a copper(I) (above). The gliding motion of one ring within the other is triggered by oxidising or reducing the metal centre (Cu(I)/Cu(II)).

1.2 Dendrimers

1.2.1 History and terminology

The concept of highly branched polymers was initially proposed in the early 1940s by P. J. Flory and W. H. Stockmayer.[73, 74] Although synthetic efforts failed,[75] P. J. Flory predicted the possibility of such polymers in 1952 by suggesting that it should be possible to polymerise AB_x-type monomers (where A reacts with B and $x \geq 2$) to high molecular weight, multibranched products without gelation to an infinite network.[76] The first dendrimers, named *cascade* molecules, were synthesised by E. Buhleier *et al*. in 1978 (Scheme 1.8).[77]

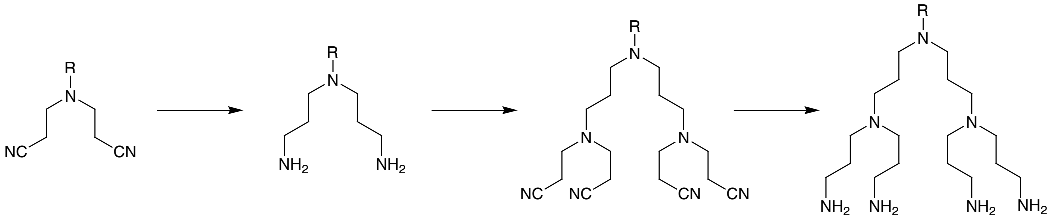

Scheme 1.8 The first iterative *cascade* synthesis of tetraamines reported by E. Buhleier *et al.*[77]

Cascade synthesis implies that the reaction sequences can be carried out repeatedly, where a functional group is able to react in such a way that it appears twice in the subsequent molecule. Since then much of the pioneering work has been credited to the research groups of R. G. Denkewalter,[78-80] D. A. Tomalia,[81-83] G. R. Newkome,[84] J. M. J. Fréchet,[85] T. M. Miller,[86, 87] J. Moore,[88-90] E. W. Meijer,[91] and F. Vögtle.[92, 93]

The term *dendrimer* originates from the Greek and is a combination of the words *dendron* (tree) and *meros* (part) and was introduced by D. A. Tomalia.[81] Although a strict definition of the generally used term has not emerged to date, it is widely accepted that dendrimers are highly branched, yet structurally perfect molecules, prepared via iterative synthesis.[94] Relliance on the IUPAC nomenclature would produce extremely long names that are almost impossible to interpret. Therefore, effort aimed at a more simple nomenclature have been proposed by G. D. Mendenhall and G. R. Newkome.[95, 96]

Hyperbranched dendrimers, in contrast to simple polydispersed, long-chain polymers, are unique macromolecular models for the study of a wide range of biological processes.[97] Because they are monodispersed, and have a highly ordered architecture, the properties of functional dendrimers can be easily correlated to their molecular dimension and topology. They are ideal artificial models of biomolecules such as proteins and enzymes and can be used to mimic biological processes that are inaccessible with lower molecular weight models.

1.2.2 Construction of dendrimers

Dendrimers are constructed in a stepwise manner in repeatable synthetic steps. Each repetition cycle creates an additional layer of branches, called *generation*. Branching multiplicity is dependent on the building block valency, although it can be generated during the growth step from a non-branched building block as well. In a four valent core, the number of functional groups at the periphery follows the rate 4, 8, 16, 32 when AB_2-type chain extenders are employed, or the rate 4, 12, 36, 108 for AB_3-type chain extenders, providing that the branching is perfect. Defects occur in branch errors. Errors that occur in the early stage of growth are generally more problematic than those occurring at higher generations, since defects in the dendrimer structure accumulate with each iteration. The problem is not the individual steps in a synthesis, but rather the number of successful reactions needed to be done on the same molecule. In addition, each synthesis is only specific to one particular dendrimer.

Two major synthetic approaches have emerged: the divergent approach where growth starts from the inside proceeding outwards (Scheme 1.9), and the convergent approach proceeding outside-in, i.e. by first producing *dendrons* which are coupled to a central branching unit (Scheme 1.10). Both methods require two steps for the growth of each generation: the activation of the dendritic unit and the addition of a new monomer.

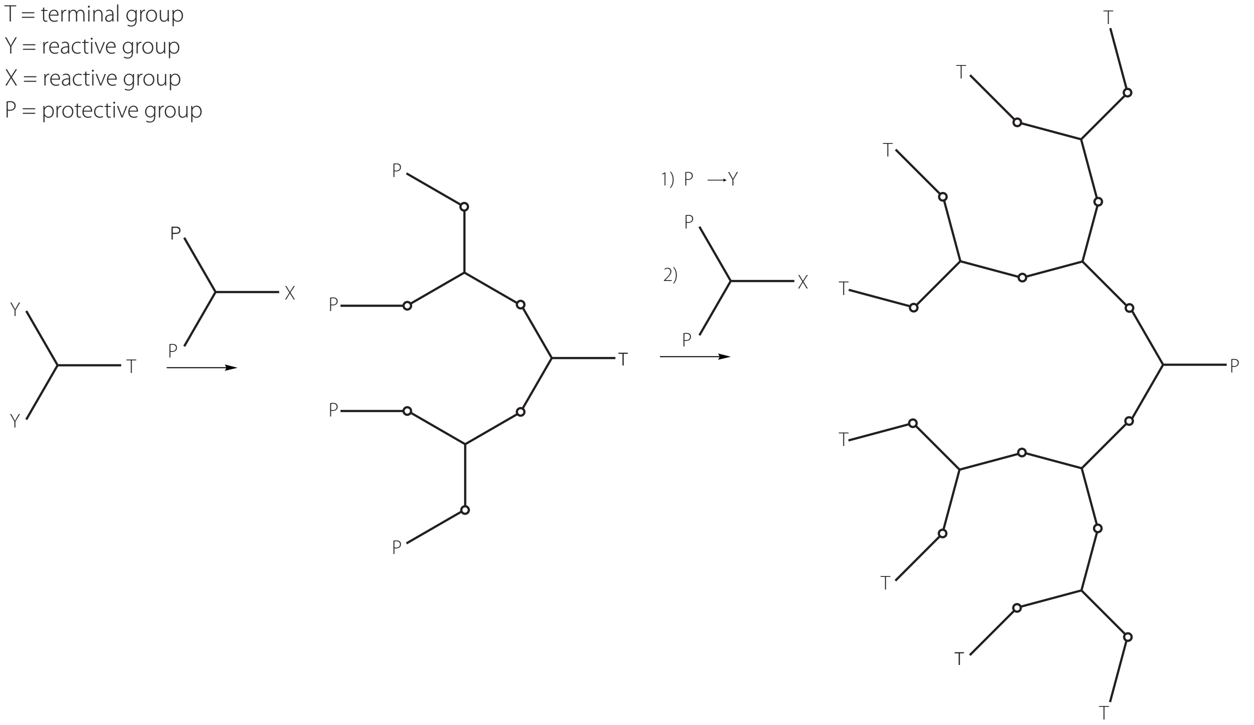
T = terminal group
Y = reactive group
X = reactive group
P = protective group
Y
Y
T
P
P
X
P
P
P
P
T
1) P → Y
2)
P
P
X
T
P

Scheme 1.9 Dendritic growth via a divergent approach with AB$_2$-type extenders. Protection/deprotection steps (P→Y) are not necessary if selective chemistry can be adopted. Dots represent the bonds formed between two reactive groups Y and X.

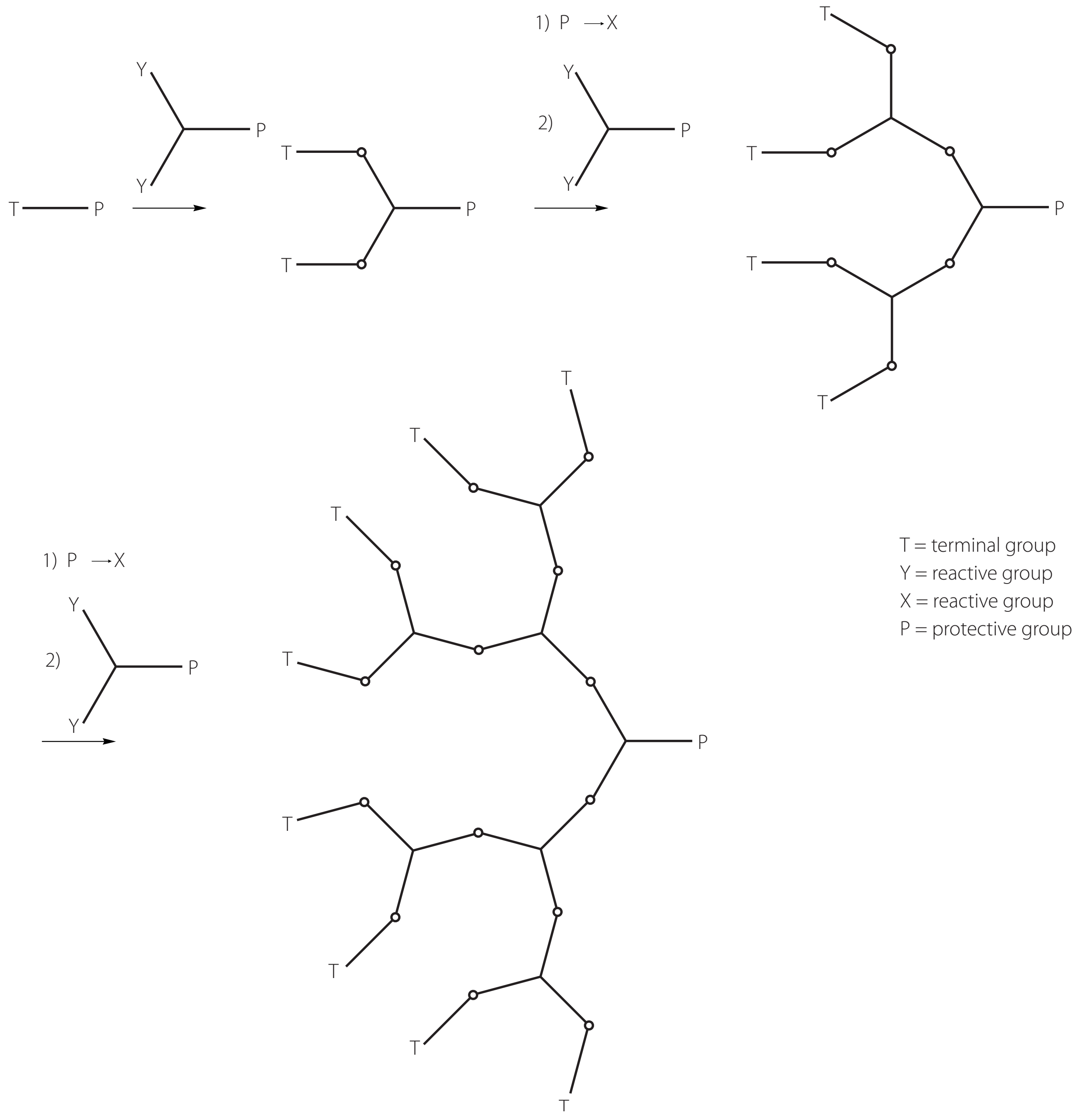
T — P
Y
Y
P
T
T
P
1) P →X
2)
Y
Y
P
T
T
T
T
T
T
P
1) P →X
2)
Y
Y
P
T
T
T
T
T
T
T
T
P
T = terminal group
Y = reactive group
X = reactive group
P = protective group

Scheme 1.10 Convergent route of a dendritic growth. Dots represent the bonds formed between two reactive groups Y and X.

Comparison of these methods shows that generally dendrimers prepared by the divergent approach are more polydispersed than those prepared by the convergent route.[97] Initial synthetic work were primarily directed towards the synthesis of dendritic macromolecules by a divergent methodology. In these cases, growth occurs from a central core by successive stepwise addition and activation steps which multiply the number of branches. A significant feature of this methodology is the rapid increase in the number of reactive groups at the periphery of the growing macromolecule. Potential problems which may arise as growth is pursued include incomplete reaction of these terminal groups – especially at higher generations when large numbers of reactions have to occur on a sterically hindered dendrimers surface – which would lead to imperfections in the next generation, or the large excess of reagents that are required to force reactions to completion. This, in turn, presents difficulties in purification.

The convergent method is usually limited to dendrimers of lower generations and yields due to the steric hindrance at the focal points of large dendrons. Extremely high yields and stoichiometric reactions are therefore necessary for every step.

1.2.3 Fréchet-type dendrimers

Fréchet-type dendrimers were the first example of dendrimers constructed by the convergent approach.[85, 98] The polyether dendritic fragments are prepared by starting from what will become the periphery of the molecule and progressing inward. In the first step, 2 equivalents of a benzylic bromide are condensed with the two phenolic groups of the monomer, 3,5-dihydroxybenzyl alcohol. After transformation of the benzylic alcohol functionality of the growing molecule into the corresponding leaving group (e. g. bromide or mesylate), the procedure is repeated with stepwise addition of the monomer followed again by activation of the benzylic site. This method of building up dendrimers has been established as the ideal system to construct dendrimers, when dendrimers of lower generations are needed. A very large number of studies has been made using Fréchet-type dendrimers. In this thesis, the solid-state structures of different Fréchet-type dendrimers were investigated and compared with their 2D self-assembled monolayers on graphite. The Fréchet-type dendrimers turned out to be ideal "chromophores" for STM imaging (see Chapter 7). Figure 1.18 shows an example of a solid-state structure of a bis(2,2':6',2''-terpyridine) cobalt(II) complex with first generation Fréchet-type dendrons attached at the 4'-position.[44]

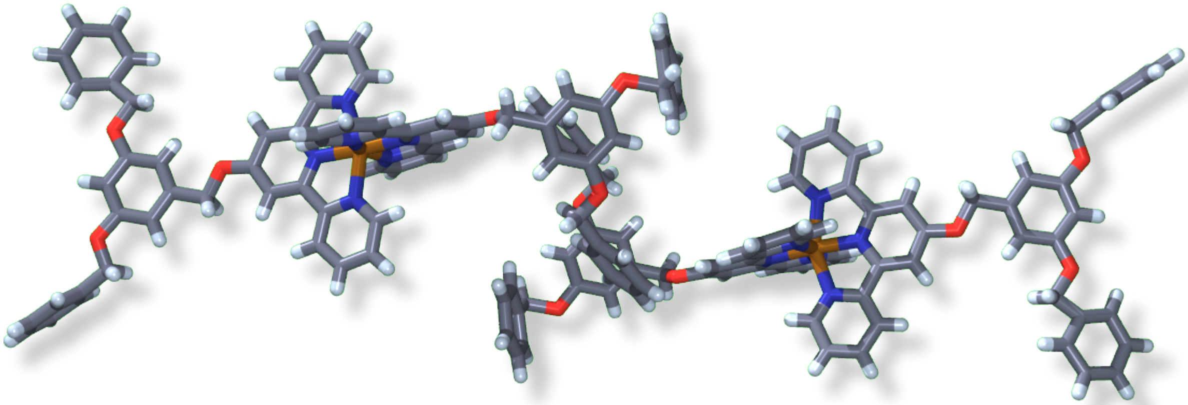

Figure 1.18 Two bis(2,2':6',2''-terpyridine) cobalt(II) complexes with a first generation Fréchet-type dendron attached at the 4'-position of the terpyridine unit.[44] Two T-shaped aryl(C–H)···π-phenyl interactions could be detected between the aryl groups of adjacent molecules.

1.3 References

[1] F. Wöhler, *Poggendorfs Ann. Physik* **1828**, *12*, 253.

[2] E. J. Corey, *Pure Appl. Chem.* **1967**, *14*, 19.

[3] E. J. Corey, X.-M. Cheng, *The logic of chemical synthesis*, Wiley, New York, **1989**.

[4] J.-M. Lehn, *Supramolecular Chemistry*, VCH, Weinheim, **1995**.

[5] M. Bergmann, *Z. Angew. Chem.* **1925**, *38*, 1141.

[6] E. Fischer, *Ber. Deutsch. Chem. Ges.* **1894**, *27*, 2985.

[7] P. Ehrlich, *Studies on Immunity*, Wiley, New York, **1906**.

[8] A. Werner, *Z. Anorg. Chem.* **1893**, *3*, 267.

[9] R. J. E. Cumberbirch, *Rep. Prog. Appl. Chem.* **1961**, *46*, 233.

[10] S. H. Zeronian, *Rep. Prog. Appl. Chem.* **1965**, *50*, 521.

[11] P. Mitchell, *Nature* **1961**, *191*, 144.

[12] A. L. Lehninger, *Naturwissenschaften* **1966**, *53*, 57.

[13] K. L. Wolf, H. Frahm, H. Harms, *Z. Phys. Chem.* **1937**, *Abt. B 36*, 237.

[14] K. L. Wolf, H. Dunken, K. Merkel, *Z. Phys. Chem.* **1940**, *Abt. B 46*, 287.

[15] K. L. Wolf, R. Wolff, *Angew. Chem.* **1949**, *61*, 191.

[16] C. J. Pedersen, *J. Am. Chem. Soc.* **1967**, *89*, 7017.

[17] B. Dietrich, J.-M. Lehn, J.-P. Sauvage, *Tetrahedron Lett.* **1969**, 2885.

[18] B. Dietrich, J.-M. Lehn, J.-P. Sauvage, J. Blanzat, *Tetrahedron* **1973**, *29*, 1629.

[19] B. Dietrich, J.-M. Lehn, J.-P. Sauvage, *Tetrahedron* **1973**, *29*, 1647.

[20] J.-M. Lehn, *Struct. Bonding* **1973**, *16*, 1.

[21] D. J. Cram, J. M. Cram, *Science* **1974**, *183*, 803.

[22] J.-M. Lehn, *Pure Appl. Chem.* **1978**, *50*, 871.

[23] J.-M. Lehn, *Angew. Chem. Int. Ed.* **1988**, *27*, 89.

[24] I. Dance, *New J. Chem.* **2003**, *27*, 1.

[25] P. A. Brady, R. P. Bonar Law, S. J. Rowan, C. J. Suckling, J. K. M. Sanders, *Chem. Commun.* **1996**, 319.

[26] L. Pauling, *The Nature of the Chemical Bond*, 2 ed., Cornell University Press, Ithaca, **1939**.

[27] http://www.ccdc.cam.uk/products/csd/.

[28] http://www.rosb.org/pdb/.

[29] M. Mammen, S.-K. Chio, G. M. Whitesides, *Angew. Chem. Int. Ed.* **1998**, *37*, 2755.

[30] G. Ercolani, *J. Am. Chem. Soc.* **2003**, *125*, 16097.

[31] J. J. Lundquist, E. J. Toone, *Chem. Rev.* **2002**, *102*, 555.

[32] P. I. Kitov, D. R. Bundle, *J. Am. Chem. Soc.* **2003**, *125*, 16271.

[33] J. D. Badjic, A. Nelson, S. J. Cantrill, W. B. Turnbull, J. F. Stoddart, *Acc. Chem. Res.* **2005**, *38*, 723.

[34] Y. C. Lee, R. T. Lee, *Acc. Chem. Res.* **1995**, *28*, 321.

[35] T. Steiner, *Angew. Chem. Int. Ed.* **2002**, *41*, 48.

[36] G. Gilli, P. Gilli, *J. Mol. Struct.* **2000**, *552*, 1.

[37] J. D. Dunitz, A. Gavezzoti, *Angew. Chem. Int. Ed.* **2005**, *44*, 1766.

[38] R. K. Castellano, *Curr. Org. Chem.* **2004**, *8*, 845.

[39] G. R. Desiraju, *Acc. Chem. Res.* **2002**, *35*, 565.

[40] T. Steiner, A. M. M. Schreurs, M. Lutz, J. Kroon, *New J. Chem.* **2001**, *25*, 174.

[41] J. Langlet, P. Claverie, F. Caron, J. C. Boeuve, *Int. J. Quantum. Chem.* **1981**, *19*, 299.

[42] S. L. Price, A. J. Stone, *J. Phys. Chem.* **1987**, *86*, 2859.

[43] C. A. Hunter, J. K. M. Sanders, *J. Am. Chem. Soc.* **1990**, *112*, 5525.

[44] E. C. Constable, C. E. Housecroft, M. Neuburger, S. Schaffner, L. J. Scherer, *Dalton Trans.* **2004**, 2635.

[45] G. R. Desiraju, *Angew. Chem. Int. Ed.* **1995**, *34*, 2311.

[46] E. C. Constable, M. D. Ward, D. A. Tocher, *J. Chem. Soc., Dalton Trans.* **1991**, 1675.

[47] S. Rüttimann, C. Piguet, G. Bernardinelli, B. Bocquet, A. F. Williams, *J. Am. Chem. Soc.* **1992**, *114*, 4230.

[48] T. M. Garret, U. Koert, J.-M. Lehn, A. Rigault, D. Meyer, J. Fischer, *J. Chem. Soc., Chem. Commun.* **1990**, 557.

[49] E. C. Constable, M. D. Ward, *J. Am. Chem. Soc.* **1990**, *112*, 1256.

[50] O. Mamula, A. Von Zelewsky, G. Bernardinelli, *Angew. Chem. Int. Ed.* **1998**, *37*, 290.

[51] E. Stulz, S. M. Scott, A. D. Bond, S. J. Teat, J. K. M. Sanders, *Chem. –Eur. J.* **2003**, *9*, 6039.

[52] K. S. Chichak, S. J. Cantrill, A. R. Pease, S.-H. Chiu, G. W. V. Cave, J. L. Atwood, J. F. Stoddart, *Science* **2004**, *304*, 1308.

[53] S. J. Cantrill, K. S. Chichak, A. J. Peters, J. F. Stoddart, *Acc. Chem. Res.* **2005**, *38*, 1.

[54] D. J. Duchamp, R. E. Marsh, *Acta Crystallogr.,Sect.B* **1969**, *25*, 5.

[55] F. H. Herbstein, M. Kapon, V. Shteiman, *Acta Crystallogr.,Sect.B* **2001**, *57*, 692.

[56] B.-Q. Ma, P. Coppens, *Chem. Commun.* **2003**, 2290.

[57] S. Griessl, M. Lackinger, M. Edelwirth, M. Hietschols, W. M. Heckl, *Single Mol.* **2002**, *1*, 25.

[58] S. Griessl, M. Lackinger, F. Jamitzky, T. Markert, M. Hietschold, W. M. Heckl, *Langmuir* **2004**, *20*, 9403.

[59] Z. Li, B. Han, L. J. Wan, T. Wandlowski, *Langmuir* **2005**, *21*, 6915.

[60] B. J. Gyarfas, B. Wiggins, M. Zosel, K. W. Hipps, *Langmuir* **2005**, *21*, 919.

[61] M. Lackinger, S. Griessl, W. M. Heckl, M. Hietschold, G. W. Flynn, *Langmuir* **2005**, *21*, 4984.

[62] J. L. Atwood, G. A. Koutsantonis, C. L. Raston, *Nature* **1994**, *368*, 229.

[63] G.-B. Pan, J.-M. Liu, H.-M. Zhang, L.-J. Wan, Q.-Y. Zheng, C.-L. Bai, *Angew. Chem. Int. Ed.* **2003**, *42*, 2747.

[64] S. De Feyter, F. C. De Schryver, *Chem. Soc. Rev.* **2003**, *32*, 139.

[65] S. De Feyter, F. C. De Schryver, *J. Phys. Chem. B* **2005**, *109*, 4290.

[66] L. C. Giancarlo, G. W. Flynn, *Acc. Chem. Res.* **2000**, *33*, 491.

[67] H. Ohtani, R. J. Wilson, S. Chiang, C. M. Nate, *Phys. Rev. Lett.* **1988**, *60*, 2398.

[68] P. Jonkheijm, A. Miura, M. Zdanowska, F. J. M. Hoeben, S. De Feyter, A. P. H. J. Schenning, F. C. De Schryver, E. W. Meijer, *Angew. Chem. Int. Ed.* **2004**, *43*, 74.

[69] R. P. Feynman, *The Pleasure of Finding Things Out*, Perseus Books, Cambridge, MA, **1999**.

[70] S. Zhang, *Mater. Today* **2003**, *6*, 20.

[71] Y. Liu, A. H. Flood, P. A. Bonvallet, S. A. Vignon, B. H. Northrop, H.-R. Tseng, J. O. Jeppesen, T. J. Huang, B. Brough, M. Baller, S. Magonov, S. D. Solares, W. A. Goddard, C.-M. Ho, J. F. Stoddart, *J. Am. Chem. Soc.* **2005**, *127*, 9745.

[72] A. Livoreil, C. O. Dietrich-Buchecker, J.-P. Sauvage, *J. Am. Chem. Soc.* **1994**, *116*, 9399.

[73] P. J. Flory, *J. Am. Chem. Soc.* **1941**, *63*, 3083.

[74] W. H. Stockmayer, *J. Phys. Chem.* **1943**, *46*, 45.

[75] J. R. Schaefgen, P. J. Flory, *J. Am. Chem. Soc.* **1948**, *70*, 2709.

[76] P. J. Flory, *J. Am. Chem. Soc.* **1952**, *74*, 2718.

[77] E. Buhleier, W. Wehner, F. Vögtle, *Synthesis* **1978**, *2*, 155.

[78] R. G. Denkewalter, J. Kolc, W. J. Lukasavage, US Patent 4,289,872, **1981**.

[79] R. G. Denkewalter, J. Kolc, W. J. Lukasavage, US Patent 4,360,646, **1982**.

[80] R. G. Denkewalter, J. Kolc, W. J. Lukasavage, US Patent 4,410,688, **1983**.

[81] D. A. Tomalia, H. Baker, J. R. Dewald, M. Hall, G. Kallos, S. Martin, J. Roeck, J. Ryder, P. Smith, *Polym. J. (Tokyo)* **1985**, *17*, 117.

[82] D. A. Tomalia, H. Baker, J. R. Dewald, M. Hall, G. Kallos, S. Martin, J. Roeck, J. Ryder, P. Smith, *Macromolecules* **1986**, *19*, 2466.

[83] D. A. Tomalia, M. Hall, D. M. Hedstrand, *J. Am. Chem. Soc.* **1987**, *109*, 1601.

[84] G. R. Newkome, C. N. Moorefield, G. R. Baker, *Aldrichimica Acta* **1992**, *25*, 31.

[85] C. J. Hawker, J. M. J. Fréchet, *J. Am. Chem. Soc.* **1990**, *112*, 7638.

[86] T. M. Miller, T. X. Neenan, *Chem. Mater.* **1990**, *2*, 346.

[87] T. M. Miller, T. X. Neenan, R. Zayas, H. E. Bair, *J. Am. Chem. Soc.* **1992**, *114*, 1018.

[88] J. Moore, Z. Xu, *Macromolecules* **1991**, *24*, 5893.

[89] Z. Xu, J. Moore, *Angew. Chem. Int. Ed.* **1993**, *32*, 246.

[90] Z. Xu, J. Moore, *Angew. Chem. Int. Ed.* **1993**, *32*, 1354.

[91] E. M. M. Brabander-van den Berg, E. W. Meijer, *Angew. Chem. Int. Ed.* **1993**, *32*, 1308.

[92] H.-B. Meckelburger, W. Jaworek, F. Vögtle, *Angew. Chem. Int. Ed.* **1992**, *31*, 1571.

[93] J. Issberner, R. Moors, F. Vögtle, *Angew. Chem. Int. Ed.* **1994**, *33*, 2413.

[94] N. Feuerbacher, F. Vögtle, *Top. Curr. Chem.* **1998**, *197*, 1.

[95] G. D. Mendenhall, S. X. Liang, E. H.-T. Chen, *J. Org. Chem.* **1990**, *55*, 3607.

[96] G. R. Baker, J. K. Young, in *Advances in dendritic macromolecules, Vol. 1* (Ed.: G. R. Newkome), JAI Press, **1994**.

[97] M. L. Mansfield, *Macromolecules* **1993**, *26*, 3811.

[98] C. J. Hawker, J. M. J. Fréchet, *J. Chem. Soc., Chem. Commun.* **1990**, 1010.

For the great things are not done by impulse, but by a series of small things brought together.

Vincent van Gogh

2 Methods and Instruments

In the first part of this Chapter, the instruments used for characterising the compounds are presented. In the second part, STM is introduced and artefacts occurring during the STM measurements are discussed. At the end of this Chapter, the processes and programs used to obtain STM images from the raw data are presented.

2.1 General experimental

Chemicals

If not otherwise noted, the chemicals were commercially available and used without further purification.

NMR Spectroscopy

^{1}H NMR spectra were recorded on Bruker AM250 (250 MHz), Bruker DRX400 (400 MHz), Bruker DRX500 (500 MHz) and on Bruker DRX600 (600 MHz). For full assignments COSY, DEPT, HMBC and HMQC experiments were recorded on the Bruker DRX500 by either V. Jullien or K. Kulicke. The measurements on the Bruker DRX600 were conducted by D. Häussinger. In the ^{1}H and ^{13}C NMR measurements, δ is relative to TMS, internally referenced to solvent; in the ^{31}P NMR spectra, δ is relative to H_3PO_4.

Mass Spectrometry

ESI mass spectra were recorded on a Bruker Esquire 3000 plus instrument at 250 °C if not noted otherwise. MALDI-TOF spectra were recorded on a Vestec Voyager Elite instrument. When a matrix was used, it is given in parenthesis. FAB mass spectra were conducted on a Finnigan MAT 312 and 3-nitrobenzyl alcohol was used as supporting matrix. EI mass spectra were measured on a Finnigan MAT 95Q apparatus. The bias is given in parenthesis. Both FAB and EI measurements were conducted by P. Nadig.

Infrared Spectroscopy

IR spectra were recorded on a Shimadzu FTIR-8400S spectrophotometer with neat samples using a golden gate attachement. If the sample was too oily to handle it neat, a solution was placed on the gate and the solvent was evaporated.

UV-vis Spectroscopy

UV-vis spectra measurements were performed using a Perkin-Elmer Carey 5000 spectrophotometer. The solvent is given in parenthesis.

Microanalysis

The microanalyses were performed with a Leco CHN-900 microanalyser by W. Kirsch.

Electrochemistry

Electrochemical measurements were done with an Eco Chemie Autolab PGSTAT 20 system using glassy carbon working and auxiliary electrodes with an Ag/AgCl electrode as reference using acetonitrile (dried over molecular sieves 4Å) as solvent and 0.1 M $[n\text{-Bu}_4\text{N}][\text{PF}_6]$ as supporting electrolyte; ferrocene was added at the end of each experiment as an internal reference.

Differential Scanning Calorimetry

The differential scanning calorimetry measurements were performed using a Perkin Elmer DSC 6 apparatus.

Optical Polarised Microscopy

Optical polarised microscopy experiments were done using a Leica DM L microscope.

X-ray diffraction

The determination of the cell parameters and the collection of the reflection intensities of the single crystals were performed on an Enraf-Nonius Kappa CCD diffractometer (graphite monochromated $\text{Mo}_{K\alpha}$ radiation) by M. Neuburger. For the data reduction, solution and refinement the programs COLLECT,[1] SIR97,[2] and CRYSTALS (version12)[3] were used. This was done either by M. Neuburger or S. Schaffner. The data processing of the .cif-file so obtained is explained in Section 2.3.1.

2.2 Scanning probe microscopy

2.2.1 Overview

Scanning probe microscopy (SPM) covers a lateral range of imaging from several 100 µm to 10 pm. Surfaces of solids can be mapped with atomic resolution, revealing not only the structure of perfect crystalline surfaces but also the distribution of point defects like steps. SPM has become an essential tool in the emerging field of nanoscience, as local experiments with single atoms or molecules can be performed. Furthermore, the local probe can be used to manipulate single atoms or molecules and hence to form artificial structures on the atomic scale.[4]

The starting point of SPM was the invention in 1982 of the scanning tunnelling microscope (STM) by G. Binnig and H. Rohrer,[5, 6] who were awarded the Nobel prize for Physics in 1986.

The family of scanning probe microscopes has several members, based on a variety of tip–sample interactions. The first and most important extension of the STM was the scanning force microscope, invented in 1986 by G. Binnig, C. F. Quate and C. Gerber.[7] In this modus, the tip height is controlled in such a way that the force between tip and sample is constant. While the use of the STM is restricted to at least weakly conducting surfaces, the scanning force microscopy is in principle capable of determining the topography of any surface, conducting or not. Based on the assumption that forces between the atoms at the tip apex and the atoms of the surface determine the resolution of this instrument, it is commonly called atomic force microscopy (AFM). The third distinguished member of the family of SPMs is the scanning near-field optical microscope (SNOM), which uses short-range components of the electromagnetic field as tip–sample interaction.[4, 8, 9]

Another important strength of SPM beyond topographic imaging and local measurements of surface properties is the manipulation of surfaces. Single atoms of the surface or adsorbates on it have been systematically moved in STM in order to build nanometer-sized structures (Figure 2.1). This can be accomplished by pushing or pulling the atoms with the tip, or even by transfer of atoms to and from the tip. Such experiments establish a lithography on the molecular scale.[10] Another perspective of imaging under ambient conditions are *in-situ* studies of surface processes. Such processes can also be investigated under controlled electrochemical potential by means of special electrochemical cells. In the literature the technique is often referred to as electrochemical STM.[8] The electrochemical STM has already been used successfully to study processes at electrode surfaces down to atomic scale.[11, 12] The STM is not the only tool for surface manipulation. The tip of an SFM can be used to deposit charges on insulating samples, or to study microscopic effects by scratching the surface. Single molecules can be optically bleached by a SNOM. All these examples share the fact that the results and effects of manipulation are studied with the same tip that was used as a tool to perform it.

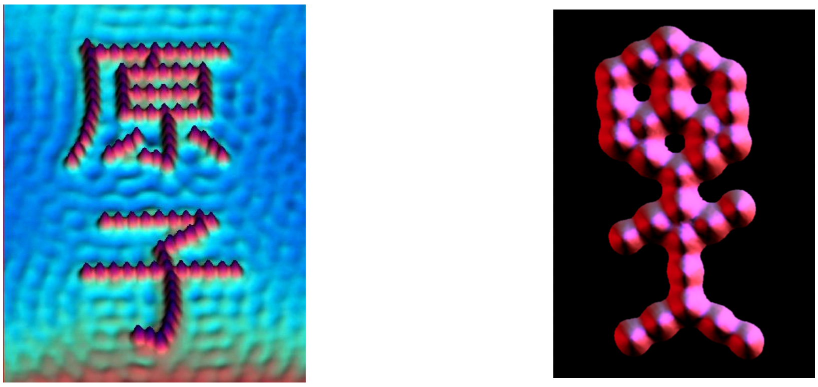

(a) (b)

Figure 2.1 Two STM images after manipulating the surface with an STM-tip. (a) "Atom" was written in Chinese with single iron atoms on copper. (b) A "nanoman" was constructed with single CO molecules on a platinum surface.[13]

Scanning probe microscopy has found wide applications in surface science, where problems like surface structure, adsorption of molecules, or local electronic properties may be studied. The first nanostructures have been built atom-by-atom and characterised. More industrial applications include surface control in materials science. Roughness and hardness are being measured on the nanometer scale. Magnetic structures on data storage devices can be analysed as well as the optical quality of coatings. The microscopic origins of friction have been investigated by SFM. Force microscopy allows nanometer-scale imaging of biological and non-biological nano-sized materials which are not accessible to electron microscopy for preparative reasons. Beyond imaging, force measurements between functional molecular groups have stimulated great interest in supramolecular chemistry and in biophysics.[4]

2.2.2 Scanning tunnelling microscopy

In STM, a sharp metallic needle is scanned over the surface at a distance of less than 1 nm. This distance is controlled by the tunnelling current between the tip and the conducting surface. The tunnelling current is a quantum mechanical effect, with two properties important for STM. Firstly, it flows between two electrodes through a thin insulator or a vacuum gap, and it decays roughly by a factor of 450 on a length scale of one atomic radius. Secondly, therefore in STM, the tunnelling current flows from the very last atom of the tip apex to single atoms at the surface, inherently providing atomic resolution.[4, 8]

Therefore, STM does *not* measure the real topography of the surface, but rather a surface of constant tunneling probability, which is connected with the local density of state near the Fermi level. For example, a molecule adsorbed on top of a metal surface may reduce the local density of states and may actually be imaged as a depression, as e. g. carbon on nickel(100).[14] D. Eigler *et al.* used this peculiarity of STM to image standing electron waves on a copper surface, confined by a corral of deposited iron atoms (Figure 2.2).[15, 16]

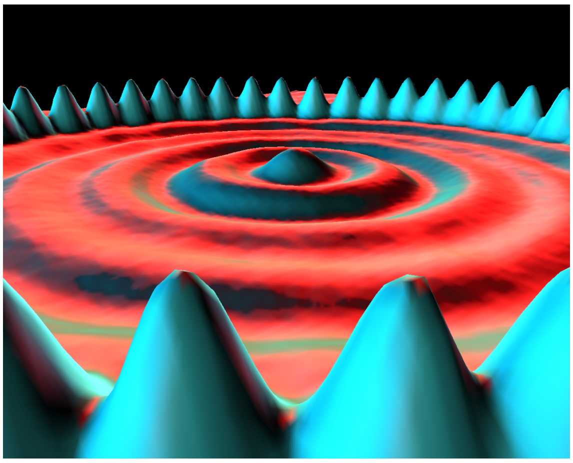

Figure 2.2 48 iron atoms were positioned into a circular ring in order to "corral" some surface state electrons and forced them into standing waves inside the cicular structure. [17]

2.2.2.1 Mode of operation

In a standard experiment (Figure 2.3), the tip is moved in three dimensions by piezoelectric actuators. Using the combination of a coarse approach and piezoelectric transducers, a sharp, metallic probing tip is brought into close proximity with the sample. The distance between tip and sample is only a few ångstrøm units, which means that the electron wave functions of tip and sample start to overlap. A bias voltage between tip and sample causes electrons to tunnel through the barrier. An electronic controller guides the tip at a tip–sample distance corresponding to a constant tunnelling current. The tunnelling current is in the range of pA to nA and is measured with a preamplifier. This signal is the input signal of the feedback loop, which is designed to keep the tunnelling current constant during (x, y)-scanning. The output signal is amplified and connected to the z-piezo. According to the feedback output voltage and the sensitivity of the piezo, the tunnelling tip is moved backwards and forwards and the tunnelling current is kept constant during acquisition of the image. The z-position is measured at discrete (x, y)-positions. This distance is recorded by a computer as a function of the lateral position and displayed as a microscope image. This operation is called *constant current* mode. There exist other modes, such as the *constant height* mode, where the tip is moved at constant height and variations in the current are measured.

Generally, the (x, y)-movement of the tip is controlled by a computer. High mechanical stability of the experimental setup turns out to be a prerequisite for successful measurements on the atomic scale.[4,8]

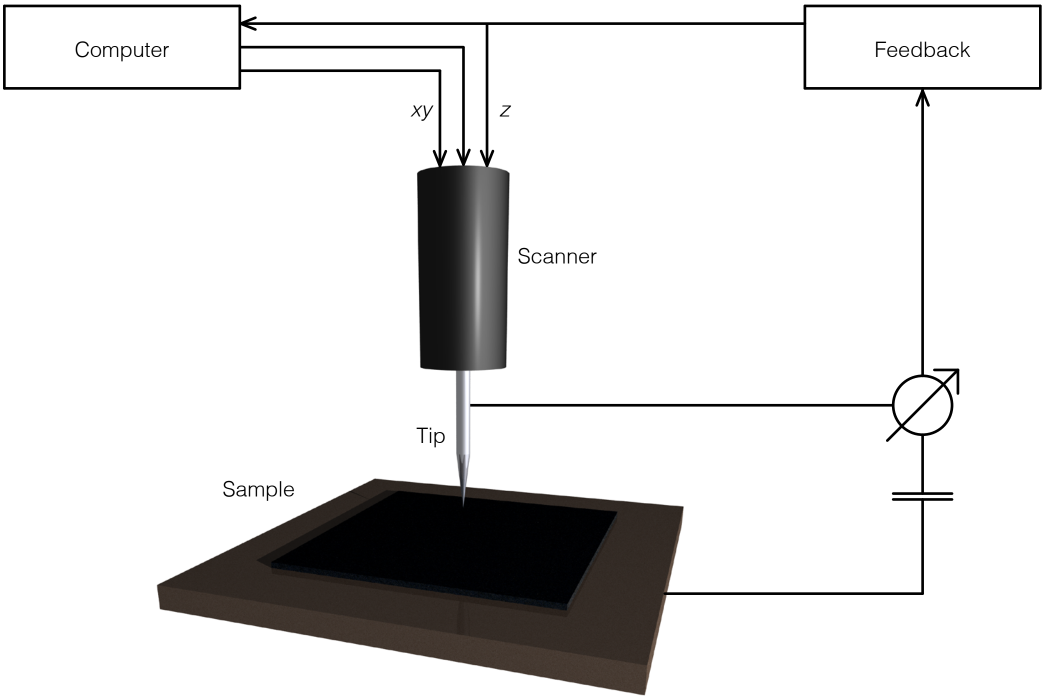

Figure 2.3 Basic setup for an STM measurement. The difference in the tunnelling current to the setpoint is used to control the tip–sample distance *z* via a feedback circuit. The distance *z* is recorded by a computer as a function of the scanned coordinates *x* and *y*. Good vibrational isolation of the experiment is a prerequisite for high-resolution imaging.

The tip has to be conducting, should have as little electronic structure around the Fermi-level as possible, and it has to be atomically sharp. All tips used for the measurements of this thesis were made of mechanically cut platinum:iridium wire (90:10, d = 0.25 mm). The shape of the tip is not that critical, because the tunnelling current I_t decays exponentially with the distance between tip and sample, as a consequence the tunnelling current flows mainly trough the atom at the very end of the tip. It is necessary to position the tip at sub-Å precision in the *z*-direction.

As already mentioned, the scanner is made of a piezoelectric actuator. Single crystalline piezoelectric materials elongate or compress their shape in an electric field. They are anisotropic materials, what means that they change the shape depending on the direction of the electric field. This effect is due to the fact that some atoms in the crystal packing undergo some changes in their position when an electric field is applied to it.[18] The standard material for piezoelectric actuators in SPMs is PZT (lead zirconium titanate).[4] Above a specific temperature, called the Curie temperature, the lattice has a cubic, perovskite-like structure consisting of regularly arranged oxygen cubic units in the centre of which the titanium or zirconium is placed (Figure 2.4). Below the Curie temperature the perovskite-like lattice structure reorders in such a way that the titanium or zirconium is no longer placed in the centre and so a separation of charges takes place and electrical dipoles are formed. Using the transverse piezoelectric effect, the length of a bar of material can be adjusted by applying a voltage to electrodes attached to its side wall. The 3D positioning of the scanning probe can be obtained by three piezoelectric bars in an orthogonal assembly.[19]

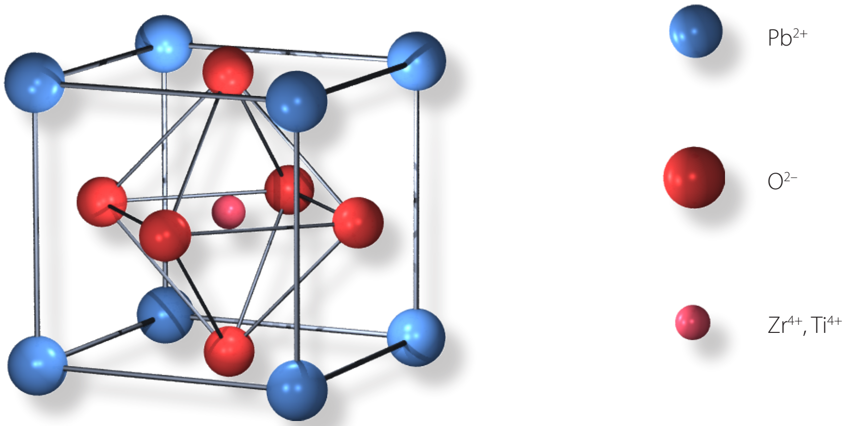

Figure 2.4 The basic perovskite-like structure of lead zirconium titanate. Below the Curie temperature, the lattice structure reorders in which the central atom (Ti^{4+} or Zr^{4+}) is no longer placed in the centre and so a separation of charges takes place and electrical dipoles are formed.

The data $z(x_i, y_i)$ can be displayed in several ways. The grey-scale scan image was used for all images obtained during this thesis. Bright spots represent hillocks or protrusions and dark spots represent valleys or depressions.

The STM experiments for this thesis were all carried out in constant current mode using a NanoscopeIII, Digital Instruments (Figure 2.5) equipped with a low current converter, that is capable of measuring currents below 10 pA under ambient conditions (air, “room temperature” – as will be shown in Chapter 5, warming of the scan head during measurements up to about 35 °C can significantly influence the ordering).

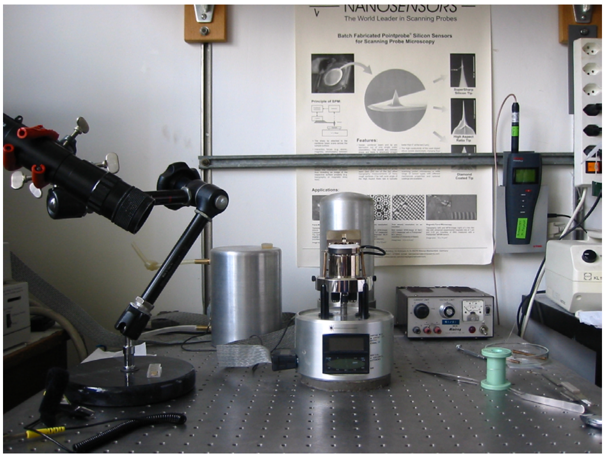

Figure 2.5 The NanoscopeIII (Digital Instruments) used for conducting STM measurements in this thesis. The measurements were performed under ambient conditions.

2.2.2.2 Substrates used for STM measurements

One of the most exciting applications of STM is the imaging of adsorbates and single molecules on surfaces. J. S. Foster *et al.* first presented images of single molecules.[20] The surface onto which the compound of interest is placed is called the *substrate*. For STM measurements, the substrates have to be weakly conductive and atomically flat as well as clean. Measurements in ambient air demand additionally an inert substrate. Since the measurements conducted for this thesis are all measured on a flat graphite surface, other possible substrates (e. g. copper, platinum or gold) are not described here.

Graphite

The graphite is commercially available as highly oriented pyrolytic graphite (HOPG). The advantages of HOPG are its easy preparation to obtain a flat surface and its inertness. A few layers are cleaved off with adhesive tape shortly before the use. This treatment results in clean, atomically flat terraces. The used HOPG is α-graphite. That means that the layers are stacked in an ABA pattern. Therefore, only every second carbon atom has a nearest neighbour (orthogonal below the layer) in the layer below. This is clearly visible in STM, where only three atoms (out of a hexagon) can be seen (Figure 2.6).[21-23]

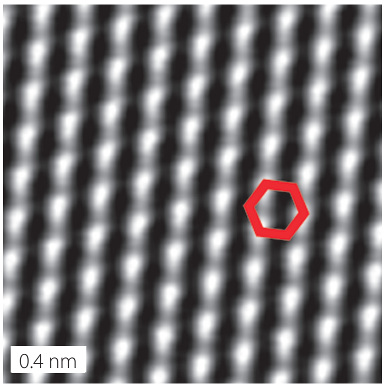

Figure 2.6 A 5 nm x 5 nm STM image of a HOPG surface. One single hexagon of a graphite layer is marked in red. Only three carbon atoms (out of six) are visible. Scan parameters: $U_b = -700$ mV, $I_t = 300$ pA.

Hence, the graphite surface has a *threefold* symmetry, not a sixfold as expected from a single layer. This often results in three symmetrical arrangements of domains of molecular monolayers.[24-26] Graphite is the easiest substrate to handle, but the most dangerous in respect of artefacts.

2.2.2.3 Sample preparation

Each measurement technique requires specific substrates and preparation methods. Three different methods of preparation were used in this thesis to obtain molecular assemblies on the HOPG surface. The formation of a monolayer out of a Langmuir-Blodget film is discussed in Section 3.5.

Solution casting

Solution casting was the most frequently used method to obtain a monolayer in this thesis. If not otherwise noted, this preparation is used.

A dilute solution of the compound (≈0.2 mM) was prepared. Hexane was the most commonly used solvent, since most compounds studied dissolved very well in hexane. For metal bis(tpy) complexes, acetonitril was used. If another solvent was used it is noted in the figure capture. One droplet of this solution was then placed on a freshly cleaved graphite surface (see Section 2.2.2.2) of an area of about 10 mm^2. The solvent was then allowed to evaporate.

As a consequence of the gradual evaporation of the droplet, the concentration increases and a gradient of concentrations is formed on the surface ("coffee-cup effect").[28] The monolayer so formed can be regarded as a 2D imprint of the preformed organisation in solution (Chapter 5), as opposed, e. g., to vapour phase deposition.

The so formed monolayer can also be *annealed*. This means that the substrate with the self-assembled monolayer is heated in an oven for a period of time before measuring.

Solid–liquid interface

Another possibility for measuring self-assembled monolayers is at the solid–liquid interface. As described for "solution casting", one droplet of a ≈0.2 mM solution was placed on the graphite surface. The measurement was then carried out by positioning the tip into the solution and the measurements were conducted in the solution.

The organic solvents used at the liquid–solid interface comply with the following criteria: (a) they must have a suitable vapour pressure to allow the performance of the STM measurements in only a drop of liquid without the need of a closed cell, (b) they are electrochemically inert under the experimental conditions (c) they solubilise the compound of interest, and (d) they have a low affinity for adsorption on the substrate used.

In this thesis, 1-phenyloctane was always used. Other possible solvents are e. g. 1-octanol, 1-octanoic acid, 1-phenyltetradecane or dodecane. With all of these solvents criterium (d) is not fulfilled since alkyl chains interact with graphite.[29, 30] Therefore, a co-adsorption with the molecule on the surface can take place.[31-35]

2.2.2.4 Artefacts and peculiarities of the graphite surface

For STM measurements, certain limitations and possible sources of artefacts should be addressed. First of all, the influence of the tip on the data obtained should be noted. In the case of STM, both electronic and geometric effects must be considered. Moiré-patterns (Figure 2.7) of the graphite have been observed with and without monolayers. The Moiré-pattern is a result of one or more graphite layers which are slightly moved and therefore the graphite shows a superstructure.[27]

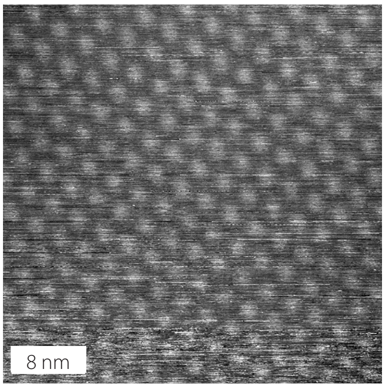

Figure 2.7 A typical Moiré-pattern. Scan parameters: 40 nm x 40 nm, $U_b = -800$ mV, $I_t = 9$ pA.

Another peculiarity which was quite often observed were stripes as shown in Figure 2.8. These stripes were never visualised on pure graphite. The dimensions of the stripes did not depend on the compound forming the self-assembled monolayer. Interestingly, S.-B. Lei *et al.* interpreted a very similar pattern as a self-assembly ordering of their deposited polymer on graphite.[36]

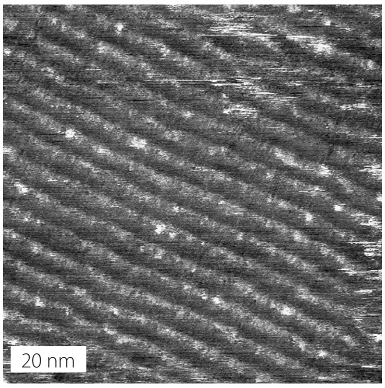

Figure 2.8 A typical striped pattern as it was often observed for various self-assembled monolayers. The dimensions did not depend on the compound and therefore it could be concluded that the stripes are not representing the monolayer. Scan parameters: 100 nm x 100 nm, $U_b = -700$ mV, $I_t = 8.33$ pA.

Sometimes, graphite steps can lead to misinterpretation. The domains normally end at a graphite step and do not continue afterwards as illustrated in Figure 2.9.

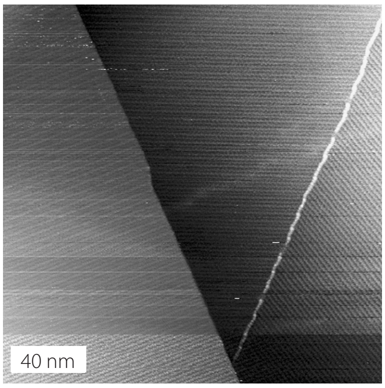

Figure 2.9 A graphite step from the upper left to the lower right. On the next graphite layer, a new domain started. The resolution depends significantly on the tip as can be seen in the lower part of the STM image. Scan parameters: 200 nm x 200 nm, $U_b = -800$ mV, $I_t = 8$ pA.

Sometimes, bright spots arranged in lines could be detected (Figure 2.10). The fact that they were observed with different compounds in the same size, implies that they did not arise from single molecules. In Figure 2.10, the spotted line was imaged double what could be attributed as a double STM tip.[4]

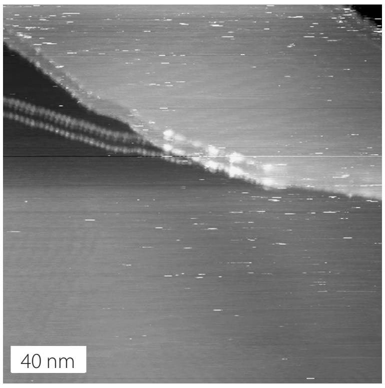

Figure 2.10 On the upper half of the image, parallel lines of bright spots can be seen. The multiplicity of the stripes could be attributed to a multiple STM tip. Scan parameters: 200 nmx 200 nm, $U_b = -800$ mV, $I_t = 8$ pA.

Since all the measurements were conducted at room temperature, thermal drift of the monolayer was often a problem for their interpretation (Figure 2.11). The drift could be controlled by recording two following images, one in up direction and one in down direction. The selected images of this thesis showed practically no drift, if not otherwise noted.

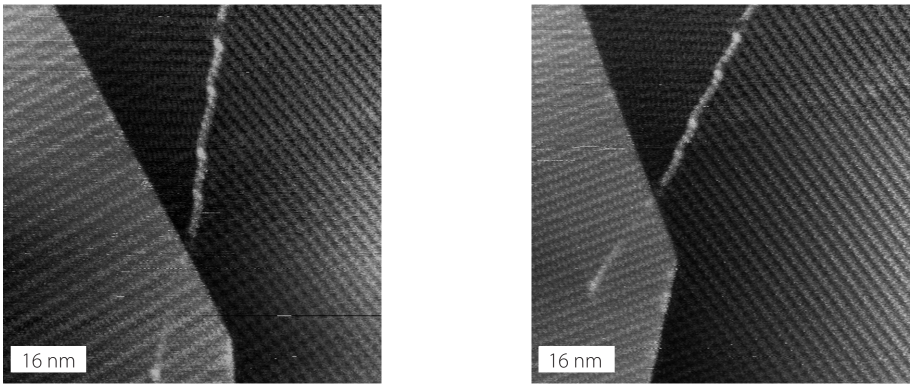

(a) (b)

Figure 2.11 Two images of a monolayer of compound **10**, recorded in up and down direction (see Section 4.2). It can be clearly seen that (a) and (b) look quite different, not only because the left domain has moved upwards, but also because the dimensions of the rows differ. The white spotted line crossing the image is an artefact similar to the lines discussed in Figure 2.10.

2.3 Data processing

In this section, it will be shown how the raw data are processed to obtain images displayed in this thesis. In a first part it is shown how images of the X-ray data were made and in a second part the analysis of self-assembled monolayers is explained.

2.3.1 Using X-ray data to prepare figures for overlay on STM images

The .cif-file of the crystal-data was processed using Mercury.[37] In Mercury, e.g. layers can be cut from the crystal structure. Usually, the files obtained in Mercury were saved as .mol2-files, which can be opened in different softwares as e.g. ChemDraw,[38] ViewerLite[39] or Spartan.[40] In these software programs, the .mol2-files could be saved as .pdb-files. Special attention should be paid since not all the programs write the same .pdb-files, and sometimes bonds are not recognised. Spartan was most often used, since the .pdb-file could be read without problems by PovChem.[41] PovChem writes .pov-files which can then be rendered in POV-Ray.[42] Subsequently, .bmp-image files were created, which were sometimes further processed using Adobe Photoshop[43] and then saved as .tif-files.

2.3.2 STM data

Most data processings in this thesis were done with the program SXM-Shell which was designed and written at the University of Basel. A few basic manipulations shall be explained:

Data substraction

The relevant STM data span only a few ångstrøms in height, the colour code dark to light is restricted in the z-histogram, so that the fine differences in z become visible. This data subtraction was done for all the images in this thesis.

Flattening

This denotes a procedure which fits a polynomical function (of a chosen degree) to every scanline and substracts it to remove tilt and contortion. All images in this thesis were flattened.

Topview

Topview is the 2D representation of the data, normally from black to white.

Linescan

This is a cut along a straight line through the measurement. This can be along x,y or any mixture thereof and is displayed in a x,z-plot. This procedure was done using the program WSxM.[44]

Correlation averaging

An interactive correlation averaging procedure was used, which was programmed for SXM-Shell. A part of the image can be selected, which is then used as reference. In a cross-correlation of the selection and the original image, the positions of the best fit are picked. In all these positions, a sub-image with a size of the selection is cut and these sub-images are then averaged. Single locations as scratches or noise can be excluded manually from the averaging procedure. If an image is averaged the number of chosen positions for the averaging is mentioned in the figure capture.

The analysis of the conformation and of the packing of the self-assembled monolayer was done electronically (Figure 2.12). If the crystal data of the molecule was known, the .tif-file of the crystal structure (see Section 2.3.1) was overlaid the averaged .tif-file of the STM image obtained from SXM-Shell using Adobe Photoshop. The molecule could be scaled to the right size using the tools of Adobe Photoshop (raster or measuring tool). A more detailed description for the conformational analysis is given in Chapter 3. If no crystal structure of the molecule was known, the conformation was calculated using semi-empirical PM3 implementations in Spartan. The obtained .pdb-file of the molecule could be rendered in POV-Ray as described in Section 2.3.1.

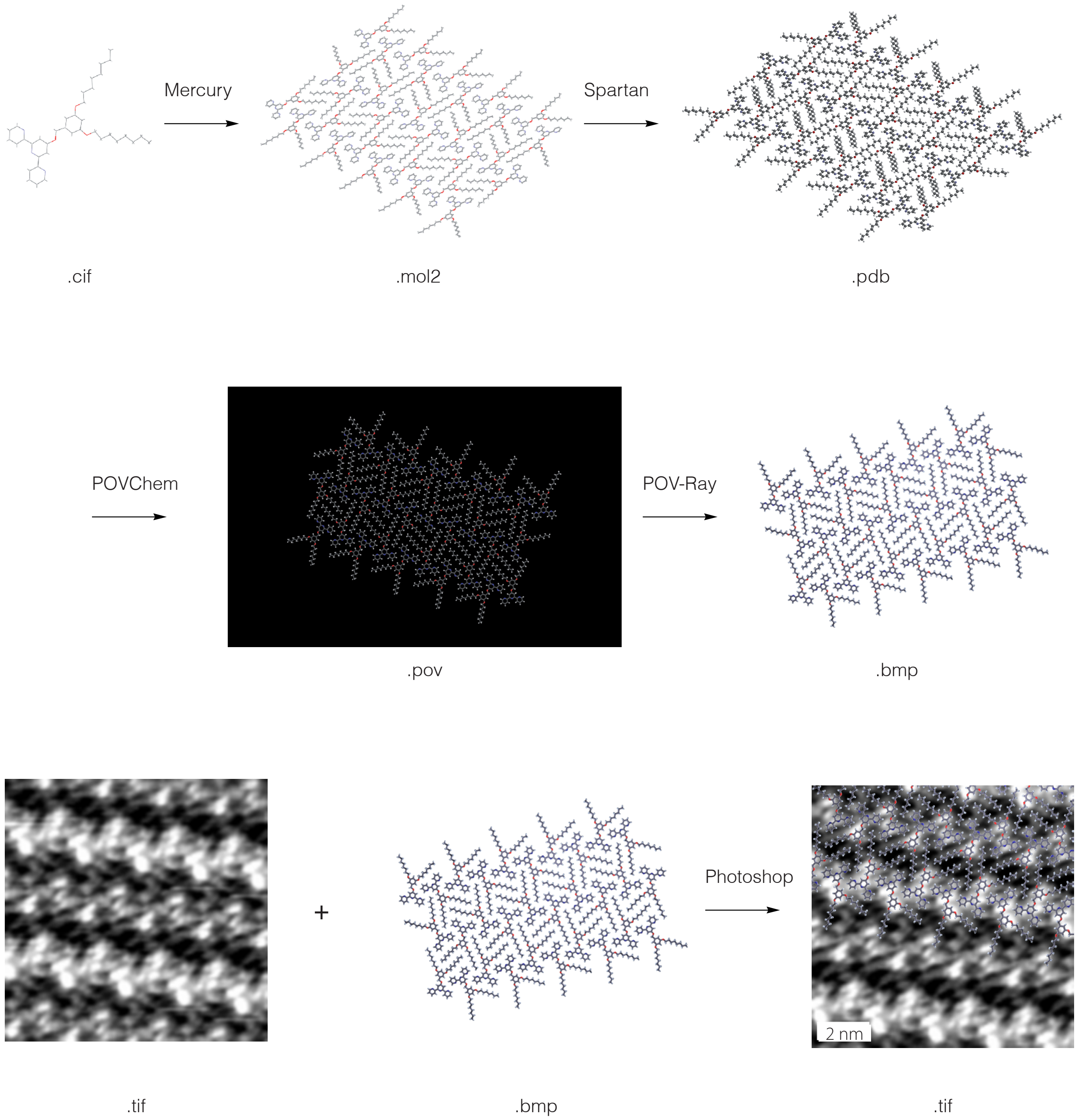
Mercury
Spartan
.cif
.mol2
.pdb
POVChem
POV-Ray
.pov
.bmp
+
Photoshop
2 nm
.tif
.bmp
.tif

Figure 2.12 An example of how to produce an STM image (e.g. here, compound **10**) with overlaid molecules of a single layer of the crystal structure of the compound (see Section 4.2). One layer of the 3D crystal structure is cut using Mercury. To get the final .bmp.-file, the .mol2-file has to pass several programs. In a final step, using Adobe Photoshop, the layer is overlaid the raw data (.tif-file) of the monolayer which is obtained using the averaging procedure in SXM-Shell.

2.4 HOMO, LUMO calculations

The contrast in STM on organic molecules has often been successfully compared to the respective frontier orbitals, either the HOMO or LUMO, according to the polarity of the applied potential.[25, 26, 45-48] The calculations in this thesis were made using the PM3 implementation in Spartan. The number of molecular orbitals is given in the figure capture.

2.5 References

[1] *Collect* Software, Bruker Nonius BV: Delft, **1997–2001**.

[2] A. Altomare, M. C. Burla, M. Camalli, G. L. Cascarano, C. Giacovazzo, A. Guagliardi, A. Grazia, G. Moliterni, G. Polidori, R. Spagna, *J. Appl. Crystallogr.* **1999**, *32*, 115.

[3] P. W. Betteridge, J. R. Carruthers, R. I. Cooper, Prout. K, D. J. Watkin, *J. Appl. Crystallogr.* **2003**, *36*, 1487.

[4] E. Meyer, H.-J. Hug, R. Bennewitz, *Scanning Probe Microscopy, The lab on a Tip*, Springer-Verlag, Berlin Heidelberg, **2003**.

[5] G. Binnig, H. Rohrer, *Helv. Phys. Acta* **1982**, *55*, 726.

[6] G. Binnig, H. Rohrer, C. Gerber, E. Weibel, *Phys. Rev. Lett.* **1983**, *50*, 120.

[7] G. Binnig, C. F. Quate, C. Gerber, *Phys. Rev. Lett.* **1986**, *56*, 930.

[8] G. Friedbacher, H. Fuchs, *Pure Appl. Chem.* **1999**, *71*, 1337.

[9] G. Friedbacher, H. Fuchs, *Angew. Chem.* **2003**, *115*, 5804.

[10] S. Krämer, R. R. Fuierer, C. B. Gorman, *Chem. Rev.* **2003**, *103*, 4367.

[11] D. A. Bonnell, *Scanning Tunneling Microscopy and Spectroscopy. Theory, Techniques and Applications.*, VCH Pubishers Inc., New York, **1993**.

[12] O. M. Magnussen, J. Hotlos, G. Beitel, D. M. Kolb, R. J. Behm, *J. Vac. Sci. Technol. B.* **1991**, *9*, 969.

[13] http://www.almaden.ibm.com/vis/stm/atomo.html.

[14] C. Klink, L. Olesen, *Phys. Rev. Lett.* **1993**, *71*, 4350.

[15] M. F. Crommie, C. P. Lutz, D. M. Eigler, *Science* **1993**, *262*, 218.

[16] G. A. Fiete, J. S. Hersch, E. J. Heller, H. C. Manoharan, C. P. Lutz, D. M. Eigler, *Phys. Rev. Lett.* **2001**, *86*, 2392.

[17] http://www.almaden.ibm.com/vis/stm/corral.html.

[18] C. E. Housecroft, A. G. Sharpe, *Inorganic Chemistry*, 2nd Edition ed., Pearson, Essex, **2005**.

[19] http://www.stelco.de/pdf/4300.

[20] J. S. Foster, J. E. Frommer, P. C. Arnett, *Nature* **1988**, *331*, 324.

[21] D. Tománek, S. G. Louie, *Phys. Rev. B* **1988**, *37*, 8327.

[22] G. Binnig, H. Fuchs, C. Gerber, H. Rohrer, E. Stoll, E. Tosatti, *Europhys. Lett.* **1986**, *1*, 31.

[23] I. P. Batra, N. García, H. Rohrer, H. Salemink, E. Stoll, S. Ciraci, *Surf. Sci.* **1987**, *181*, 126.

[24] R. Azumi, G. Götz, T. Debaerdemaeker, P. Bäuerle, *Chem. –Eur. J.* **2000**, *6*, 735.

[25] R. Lim, J. Li, J. Li, Z. Feng, S. Valiaveettil, *Langmuir* **2000**, *16*, 7023.

[26] L. J. Scherer, L. Merz, E. C. Constable, C. E. Housecroft, M. Neuburger, B. A. Hermann, *J. Am. Chem. Soc.* **2005**, *127*, 4033

[27] F. I. Dalidchik, M. V. Grishin, S. A. Kovalesvskii, *Phys. Low-Dim. Struct.* **2003**, *3/4*, 45.

[28] X. Fang, B. Li, E. Petersen, Y. Ji, J. C. Sokolov, M. H. Rafailovich, *J. Phys. Chem. B* **2005**, *109*, 20554.

[29] S. Yin, C. Wang, X. Qiu, B. Xu, C. Bai, *Surf. Interface Anal.* **2001**, *32*, 248.

[30] C. Claypool, F. Faglioni, W. A. Goddard III, H. B. Gray, N. S. Lewis, R. A. Marcus, *J. Phys. Chem. B* **1997**, *101*, 5978.

[31] W. Mamdouh, H. Uji-I, J. S. Ladislaw, A. E. Dulcey, V. Percec, F. C. De Schryver, S. De Feyter, *J. Am. Chem. Soc.* **2006**, *128*, 317.

[32] B. Venkataraman, J. J. Breen, G. W. Flynn, *J. Phys. Chem.* **1995**, *99*, 6608.

[33] M. Lackinger, S. Griessl, W. M. Heckl, M. Hietschold, G. W. Flynn, *Langmuir* **2005**, *21*, 4984.

[34] S. Griessl, M. Lackinger, M. Edelwirth, M. Hietschols, W. M. Heckl, *Single Mol.* **2002**, *1*, 25.

[35] I. Widmer, U. Huber, M. Stöhr, L. Merz, H.-J. Güntherodt, B. A. Hermann, P. Samorí, J. P. Rabe, P. B. Rheiner, G. Creiveldinger, P. Murer, *Helv. Chim. Acta* **2002**, *85*, 4255.

[36] S.-B. Lei, L.-J. Wan, C. Wang, C.-L. Bai, *Adv. Mater.* **2004**, *16*, 828.

[37] Mercury, **2004**, *Version 1.3*, http://www.ccdc.cam.ac.uk/mercury/.

[38] Chem3D Ultra, **2004**, *Version 9.0*, *CambridgeSoft,* http://www.cambridgesoft.com.

[39] ViewerLite, **2002**, *Version 5.0, Accelrys,* http://www.accelrys.com.

[40] Spartan, **2003**, *Version 04, Wavefunction Inc.*

[41] PovChem, **2000**, *Version 2.1.1*, http://www.ChemicalGraphics.com.

[42] POV-Ray for Windows, **2004**, *Version 3.6.1*, http://www.ChemicalGraphics.com.

[43] Adobe Photoshop CS2, **2005**, *Version 9.0, Adobe Systems Inc.*

[44] WSxM, **2005**, *Version 2.2, Nanotec Electronica S.L.*, http://www.nanotec.es.

[45] G. M. Florio, T. L. Werblowsky, T. Müller, B. J. Berne, G. W. Flynn, *J. Phys. Chem. B* **2005**, *109*, 4520.

[46] X. Qiu, C. Wang, Q. Zeng, B. Xu, S. Yin, C. Wang, S. Xu, C. Bai, *J. Am. Chem. Soc.* **2000**, *122*, 5550.

[47] A. Miura, Z. Cheng, H. Uji-I, S. De Feyter, M. Zdanowska, P. Jonkheijm, A. P. H. J. Schenning, E. W. Meijer, F. Würthner, F. C. De Schryver, *J. Am. Chem. Soc.* **2003**, *125*, 14968.

[48] X. Qiu, C. Wang, S. Yin, Q. Zeng, B. Xu, C. Bai, *J. Phys. Chem. B* **2000**, *104*, 3570.

He who controls the self-assembly, controls the future.

J. Gimzewski

3 Studying Self-Organised Monolayers of Bpy decorated with Fréchet-type Dendritic Wedges using STM

In this chapter, the analysis by STM of a system that exhibits multiple conformers on a graphite surface will be discussed. A bipyridine ligand[1] functionalised with Fréchet-type dendritic wedges of various generations as the core structural unit has been chosen. The coordination chemistry of 2,2'-bipyridine ligands (bpy)[2] is well understood[3] and the coordination to a metal centre results in a loss of conformational freedom, locking the ligand in a *cis*-conformation, in contrast to the time-averaged *trans*-conformation in the free ligand.[3, 4] Therefore, the conformation of a ligand within a monolayer by reaction with metal salts can be addressed.[5]

As will be discussed in Chapter 7, the aromatic-rich system of the Fréchet-type dendrimer[6] is ideally suited to visualisation by tunnelling methods.[7-12] In this Chapter, it will be shown that deposition of a dendritic wedge-functionalised ligand on a HOPG surface resulted in the formation of well-defined monolayers exhibiting different conformations of the molecule. The near atomic resolution makes a clear assignment of two conformers possible. Both conformers spontaneously and rapidly form molecular domains under ambient conditions. Within a molecular domain, only one conformer is present and domains of different conformers are observed side by side. No preference for one conformer is observed. Bipyridines substituted with higher generation dendrons also show at least two different conformers in self-assembled monolayers.

3.1 Compound synthesis and discussion of the single crystal structure of compound 8

The synthetic strategy adopted was the reaction of a nucleophilic bipyridine derivative 4,4'-dihydroxy-bpy[13] with an electrophilic dendritic wedge (Scheme 3.1).

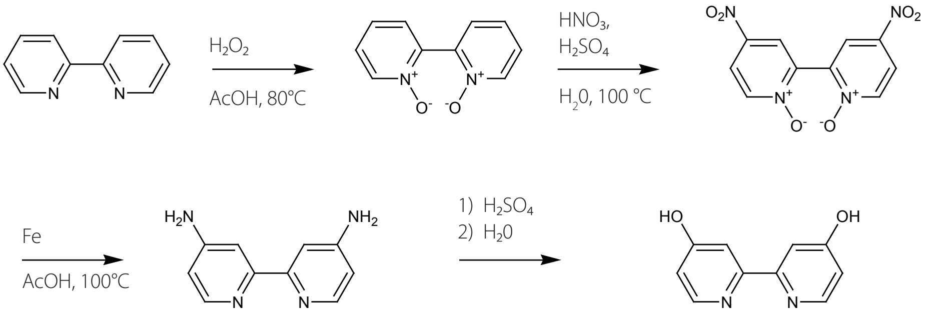

Scheme 3.1 Four step synthesis of 4,4'-dihydroxy-bpy starting from bpy. Yields: a) 80%, b) 42%, c) 69%, d) 60%.

In the four step synthesis of 4,4'-dihydroxy-bpy, the starting material was bipyridine. Firstly, the pyridine units were oxidised with H_2O_2 as the oxidising agent in 80% yield. The 4,4'-dinitro-2,2'-bipyridine-*N, N'*-dioxides so-obtained could then easily be nitrated at the 4- and 4'-positions using a mixture of concentrated nitric acid and concentrated sulfuric acid. The low yields could be explained by the formation of 4-nitropicolinic acid, as observed by A. Mahmood in our group.[14] The most problematic and time-consuming step was the reduction of the nitro group into the corresponding amine. Iron in acetic acid was chosen as the reducing agent. The work up, especially the filtration, was the cause of many problems. It was shown by O. Maury *et al*[15] and later by S. Graber in our group[16] that palladium on activated carbon and hydrazine were much more effective. The 4,4'-diamino-bpy could then be converted to the corresponding dihydroxy compound under non-classical Sandmayer-conditions in reasonable yield (60%).

3.1.1 Synthesis of compounds 3, [Pd(3)Cl$_2$] and [Pd(3)$_2$][PF$_6$]$_2$

The first generation mesylate wedge **2**[17, 18] was prepared in 80% yield by mesylation of the benzylic alcohol **1**[6, 19-21] under standard reaction conditions (Scheme 3.2). Mesylates are better leaving groups than bromides. The crude mesylate **2** was not purified and used directly for the coupling reaction with 4,4'-dihydroxy-bpy.

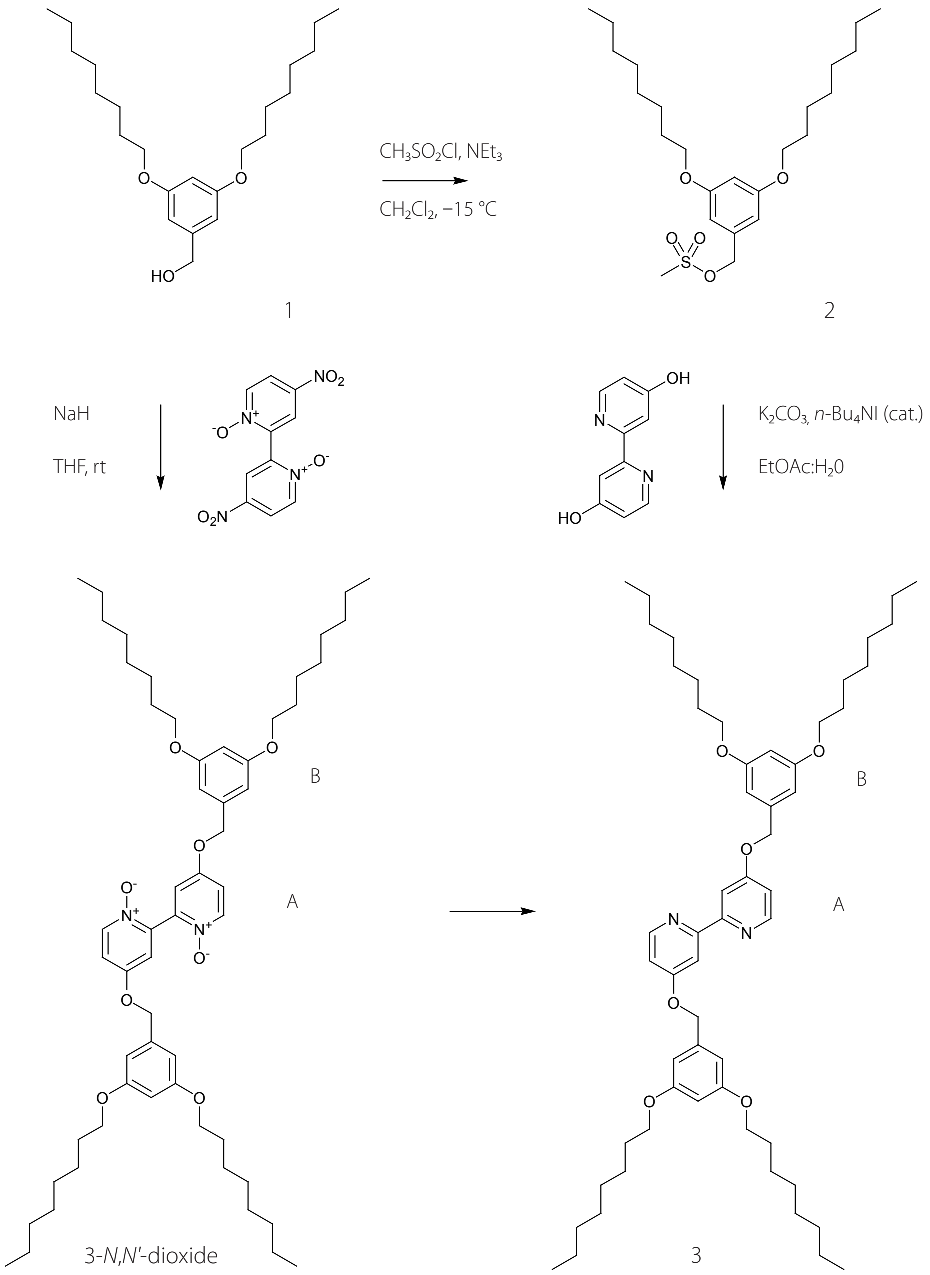

Scheme 3.2 Mesylation of alcohol **1**. The crude mesylated dendron **2** was subsequently coupled with 4,4'-dihydroxy-bpy using phase transfer conditions (right). Yield: 74%. In another route, the alcohol **1** was reacted with 4,4'-dinitro-2,2'-bipyridine-*N, N'*-dioxide. Yield: 16 %. Ring labels are used for NMR spectroscopic assignments.

Finding suitable conditions for the coupling between the bipyridine unit and the dendritic wedge was quite demanding. Under standard conditions (K_2CO_3 as base; in refluxing acetone or in DMF at 110 °C or even by addition of catalytic amounts of 18-crown-6 in a solution of DMSO (10%) in acetone), only traces of the desired bis-functionalised compound were obtained, even with reaction times of several days. Due to the difficult separation of the bis- from the mono-functionalised bipyridine, reaction conditions with high yields were necessary. This was finally obtained under phase transfer conditions using *n*-Bu_4NI (10%) as the phase transfer catalyst in ethyl acetate and H_2O in the presence of K_2CO_3 at 60 °C. High concentrations (ca. 10 M of the start-up material in ethyl acetate: water) and vigorous stirring were important to obtain a yield of 74%.

Compound **3** was characterised by routine techniques. The major peaks at *m/z* 903.5 and 881.6 in the electrospray mass spectrum were assigned to $[M + Na]^+$ and $[M + H]^+$ respectively. Signals in the ^1H NMR spectrum were assigned by COSY. The solution room temperature ^1H NMR spectrum was sharp and well-resolved indicating that rotation about the C−C and C−O single bonds is unhindered.

In another route, the alcohol **1** was reacted with 4,4'-dinitro-2,2'-bipyridine-*N*,*N*'-dioxide (Scheme 3.1) using NaH as base in THF at room temperature. Although the yield was not good (16.4%), this nucleophilic aromatic substitution seems to be interesting, since the starting materials were easily obtained. **3-*N,N'*-dioxide** could be characterised by the standard methods, the doublet of H^{6A} in the ^1H NMR is shifted by 0.27 ppm to higher field compared to compound **3** and the coupling constant is larger with 7.3 Hz compared to 5.7 Hz for compound **3**. The oxidised bpy unit can then be reduced to get compound **3**.

It is also possible to form the bpy−O−R ether bridge by coupling 4,4'-dihydroxy-bpy with the desired alcohol under Mitsunobu conditions. This route is interesting when a chiral alcohol has to be attached to a bpy unit without loosing the chiral information.[16]

The formation of the corresponding Pd(II)-complex from ligand **3** turned out to be quite challenging. No complexation occurred by treating **3** with $[Pd(OAc)_2]_3$ in a dichloromethane:methanol (1:1) or in a propan-1-ol solution. Starting with a $[PdCl_4]^{2-}$ complex as the palladium(II) source, a two step synthesis was needed to form the bis ligand Pd(II)-complex. In the first step, one equivalent of ligand **3** was reacted with one equivalent of a $[PdCl_4]^{2-}$ salt (either with the commercially available $K_2[PdCl_4]$ in refluxing ethanol or with preformed $[NH_4]_2[PdCl_4]$ in refluxing dichloromethane) in near quantitative yield forming the **[Pd(3)Cl₂]** complex. The replacement of the two chloro ligands by ligand **3** turned out to be difficult, presumably because of the strong Cl-Pd bonds. Precipitation of insoluble halide metal salt was necessary to force the equilibrium to the product side. In such cases, Ag^+ is often used.[22, 23] Treating the **[Pd(3)Cl₂]** complex in dichloromethane with two equivalents of $AgBF_4$ and one equivalent of **3** resulted in a mixture of the tetrafluoroborate salts of $\mathbf{[Pd(3)_2]^{2+}}$ and $\mathbf{[Ag(3)_2]^{+}}$, which could not be separated from each other. Therefore, $TlPF_6$ was used, since TlCl is not soluble in any common solvent and thallium(I) is known not to form metal complexes with oligopyridine ligands.[3] In fact, stirring two equivalents of $TlPF_6$ and one equivalent of $\mathbf{[Pd(3)Cl_2]}$ and **3** in dichloromethane formed the desired $\mathbf{[Pd(3)_2][PF_6]_2}$ in quantitative yield. The compound could be characterised using conventional methods. On the electrospray mass spectrum the two fragments $[M - PF_6]^+$ and $[M - 2PF_6]^{2+}$ could be nicely seen with their characteristic isotopic pattern at *m/z* 2012.3 and 933.3 respectively. The compound showed no liquid crystalline properties and melted at 173 °C.

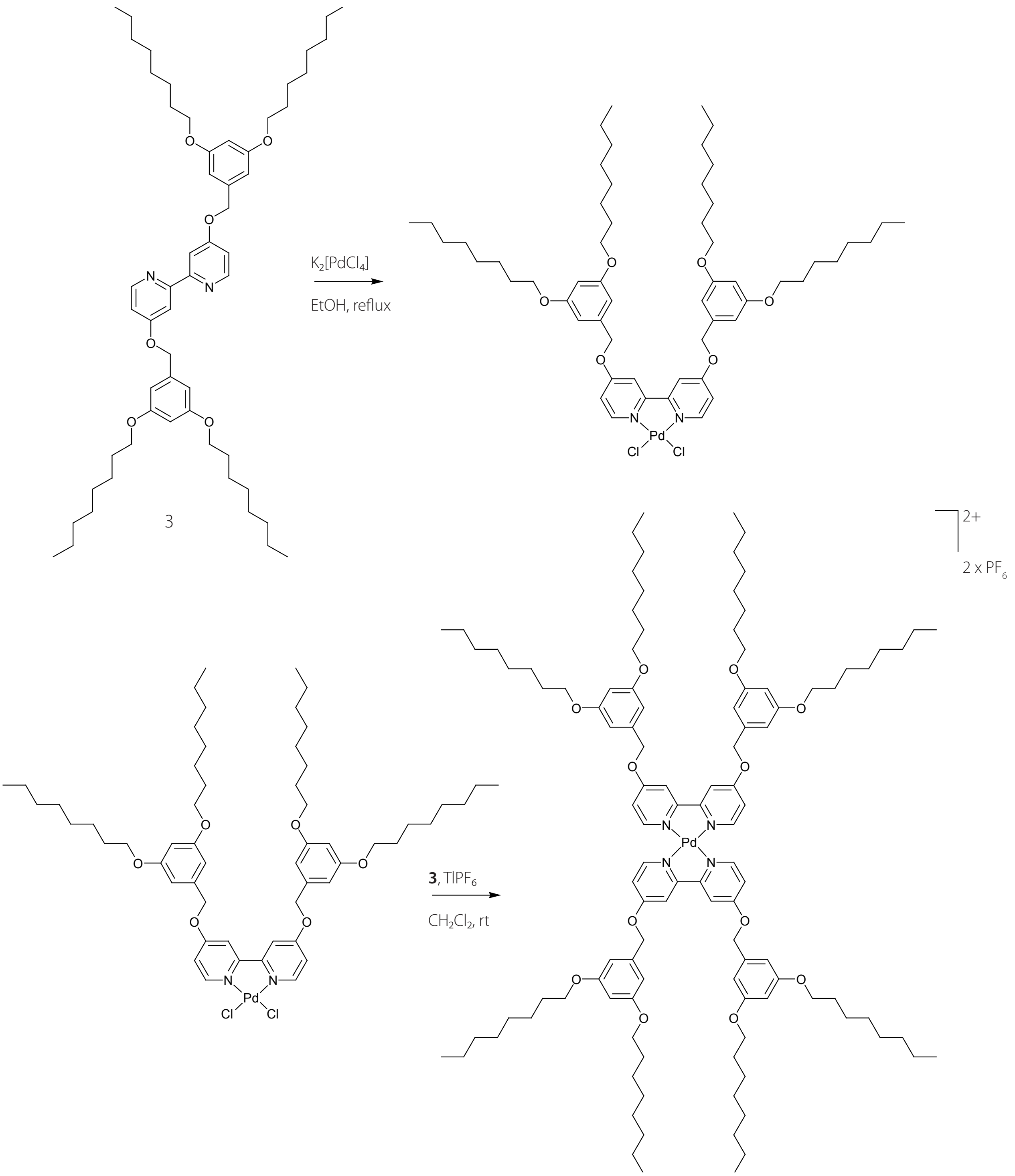
K2[PdCl4]
EtOH, reflux
3
3, TlPF6
CH2Cl2, rt
2+
2 x PF6
N
Pd
Cl
O

Scheme 3.3 Formation of **[Pd(3)$_2$][PF$_6$]$_2$**. In the first step, one ligand **3** was reacted with K$_2$[PdCl$_4$]. To add the second ligand, TlPF$_6$ was necessary to remove the chloro ligands from the metal centre.

The complexation could be followed by NMR spectroscopy. In Figure 3.1, the ^{1}H NMR of ligand **3**, **[Pd(3)Cl$_2$]** and **[Pd(3)$_2$][PF$_6$]$_2$** are shown. No splitting of signals was observed, which can be interpreted in terms of keeping the symmetry, although the signals for H^{4A} and H^{5A} of **[Pd(3)$_2$][PF$_6$]$_2$** were broadened.

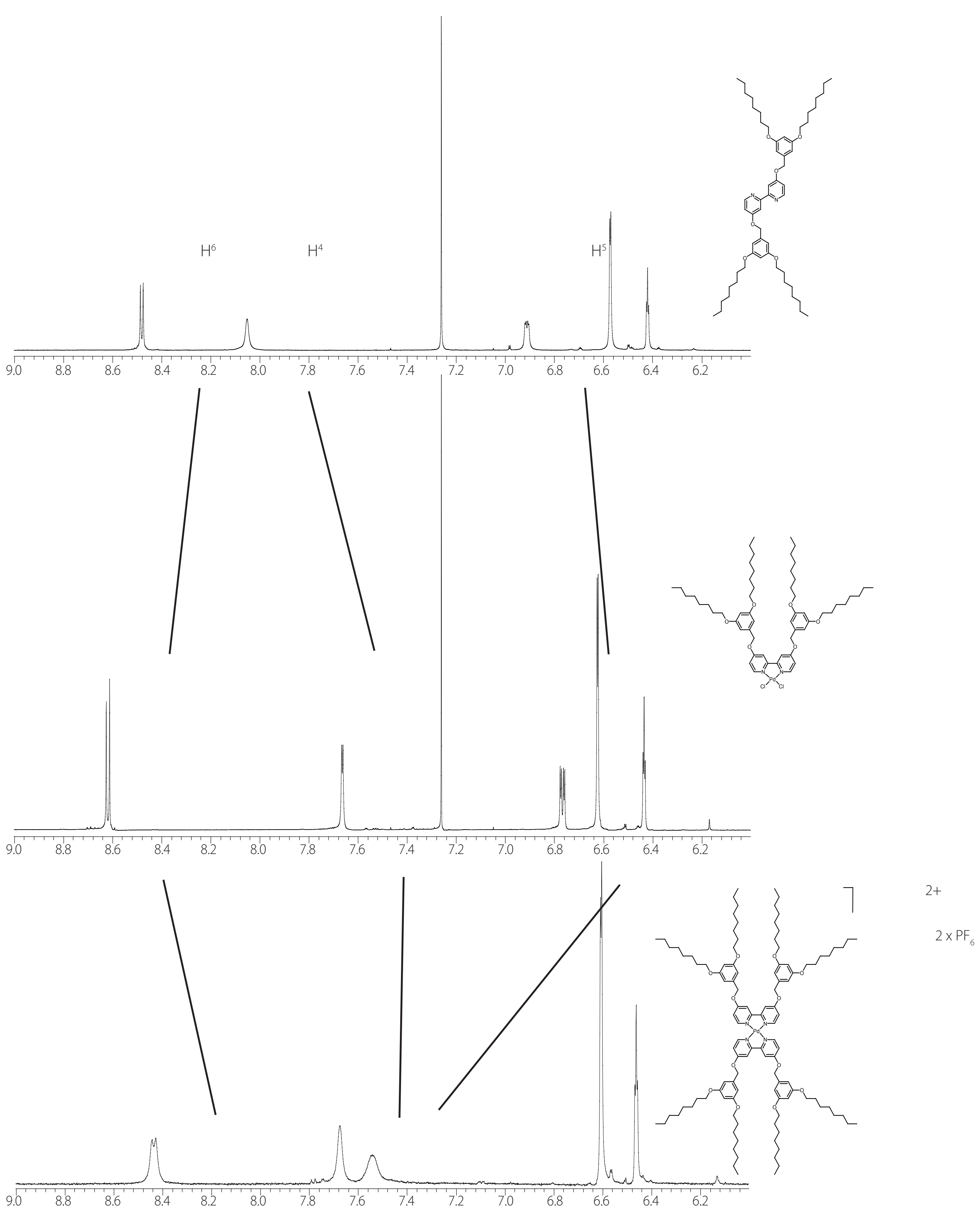

Figure 3.1 ^{1}H NMR of ligand **3**, **[Pd(3)Cl$_2$]** and **[Pd(3)$_2$][PF$_6$]$_2$** are shown. Interestingly, the most remarkable shift was observed from H^{5A} during the formation of **[Pd(3)Cl$_2$]**.

The doublet of H^{6A} shifted only by 0.14 ppm to lower field during the first complexation and shifted back to higher field during the second complexation. This was expected, since signals for H^{6A} *cis* to a chloro ligand also shift to lower field in other examples.[24] The most remarkable shift difference was observed for H^{5A} between the spectra of **[Pd(3)Cl$_2$]** and of **[Pd(3)$_2$][PF$_6$]$_2$** of 0.73 ppm at lower field in the spectrum of **[Pd(3)$_2$][PF$_6$]$_2$**.

3.1.2 Synthesis of second generation compounds 4 and 6

The second generation alcohol **4** was already known.[19, 25] A modification of the literature method for the preparation of **4** was used. Instead of starting from the first generation bromide as an electrophile, the corresponding mesylate derivative was taken,[17, 26] since the preparation of the bromide was not reproducible and bromide derivatives are much less reactive than the corresponding mesylate derivatives.[17] The alcohol **4** was formed in 76% yield by refluxing a suspension of **2**, 3,5-dihydroxybenzyl alcohol, K_2CO_3 and catalytic amount (10%) of 18-crown-6 in acetone. By using harsher conditions (for example, by reacting all reagents in refluxing DMF), the triply protected product would be achieved.[27] Single crystals of **4** were also obtained and the structure determination of **4** is discussed later (Chapter 5).

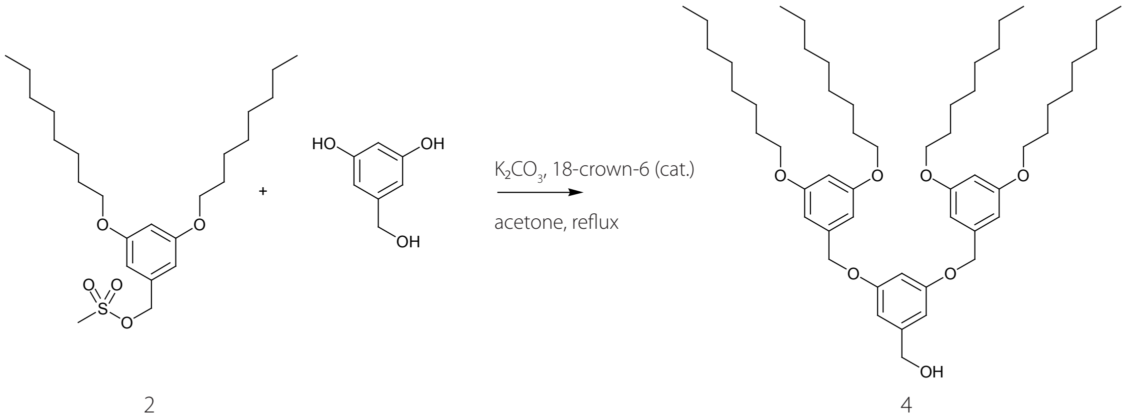

Scheme 3.4 Formation of the second generation alcohol **4**. The synthesis was modified from that presented in literature.[19, 25]

The second generation mesylate wedge, **5**, was prepared from the corresponding alcohol **4**[19] by an analogous strategy to the first generation wedge. Compound **5** was coupled to 4,4'-dihydroxy-bpy to give **6** using the same conditions as for the formation of **3** (Scheme 3.5). Under standard conditions, compound **6** was obtained as a white powder in 44 % yield and was characterised by ^1H (COSY), ^{13}C NMR, UV-vis and IR spectroscopies, mass spectrometry and elemental analysis.

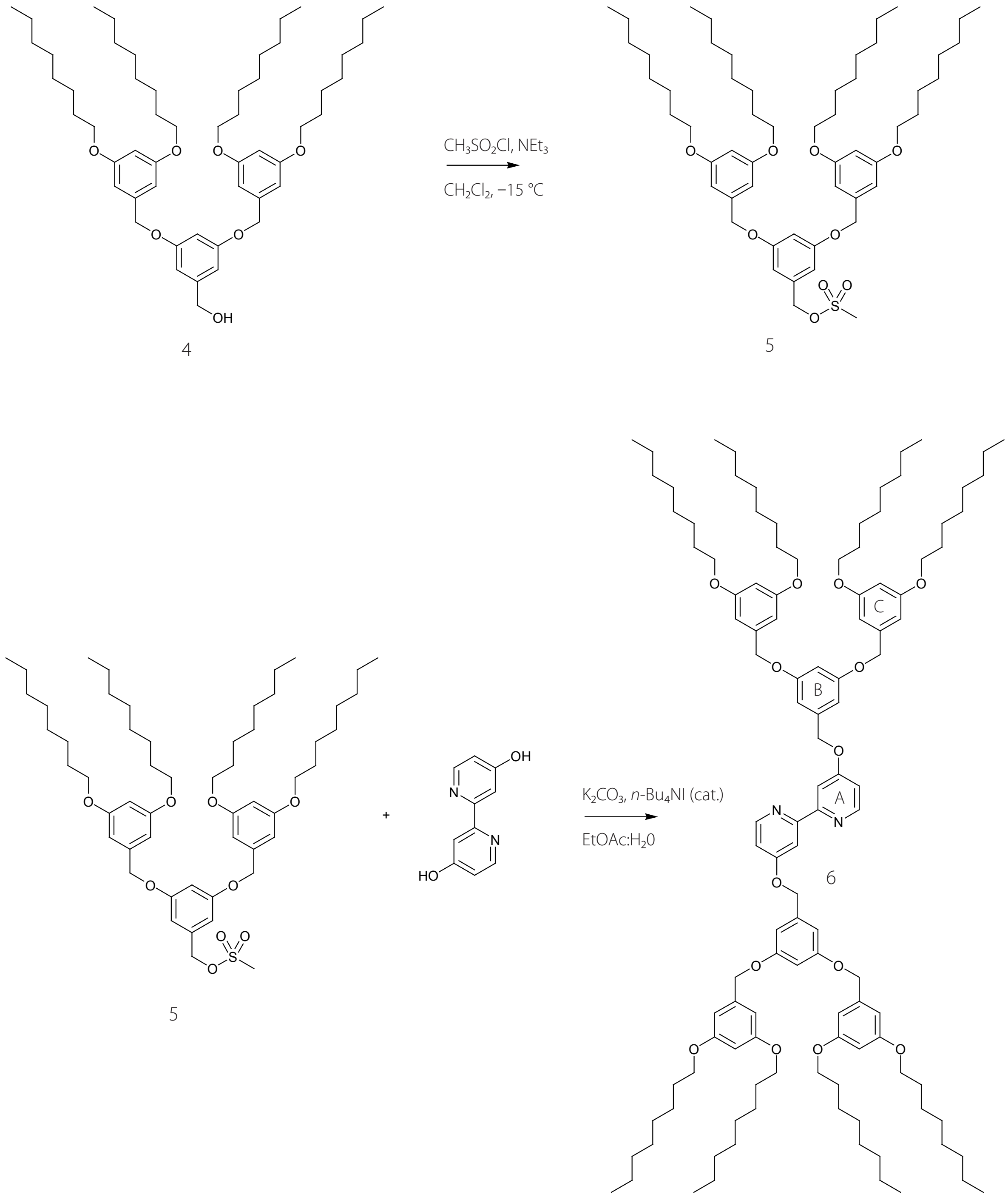
OH
O
CH₃SO₂Cl, NEt₃
CH₂Cl₂, −15 °C
O
S
+
OH
N
N
HO
K₂CO₃, n-Bu₄NI (cat.)
EtOAc:H₂0
A
B
C

4

5

5

6

Scheme 3.5 Mesylation of alcohol **4**. The crude mesylated dendron **5** was subsequently coupled with 4,4'-dihydroxy-bpy using phase transfer conditions. Yield: 44%. Ring labels are used for NMR spectroscopic assignments.

3.1.3 Synthesis and single crystal structure of compound 8

In parallel with the studies of monolayers, solution and solid state structural properties of related molecular systems were investigated as will be shown in Chapter 7.

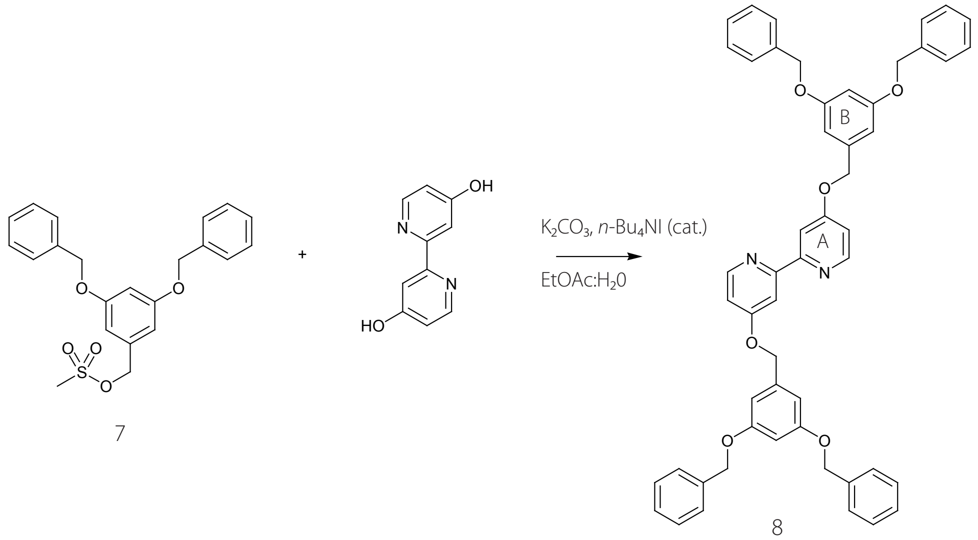
K$_2$CO$_3$, n-Bu$_4$NI (cat.)
EtOAc:H$_2$0
7
8
A
B
OH
HO
N

Scheme 3.6 The crude mesylated dendron **7**[26] was subsequently coupled with 4,4'-dihydroxy-bpy using phase transfer conditions forming **8** in 35% yields. Ring labels are used for NMR spectroscopic assignments.

Compound **8** was prepared in 35% yield by the same methodology used for compound **6** (Scheme 3.6). A related ligand with an ethyl spacer between the bpy domain and the wedge was reported by F. Vögtle *et al.*[28]

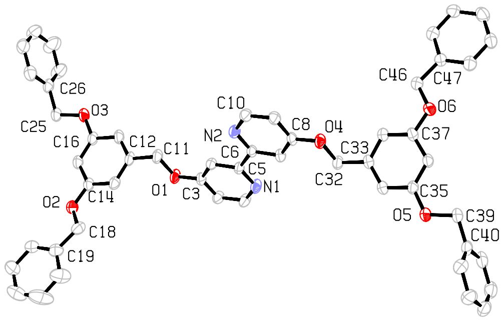
C26
O3
C25
C16
C12
C11
C10
N2
C6
C5
N1
C8
O4
C33
C32
C46
C47
O6
C37
C35
O5
C39
C40
O1
C3
O2
C14
C18
C19

Figure 3.2 Molecular structure of compound **8**. For clarity, hydrogen atoms are omitted and selected atoms only are numbered. Important bond lengths and angles: N(1)-C(5) = 1.342(3), N(2)–C(6) = 1.343(3), C(5)–C(6) = 1.491(3), O(1)–C(3) = 1.368(3), O(1)–C(11) = 1.433(3), O(2)–C(14) = 1.369(3), O(2)–C(18) = 1.432(3), O(3)–C(16) = 1.372(3), O(3)–C(25) = 1.440(3), O(4)–C(8) = 1.363(3), O(4)–C(32) = 1.440(3), O(5)–C(35) = 1.368(3), O(5)–C(39) = 1.441(3), O(6)–C(37) = 1.374(3), O(6)–C(46) = 1.430(3) Å; C(3)–O(1)–C(11) = 116.6(2), C(14)–O(2)–C(18) = 116.7(2), C(16)–O(3)–C(25) = 117.2(2), C(8)–O(4)–C(32) = 116.5(2), C(35)–O(5)-C(39) = 117.3(2), C(37)–O(6)–C(46) = 116.7(2)°.

The structure of compound **8** has been determined by single-crystal X-ray diffraction. Single crystals of **8** grown by diffusion of hexane into a chloroform solution of **8** were suitable for X-ray diffraction studies. The triclinic unit cell contains one complete molecule which is non-centrosymmetric, and one molecule located on the centre of symmetry. Figure 3.2 shows the structure of the non-centrosymmetric molecule. In both molecules, the bpy unit adopts the expected *trans*-conformation with the two pyridine rings coplanar (dihedral angle between least squares planes = 2°). Also in both molecules, the two inner benzyl substituents adopt *syn*-conformations with respect to the bpy unit (see Scheme 3.7). The outer benzyl groups adopt *syn*- and *anti*-conformations with respect to the C^4 proton (Scheme 3.7). In compound **8**, these torsion angles lie in the range 1.0 to 20.8° for the two different molecules; the dihedral angles between the least squares planes of adjacent pairs of aromatic rings vary from 4.2 to 88.2°.

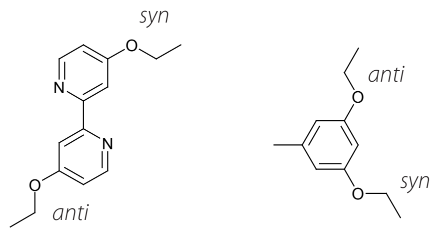

Scheme 3.7 *Syn*- and *anti*-conformations of the benzyl groups are defined a) with respect to the transannular C–C bond of the bpy unit, or b) with respect to the C^4–H bond of a benzyl group.

3.2 Conformational analysis of self-organised monolayers of the first and second generation dendrons 3 and 6

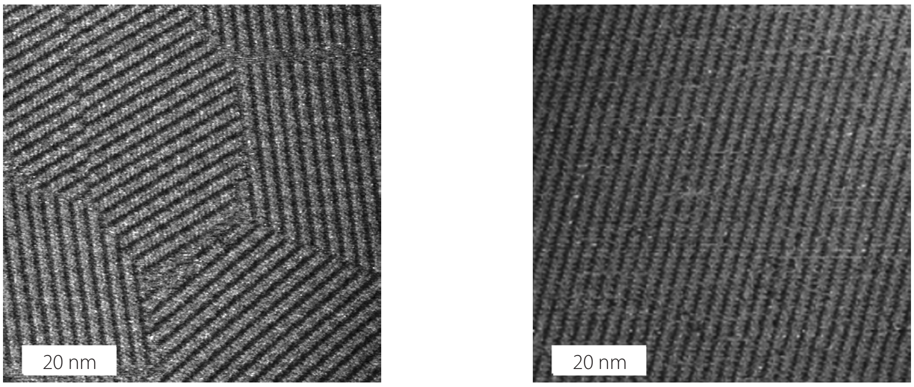

(a) (b)

Figure 3.3 STM images of **3**. The monolayers were formed from a solution of (a) dichloromethane and (b) hexane. The domains formed from the hexane solution were of much larger size. Scan parameters: (a) 80 nm x 80 nm, $U_b = -700$ mV, $I_t = 8$ pA; (b) 80 nm x 80 nm, $U_b = -700$ mV, $I_t = 10$ pA.

Good quality and extensive self-assembled monolayers of **3** were obtained upon allowing solutions in volatile solvents to evaporate under ambient conditions. In STM images of self-organised monolayers of molecule **3**, multiple domain formation was observed with a lamellar arrangement of **3** (Figure 3.3). The individual domain size ranged from some 50 nm^2 up to 1000 nm^2 depending on the exact preparation conditions. These multiple domains were prepared from hexane and dichloromethane solutions. Those from hexane were typically and reproducibly of much larger size than those from dichloromethane (Figure 3.3). This is consistent with a slower rate of evaporation of hexane (b.p. 342 K, $\Delta\mathrm{vap}H^\circ$ = 31.56 kJ mol^{-1}) than dichloromethane (b.p. 313 K, $\Delta\mathrm{vap}H^\circ$ = 28.82 kJ mol^{-1}).

While on first sight the orientations of domains in Figure 3.3(a) appeared to reflect the threefold symmetry of the frontier orbitals of the graphite surface (see Chapter 2),[29] detailed analysis revealed the additional presence of small angle domain boundaries (as indicated in Figure 3.4(a)). These two sets of three domains were regularly observed with a reproducible small angle relationship between the sets of 6.5°.

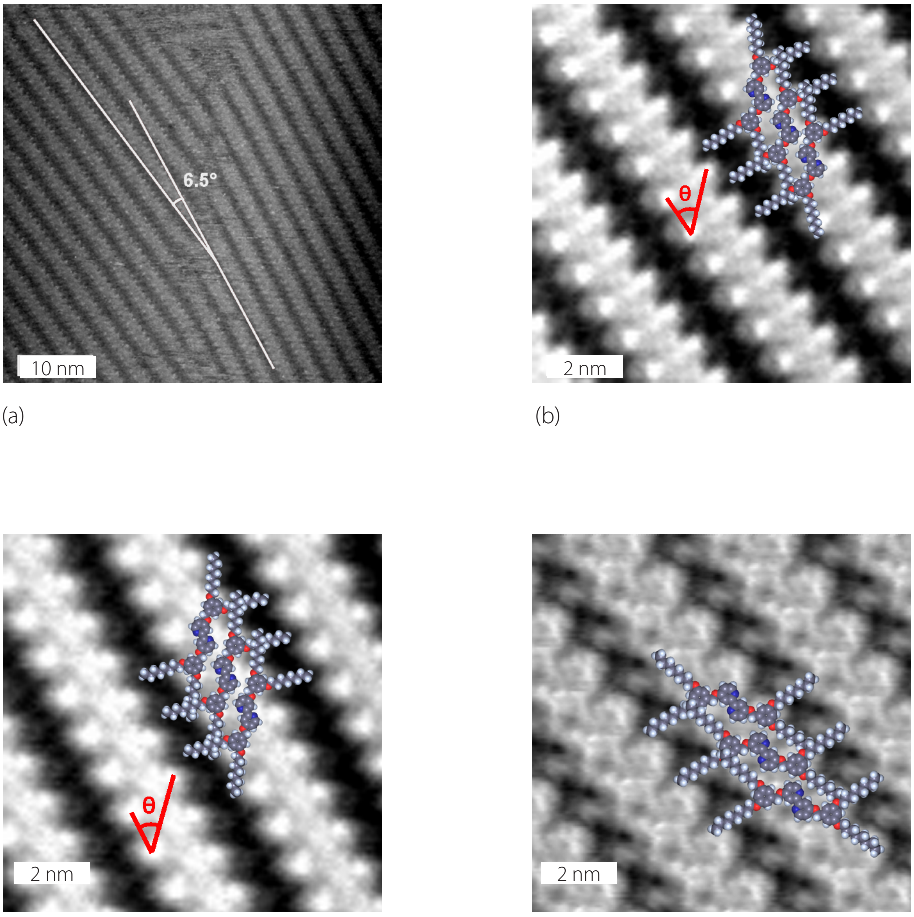

(a) (b) (c) (d)

Figure 3.4 STM images of two domains of **3**. (a) The angle difference between the two domains is 6.5 °. (b) Expanded image of the left domain of (a) and (c) of the right domain. Scan parameters: (a) 50 nm x 50 nm, U_b = −1111 mV, I_t = 15 pA. (d) 10 nm x 10 nm image of another domain showing another 2D-packing. U_b = −900 mV, I_t = 40 pA. Figures (b), (c) and (d) are shown with an overlaying molecular model with the best-fit conformation.

With such weakly physisorbed molecules, very low tunnelling current (pico-Ampere range) must be used in order not to destroy the self-ordered monolayers. Despite this, remarkably high-resolution images were obtained. In the high-resolution images in Figure 3.4(b)–Figure 3.4(d), the two peripheral benzyl groups of molecule **3** appear as regions of highest intensity, consistent with the occupied frontier orbitals being localised on these sites. The contrast in STM on organic molecules has often been successfully compared to the respective frontier orbitals, either the HOMO or LUMO, according to the polarity of the applied potential.[29-33]

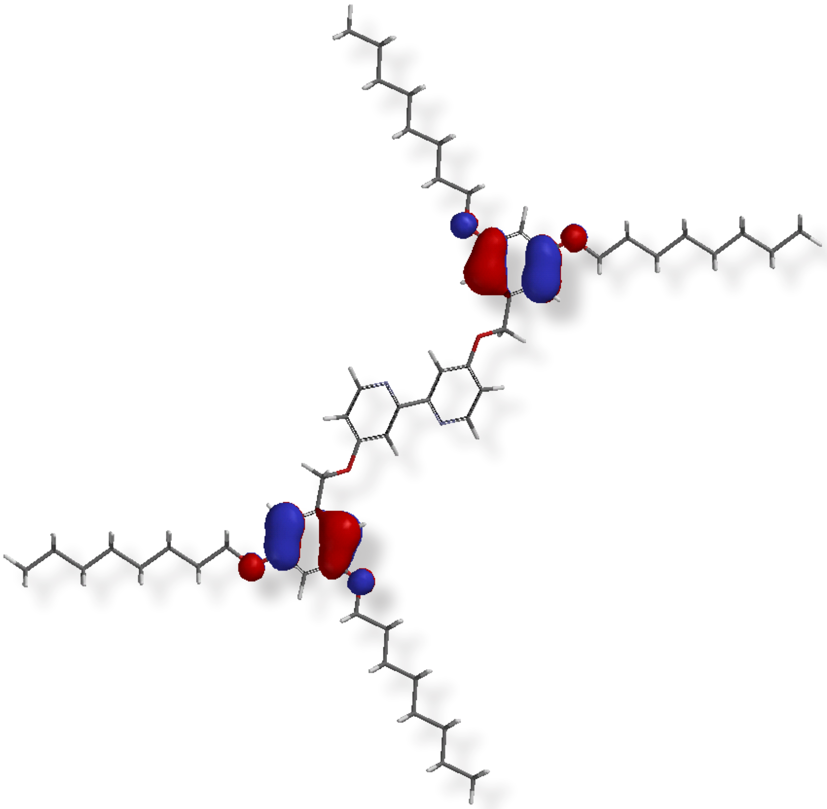

Figure 3.5 The sum of the four highest filled orbitals of **3**. It can clearly be seen, that the HOMOs are located on the benzyl substituents.

Semi-empirical calculations at the PM3 level confirmed that the highest filled orbitals of **3** are located on the benzyl-substituents, and even extend to the oxygens (see Figure 3.5). The orbitals located on the central bpy have a slightly lower energy. In the STM images of **3**, the bpy rings are harder to identify than the benzyl groups. A detailed analysis is described later in this Chapter, and allows a clear identification of the molecular conformation. Figure 3.4(b) and Figure 3.4(c) were obtained by averaging a 10 nm by 10 nm window over 121 and 104 positions for the left and right side of Figure 3.4(a), respectively. Two differences are apparent: (i) the alignment of the individual molecules within the rows and (ii) different "internal" structure of the molecules. These differences in terms of *anti, syn*- and *anti, anti*-conformations of molecules of **3** are discussed in the next section.

Evaporation of solutions of the second generation compound **6** also gave good quality monolayers in which multiple domains were observed. Figure 3.6(a) depicts the STM images of two domains showing a slightly different arrangement of the rows and different internal structure of the molecules. For these images, the averaging analysis of the upper and lower domain in Figure 3.6(a) was performed over 62 and 44 positions, respectively, allowing the identification of single molecules almost without further interpretation. In the upper domain (Figure 3.6(c)), the molecule is stretched in an X-like configuration. However, in the lower domain (Figure 3.6(b)), molecule **6** clearly adopts a different conformation on the graphite surface. In contrast to **3**, the second generation compound **6** does not form lamellar stripes. The bpy rings of molecule **6** are imaged with higher contrast than in molecule **3**, and this allows a straightforward interpretation of the structure of monolayers of **6** since all of the aromatic rings are directly observed.

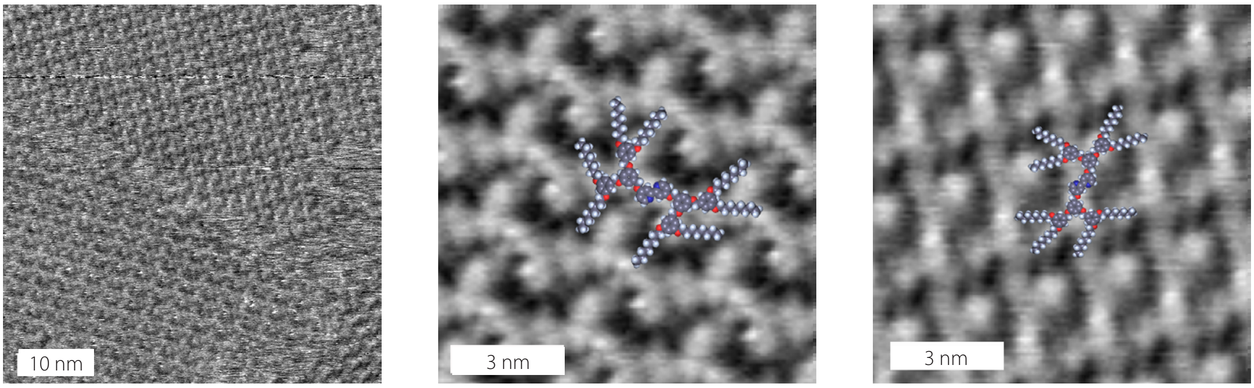

(a) (b) (c)

Figure 3.6 (a) STM images of two domains of **6**. (b) Expanded image of the lower domain of (a) and (c) of the upper domain. Scan parameters: (a) 50 nm x 50 nm, U_b = −750 mV, I_t = 6.5 pA. Figures (b), and (c) are shown with a overlaying molecular model with the best-fit conformation.

3.3 Data analysis and discussion of the monolayers of 3 and 6

While the analysis of pattern formation in STM-images of self-organised monolayers is at a very advanced stage,[34-36] studies including conformational analysis of flexible molecules are still scarce.[37-40] There are several factors for this. Usually, very high-resolution images are necessary to identify individual conformations, but this is often difficult to obtain with highly flexible molecules. Additionally, most high-resolution STM studies are still performed in ultra-high vacuum with sublimated molecules; this is often impossible for large, flexible molecules. Many researchers refrain from measuring in air at room temperature because there are many more uncertainties, impurities and thermal motion associated with the surface molecules. Thus, it remains a challenge to obtain high-resolution images under ambient conditions. The exclusion of measurement artefacts, errors due to drift, and averaging artefacts is very important. Also the reproducibility of experimental results is essential, as measurements of single events/molecules sometimes show noise (irregularities etc.) and impurities on the same scale as the measured molecules. Errors due to thermal drift of the apparatus can be excluded by carefully checking follow-up scans of the opposite slow scanning direction. Any compression/elongation due to drift is then easily recognised. A general observation in the STM images of the systems was that the domains were present from the first scan-lines and remained very stable over time; no bleeding or migration was observed. Even though the monolayers were stable over time, they were very easily disturbed by scanning with tunnelling currents above a few nanoampères. In rare cases, a growth of domains was observed at the cost of unordered phases. Only measurements that meet the rigorous requirements listed above could be used for a successful conformational analysis.

One possible unit cell of the measurement discussed in Section 3.2 is shown in Figure 3.7(c). The averaged image is printed with different contrast settings, even with contour plots (Figure 3.7(d)). Molecular models of all relevant conformations were analysed using computer graphics; the models were overlaid on the STM images in order to find the best fits. Molecular orbital calculations were run on molecule **3** in different conformations in order to confirm that there was no significant change in either composition or relative ordering of the highest filled orbitals (see Figure 3.5).

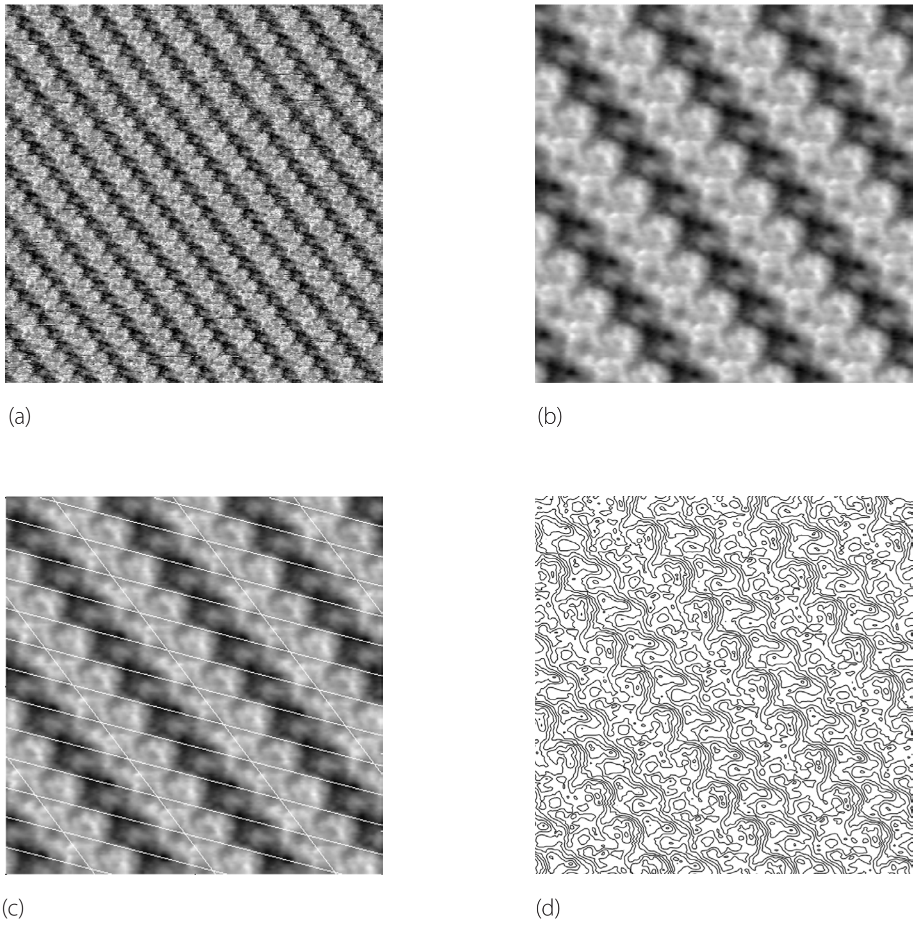
(a)
(b)
(c)
(d)

Figure 3.7 (a) Process of data analysis of a measurement of a domain containing **3** after (a) flattening and (b) enlargement and averaging over 46 positions. Panel (c) shows overlaid unit cells and (d) shows a contour plot of (b). Scale: (a) 30 nm x 30 nm; (b)–(d) 10 nm x 10 nm.

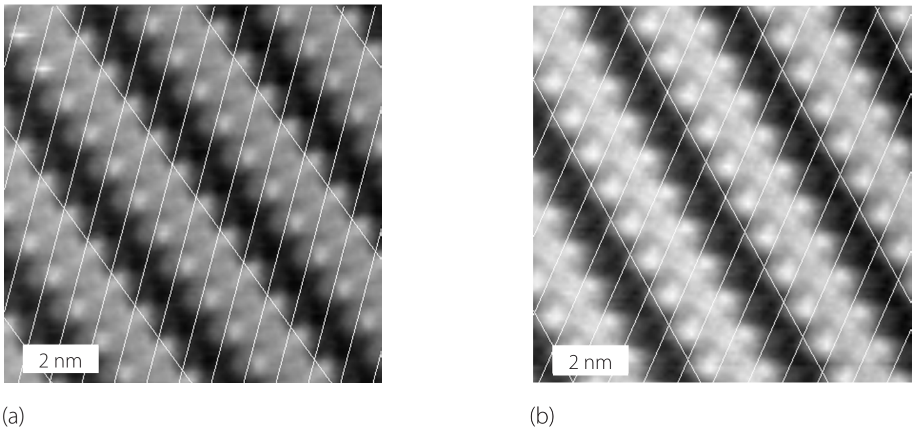

(a) (b)

Figure 3.8 Images from (a) Figure 3.4(b) and (b) Figure 3.4(c) with their corresponding unit cells.

Following this analysis procedure, the unit cells, the molecular ordering, and the molecular conformation within the domains in Figure 3.4(b)–Figure 3.4(d) could be identified. As the alkyl-chains are insulating, and therefore hardly seen in STM images,[41, 42] the following discussion is focused on the *syn*- and *anti*-conformations of the $ArOCH_2Ar$ groups. Two different conformations of **3** could be determined and these are shown in Scheme 3.8. In addition to this, the molecules were found in different assembly patterns. Figure 3.6(c), Figure 3.7(a) and Figure 3.2(b) show the averaged images with their respective unit cells. The plane group of all two-dimensional monolayers is *p*1. The unit cell dimensions are a = 3.8 nm, b = 1.1 nm, α = 51° (Figure 3.8(a)), a = 3.8 nm, b = 1.1 nm, α = 52° (Figure 3.8(b)), and a = 4.1 nm, b = 1.2 nm, α = 38° (Figure 3.7(c)). Although the alkyl-chains could not be seen on the STM images, the spacing between the molecules was exactly the right width for an all-*trans* octyl-chain arrangement; it was assumed that they form an interdigitated pattern and thereby minimize the two-dimensional crystallisation energy. Only two of the possible conformations were found, but the *anti, syn*-conformation at each B ring at each side of molecule **3** was also found in the 3D single-crystal X-ray structure of **8**. It is noteworthy, that although the conformations and the molecular arrangements in Figure 3.7(c), Figure 3.8(a) and Figure 3.8(b) were different, the two-dimensional packing density per molecule was roughly the same. In the domain of Figure 3.7(c), the molecules are tilted much more along the row of molecules than for the other two domains shown.

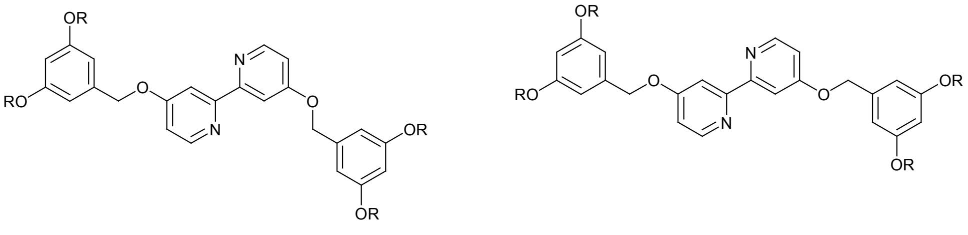

Scheme 3.8 Two different conformations of **3** observed in the self-assembled monolayers.

The monolayer of **6** was less stable than those of **3**, and therefore it was much more challenging to obtain images with a resolution as high as for the first generation **3**. The domains obtained from a dichloromethane solution were of very small size and therefore unstable with a lot of drift. Hexane as solvent (or other weak evaporating solvents) was necessary. The analysis for the second generation compound **6** proved to be much easier, since there were three electron-rich aromatic rings per wedge instead of only one as in compound **3**. As a consequence, most conformations could easily be excluded and the conformation could be assigned with a high certainty. Figure 3.6(b) and Figure 3.6(c) show the observed molecular conformations of **6** in the two different domains displayed in Figure 3.6(a). In one domain (Figure 3.6(b)), the bpy unit was in a *trans*-conformation and the molecule was in an *anti, syn*-conformation with respect to the $C^{bpy}–O–CH_2$ units. The outer generation of benzyl groups attached to the inner generation anti-benzyl group adopted an *anti, syn*-conformation; the outer generation of benzyl groups attached to *syn*-benzyl ring exhibited an *anti, anti*-conformation. In the other domain (Figure 3.6(c)), all the benzyl groups were *anti* with respect to the ring to which they were attached.

3.4 Switching molecular conformation

Large dendritic substituents are expected to impose a significant mechanical barrier to conformational change involving the bpy unit when the molecule is constrained on a surface. In particular, the conformational change from the *trans*-arrangement of nitrogen atoms in a free ligand to the *cis*-conformation within a coordinated ligand is expected to have a high activation barrier associated both with the mechanical motion of the dendritic substituents and the necessary involvement of non-planar bpy which cannot lie flat on the surface during the conformational change. Despite this, to address the conformation of the bpy domain of molecule **3** through interaction with metal ions or protons was attempted, both of which result in the formation of *cis* species under solution and normal solid state conditions.[43-47] Treating the adsorbed monolayer of **3** with dilute aqueous solutions of metal salts (copper(II) sulfate or palladium(II) acetate) destroyed the ordered domains. After such treatment, no organised monolayers were observed with STM. The complexes **[Pd(3)₂][PF₆]₂** and **[Pd(3)Cl₂]** were prepared from **3** (Scheme 3.3). These complexes contained square planar PdN_4 and PdN_2Cl_2 units, respectively, which were expected to interact optimally with the graphite surface. However, treatment of the graphite surface with hexane solutions of either of these complexes did not result in the formation of ordered monolayers. Treating the monolayers of **3** with aqueous acidic solutions (0.1 M HCl or 0.1 M AcOH) did not influence the structure of the monolayers, which were imaged unchanged after this treatment. However, passing gaseous HCl over the monolayers for about 15 seconds resulted in a conformational change of all molecules in small domains, and the formation of a highly ordered structure with new periodic properties (Figure 3.9). The molecules were no longer stacked side by side in a *trans*-conformation, forming lamellar stripes as in Figure 3.4(d). In contrast, the domains in the protonated system were built from large X-like structures. In many hundreds of recorded images of compound **3**, these structures have never been observed and therefore they have to be a result of treatment with HCl. The smaller size of the domains makes them less stable for imaging. Drift in the images was frequently observed, and this made it impossible to record images of the protonated monolayer of the quality used for the conformational analysis of **3.**

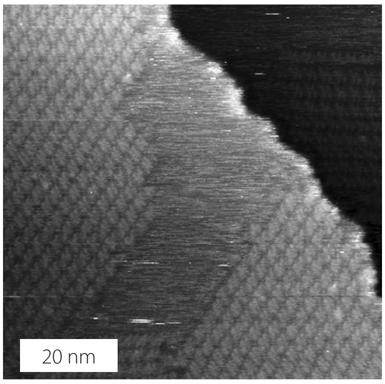

Figure 3.9 STM image of a monolayer of **3** after treatment with gaseous HCl for about 15 seconds. Scan parameters: 80 nm x 80 nm, $U_b = -800$ mV, $I_t = 9$ pA.

Although the protonation itself could not be seen directly, the conformational change after treatment with HCl was dramatic and characteristic. Qualitative modelling and the known protonation chemistry of bpy were consistent with the molecule adopting a cis-conformation. Even after treatment with gaseous HCl, some large domains in the monolayers retained a lamellar structure similar to those observed for unprotonated **3**. It was proposed that the cis domains were formed in a concerted conformational change in which a number of molecules in a domain changed simultaneously. This conclusion followed from observations that (i) only small domains were observed, and (ii) no domains showed mixtures of both cis- and *trans*-conformations. At this stage, no speculation on the stoichiometry of the protonated species could be made. However these preliminary results offered an indication of the use of STM to monitor chemical changes within a self-assembled monolayer.

3.5 Studies of self-assembled monolayers obtained from Langmuir-Blodget films

Another method of forming self-assembled monolayers on a graphite surface is by pulling the graphite through a Langmuir-Blodget film. Interestingly, no difference was observed either if the Langmuir-Blodget film is preformed and then the graphite surface was treated twice with the Langmuir-Blodget film (by putting the graphite into the solution and by taking it out) or if the graphite was firstly added into water and then the Langmuir-Blodget film was formed, so that the graphite surface was in contact with the Langmuir-Blodget layer only once. One would expect that the first method resulted in the formation of a bilayer and the second method, a monolayer. But the self-assembled monolayers obtained in either case were the same. By adding a droplet of a 0.2 mM solution of compound **3** in hexane on an aqueous solution (surface: ≈80 cm^2), the Langmuir-Blodget film was spontaneously formed (Figure 3.10). Interestingly, they differed enormously from the monolayers obtained with the solution casting method. Unfortunately, the conformation of the molecules forming this monolayer could not be assigned. However, due to the very dense packing, it is assumed, that the molecule does not have a flat conformation.

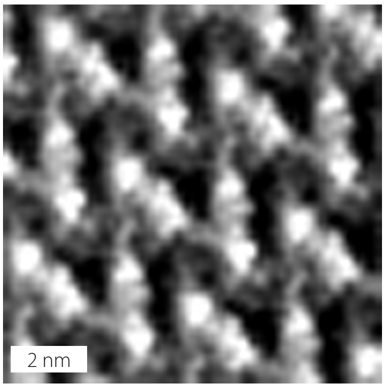

Figure 3.10 STM image of a monolayer of **3** obtained from a Langmuir-Blodget film. Scan parameters: 10 nm x 10 nm, $U_b = -800$ mV, $I_t = 7$ pA, averaged over 90 points.

What makes this method interesting is the fact that, for example, the pH of the aqueous phase can be varied. One can also imagine that if the aqueous solution contains metal ions which can coordinate with the bpy forming the monolayer, these metal complexes then could potentially form a Langmuir-Blodget film.

A Langmuir-Blodget film was spontaneously formed by the same method described above but on a aqueous 30 mM HCl solution. Graphite was dipped into the solution and the surface was immediately investigated with the STM. Occasionally, small domains could be observed which had a lot of drift and were therefore useless for further investigations, as conformational analysis (Figure 3.11). The monolayer formed on top of a neutral solution clearly differed from the one formed on top of a strongly acidic solution. These observations were interpreted in terms of the different conformation of the bpy unit.

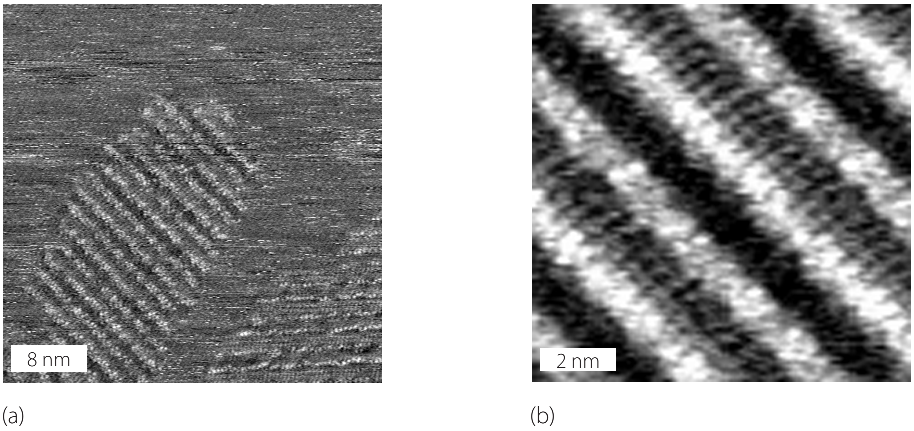

(a) (b)

Figure 3.11 (a) STM image of a monolayer of **3** obtained from a Langmuir-Blodget film under acidic conditions. Scan parameters: 50 nm x 50 nm, U_b = -800 mV, I_t= 7 pA; (b) expanded image and averaged over 90 points.

3.6 Data analysis and discussion of the monolayers containing 8

As it will be discussed in Chapter 7 the octyl-chains help the formation of lamellar structures due to their ability to interdigitate with each other. In addition, they have a better interaction with the graphite surface than benzyl rings (see Chapter 7). As shown with the self-assembled monolayer of **6** for example**,** molecules with octyl-chains do not always form lamellar structures. Therefore, it was thought that molecule **6** does not need the octyl-group to form self-assembled monolayers.

Since the 3D crystal structure of **8** was known (see Section 3.1.3), it was interesting to compare the 3D structure with the 2D monolayer. As expected, the formation of a self-assembled monolayer of **8** was not as spontaneous as with **3** or **6**. Nevertheless, using chloroform as solvent and using the solution casting method, self-assembled monolayers could be observed and imaged, although the monolayers suffered from drift due to too small domains.

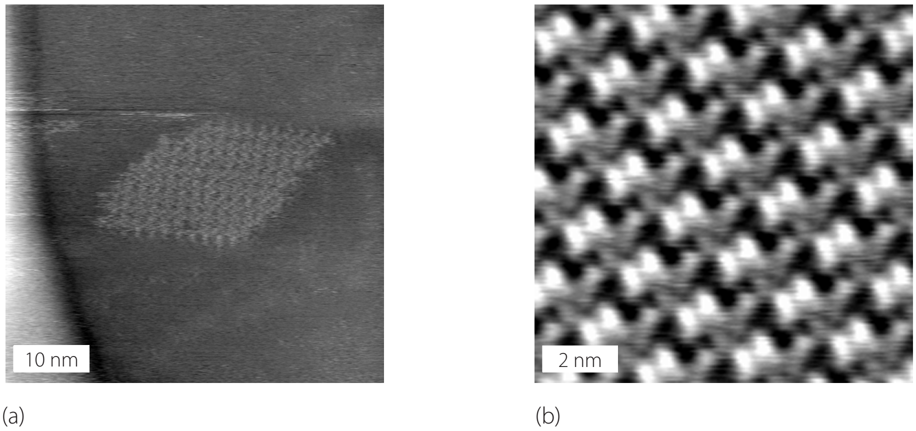

(a) (b)

Figure 3.12 (a) A typical STM-image of a monolayer of **8** (50 nm x 50 nm, U_b = −800mV, I_t= 8 pA). The domain is very small in size. (b) An image of a monolayer of **8** averaged over 80 positions (10 nm x 10 nm, U_b = −800 mV, I_t= 8 pA).

The conformation could therefore not be assigned. The monolayers showed a *p*1 plane group. Overlaying of calculated flat molecules clearly showed a lack of space (Figure 3.13). Hence, it can be concluded, that the molecules do not lie flat on the surface. Another indication therefore was the fact that the bpy unit showed the clearest contrast and as discussed before, the electron-rich aromatics of the Fréchet-dendrons should have had much more contrast than the bpy core. It was concluded that the bpy laid flat on the surface and the dendritic wedges did not lay parallel to the graphite surface, probably due to π-stacking interactions with benzyl-rings of adjacent molecules. A similarity between the 3D crystal structure and the 2D monolayer could be excluded, which was not surprising since the 3D X-ray structure did not show any molecules ordered in layers.

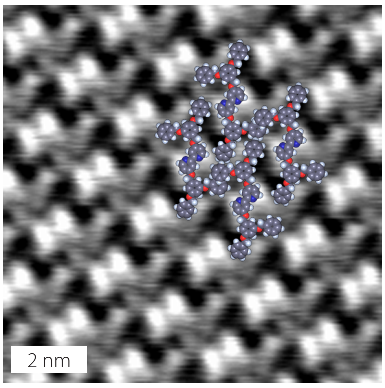

Figure 3.13 Overlaying of flat molecules with an *anti, anti*-conformation with respect to the C^{bpy}–O–CH_2 units. For these flat molecules, the peripherial benzyl groups of the adjacent molecules come in contact with each other. This lack of space is a clear indication for a "non-flat" conformation of the molecule.

Deposition of a dendritic wedge functionalised bpy ligand on a HOPG surface resulted in the formation of well-defined monolayers exhibiting different conformations of the molecule. The near atomic resolution made assignment of two conformers possible. Both of them spontaneously and rapidly formed molecular domains under ambient conditions. Within a molecular domain, only one conformer was present and domains of different conformers were observed side by side. No preference for one conformer was observed. Higher generation dendrons to the bpy also showed at least two different conformers in self-assembled monolayers. An additional conformational effect was found upon treating the domains with HCl gas, when a partial rearrangement of the bpy from *trans* to *cis* occured, concomitant with protonation.

3.7 Experimental part

Compound 3: Methanesulfonyl chloride (1.04 mL, 13.5 mmol) was added over 15 min to a mixture of **1** (1.23 g, 3.38 mmol) and NEt_3 (2.08 mL, 16.9 mmol) in dry dichloromethane (20 mL) at −15 °C under nitrogen. After stirring for 1 hour at −15 °C, the reaction mixture was poured into a mixture of crushed ice (100 mL) and concentrated HCl (10 mL). The dichloromethane layer was separated, washed with saturated $NaHCO_3$ solution, dried (Na_2SO_4) and evaporated to give **2** (1.80 g, ca. 80% pure, 3.20 mmol) as an oil. Crude **2** (41.5 mg, ca. 80% pure, 75.0 µmol), 4,4'-dihydroxy-bpy (6.90 mg, 35.0 µmol), K_2CO_3 (50.0 mg, 362 µmol) and *n*-Bu_4NI (2 mg, 6 µmol) were stirred vigorously in ethyl acetate (400 µL) and water (400 µL) at 60 °C for 20 hours. Water (20 mL) was added and the mixture extracted three times with ethyl acetate (20 mL). The combined organic layers were dried ($MgSO_4$) and evaporated. Preparative chromatography on silica (dichloromethane:methanol 10:1) yielded **3** as a white powder (23.1 mg, 26.1 µmol, 74%). m. p. 57 °C. ^1H NMR (500 MHz, $CDCl_3$): δ 8.48 (d, J = 5.7 Hz, 2H, H^{6A}), 8.05 (d, J = 2.7 Hz, 2H, H^{3A}), 6.91 (dd, J = 5.7, 2.7 Hz, 2H, H^{5A}), 6.57 (d, J = 2.1 Hz, 4H, H^{2B}), 6.42 (t, J = 2.2 Hz, 2H, H^{4B}), 5.15 (s, 4H,H^{OCH_2B}), 3.94 (t, J = 6.6 Hz, 8H, $H^{OCH_2CH_2}$), 1.77 (tt, J = 6.8, 6.5 Hz, 8H, $H^{OCH_2CH_2}$), 1.45 (tt, J = 7.5, 7.3 Hz, 8H, $H^{OCH_2CH_2CH_2}$), 1.25−1.37 (m, 32H, $H^{(CH_2)_4}$), 0.88 ppm (t, J = 7.0 Hz, 12H, H^{CH_3}). ^{13}C NMR (125 MHz, $CDCl_3$): δ 166.1, 160.7, 157.7, 150.4, 138.0, 111.7, 107.5, 105.9, 101.2, 70.1, 68.3, 32.0, 29.5, 29.4 (2 overlapping signals), 26.2, 22.8, 14.3 ppm. IR (neat): ($\tilde{\nu}$, cm^{-1}) 2924 s, 2855 m, 1582 s, 1458 s, 1296 m, 1234 m, 1173 s, 1057 s, 995 s, 833 s. MS (ESI+): *m/z* 903.5 $[M + Na]^+$, 881.6 $[M + H]^+$. UV-vis (CH_2Cl_2): λ/nm ($\varepsilon/M^{-1}\ cm^{-1}$) 274 (22 000). Anal. Calcd for $C_{56}H_{84}N_2O_6$: C, 76.32; H, 9.61; N, 3.18; found: C, 76.10; H, 9.80; N, 2.78%.

Compound 3-*N,N'*-dioxide: Compound **4** (500 mg, 1.37 mmol) and NaH (50%, 55mg, 1.3 mmol) was stirred in in dry THF (20 mL) at room temperature under nirogen. After stirring for 1 hour, 4,4'-dinitro-2,2'-bipyridine-*N,N'*-dioxide was added and stirred at room temperature for another 18 hours.The solvent was removed *in vacuo*. Chromatography on silica (dichloromethane: methanol 10:1) yielded **3-*N,N'*-dioxide** as a yelllow oil (90.0 mg, 99.0 µmol, 16%). ^1H NMR (250 MHz, $CDCl_3$): δ 8.21 (d, J = 7.3 Hz, 2H, H^{6A}), 7.55 (d, J = 3.4 Hz, 2H, H^{3A}), 6.96 (dd, J = 7.4, 3.3 Hz, 2H, H^{5A}), 6.51 (d, J = 2.3 Hz, 4H, H^{2B}), 6.42 (t, J = 2.2 Hz, 2H, H^{4B}), 5.07 (s, 4H,H^{OCH_2B}), 3.92 (t, J = 6.5 Hz, 8H, $H^{OCH_2CH_2}$), 1.76 (tt, J = 6.8, 6.5 Hz, 8H, $H^{OCH_2CH_2}$), 1.43 (tt, J = 7.5, 7.3 Hz, 8H, $H^{OCH_2CH_2CH_2}$), 1.25−1.37 (m, 32H, $H^{(CH_2)_4}$), 0.88 ppm (t, J = 6.6 Hz, 12H, H^{CH_3}). ^{13}C NMR (100 MHz, $CDCl_3$): δ 161.1, 158.0, 142.4, 141.2, 137.3, 114.8, 114.8, 106.2, 101.7, 71.7, 68.6, 32.2, 29.8, 29.6 (2 overlapping signals), 26.4, 23.1, 14.5 ppm. IR (neat): ($\tilde{\nu}$, cm^{-1}) 2924 s, 2854 m, 1597 s, 1450 s, 1380 w, 1296 m, 1157s, 1057 w, 995 m, 825 s. MS (MALDI-TOF+): *m/z* 916.4 $[M + 4H]^+$, 900.3 $[M - O + 4H]^+$, 884.3 $[M - 2O + 4H]^+$.

Compound 4: Methanesulfonyl chloride (1.04 mL, 13.5 mmol) was added over 15 min to a mixture of **1** (1.23 g, 3.38 mmol) and NEt_3 (2.08 mL, 16.9 mmol) in dry dichloromethane (20 mL) at −15 °C under nitrogen. After stirring for 1 hour at −15 °C, the reaction mixture was poured into a mixture of crushed ice (100 mL) and concentrated HCl (10 mL). The dichloromethane layer was separated, washed with saturated $NaHCO_3$ solution, dried (Na_2SO_4) and evaporated to give **2** (1.80 g, ca. 80% pure, 3.20 mmol) as an oil. Crude **2** (1.33 g, ca. 80% pure, 75.0 μmol), 3,5-dihydroxybenzylalcohol (210 mg, 1.50 mmol), K_2CO_3 (840 mg, 6.00 mmol) and 18-crown-6 (15.8 mg, 60.0 μmol) were stirred vigorously in acetone (30 ml) at 60 °C for 48 hours. The solvent was evaporated, water (20 mL) was added and the mixture extracted three times with dichloromethane (20 mL). The combined organic layers were dried ($NaSO_4$) and evaporated. Chromatography on silica (ethyl acetate:hexane 1:7) yielded **4** as an off-white powder (950 mg, 1.14 mmol, 76%).

^{1}H NMR, IR and MS were identical to those reported.[19] m.p. 38 °C.

Compound 6: Methanesulfonyl chloride (0.12 mL, 1.54 mmol) was added over 15 min to a mixture of **4** (330 mg, 0.390 mmol) and NEt_3 (0.260 mL, 2.12 mmol) in dry dichloromethane (5 mL) at −15 °C under nitrogen. After stirring for 1 hour at −15 °C, the reaction mixture was poured into a mixture of crushed ice (50 mL) and concentrated HCl (4 mL). The dichloromethane layer was separated, washed with saturated $NaHCO_3$ solution, dried (Na_2SO_4) and evaporated to give mesylate **5** (390 mg, ca. 80% pure, 0.35 mmol) as an oil. Crude **5** (170 mg, ca. 0.15 mmol), 4,4'-dihydroxy-2,2'-bpy (11.8 mg, 60.0 μmol), K_2CO_3 (50.0 mg, 362 μmol) and *n*-Bu_4NI (2 mg, 6 μmol) were stirred vigorously in ethyl acetate (500 μL) and water (500 μL) at 60 °C for 20 hours. Water (20 mL) was added and the mixture extracted three times with ethyl acetate (20 mL). The combined organic layers were dried ($MgSO_4$) and evaporated. Preparative chromatography on silica (dichloromethane:methanol 10:1) yielded **6** as a white powder (49.2 mg, 27.1 μmol, 44%). ^{1}H NMR (500 MHz, $CDCl_3$): δ 8.50 (d, *J* = 5.7 Hz, 2H, H^{6A}), 8.14 (s br, 2H, H^{3A}), 6.93 (dd, *J* = 5.5, 2.1 Hz, 2H, H^{5A}), 6.71 (d, *J* = 2.1 Hz, 4H, H^{2B}), 6.60 (t, *J* = 2.2 Hz, 2H, H^{4B}), 6.56 (d, *J* = 2.2, 8H, H^{2C}), 6.41 (t, *J* = 2.2 Hz, 4H, H^{4C}), 5.18 (s, 4H, $H^{\mathrm{OC}\mathit{H}_2\mathrm{B}}$), 4.97 (s, 8H, $H^{\mathrm{OC}\mathit{H}_2\mathrm{C}}$), 3.94 (t, *J* = 6.6 Hz, 16H, $H^{\mathrm{OC}\mathit{H}_2\mathrm{CH}_2}$), 1.77 (tt, *J* = 7.3, 6.6 Hz, 16H, $H^{\mathrm{OCH}_2\mathrm{C}\mathit{H}_2}$), 1.45 (tt, *J* = 7.5, 7.3 Hz, 16H, $H^{\mathrm{OCH}_2\mathrm{CH}_2\mathrm{C}\mathit{H}_2}$), 1.29−1.38 (m, 4H, $H^{(\mathrm{C}\mathit{H}_2)_4}$), 0.89 ppm (t, *J* = 6.9 Hz, 24H, $H^{\mathrm{C}\mathit{H}_3}$). ^{13}C NMR (125 MHz, $CDCl_3$): δ 166.2 160.7 160.3, 157.2, 150.0, 139.0, 138.1, 112.0, 107.5, 106.6, 105.8, 102.1, 101.0, 70.3, 70.1, 68.2, 32.0, 29.5, 29.4, 29.4, 26.2, 22.8, 14.2 ppm. IR (neat): ($\tilde{\nu}$, cm^{-1}) 2924 m, 2854 m, 1589 s, 1450 s, 1373 m, 1157 s, 1049 s, 825 m. MS (MALDI-TOF+): *m/z* 1818.7 $[M]^+$, 1880.6 $[M + Na + K]^+$. UV-VIS (CH_2Cl_2): λ/nm (ε/M^{-1} cm^{-1}) 276 (37000). Anal. Calcd for $C_{116}H_{172}N_2O_{14}$: C, 76.61; H, 9.53; N, 1.54; found: C, 76.07; H, 9.37; N, 1.76%.

Compound 8: Crude Mesylate **7** (400 mg, ca. 80% pure, 800 µmol), 4,4'-dihydroxy-bpy (60.0 mg, 305 µmol), K_2CO_3 (240 mg, 1.74 mmol) and *n*-Bu_4NI (10 mg, 30 µmol) were stirred vigorously in ethyl acetate (1 mL) and water (1 mL) at room temperature for 20 hours. Water (20 mL) was added and the mixture extracted three times with ethyl acetate (20 mL). The combined organic layers were dried (Na_2SO_4) and evaporated. Chromatography over silica (dichloromethane:methanol 15:1) yielded **8** as a white powder (82.5 mg, 104 µmol, 34%). ^1H NMR (500 MHz, $CDCl_3$): δ 8.48 (d, ^3J = 5.7 Hz, 2H; H^{6A}), 8.06 (d, J = 2.4, 2H; H^{3A}), 7.42 (d, J = 7.1 Hz; 8H, H^{2C}), 7.37 (dd, J = 7.6, 7.6 Hz; 8H, H^{3D}), 7.32 (dd, J = 7.3 Hz, 7.1 Hz; 4H, H^{4C}), 6.89 (dd, J = 5.6, 2.5 Hz, 2H; H^{5A}), 6.70 (d, J = 2.1 Hz, 4H; H^{2B}), 6.60 (t, J = 2.2, 2H; H^{4B}), 5.16 (s, 4H; H^{OCH_2B}), 5.05 ppm (s, 8H; H^{OCH_2Ph}). ^{13}C NMR (125 MHz, $CDCl_3$): δ 165.85, 160.36, 157.98, 150.40, 138.34, 136.82, 128.76, 128.20, 127.70, 111.67, 107,32, 106.57, 102.02, 70.30, 69.89 ppm. IR (neat): ($\tilde{\nu}$, cm^{-1})3032 w, 2901 w, 2870 w, 1967 w, 1875 w, 1736 w, 1590 s, 1443 m, 1373 m, 1296 s, 1149 s, 1027 s, 864 m, 825 s, 733 m, 694 s. MS (ESI+): *m/z* 793 $[M]^+$. Anal. Calcd for $C_{52}H_{44}N_2O_6{\cdot}2H_2O$: C 75.34, H 5.86, N 3.38; found: C 75.56 H 5.67 N 3.05%.

[Pd(3)Cl$_2$]: Compound **3** (35 mg, 39 µmol) and $K_2[PdCl_4]$ (13 mg, 40 µmol) were refluxed in ethanol (20 mL) for 16 hours. The solvent was evaporated, hexanes added to the yellow residue, and the resultant suspension was filtered through Celite to give a yellow filtrate. The solvent was evaporated to give **[Pd(3)Cl$_2$]** as a yellow oil (41 mg, 39 µmol, 98%). ^1H NMR (500 MHz, $CDCl_3$): δ 8.62 (d, J = 6.7 Hz, 2H, H^{6A}), 7.66 (d, J = 2.6 Hz, 2H, H^{3A}), 6.77 (dd, J = 6.7, 2.6 Hz, 2H, H^{5A}), 6.62 (d, J = 2.2 Hz, 4H, H^{2B}), 6.43 (t, J = 2.2 Hz, 2H, H^{4B}), 5.32 (s, 4H, H^{OCH_2B}), 3.94 (t, J = 6.6 Hz, 8H, $H^{OCH_2CH_2}$), 1.74 (tt, J = 6.8, 6.5 Hz, 8H, $H^{OCH_2CH_2}$), 1.42 (tt, J = 7.5, 7.3 Hz, 8H, $H^{OCH_2CH_2CH_2}$), 1.25−1.37 (m, 32H, $H^{(CH_2)_4}$), 0.88 ppm (t, J = 7.0 Hz, 12H, H^{CH_3}). ^{13}C NMR (125 MHz, $CDCl_3$): δ 167.2, 160.8, 157.2, 150.8, 136.4, 113.1, 110.3, 106.3, 101.6, 71.8, 68.3, 31.8, 29.4, 29.3 (2 overlapping signals), 26.1, 22.7, 14.1 ppm. IR (neat): ($\tilde{\nu}$, cm^{-1})2924 s, 2854 m, 1736 m, 1605 s, 1450 m, 1335 m, 1219 w, 1165 s, 1041 m, 841 m, 764 m. MS (FAB): *m/z* 985 $[M - 2Cl]^+$. UV-vis (CH_2Cl_2): λ/nm ($\varepsilon/M^{-1}\,cm^{-1}$) 301 (10 000), 289 (9800). Anal. Calcd for $C_{56}H_{84}Cl_2N_2O_6Pd$: C, 63.54; H, 8.00; N, 2.65; found: C, 63.90; H, 8.09; N, 2.42%.

[Pd(3)$_2$][PF$_6$]$_2$: **[Pd(3)Cl$_2$]** (38.0 mg, 35.9 µmol), compound **3** (31.6 mg, 35.9 µmol) and $TlPF_6$ (26.2 mg, 75 µmol) were stirred in dichloromethane (20 mL) at room temperature for 4 hours. The suspension was filtered through Celite and the solvent of the filtrate was evaporated. Sonicating in methanol (15 mL) for 2 minutes afforded **[Pd(3)$_2$][PF$_6$]$_2$** as a pale yellow powder (68.0 mg, 31.5 µmol, 88%). m. p. 173 °C. ^1H NMR (500 MHz, CD_2Cl_2): δ 8.38 (d, J = 6.8 Hz, 4H, H^{6A}), 7.69 (d, J = 2.1 Hz, 4H, H^{3A}), 7.50 (br s, 4H, H^{5A}), 6.58 (d, J = 2.2 Hz, 8H, H^{2B}), 6.42 (t, J = 2.1 Hz, 4H, H^{4B}), 5.27 (s, 8H, H^{OCH_2B}), 3.92 (t, J = 6.5 Hz, 16H, $H^{OCH_2CH_2}$), 1.73 (tt, J = 6.7, 6.5 Hz, 16H,

$\mathrm{H}^{\mathrm{OCH_2}\mathit{CH_2}}$), 1.42 (tt, *J* = 7.5, 6.7 Hz, 16H, $\mathrm{H}^{\mathrm{OCH_2CH_2}\mathit{CH_2}}$), 1.23−1.37 (m, 64H, $\mathrm{H}^{\mathrm{OCH_2CH_2}\mathit{CH_2}}$), 0.87 ppm (t, *J* = 7.1 Hz, 24H, $\mathrm{H}^{\mathit{CH_3}}$). ^{13}C NMR (125 MHz, CD_2Cl_2): δ 168.7, 160.8, 157.2, 151.8, 135.9, 114.3, 111.6, 105.9, 101.5, 72.1, 68.2, 31.8, 29.3, 29.2, 29.2, 26.0, 22.6, 13.9 ppm. IR (neat): ($\tilde{\nu}$, cm^{-1}) 2924 s, 2854 m, 1605 s, 1443 m, 1335 m, 1227 w, 1165 s, 1041 m, 825 s, 687 m. MS (ESI+): *m/z* 2012.3 $[M - PF_6]^+$, 933.3 $[M - 2PF_6]^{2+}$. UV-vis (CH_2Cl_2): λ/nm (ε/M^{-1} cm^{-1}) 288 (28000), 236 (92000). Anal. Calcd for $C_{112}H_{168}F_{12}N_4O_{12}P_2Pd$: C, 62.31; H, 7.84; N, 2.60; found: C, 63.38; H, 7.80; N, 3.05%.

3.8 References

[1] L. S. Pinheiro, M. L. A. Temperini, *Surf. Sci.* **1999**, *441*, 45.

[2] G. R. Newkome, A. K. Patri, E. Holder, U. S. Schubert, *Eur. J. Org. Chem.* **2004**, 235.

[3] E. C. Constable, *Adv. Inorg. Chem. Radiochem.* **1986**, *30*, 69.

[4] E. C. Constable, *Metals and Ligand Reactivity*, 2nd ed., VCH, Weinheim, **1996**.

[5] M. M. S. Abdel-Mottaleb, N. Schuurmans, S. De Feyter, J. van Esch, B. L. Feringa, F. C. De Schryver, *Chem. Commun.* **2002**, 1894.

[6] C. J. Hawker, J. M. J. Fréchet, *J. Am. Chem. Soc.* **1990**, *112*, 7638.

[7] I. Widmer, U. Huber, M. Stöhr, L. Merz, H.-J. Güntherodt, B. A. Hermann, P. Samorí, J. P. Rabe, P. B. Rheiner, G. Creiveldinger, P. Murer, *Helv. Chim. Acta* **2002**, *85*, 4255.

[8] P. Wu, Q. Fan, G. Deng, Q. Zeng, C. Wang, C. Bai, *Langmuir* **2002**, *18*, 4342.

[9] S. A. Prokhorova, S. S. Sheiko, A. Mourran, R. Azumi, U. Beginn, G. Zipp, C. H. Ahn, M. N. Holerca, V. Percec, M. Möller, *Langmuir* **2000**, *16*, 6862.

[10] P. Wu, Q. Fan, Q. Zeng, C. Wang, G. Deng, C. Bai, *ChemPhysChem* **2002**, 633.

[11] E. C. Constable, B. A. Hermann, C. E. Housecroft, L. Merz, L. J. Scherer, *Chem. Commun.* **2004**, 928.

[12] L. J. Scherer, L. Merz, E. C. Constable, C. E. Housecroft, M. Neuburger, B. A. Hermann, *J. Am. Chem. Soc.* **2005**, *127*, 4033

[13] F. H. Case, *J. Org. Chem.* **1962**, *27*, 640.

[14] E. C. Constable, C. E. Housecroft, B. Kariuki, A. Mahmood, *Supramolecular Chemistry* **2006**, *in press*.

[15] O. Maury, J.-P. Guégan, T. Renouard, A. Hilton, P. Dupau, N. Sandon, L. Toupet, H. Le Bozec, *New J. Chem.* **2001**, *25*, 1553.

[16] S. Graber, oral communication, **2005**.

[17] B. Forier, W. Dehaen, *Tetrahedron* **1999**, *55*, 9829.

[18] K. Ichinose, Y. Ebizuka, U. Sankawa, *Chem. Pharm. Bull.* **2001**, *49*, 192.

[19] P. B. Rheiner, D. Seebach, *Chem. –Eur. J.* **1999**, *5*, 3221.

[20] J.-F. Nierengarten, D. Felder, J.-F. Nicoud, *Tetrahedron Lett.* **1999**, *40*, 269.

[21] D. Felder, M. G. Nava, M. D. P. Carreon, J.-F. Eckert, M. Luccisano, C. Schall, P. Masson, J.-L. Gallani, B. Heinrich, D. Guillon, J.-F. Nierengarten, *Helv. Chim. Acta* **2002**, *85*, 288.

[22] Z. Qin, M. C. Jennings, R. J. Puddephatt, *Inorg. Chem.* **2002**, *41*, 3967.

[23] Z. Qin, M. C. Jennings, R. J. Puddephatt, *Inorg. Chem.* **2003**, *42*, 1956.

[24] O. Maury, J.-P. Guégan, T. Renouard, A. Hilton, P. Dupau, N. Sandon, L. Toupet, H. Le Bozec, *New J. Chem.* **2001**, *25*, 1553.

[25] Z. Bo, X. Zhang, X. Yi, M. Yang, J. Shen, Y. Rehn, *Pol. Bull.* **1997**, *38*, 257.

[26] E. C. Constable, C. E. Housecroft, M. Neuburger, S. Schaffner, L. J. Scherer, *Dalton Trans.* **2004**, 2635.

[27] L. J. Scherer, *Diploma Work*, University of Birmingham, Birmingham, **2001**.

[28] F. Vögtle, M. Plevoets, M. Nieger, G. C. Azzelini, A. Credi, L. De Cola, V. De Marchis, M. Venturi, V. Balzani, *J. Am. Chem. Soc.* **1999**, *121*, 6290.

[29] R. Lim, J. Li, S. F. Y. Li, Z. Feng, S. Valiaveettil, *Langmuir* **2000**, *16*, 7023.

[30] G. M. Florio, T. L. Werblowsky, T. Müller, B. J. Berne, G. W. Flynn, *J. Phys. Chem. B* **2005**, *109*, 4520.

[31] X. Qiu, C. Wang, Q. Zeng, B. Xu, S. Yin, H. Wang, S. Xu, C. Bai, *J. Am. Chem. Soc.* **2000**, *122*, 5550.

[32] A. Miura, Z. Cheng, H. Uji-I, S. De Feyter, M. Zdanowska, P. Jonkheijm, A. P. H. J. Schenning, E. W. Meijer, F. Würthner, F. De Schryver, *J. Am. Chem. Soc.* **2003**, *125*, 14968.

[33] X. Qiu, C. Wang, S. Yin, Q. Zeng, B. Xu, C. Bai, *J. Phys. Chem. B* **2000**, *104*, 3570.

[34] S. De Feyter, F. C. De Schryver, *Chem. Soc. Rev.* **2003**, *32*, 139.

[35] S. De Feyter, A. Gesquière, M. M. Abdel-Mottaleb, P. C. M. Grim, F. C. De Schryver, C. Meiners, M. Sieffert, S. Valiyaveettil, K. Müllen, *Acc. Chem. Res.* **2000**, *33*, 520.

[36] L. C. Giancarlo, G. W. Flynn, *Acc. Chem. Res.* **2000**, *33*, 491.

[37] T. A. Jung, R. R. Schlittler, J. K. Gimzewski, *Nature* **1997**, *386*, 696.

[38] K. Kim, K. E. Plass, A. J. Matzger, *Langmuir* **2003**, *19*, 7149.

[39] K. E. Plass, K. Kim, A. J. Matzger, *J. Am. Chem. Soc.* **2004**, *126*, 9042.

[40] N. Schuurmans, H. Uji-I, W. Mandouh, F. C. D. Schryver, B. L. Feringa, J. van Esch, S. De Feyter, *J. Am. Chem. Soc.* **2004**, *126*, 13884.

[41] J. P. Rabe, S. Buchholz, *Science* **1991**, *253*, 424.

[42] Y. Cai, S. L. Bernasek, *J. Am. Chem. Soc.* **2004**, *126*, 14234.

[43] E. C. Constable, *Adv. Inorg. Chem.* **1989**, *34*, 1.

[44] S. Stepanow, M. A. Lingenfelder, A. Dimitriev, H. Spillmann, R, Delvigne, N. Lin, X. Deng, C. Cai, J. V. Barth, K. Kern, *Nat. Mater.* **2004**, *3*, 229.

[45] N. Lin, A. Dimitriev, J. Weckesser, J. V. Barth, K. Kern, *Angew. Chem. Int. Ed.* **2002**, *41*, 4779.

[46] A. Dimitriev, H. Spillmann, R, Delvigne, N. Lin, J. V. Barth, K. Kern, *Angew. Chem. Int. Ed.* **2003**, *42*, 2670.

[47] M. Ruben, *Angew. Chem.* **2005**, *117*, 1620.

One can certainly plan research, but not the results!

D. Seebach

4 STM Studies and Synthesis of Tpy Decorated with Fréchet-Type Dendritic Wedges

As will be explained theoretically in Chapter 7, and as shown in Chapter 3 with examples of bipyridines functionalised with Fréchet-type dendrons,[1] Fréchet-type dendrons with octyl end groups[2] are useful for self-assembly on graphite surfaces and therefore can be considered as *STM-chromophores*. In order to show the generality of Fréchet-dendrons as *STM-chromophores*, examples are extended to 2,2':6',2''-terpyridines (tpy)[3-7] functionalised with Fréchet-type wedges. In this Chapter, it will be shown that also tpy decorated at the 4'-position with the first and second generation dendrons show reliable and reproducible properties to form stable monolayers on graphite surfaces. For one compound, the analysis of the packing and of the conformation of each molecule of the monolayer was made with help of its X-ray crystal structure.

The synthesis of a 2,2':6',2''-terpyridine-4'(1'*H*)-thione is also shown, which can be an important building block in tpy chemistry.

4.1 Compound synthesis and discussion of single crystal structures

4.1.1 Synthesis and crystal structure analysis of 2,2':6',2''-terpyridine-4'(1'*H*)-thione 9

Although a wide variety of substituents have been introduced onto the basic 2,2':6',2''-terpyridine scaffold[4, 8], sulfur-containing substituents have not been widely investigated. Examples are primarily limited to thioethers and sulfones. Thioethers are the primary products of the Pott's synthetic method,[9] although examples to date are limited to MeS, EtS and *n*-PrS substituents. The thioethers are readily oxidised to the sulfones which have interesting photophysical properties.[10-12] General access to thioether derivatives is analogous to the ether analogues.[13-15] An alkanethiol is therefore reacted with a 4'-halo-tpy. Tpy ethers are often synthesised by reaction of 2,2':6',2''-terpyridine-4'(1'*H*)-one[16] with a haloalkane. Tpy thioethers should be accessible in the same way. Since thiols are known to have more nucleophilic character than alcohols, it is expected that the preparation of the thioether may be easier than that of the corresponding ether.

In the literature, there was just one reference of 2,2':6',2''-terpyridine-4'(1'*H*)-thione with a short synthesis description, which was rather complicated and without characterisation of the product.[17] Although 4'-(4-Mercaptophenyl)-tpy was known,[18] the aim was to get the mercapto group directly attached to the tpy unit. 2,2':6',2''-Terpyridine-4'(1'*H*)-thione **9** was synthesised from 4'-chloro-tpy[16] using sodium hydrogen sulfide as sulfur source in DMF at 140 °C. The ligand so-obtained was washed by removing the solvent and dissolving it in water, where the deprotonated but not the protonated form is soluble. Therefore, after filtering impurities from the basic aqueous solution, the pH was adjusted to 7 and the yellow precipitate formed was collected by filtration.

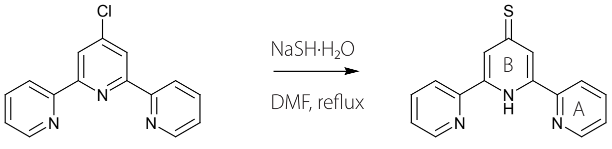

9

Scheme 4.1 Synthesis of **9** by reacting 4'-chloro-tpy with $NaSH·H_2O$ in DMF at 140 °C. Ring labels are used for NMR spectroscopic assignments.

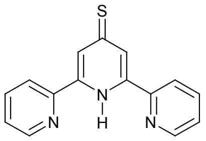

9a

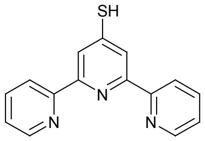

9b

Scheme 4.2 The two possible tautomeric forms of compound **9**, the thione tautomer **9a** and the thiol tautomer **9b**.

The ^1H NMR spectrum of a d_6-DMSO solution of **9** confirmed the high symmetry of the molecule and exhibited a broad singlet at δ 12.4 ppm which should most probably be assigned to an NH proton.[19] The assignment of the correct tautomeric formed in solution was not trivial since in HMBC NMR experiments, no cross coupling between the proton of NH and any carbon signal could be detected, due to the broadness of the signal of NH in the ^1H NMR spectrum. Pyridine-4-(1*H*)-thione is known to favour enormously the thione tautomer **9a** (Scheme 4.2) in the solid state and in polar solvents.[20-22] The ^{13}C NMR spectrum of a d_6-DMSO solution of **9** exhibited a lowest field peak at δ 195.3 ppm assigned to C^{4B} and this correlated well with the reported signal at δ 192.8 ppm for pyridine-4-(1*H*)-thione.[23, 24] Unfortunately, in more apolar solvents such as *d*-chloroform or d_6-toluene the peak for C^{4B} could not be detected. However, since the signal for the NH in the ^1H NMR and all other signals in the ^1H NMR spectrum and in the ^{13}C NMR spectrum were in the same range as in the spectra measured in d_6-DMSO, it was assumed that also in more apolar solvents, **9** is in the thione tautomeric form **9a**.

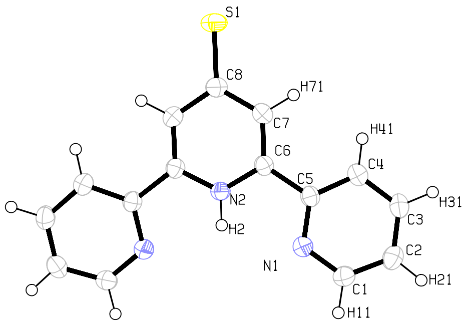

Figure 4.1 The molecular structure of **9**, crystals of which were obtained by diffusion of hexane into a dichloromethane solution of **9**. Important bond lengths and angles: N(1)−C(5) = 1.347(3), N(2)−C(6) = 1.357(2), C(8)−S(1) = 1.702(3), C(1)−N(1) = 1.341(3), C(5)−C(6) = 1.480(3), C(7)−C(8) = 1.414(3) Å; C(2)−C(1)−N(1) = 123.5(2), C(4)−C(5)−C(6) = 121.68(18), C(6)−C(5)−N(1) = 115.41(17), C(5)−C(6)−N(2) = 115.60(17), C(7)−C(8)−S(1) = 121.86(13), C(6)−N(2)−C(6) = 122.5(2)°.

2,2':6',2''-Terpyridine-4'(1'*H*)-thione **9** was not extremely sensitive to air oxidation, probably due to the fact that the molecule was in the thione tautomer in the solid state as it was confirmed by X-ray analysis. Single crystals of **9** were obtained by diffusion of hexane into a solution of **9** in dichloromethane.

The solid state structure consists of **9** and dichloromethane with no close contacts between them. Compound **9** is present in the crystal as the thione tautomer **9a**. There are no classical hydrogen bonds N−H···Y between adjacent molecules of **9**.[25, 26] The tpy unit adopts an unusual *cis, cis*-conformation, as a result of intermolecular hydrogen-bonding between the nitrogen of the terminal rings B and the NH of the central ring B (see labels in Scheme 4.1). The hydrogen atoms are located directly from different Fourier analyses and the interactions between the *cis, cis*-tpy were characterised by an N−H···N angle of 105.76° and an H···N distance of 2.26 Å, and therefore shorter than the van der Waals distance of 2.74 Å.[27] The torsion angle between the pyridine units N−C−C−N is 10.37°. Bond lengths and angles within the central ring B closely resemble those in pyridine-4-(1*H*)-thione and the C−S bond length of 1.702(3) Å provided further evidence for the thione tautomer in solid state.[25, 26]

Although no conventional hydrogen bonds are present, the molecules of **9** and dichloromethane formed sheets exhibiting a number of non-classical C(1)−H(11)···Cl hydrogen bonds with a C(1)···Cl distance of 3.74 Å and an angle C(1)−H(11)···Cl of 139°. Rows of molecules were formed with a shortest contact between H(31) of adjacent molecules of 2.3 Å. This is supported by short C(3)−H(31)···S interactions with the thione sulfur of a molecule in the next row with a C(3)···S distance of 3.70 Å to give a triangular arrangement with a C(3)−H(31)···S angle of 130° (Figure 4.2).

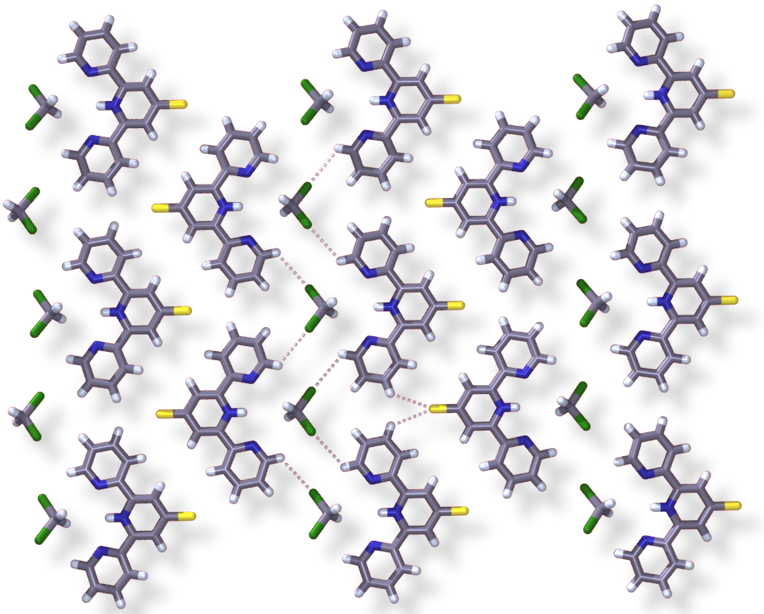

Figure 4.2 Sheets were formed containing compound **9** and dichloromethane which are linked by non-classical C–H···Cl and C–H···S interactions.

Another pseudo-polymorph (not the same solvent encapsulated in the crystal structure) was obtained by diffusing hexane into a solution of **9** in chloroform (instead of dichloromethane as above). The solid state structure consists of **9** and one molecule of water. Compound **9** in this crystal is no longer centrosymmetric as in the structure discussed above.

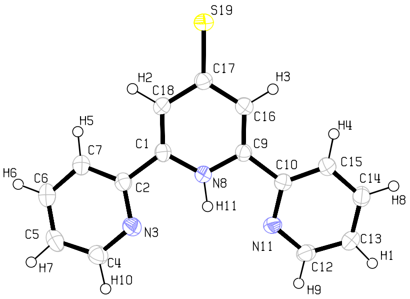

Figure 4.3 The molecular structure of **9** obtained by diffusion of hexane into a chloroform solution of **9**. Important bond lengths and angles: C(1)–C(2) = 1.483(2), C(9)–C(10) = 1.482(2), C(10)–N(11) = 1.343(2), N(11)–C(12) = 1.334(2), C(17)–S(19) = 1.7003(18), N(8)–(C9) = 1.354(2), C(1)–N(8) = 1.356(2), N(3)–C(4) = 1.340(2) Å; C(2)–C(1)–N(8) = 114.44(15), C(1)–C(2)–N(3) = 114.33(15), C(2)–N(3)–C(4) = 117.52(16), C(1)–N(8)–C(9) = 122.83(15), C(9)–C(10)–N(11) = 114.32(15), C(16)–C(17)–S(19) = 121.88(14), C(1)–N(8)–H(11) = 126.347, C(9)–N(8)–H(11) = 110.755°.

The tpy unit also showed a *cisoid* conformation, although with different torsion angles for each terminal Ring A (2.17° respective 13.89°). All other bond lengths and angles are similar to those in the molecular structure of **9** crystallised from dichloromethane and hexane (Figure 4.1 and Figure 4.3).

Compound **9** obtained from chloroform:hexane also formed sheets in the crystal structure, but not containing solvent molecules as above (Figure 4.5). The water molecules are always between the sheets and formed two hydrogen bonds with two sulfur atoms of **9** from different layers (Figure 4.4 and Figure 4.6). Within the plane, the rows are held together by non-classical hydrogen bonds C(14)–H(10)···S with a C(14)···S distance of 3.71 Å (Figure 4.5). The plane group of each layer is *pg* as in the layers from the crystal obtained from dichloromethane:hexane.

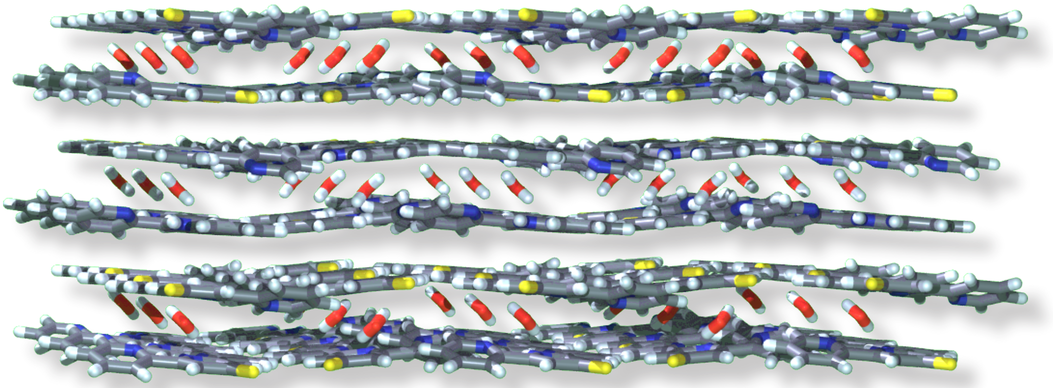

Figure 4.4 The water molecules lie between the sheets, which are formed from compound **9**.

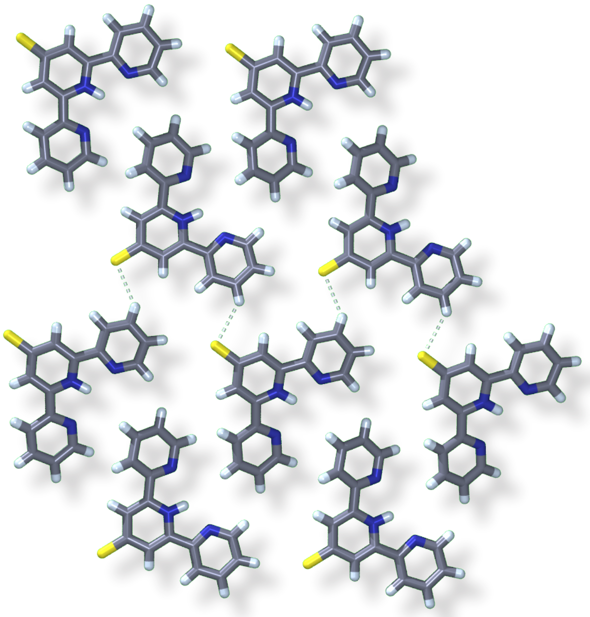

Figure 4.5 One layer from the packing of molecules of **9** obtained from chloroform:hexane. Non-classical hydrogen bonds C(14)–H(10)···S were observed.

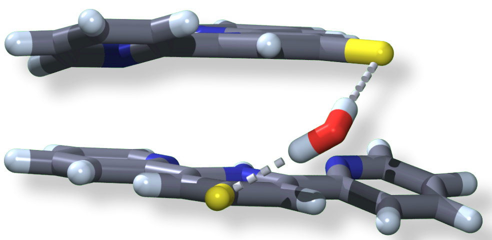

Figure 4.6 The water molecule formed two O–H···S hydrogen bonds with a O···S distance of 2.29 Å with two sulfur atoms of **9** from different layers.

4.1.2 Synthesis of compound 10 and 11 and crystal structure analysis of 10

As mentioned in the introduction, tpy functionalised at the 4'-position with Fréchet-type dendrons with benzylic end groups were known.[28] The complexes of the different generations showed similar electrochemical behaviour. The aim was to form the same dendrons of first and second generation, but with octyl end groups. The synthetic strategy was adopted from the literature,[28] although the chemical behaviour of compounds containing several long-chained alkylic groups can differ enormously from compounds without alkylic long chains. Nevertheless, the synthesis of tpy functionalised with the first and second generation dendritic wedges with octyl end-groups worked without significant differences to that with benzylic end groups. The synthesis of the mesylated wedges **2** and **5** was already reported in Chapter 3. These two electrophilic dendrons were then reacted with 2,2':6',2''-terpyridine-4'(1'*H*)-one[16] and excess of K_2CO_3 as base in refluxing acetone for about two days. Longer reaction times were necessary than with the dendrons having benzylic end groups.[28] The yields were also slightly lower (63% for **10** and 69% for **11**) than than those obtained for the corresponding benzyl-protected molecules.

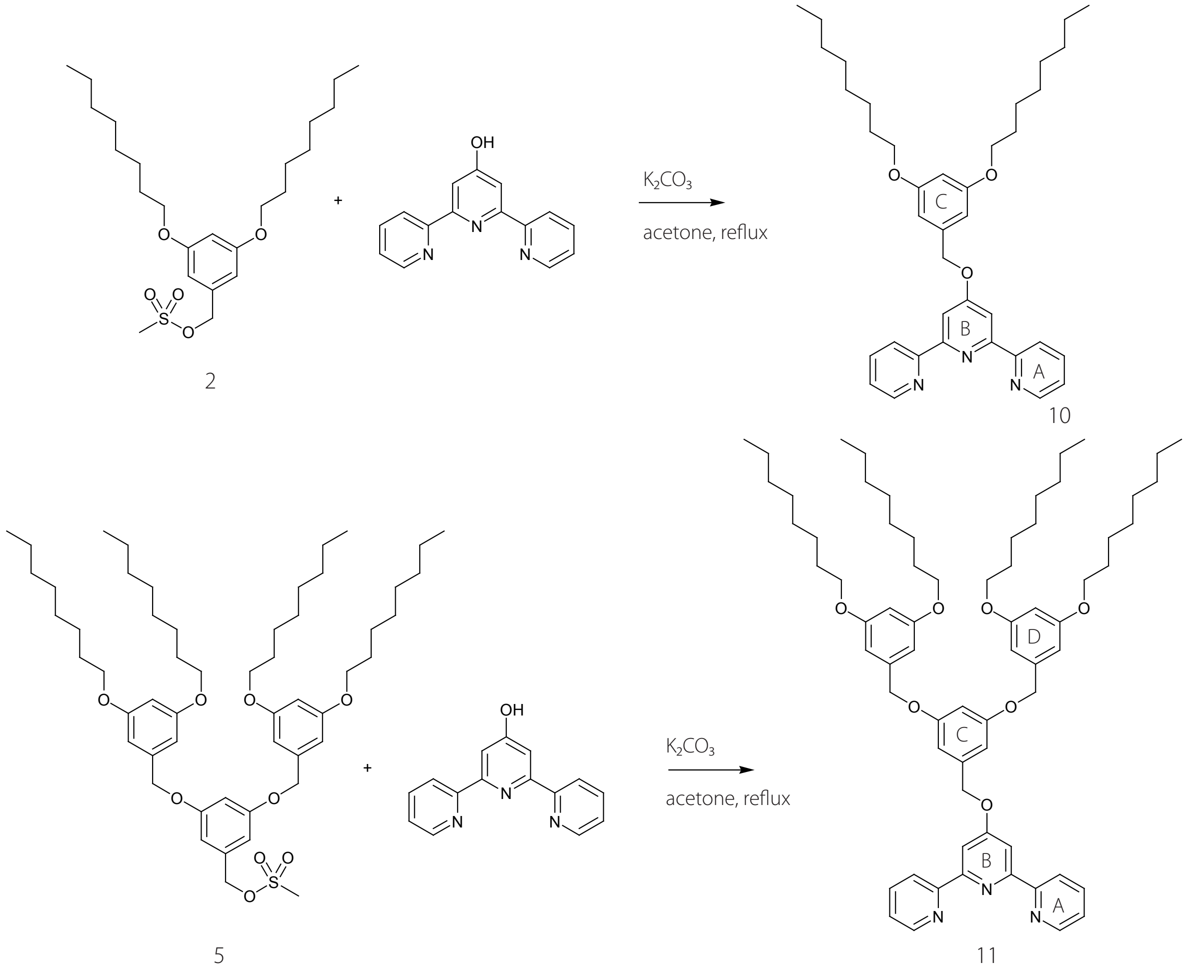

Scheme 4.3 Synthesis of tpy functionalised at 4'-position with first generation **10** respectively second generation **11** Fréchet-type dendron with octyl end groups. Yields: 63% for **10** and 69 % for **11**. Ring labels are used for NMR spectroscopic assignments.

Both compounds **10** and **11** were fully characterised using conventional methods. For compound **10**, single crystals were obtained by slowly evaporating an ethanolic solution of **10**. The single crystal X-ray structure was determined (Figure 4.7).

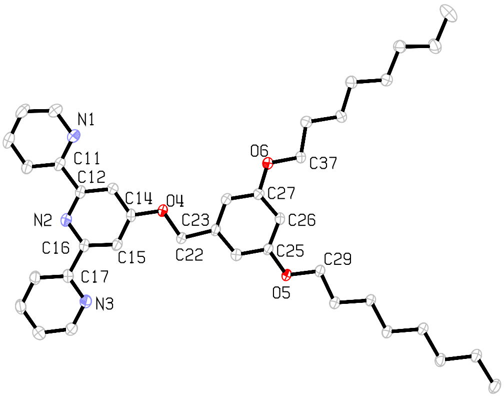

Figure 4.7 The molecular structure of **10** obtained by slowly evaporating an ethanolic solution of **10**. Important bond lengths and angles: N(1)–C(11) = 1.341(3), N(2)–C(16) = 1.346(3), N(3)–C(17) = 1.349(3), O(4)–C(14) = 1.369(2), O(4)–C(22) = 1.433(2), O(5)–(C25) = 1.378(2), O(5)–C(29) = 1.439(2), O(6)–C(27) = 1.372(2), C(11)–C(12) = 1.494(3) Å; C(12)–N(2)–C(16) = 117.46(17), C(14)–O(4)–C(22) = 115.87(16), C(25)–O(5)–C(29) = 117.78(16), C(27)–O(6)–C(37) = 117.11(15), N(1)–C(11)–C(12) = 116.48(18), C(11)–C(12)–N(2) = 116.29(18), C(13)–C(14)–O(4) = 115.90(19), O(4)–C(14)–C(15) = 124.55(18), N(2)–C(16)–C(17) = 116.37(17), O(4)–C(22)–C(23) = 110.62(16), O(5)–C(25)–C(26) = 123.61(17), C(26)–C(27)–O(6) = 122.65(18)°.

The tpy unit adopts the usual *trans, trans*-conformation. The structure is near planar, which is quite remarkable for such a flexible molecule. The important torsion angles are: N(3)–C(17)–C(16)–C(15) = 8.35°, N(1)–C(11)–C(12)–C(13) = 1.71°, C(14)–O(4)–C(22)–C(23) = 2.75°, C(26)–C(25)–O(5)–C(29) = 4.09° and C(26)–C(27)–O(6)–C(37) = 5.01°. The three phenol ether C–O bond lengths are all in the range of about 1.37 Å and the C^{Ar}–O–CH_2 angles are 115.87(16)° for the pyridine ether and 117.11(15)° respectively 117.78(16)° for the outer phenol ethers. The short C^{Ar}–O bonds and the angles close to 120° reflect the sp^2-character of the oxygens (see Chapter 8). The difference between the C(13)–C(14)–O(4) angle (115.90(19)°) and the O(4)–C(14)–C(15) angle (124.55(18)°) is quite remarkable. Steric repulsion of the dendritic wedge might be the reason.

Not only one molecule but all the sheets in the crystal structure are flat (Figure 4.8).

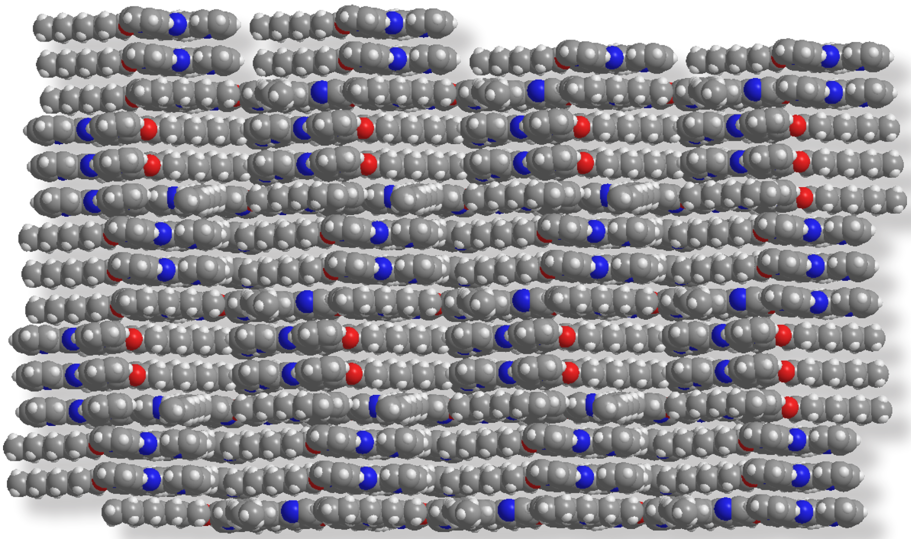

Figure 4.8 Sheets were formed just containing compound **10**. The shortest distance between the layers was 2.4 Å.

Interestingly, no classical π–π stacking interactions between aromatic rings were observed. The sheet-like structure could then be compared directly with 2D self-assembled monolayers (see Section 4.2.1).

Between adjacent molecules in one layer, hydrogen bond C−H···O with C···O contacts of 3.494 Å were observed (Figure 4.9).

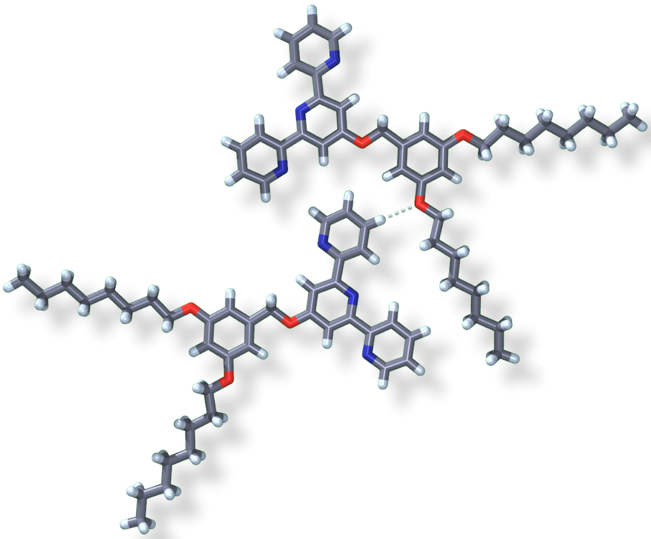

Figure 4.9 Two adjacent molecules of one layer. There is a short C–H···O contact of 2.523 Å.

4.1.3 Synthesis and crystal structure analysis of compound 12

As reported in Section 4.1.1, 2,2':6',2''-terpyridine-4-(1'*H*)-thione **9** can be an important building block for supramolecular chemistry. Alkanethiols may be reacted with 4'-halo-tpy to form tpy thioethers. [13-15] Often, the alkane thiols are difficult to access and are unstable. Consequently, they are not appropriate for the synthesis of tpy thioethers.

The reaction of mesylate **7** with thione **9** proceeded smoothly in acetone in the presence of K_2CO_3 to the desired thioether **12** in 49 % yield (Scheme 4.4).

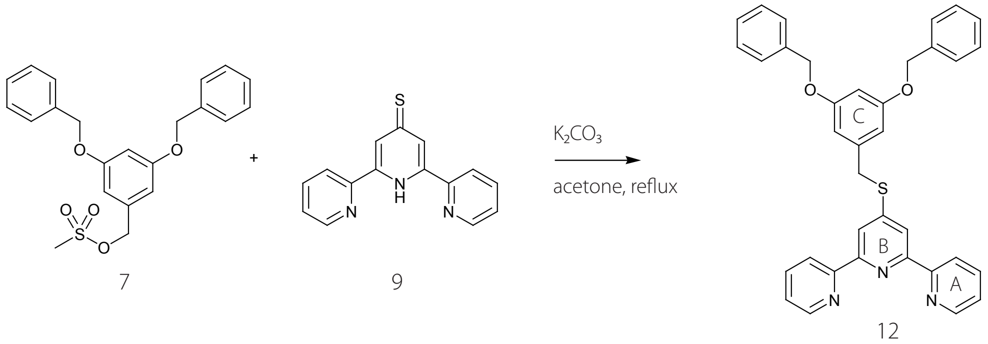

Scheme 4.4 Synthesis of **12** using thione **9** as nucleophile. The reaction time was 20 minutes. Yield: 49%. Ring labels are used for NMR spectroscopic assignments.

The short reaction time of 20 minutes was remarkable when compared to 16 hours using 2,2':6',2''-terpyridine-4'(1'*H*)-one as nucleophile.[28] Compound **12** could not be purified using chromatography due to its instability. Recrystallisation from ethanol was sufficient to get a clean product which was characterised by the standard methods.

By slowly diffusing hexane into a solution of **12** in chloroform, single crystals were obtained. These crystals were structurally characterised by single crystal X-ray diffraction techniques and showed a number of interesting features (Figure 4.10).

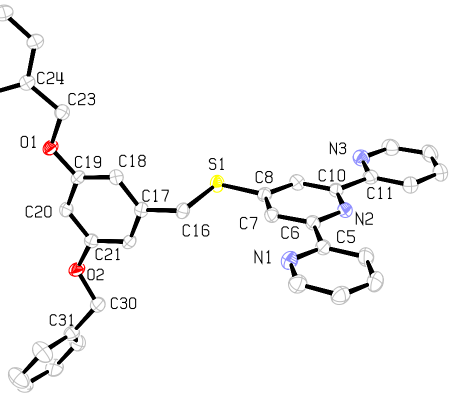

Figure 4.10 The molecular structure of **12**. Important bond lengths and angles: S(1)–C(8) = 1.7598(13), S(1)–C(16) = 1.8209(13), N(1)–C(5) = 1.3387(18), N(2)–C(6) = 1.3400(18), N(2)–C(10) = 1.3423(18), N(3)–C(11) = 1.3408(19), O(1)–C(19) = 1.3631(15), O(1)-C(23) = 1.4214(15), O(2)–C(21) = 1.3648(16), O(2)–C(30) = 1.4280(16), C(5)–C(6) = 1.4892(18), C(10)–C(11) = 1.4932(18), C(16)–C(17) = 1.5110(17), C(23)–C(24) = 1.5006(18), C(30)–C(31) = 1.5142(19) Å; C(8)–S(1)–C(16) = 102.68(6), C(6)–N(2)–C(10) = 117.40(11), C(19)–O(1)–C(23) = 116.88(10), C(21)–O(2)–C(30) = 117.79(10), C(5)–C(6)–N(2) = 116.83(11), S(1)–C(8)–C(7) = 124.57(10), S(1)–C(8)–C(9) = 117.15(10), S(1)–C(16)–C(17) = 109.47(9), O(1)–C(23)–C(24) = 109.80(10), O(2)–C(30)–C(31) = 107.65(11)°.

The tpy unit adopts the usual *trans, trans*-conformation and is very close to planar with torsion angles N(1)–C(5)–C(6)–C(7) = 1.15° respectively N(3)–C(11)–C(10)–C(9) = 1.17°. The torsion angle C(7)–C(8)–S(1)–C(16) is 7.50°. The C(8)–S(1)–C(16) angle is 102.68(6)° and the S(1)–C(8) bond length of 1.7598(13) Å is shorter than the bond to the aliphatic carbon S(1)–C(16) = 1.8209(13) Å. All these numbers are indications of a p-orbital of the sulfur atom overlapping with the aromatic π-system. As already seen in compound **10**,[28] the angles S(1)–C(8)–C(7) =124.57(10)° and S(1)–C(8)–C(9) = 117.15(10)° vary from one another, although less than in **10** (115.90(19)° versus 124.55(18)°) or in **13**[28] (116.0(3)° versus 124.8(3)°) (Figure 4.11). This might be due to the longer $\mathrm{C^{4B}}$–S bond of 1.7598(13) Å compared to the $\mathrm{C^{4B}}$–O bond lengths of compound **10** (1.369(2) Å) and compound **13** (1.363(4) Å), and therefore the steric repulsion of the dendritic wedge might be smaller for compound **12**. The tpy domain and the dendron C-ring of **12** are near orthogonal with a least squared plane angle of 88.5°. The outer phenyl ether oxygens have significant sp^2-character as shown by the short $\mathrm{C^{Ar}}$–O distances (1.3648(16) Å and 1.3631(15) Å) and the two $\mathrm{C^{Ar}}$–O–CH$_2$ angles (116.88(10)° and 117.79((10)°). One of the phenyl rings of the benzyl substituents is disordered with two equal occupancy sites related by a rotation of 74.2°about the C(30)–C(31) vector.

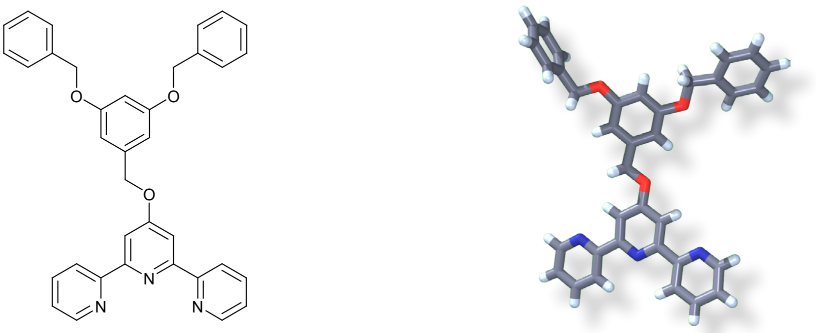

13

Figure 4.11 The molecular structure of **13**.[28]

A significant difference between the solid state structures of **12** and **13** is the angle least squared planes of the tpy unit and the inner aromatic dendron ring. Whereas in **12** this angle is 88.46°, in the molecular structure of **13** the angle is 4.73°. The space group of the crystal structure of **13** and **12** is $P\bar{1}$ and *C*2/*c*, respectively. All these differences are remarkable considering that these two relatively large molecules only differ by one atom.

In the packing of molecule **12**, there is one classical π-stacking interaction between the central pyridine ring of the tpy unit of one molecule with one terminal ring of another molecule with a distance of 3.41 Å (Figure 4.12).

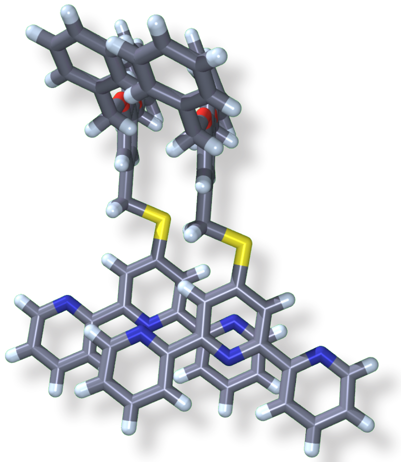

Figure 4.12 The central pyridine ring of the tpy unit of the upper molecule has a π-stacking interaction with one terminal ring of the lower molecule.

4.2 Comparison of the 3D crystal structure with the self-assembled monolayer of 10

Compound **10** formed very reproducible and stable self-assembled monolayers by solution casting, with a 0.2 mM hexane solution (Figure 4.13). Although good quality images were obtained, it was not obvious how the molecules lay on the surface. The rows were an indication of a lamellar packing with interdigitating octyl rings in the darker region. Unfortunately, the octyl-chains could not be visualised well because of the high contrast. Every second row showed a different contrast which was important to notice before averaging. Therefore, the plane group of this monolayer seemed to be quite difficult to determine.

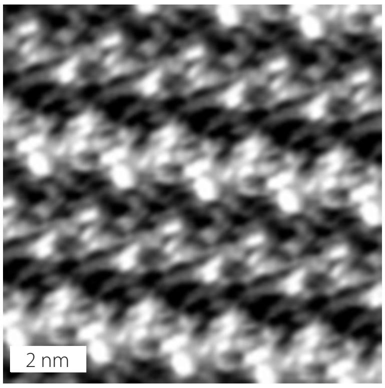

Figure 4.13 A typical STM-image of a monolayer of **10** (10 nm x 10 nm, $U_b = -700$mV, $I_t = 8$ pA) averaged over 26 positions.

The 3D crystal structure of **10** which had already been determined (Section 4.1.2) showed sheet-like layers of near planar molecules (Figure 4.14).

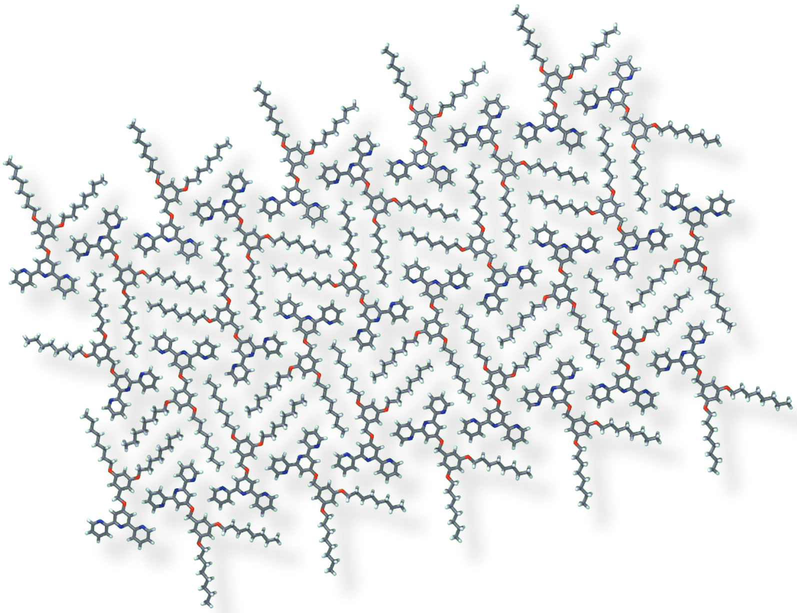

Figure 4.14 One single layer of the 3D crystal structure of compound **10**. The plane group of this layer is *p2gg*. The smallest distance between octyl-chains of adjacent molecules is 2.8 Å.

The plane group of one single layer of the 3D crystal structure is *p2gg* (a = 43.9 Å, b = 21.7 Å), which corresponds to the plane group of the images showing the monolayers of **10** on graphite. Therefore, one layer of the 3D crystal structure of **10** was directly compared with the STM images of the self-organised monolayers of **10**. The overlaid single layer from the crystal structure fitted very well onto the underlaying STM-image (Figure 4.15).[29]

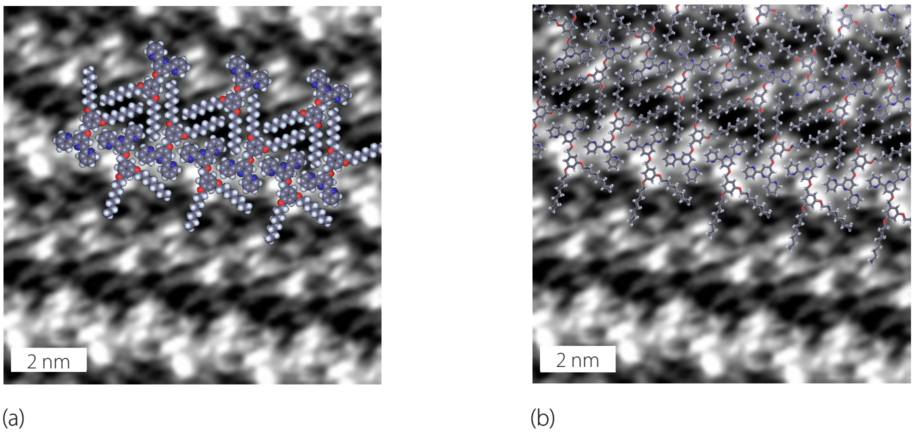

(a) (b)

Figure 4.15 STM-image of **10** with overlaid layer of the crystal structure of **10**. (a) Crystal structure represented in the *space-filling* form, and (b) in the *stick* form.

Multiple domain formation was observed. The threefold symmetry[30] of the frontier orbitals of the graphite surface was not reflected by the domains in Figure 4.16. Detailed analysis revealed the additional presence of small angle domain boundaries (as indicated in Figure 4.16). These two sets of domains were regularly observed with a reproducible small angle relationship between the sets of 15.5°.

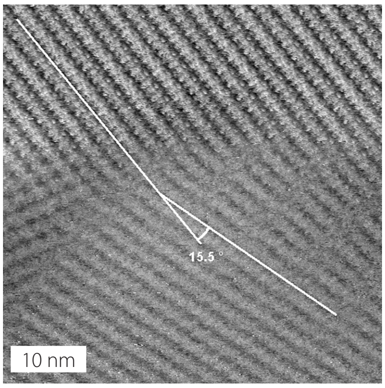

Figure 4.16 STM image of two domains of monolayers of **10**. The angle difference between the two domains is 15.5 °. At the left side of the image between the border line of the two domains, a third domain is visible.

The contrast and the resolution of the two domains always differed, whereas the cell parameters were always the same in these two domains (Figure 4.17). Therefore, domains of different molecular packing or even different conformations could be excluded (see Chapter 3).

It was assumed, that the domain with the weaker resolution came from a bilayer of **10**.[31] This was corroborated by the fact that between the two domains a borderline of free moving molecules could never be observed (Figure 4.16).

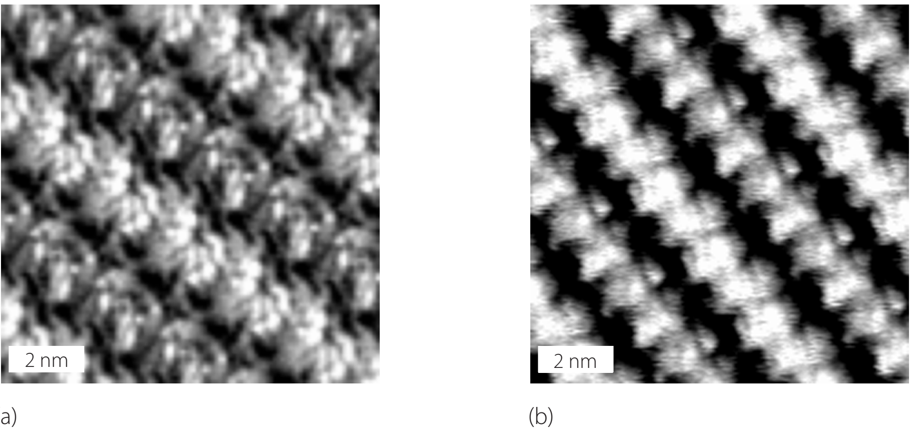

(a) (b)

Figure 4.17 Typical averaged STM images of monolayers of **10**. (a) An averaged image of a good quality domain (10 nm x 10 nm, U_b = −800 mV, I_t = 8 pA, averaged over 157 points). (b) An averaged STM image of an adjacent domain with a small angle relationship to the domain of image (a) of 15.5° (10 nm x 10 nm, U_b = −800 mV, I_t = 8 pA, averaged over 33 points). Image (b) is poorer in quality and fewer details are visible even in the same scan.

Due to the fact that the formation of multilayers could be associated with evaporating a droplet of a solution of **10** on a graphite surface, STM measurements in the liquid–solid interface were conducted (Figure 4.18). 1-Phenyloctane was chosen as solvent due to its high evaporating enthalpy and its non-conductive properties. The images were very similar to the “good quality” images obtained by the solution casting method with the same plane group (*p*2*gg*) and the same unit cell parameters. No other domains with other resolution were observed when measurements were carried out in the liquid–solid interface.

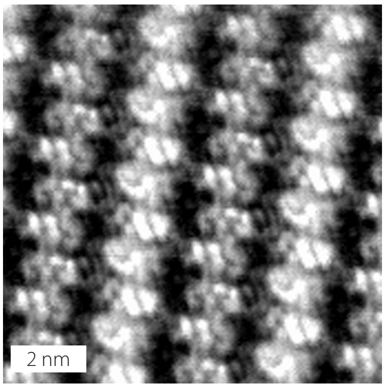

Figure 4.18 STM image obtained by measuring in the solid–liquid interface using 1-phenyloctane as solvent (10 nm x 10 nm, U_b = −800 mV, I_t = 8 pA).

4.3 Conformational analysis of self-organised monolayers of the second generation dendrons 11

The aim was to compare the self-assembled monolayer of the second generation compound **11** with the monolayer of the first generation compound **10**. To form these self-organised monolayers, one droplet of a 0.2 mM solution of compound **11** in hexane was placed on a freshly cleaved HOPG surface and the solvent was evaporated. Hexane was used as solvent, since it was known from compound **6** that solvents with a faster rate of evaporation (e. g. dichloromethane) were not adequate for the formation of stable self-assembled monolayers of large molecules such as **11** (Section 3.2).

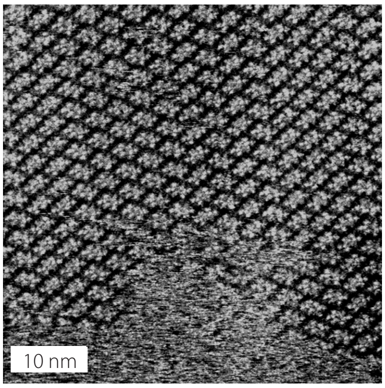

Figure 4.19 STM images of a domains of **11**. At the lower half of the image the borderline to a zone with free-moving molecules on graphite is visible. This is a clear indication of a monolayer (50 nm x 50 nm, $U_b = -700$ mV, $I_t = 8$ pA).

With solution casting, multiple domains were observed in the monolayers of **11** (Figure 4.19). An enlargement of a single domain is shown in Figure 4.20. A *brick-like* pattern is visible.

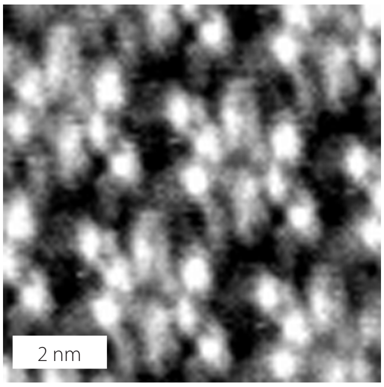

Figure 4.20 Enlargement of one domain. In the averaging procedure special care had to be taken that just domains containing horizontal bricks are averaged (8 nm x 8 nm, $U_b = -700$ mV, $I_t = 8$ pA, averaged over 43 positions).

The interpretation of the STM image was facilitated by the fact that there were three electron-rich aromatic rings, which could act as STM-markers.[32, 33] When measured with negative bias voltage, the HOMOs of the molecule will be visualised in the STM image.[34-37] Semi-empirical calculations at the PM3 level confirmed the expected ordering of orbitals with a cluster of filled orbitals of the benzyl substituents close to the HOMO-LUMO gap, and occupied tpy orbitals lying at lower energy (Figure 4.21).

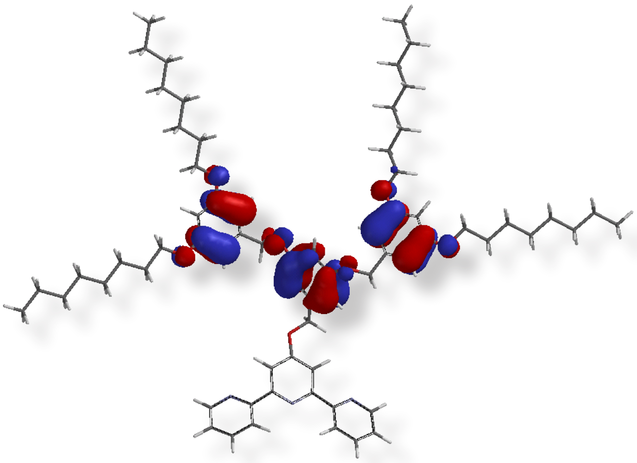

Figure 4.21 The sum of the three highest filled orbitals of **11**. It can clearly be seen, that the HOMOs are located on the benzyl substituents.

The domains comprised rows of dimers. The dimers were formed by intermeshing of the aromatic head-groups and then locking in with adjacent dimers by the interdigitation of the octyl-chains. The conformational analysis was quite simple, due to the fact that the three aromatic rings showed up as high intensity spots and therefore just the angles and distances between the three spots had to be determined and then analysed to obtain the appropriate conformation of compound **11**. The *anti, anti*-conformation gave the best fit (Section 3.1).

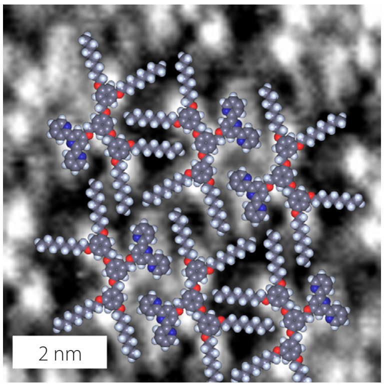

Figure 4.22 STM image from Figure 4.20 with overlaid molecules. The molecules showed an *anti, anti*-conformation.

The two molecules in the unit cell (a = 4.0 nm, b = 3.4 nm, α = 71°) showed the same conformation, and the plane group could therefore be assigned as *p*2 (or *vice versa*). The terminal pyridine rings of two adjacent molecules have a short $C^{6A}–H\cdots N^{A}$ contact,[27] but as in the monolayer of **10** the distance is over 3 Å and therefore too long for a hydrogen bond interaction. A hydrogen bond could be imagined between $C^{4}–H$ of the outer pyridine ring and one oxygen of the outer phenyl ether group. The same hydrogen bond has already been observed in the crystal structure of compound **10** (Figure 4.9).

Within the series of rows, every second to fourth row, the orientation of the molecular dimer changed as a result of rotational dislocation in the 2D array (Figure 4.18 and Figure 4.22). The two rotational orientations of the dimers (marked with black and white bars in Figure 4.23) could either arise from simple failure sequences in the growth of **11** (domains of slightly different orientation growing together) or from a lack of commensurability of the molecule with the graphite surface leading to occasional failures. From the angle between the rows (with respect to the scan-direction and the homogeneity of the rows of molecular dimers) thermal drift could be excluded as an explanation for the two different molecular arrangements. The observed packing with the monolayer resembled a row by row knitted structure. In the upper half of Figure 4.19 gradual crossover from monolayer to mobile molecules into a molecular gas could be observed.[38] This is a clear indication of the existence of monolayers and not multilayers.

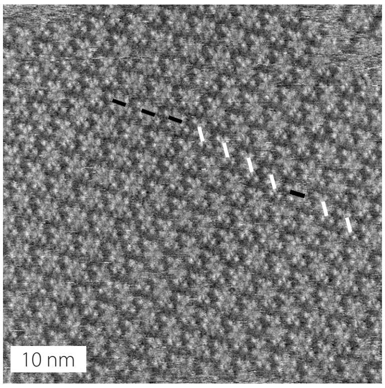

Figure 4.23 The observed packing resembled a row by row knitted structure (marked with black and white bars). Scan parameters: 50 nm x 50 nm, U_b = −700 mV, I_t = 8 pA.

4.4 Comparing the self-assembled monolayers of 12 and 13

As shown in Section 4.1.3, the 3D structure of compound **12** differs enormously from the structure obtained from compound **13**. Therefore, it was interesting to see if the change from the ether to the thioether would also affect the 2D-assembly on HOPG.

As already seen in Section 3.6 and later discussed in Chapter 7, the octyl-chains play a major role in the process of molecular organisation, although the octyl-chains are usually not visualised in the STM images.

For the preparation of monolayers on graphite, a solution casting method was used. In fact, the benzyl decorated Fréchet-type dendrimers **12** and **13** showed a worse tendency for self-assembly on graphite than the octyl decorated compounds **10** and **11**. Hence, chloroform had to be used as solvent, since dichloromethane evaporated too fast. Hexane could not be used due to the lack of solubility of compounds **12** and **13** in solvents that were too apolar. In the monolayers that were observed, it was noted that the intermolecular interactions were no longer dominated by interdigitation of the octyl groups, but rather by van der Waals interlocking of aromatic rings.

Figure 4.24 shows typical images of monolayers obtained from compounds **12** and **13**.

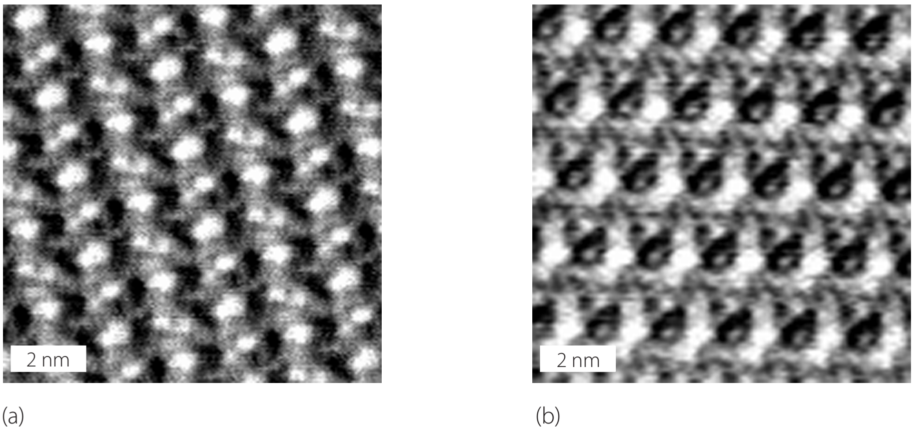

Figure 4.24 A self-assembled monolayer obtained (a) from compound **13** (10 nm x 10 nm, $U_b = -700$ mV, $I_t = 10$ pA, averaged over 44 positions) and (b) from compound **12** (10 nm x 10 nm, $U_b = -700$ mV, $I_t = 8$ pA, averaged over 210 positions).

The difference in conformation and packing for compounds **12** and **13** was immediately apparent. While the unit cell of the ether **13** contained two molecules with a plane group *pg*, compound **12** had only one molecule per unit cell with the plane group *p*1.

The exact conformation and packing analysis of these two monolayers was quite challenging. The monolayers could not be compared with the crystal structure of either compound, since the 3D structure did not contain sheets of near-planar molecules. The interpretation of the monolayer of **12** was simplified by the fact that sulfur can be used as an STM-marker;[39] indeed, this was the reason why compound **12** was synthesised. The sulfur atom showed the highest contrast (Figure 4.24(b)) and therefore its position could be easily identified. Manual fitting of all possible conformers constrained co-planar arrangements of the aromatic groups gave unique fits of the conformations to the STM-images (Figure 4.25(b)). The interpretation of the monolayer of the ether **13** was more difficult. The knowledge of the plane group (*pg*) facilitated the identification of the packing arrangement and the spot with highest contrast was assigned to the most electron rich central aromatic unit, pre-supposed that the molecule exhibited a flat conformation on graphite (Figure 4.25(a)).

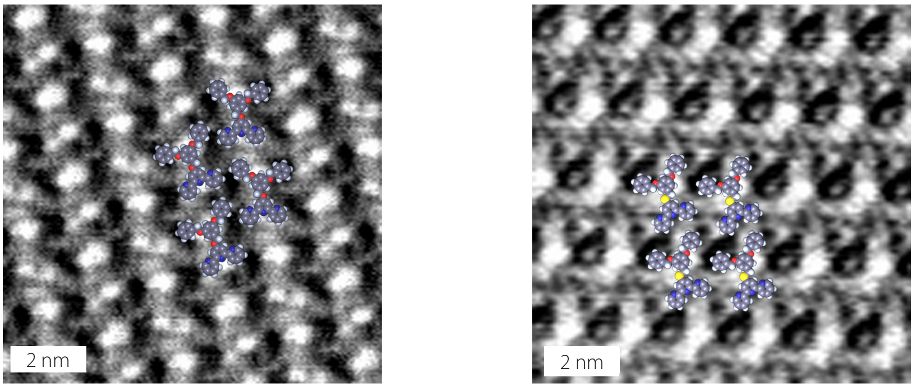

(a) (b)

Figure 4.25 STM images from Figure 4.24 with overlaid molecules.

Deposition of tpy functionalised with Fréchet-type dendrimers on HOPG resulted in the formation of well-defined monolayers exhibiting different arrangements of the molecules under ambient conditions. The structure of the observed self-organised monolayers was sensitive to the molecule structure itself. Hydrophobic octyl chains led to interdigitation and the formation of dimers. If the 3D single crystal structure exhibited sheets, then this structure was also observed in the monolayer.

4.5 Experimental part

Compound 9: A mixture of $NaSH \cdot H_2O$ (1.40 g, 18.9 mmol) and 4'-chloro-tpy[16] (200 mg, 747 μmol) was refluxed in DMF (50 ml) for 4 h. The resulting green suspension was filtered and the solvent evaporated affording a yellow residue. This was then dissolved in water (30 mL) and the pH of the solution adjusted to 7 with 2M aqueous HCl solution (ca. 2 mL) forming a yellow precipitate, which was collected by filtration and washed with water (50 mL) yielding **9** as a yellow powder (171 mg, 16.3 mmol, 86%). m.p. 181 °C. ^1H NMR (500 MHz, d_6-DMSO): δ 12.4 (br s, 1H, H^{NH}), 8.86 (d, J = 4.5 Hz, 2H, H^{6A}), 8.44 (d, J = 8.0 Hz, 2H, H^{3A}), 8.14 (s, 2H, H^{3B}), 8.06 (dd, J = 8.0, 7.4 Hz, 2H, H^{4A}), 7.64 ppm (dd, J = 7.4, 4.8 Hz, 2H, H^{4A}). ^{13}C NMR (125 MHz, d_6-DMSO): δ 150.0, 138.7, 126.3, 121.7 ppm. IR ($\tilde{\nu}$, neat): (cm^{-1}) 3248 m, 3040 w, 1605 m, 1566 s, 1458 m, 1327 m, 1119 m, 987 m, 849 m. MS (EI+, 70 eV): *m/z* 265.1 $[M]^+$. UV-vis (CH_2Cl_2): λ/nm (ε/M^{-1} cm^{-1}) 319 (12000), 278 (34000). Anal. Calcd for $C_{15}H_{11}N_3S$: C, 67.90; H, 4.18; N, 15.84; found: C, 68.34; H, 4.71; N, 15.14%.

Compound 10: $MeSO_2Cl$ (4.78 mL, 62.0 mmol) was added over 15 min to **1** (5.65 g, 15.5 mmol) and NEt_3 (9.55 mL, 15.5 mmol) in dry dichloromethane (20 mL) at −15 °C. After 1 h, the reaction mixture was poured into a mixture of crushed ice (100 mL) and concentrated HCl (10 mL). The dichloromethane layer was separated, washed with saturated $NaHCO_3$ solution, dried (Na_2SO_4) and evaporated to give **2** (8.30 g, ca. 80% pure, ca. 15 mmol) as an oil. Crude **2** (2.00 g, ca. 80% pure, 3.61 mmol), 2,2':6',2''-terpyridine-4'(1'*H*)-one[16] (900 mg, 3.62 mmol) and K_2CO_3 (1.29 g, 9.23 mmol) were stirred vigorously in acetone (100 mL) at 60 °C for 40 hours. The solvent was evaporated, water (50 mL) was added and the mixture extracted three times with dichloromethane (3 x 30 mL). The combined organic layers were dried (Na_2SO_4) and evaporated. Chromatography over silica (ethyl acetate:hexane 3:2) yielded **4** as an oil, which was crystallised in ethanol giving white needles (1.35 g, 2.27 mmol, 63%). m.p. 46 °C. ^{1}H NMR (500 MHz, $CDCl_3$): δ 8.71 (d, J = 4.1 Hz, 2H, H^{6A}), 8.64 (d, J = 8.0 Hz, 2H, H^{3A}), 8.15 (s, 2H, H^{3B}), 7.88 (dd, J = 8.0, 7.7 Hz, 2H, H^{4A}), 7.36 (dd, J = 7.7, 4.2 Hz, 2H, H^{5A}), 6.63 (d, J = 2.2 Hz, 2H, H^{2C}), 6.42 (t, J = 2.2 Hz, 1H, H^{4C}), 5.27 (s, 2H, $H^{\mathrm{O}CH_2\mathrm{C}}$), 3.95 (t, J = 6.6 Hz, 4H, $H^{\mathrm{O}CH_2\mathrm{CH_2}}$), 1.77 (tt, J = 6.8, 6.5 Hz, 4H, $H^{\mathrm{OCH_2}CH_2}$), 1.46 (tt, J = 6.6, 6.5 Hz, 4H, $H^{\mathrm{OCH_2CH_2}CH_2}$), 1.25−1.37 (m, 16H, $H^{(CH_2)_4}$), 0.89 ppm (t, J = 6.9 Hz, 6H, H^{CH_3}). ^{13}C NMR (125 MHz, $CHCl_3$): δ 167.2, 160.7, 156.9, 155.9, 148.9, 138.3, 137.3, 124.1, 121.7, 108.1, 105.7, 101.3, 70.2, 68.3, 32.0, 29.5, 29.4, 29.4, 26.2, 22.8, 14.3 ppm. IR (neat): ($\tilde{\nu}$, cm^{-1}) 2916 s, 2854 m, 1582 s, 1558 s, 1466 s, 1358 s, 1164 s, 1041 s. MS (ESI+): *m/z* 618.2 $[M + Na]^+$, 596.3 $[M + H]^+$. Anal. Calcd for $C_{38}H_{49}N_3O_3.0.5EtOH$: C, 75.69; H, 8.47; N, 6.79; found: C, 75.89; H, 8.50; N, 6.58%.

Compound 11: $MeSO_2Cl$ (51.1 µL, 0.655 mmol) was added over 15 min to **4** (140 mg, 0.165 mmol) and NEt_3 (111 µL, 0.902 mmol) in dry dichloromethane (10 mL) at −15 °C. After 1 hour, the reaction mixture was poured into a mixture of crushed ice (30 mL) and concentrated HCl (1 mL). The dichloromethane layer was separated, washed with saturated $NaHCO_3$ solution, dried (Na_2SO_4) and evaporated to give **5** (140 mg, ca. 80% pure, ca. 0.11 mmol) as an oil. Crude **5** (140 mg, ca. 80% pure, 0.11 mmol), 2,2':6',2''-terpyridine-4'(1'*H*)-one[16] (37.3 mg, 0.150 mmol) and K_2CO_3 (63.0 mg, 0.45 mmol) were stirred vigorously in acetone (30 mL) at 60 °C for 48 hours. The solvent was evaporated, water (50 mL) was added and the mixture extracted three times with dichloromethane (3 x 30 mL). The combined organic layers were dried (Na_2SO_4) and evaporated. Chromatography over alumina (hexane:dichloromethane 1:1) yielded **11** as an oil, which became a powder in the fridge (80.3 mg, 75.3 µmol, 69%). ^{1}H NMR (500 MHz, $CDCl_3$): δ 8.70 (ddd, J = 4.7, 2.0, 0.9 Hz, 2H, H^{6A}), 8.63 (ddd, J = 8.2, 1.0, 1.0 Hz, 2H, H^{3A}), 8.12 (s, 2H, H^{3B}), 7.86 (ddd, J = 8.2, 7.7, 1.6 Hz, 2H, H^{4A}), 7.33 (ddd, J = 7.7, 4.7, 1.0 Hz, 2H, H^{5A}), 6.75 (d, J = 2.2 Hz, 2H, H^{2C}), 6.59 (t, J = 2.2 Hz, 1H, H^{4C}), 6.57 (d, J = 2.2 Hz, 4H, H^{2D}), 6.41 (t, J = 2.2 Hz, 2H, H^{4D}), 5.26 (s, 2H, $H^{\mathrm{O}CH_2\mathrm{C}}$), 4.98 (s, 4H, $H^{\mathrm{O}CH_2\mathrm{D}}$), 3.94 (t, J = 6.6 Hz, 8H, $H^{\mathrm{O}CH_2\mathrm{CH_2}}$), 1.76 (tt, J = 6.8, 6.6 Hz, 8H, $H^{\mathrm{OCH_2}CH_2}$), 1.44 (tt, J = 6.8, 6.7 Hz, 8H, $H^{\mathrm{OCH_2CH_2}CH_2}$), 1.24−1.37 (m, 32H, $H^{(CH_2)_4}$), 0.88 ppm (t, J = 7.2 Hz, 12H, H^{CH_3}). ^{13}C NMR (125 MHz, $CHCl_3$): δ 167.0, 160.7, 160.3, 157.3, 156.2, 149.2, 139.0, 138.5, 137.0, 124.0, 121.5, 107.8, 106.4, 105.8, 102.1, 101.1, 70.4, 70.0, 68.2, 32.0, 29.5, 29.4, 29.4, 26.2, 22.8, 14.3 ppm. IR (neat): ($\tilde{\nu}$, cm^{-1}) 2924 s, 2854 m, 1597 s, 1566 s, 1458 m, 1358 m, 1165 s, 1057 m.

MS (MALDI-TOF+): *m/z* 1129 [M + Na + K + 2H]$^+$, 1089 ([M + Na + 3H]$^+$, 1067 [M + 4H]$^+$. Anal. Calcd for $C_{68}H_{93}N_3O_7$: C, 76.73; H, 8.81; N, 3.95; found: C,76.54; H, 8.88; N, 4.05%.

Compound 12: Mesylate **7** (50.0 mg, 0.125 mmol), **9** (33.5 mg, 0.125 mmol) and K_2CO_3 (53.0 mg, 0.375 mmol) were refluxed in acetone (5 mL) under a nitrogen atmosphere for 20 min. After cooling down to room temperature, the solvent was removed *in vacuo*. Water (20 mL) was added and extracted (3 times) with dichloromethane. The combined organic layers were dried (Na_2SO_4) and the solvent removed *in vacuo* affording a powder, which was crystallised in ethanol (35 mg, 61.3 µmol, 49%). m.p. 126 °C. ^{1}H NMR (500 MHz, $CDCl_3$): δ 8.70 (d, J = 4.1 Hz, 2H, H^{6A}), 8.62 (d, J = 7.8 Hz, 2H, H^{3A}), 8.41 (s, 2H, H^{3B}), 7.89 (dd, J = 7.1, 7.1 Hz, 2H, H^{4A}), 7.39 (dd, J = 7.8, 1.6 Hz, 4H, H^{2Ph}), 7.36 (dd, J = 7.8, 7.0 Hz, 4H, H^{3Ph}), 7.32–7.29 (m, 3H,H^{4Ph}+H^{5A}), 6.77 (d, J = 2.2 Hz, 2H, H^{2C}), 6.52 (t, J = 2.2 Hz, 1H, H^{4C}), 5.02 (s, 2H, H^{OCH_2Ph}), 4.37 (s, 4H, H^{SCH_2C}). ^{13}C NMR (125 MHz, $CDCl_3$): δ 160.1, 155.4, 154.5, 148.7, 138.2, 137.4, 136.7, 128.5, 128.2, 127.6, 124.0, 121.6, 118.1, 108.5, 108.2, 101.6, 70.1, 36.1 ppm. IR (neat): ($\tilde{\nu}$, cm^{-1}) 2923 w, 2854 w, 1605 m, 1551 s, 1443 m, 1381 m, 1319 m, 1157 s, 1057 m. MS (ESI+): *m/z* 590 [M+Na]$^+$. Anal. Calcd for $C_{36}H_{29}N_3O_2S \cdot H_2O$: C, 73.82; H, 5.33; N, 7.17; found: C, 74.24; H, 5.29; N, 7.11%.

4.6 References

[1] C. J. Hawker, J. M. J. Fréchet, *J. Am. Chem. Soc.* **1990**, *112*, 7638.

[2] P. B. Rheiner, D. Seebach, *Chem. –Eur. J.* **1999**, *5*, 3221.

[3] E. C. Constable, *Adv. Inorg. Chem. Radiochem.* **1986**, *30*, 69.

[4] H. Hofmeier, U. S. Schubert, *Chem. Soc. Rev.* **2004**, *33*, 373.

[5] J. Wang, G. S. Hanan, *Synlett* **2005**, *8*, 1251.

[6] A. M. W. Cargill Thompson, *Coord. Chem. Rev.* **1997**, *160*, 1.

[7] L. S. Pinheiro, M. L. A. Temperini, *Surface Science* **2000**, *464*, 176.

[8] D. Wouters, S. Höppener, R. Lunkwitz, L. Chi, H. Fuchs, U. S. Schubert, *Adv. Funct. Mat.* **2003**, *13*, 277.

[9] K. T. Potts, *Bull. Soc. Chem. Belg.* **1990**, *99*, 741.

[10] K. T. Potts, M. J. Cipullo, P. Ralli, G. Theodoridis, *J. Org. Chem.* **1982**, *47*, 3027.

[11] E. C. Constable, A. M. W. Cargill Thompson, N. Armaroli, V. Balzani, M. Maestri, *Polyhedron* **1992**, *11*, 2707.

[12] N. Maestri, N. Armaroli, V. Balzani, E. C. Constable, A. M. W. Cargill Thompson, *Inorg. Chem.* **1995**, *34*, 2759.

[13] P. R. Anders, H. Hofmeier, B. G. G. Lohmeijer, U. S. Schubert, *Synthesis* **2004**, 2865.

[14] U. S. Schubert, C. Eschbaumer, O. Hien, P. R. Anders, *Tet. Lett.* **2001**, *42*, 4705.

[15] P. R. Anders, U. S. Schubert, *Synthesis* **2004**, 1229.

[16] E. C. Constable, M. D. Ward, *J. Chem. Soc., Dalton Trans.* **1990**, 1405.

[17] J. Park, A. N. Pasupathy, J. I. Goldsmith, C. Chang, Y. Yaish, J. R. Petta, M. Rinkoski, J. P. Sethna, H. D. Abruña, P. L. McEuen, D. C. Ralph, *Nature* **2002**, *417*, 722.

[18] A. Auditore, N. Tuccitto, G. Marzanni, S. Quici, F. Puntoriero, S. Campagna, A. Licciardello, *Chem. Commun.* **2003**, 2494.

[19] D. Häussinger, oral communication **2005**.

[20] S. Stoyanov, I. Prtkov, L. Antonov, T. Stoyanova, *Can. J. Chem.* **1990**, *68*, 1482.

[21] P. Beak, F. S. Fry. Jr., J. Lee, F. Steele, *J. Am. Chem. Soc.* **1976**, *98*, 171.

[22] M. J. Cook, S. El-Abbady, A. R. Katritzky, C. Guimon, G. P. Guillouzo, *J. Chem. Soc., Perkin Trans. 2* **1977**, 1652.

[23] G. B. Barlin, D. J. Brown, M. D. Fenn, *Aust. J. Chem.* **1984**, *37*, 2391.

[24] M. Witanowski, L. Michal, *Bull. Pol. Acad. Sci. Chem.* **1987**, *35*, 305.

[25] S. Mutha, J. J. Vittal, *Cryst. Growth Des.* **2004**, *4*, 1181.

[26] M. C. Etter, J. C. MacDonald, R. A. Wanke, *J. Phys. Org. Chem.* **1992**, *5*, 191.

[27] C. Meier, U. Ziener, K. Landfester, P. Weihrich, *J. Phys. Chem. B* **2005**, *109*, 21015.

[28] E. C. Constable, C. E. Housecroft, M. Neuburger, S. Schaffner, L. J. Scherer, *Dalton Trans.* **2004**, 2635.

[29] R. Azumi, G. Götz, T. Debaerdemaeker, P. Bäuerle, *Chem. –Eur. J.* **2000**, *6*, 735.

[30] R. Lim, J. Li, S. F. Y. Li, Z. Feng, S. Valiaveettil, *Langmuir* **2000**, *16*, 7023.

[31] F. Jäckel, M. Ai, J. Wu, K. Müllen, J. P. Rabe, *J. Am. Chem. Soc.* **2005**, *127*, 14580.

[32] L. Merz, H.-J. Güntherodt, L. J. Scherer, E. C. Constable, C. E. Housecroft, B. A. Hermann, *Chem. –Eur. J.* **2005**, *11*, 2307.

[33] L. J. Scherer, L. Merz, E. C. Constable, C. E. Housecroft, M. Neuburger, B. A. Hermann, *J. Am. Chem. Soc.* **2005**, *127*, 4033.

[34] G. M. Florio, T. L. Werblowsky, T. Müller, B. J. Berne, G. W. Flynn, *J. Phys. Chem. B* **2005**, *109*, 4520.

[35] X. Qiu, C. Wang, Q. Zeng, B. Xu, S. Yin, H. Wang, S. Xu, C. Bai, *J. Am. Chem. Soc.* **2000**, *122*, 5550.

[36] A. Miura, Z. Cheng, H. Uji-I, S. De Feyter, M. Zdanowska, P. Jonkheijm, A. P. H. J. Schenning, E. W. Meijer, F. Würthner, F. De Schryver, *J. Am. Chem. Soc.* **2003**, *125*, 14968.

[37] X. Qiu, C. Wang, S. Yin, Q. Zeng, B. Xu, C. Bai, *J. Phys. Chem. B* **2000**, *104*, 3570.

[38] M. Henzler, W. Göpel, *Oberflächenphysik des Festkörpers* **1994**, 362.

[39] L. C. Giancarlo, G. W. Flynn, *Acc. Chem. Res.* **2000**, *33*, 491.

But to chemistry, the skies are wide open, for if it is a science, it is also an art.

J.-M. Lehn

5 STM Studies of Octyl-decorated Fréchet-Type Dendrons

As seen in Chapter 3 and Chapter 4, octyl-decorated Fréchet dendritic wedges are a powerful recognition motif for the assembly of monolayers on graphite. In this chapter, the self-assembly properties of dendritic wedges is shown. Very highly resolved STM images are observed at room temperature in air allowing the analysis of the conformation of the adsorbed molecules. These long-chain alkyl-decorated Fréchet-type dendrons are a powerful assembly motif and initially form a pattern based on trimeric units, assembling into hexagonal host structures with a pseudo-unit cell of seven or eight molecules. The assembly is the same, irrespective of whether the dendron is functionalised by an alcohol, an aldehyde or a methyl ester group. The images obtained are so well resolved that it is possible to unambiguously assign the conformation within individual molecules. Over time, the supramolecular ordering spontaneously and irreversibly changes from a trimeric to a dimeric pattern. The dimeric pattern is the thermodynamically more stable monolayer and can be compared with one layer of the crystal structure. Attempts to exchange the centre of the hexagonal pattern by a guest molecule were made.

5.1 Compound Synthesis of Compounds 14 and Single Crystal Structure of Compounds 4 and 14

The synthesis of compound **4** has already been described in Chapter 3. Compound **14** was obtained by oxidising compound **4** with PCC in dichloromethane at room temperature in 91% yield (Scheme 5.1). PCC was chosen, since the phenyl ether groups of the Fréchet-type dendrimers did not withstand treatment with MnO_2.

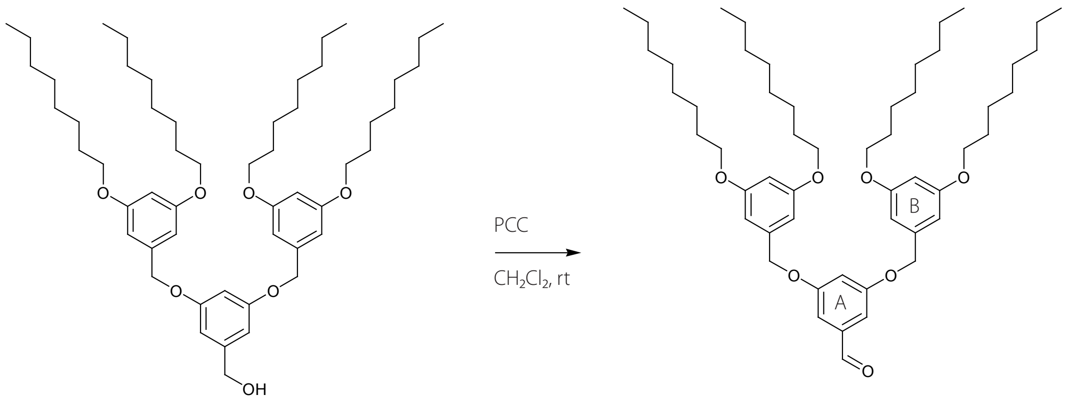

4 14

Scheme 5.1 Preparation of compound **14** by oxidising **4** with PCC in 91% yield. Ring labels are used for NMR spectroscopic assignments.

The aldehyde **14** exhibited a characteristic C=O stretching mode at 1705 cm^{-1} in the IR spectrum and in the ^{1}H NMR spectrum, the aldehyde CH was observed at δ 9.89 ppm.

The corresponding second generation methyl ester **15** (Scheme 5.2) was prepared by M. Malarek in our group using standard conditions.[1]

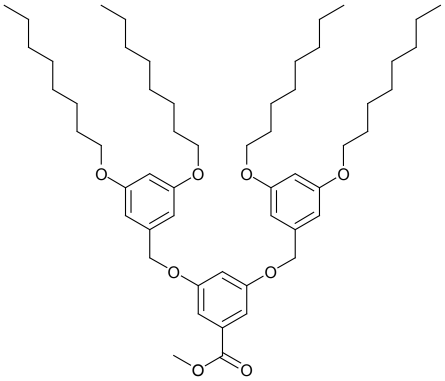

Scheme 5.2 Methyl ester **15**. Unfortunately, no single crystal structure of this compound is known.

Compound **14** was obtained as an oil and by cooling it to 4 °C, single crystals were obtained, which could be measured by X-ray diffraction. The molecular structure of **14** is shown in Figure 5.1 and selected bond lengths and angles are given in the caption.

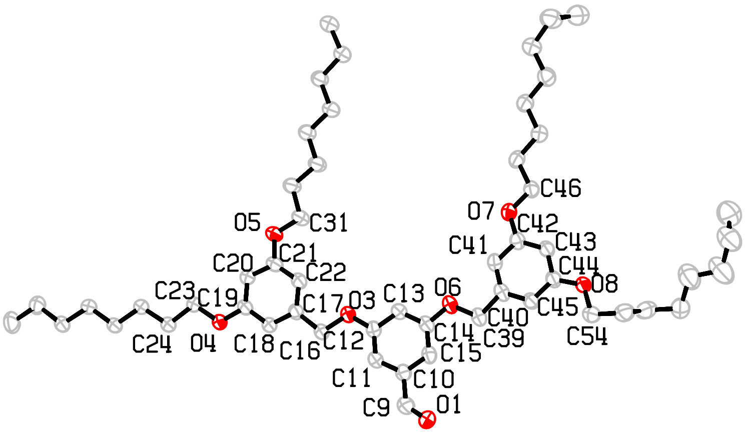

Figure 5.1 The molecular structure of **14,** hydrogen atoms are omitted. Important bond lengths and angles: O(1)–C(9) = 1.215(5), O(3)–C(12) = 1.362(3), O(3)–C(16) = 1.427(3), O(4)–C(19) = 1.371(3), O(5)–C(21) = 1.371(3), O(6)–C(14) = 1.377(3), O(6)–C(39) = 1.423(3), O(7)–C(42) = 1.365(3), O(8)–C(44) = 1.365(3), C(9)–C(10) = 1.482(4), C(16)–C(17) = 1.510(4), C(39)–C(40) = 1.514(4) Å; C(12)–O(3)–C(16) = 116.9(2), C(19)–O(4)–C(23) = 116.7(2), C(21)–O(5)–C(31) = 119.7(2), C(14)–O(6)–C(39) = 116.6(2), C(42)–O(7)–C(46) = 116.8(2), C(44)–O(8)–C(54) = 117.8(2), O(1)–C(9)–C(10) = 126.9(3), O(3)–C(12)–C(13) = 115.0(2), C(13)–C(14)–O(6) = 115.0(2), O(6)–C(14)–C(15) = 124.3(2), O(3)–C(16)–C(17) = 109.2(2), C(18)–C(19)–O(4) = 115.8(2), O(4)–C(19)–C(20) = 123.6(2), C(20)–C(21)–O(5) = 113.7(2), O(5)–C(21)–C(22) = 124.6(2)°.

Compound **14** was found to crystallise in space group $P\bar{1}$. Each molecule is nearly planar, which is quite remarkable for such a flexible molecule. The important torsions angles are: C(11)−C(12)−O(3)−C(16) = 0.39°, C(15)−C(14)−O(6)−C(39) = 0.70°, O(3)−C(16)−C(17)−C(22) = 3.51° and O(6)−C(39)−C(40)−C(41) = 9.13.° The four phenol ether O atoms are all nearly sp^2-hybridised with bond lengths in the range of 1.362(3) Å and 1.427(3) Å and an angle C^{Ar}−O−CH_2 between 116.6(2)° and 119.7(2)°. The O(1)−C(9) bond length of 1.215(5) Å is typical of a C=O double bond of an aldehyde. The aldehyde group is disordered over two positions with occupancies of 40:60 %. The disordered conformations vary in the torsion angle C(15)−C(10)−C(9)−O(1) with a torsion angle difference of 148.7°. While the two alkyl-chains of one side adopt the extended all-*trans*-conformation, both alkyl-chains of the other side have a non extended conformation. The outer benzyl groups adopt an *anti, anti*-conformation with respect to the C^4 proton of the central ring (Scheme 3.7).

As has already been seen in the crystal structure of compound **10**, the near planar molecules of compound **14** form layers within the crystal structure. The shortest distance between two adjacent layers was found between two repulsive protons of the alkyl-chain with 2.35 Å. No π–π stacking interactions between aromatic rings were observed.

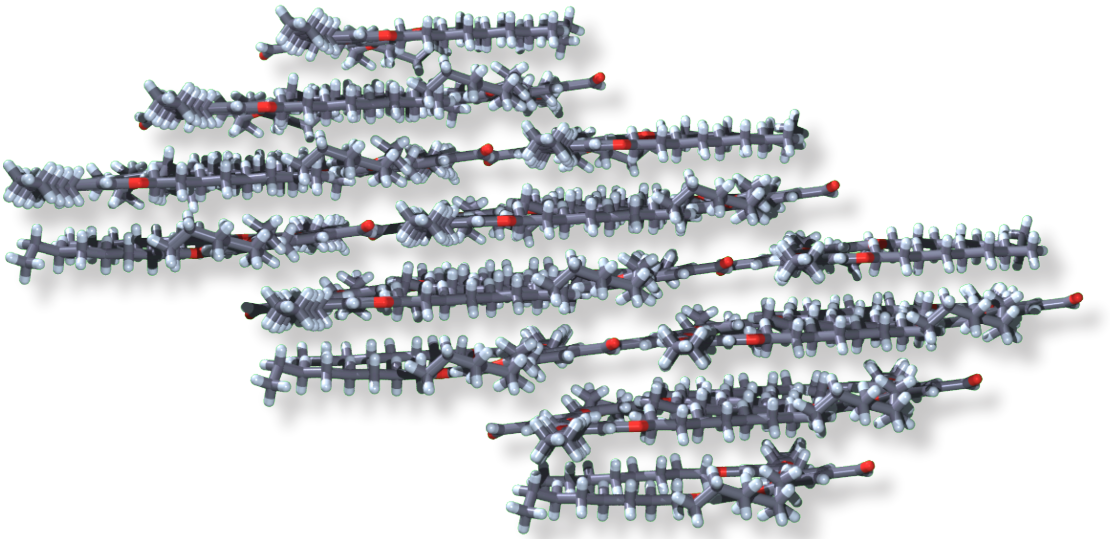

Figure 5.2 The packing in **14** showed a sheet-like structure. The nearest distance between the layers is 2.35 Å.

Within a layer no non-classical hydrogen bonds were observed. As shown in Figure 5.3, interdigitation of the alkyl-chains could be detected forming a lamellar packing.

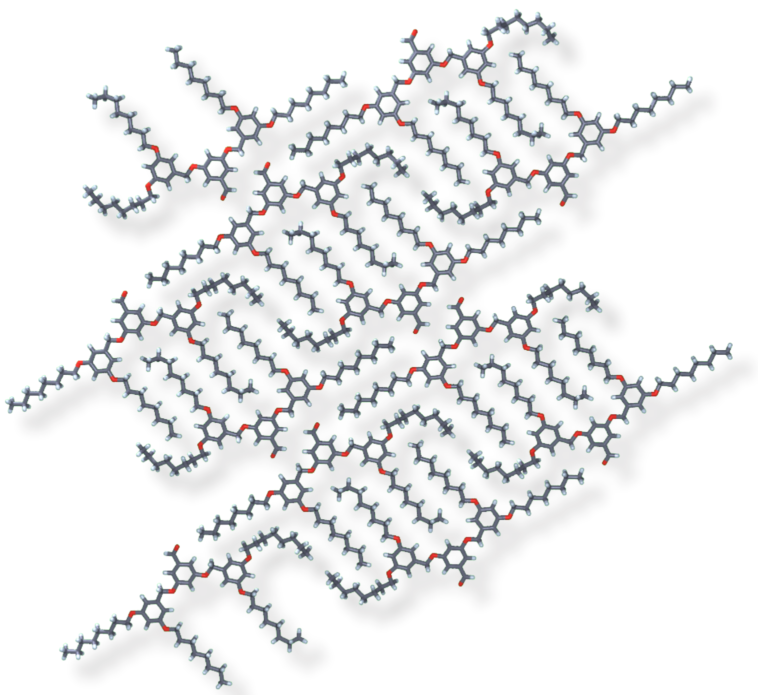

Figure 5.3 Part of one layer from the packing diagram of **14** showing the interdigitation of the alkyl-chains.

As already mentioned in Section 3.1.2, single crystals were also obtained from compound **4** by cooling the oily substance to 4 °C. The crystal structure of this compound had been published by P. B. Rheiner *et al.*[1] Data for the solid-state structure of **4** were collected at 295 K and was refined to $R = 0.0872$, $wR^2 = 0.229$. Rheiner *et al.* mentioned that no hydrogen bonding to the alcohol group was observed. There is disorder present in the structure, with the alcohol oxygen disordered over two sites with C–O distances of 1.219 Å and 1.094 Å. These values are quite short for a C–O alcohol bond and correspond more to a C=O double bond, e. g. of an aldehyde. Due to this uncertainty, the crystal structure of **4** was measured again at 123 K.

All cell dimensions were within 2.5% of those of the published structure and the structure was refined to final R and wR factors of 0.0485 and 0.0565 ($I>3\sigma(I)$). The structure at 123 K (Figure 5.4) closely resembled that at room temperature, with the exception that the alcohol was ordered with a C–O bond length of 1.417(3) Å. Since the structure obtained for **4** is isomorphous and apparently isostructural with the crystal structure of **14**, it is not clear whether the published compound of P. B. Rheiner *et al.* was the alcohol **4** or the aldehyde **14**. After collecting the X-ray data of both **4** and **14**, the compounds were characterised using IR spectroscopy to ensure that no oxidation of the measured crystal occurred during the X-ray process.

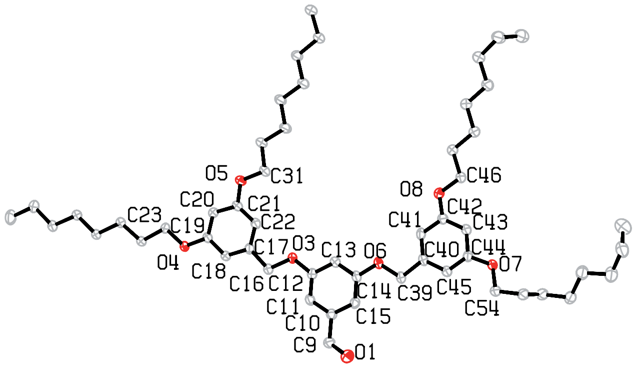

Figure 5.4 The molecular structure of **4,** hydrogen atoms are omitted. Important bond lengths and angles: O(1)–C(9) = 1.417(3), O(3)–C(12) = 1.371(2), O(3)–C(16) = 1.431(2), O(4)–C(19) = 1.374(2), O(5)–C(21) = 1.372(2), O(6)–C(14) = 1.378(2), O(6)–C(39) = 1.427(2), O(7)–C(44) = 1.375(2), O(8)–C(42) = 1.369(2), C(9)–C(10) = 1.507(3), C(16)–C(17) = 1.506(3), C(39)–C(40) = 1.516(3) Å; C(12)–O(3)–C(16) = 117.16(15), C(19)–O(4)–C(23) = 116.19(15), C(21)–O(5)–C(31) = 119.03(16), C(14)–O(6)–C(39) = 116.36(15), C(44)–O(7)–C(54) = 117.77(15), C(42)–O(8)–C(46) = 116.76(15), O(1)–C(9)–C(10) = 115.95(17), O(3)–C(12)–C(13) = 114.70(17), C(13)–C(14)–O(6) = 114.59(18), O(6)–C(14)–C(15) = 124.39(18), O(3)–C(16)–C(17) = 108.82(16), C(18)–C(19)–O(4) = 115.60(16), O(4)–C(19)–C(20) = 123.57(17), C(20)–C(21)–O(5) = 113.21(17), O(5)–C(21)–C(22) = 124.88(17)°.

As already mentioned, the bond lengths and angles of compound **4** were similar to compound **14** with the only difference of the two bond lengths O(1)–C(9) = 1.417(3) Å and C(9)–C(10) = 1.507(3) Å (for the aldehyde: O(1)–C(9) = 1.215(5) Å and C(9)–C(10) = 1.482(4) Å respectively). The shorter C(9)–C(10) bond of the aldehyde can be explained with delocalisation of π-electron density over the aldehyde and the aromatic ring.

Two adjacent molecules in different layers showed hydrogen bond interactions O(1)–H···O(7) with a distance O(1)···O(7) of 3.02 Å (Figure 5.5).

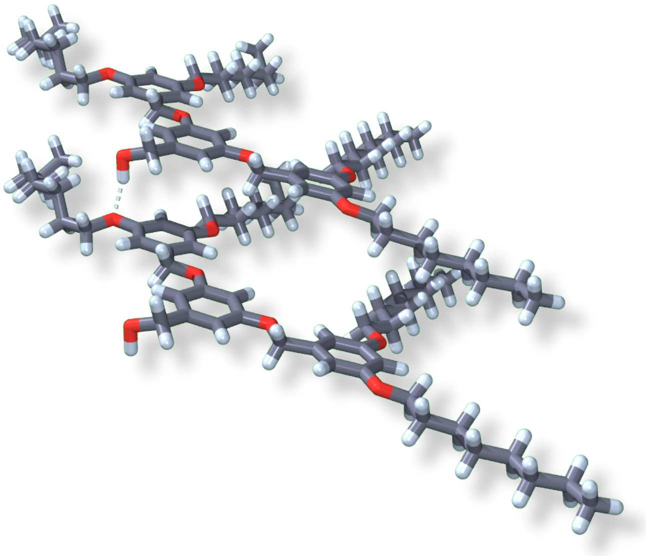

Figure 5.5 Two adjacent molecules of different layers. A short O(1)–H···O(7) contact was observed.

5.2 Self-organised monolayers of compounds 4, 14 and 15

5.2.1 The trimeric pattern of the monolayer formed by compounds 4, 14 and 15

Monolayers of **4**, **14** and **15** were prepared at room temperature in air by placing a droplet of a dilute solution (about 0.2 mM) onto a freshly cleaved sample of HOPG. For **4** and **14** a variety of different solvents was used to investigate whether that could have an influence on the 2D pattern (*n*-pentane, *n*-hexane, *n*-decane, toluene, dichloromethane, acetone, DMF, or 1:1 dichloromethane:methanol). For compound **15,** just hexane and DMF were used; the monolayer obtained by taking a solution of DMF will be discussed in the next Section. After evaporation of the solvent, the samples were mounted in an STM apparatus. Immediately after the approach of the STM tip, a periodic pattern was observed. STM images of organic molecules are often compared to representations of frontier orbitals (see also Sections 3.2 and 4.3).[2-4] In a simplified treatment, a high conductivity results in a high intensity in the STM image and aromatic rings give particularly high contrasts. On the other hand, STM images of alkyl-chains are usually of low intensity and low contrast (see also Sections 3.3 and 4.3).

To maximise the 2D crystallisation energy, the alkyl-chains formed interdigitating patterns with the alkyl-chains of the neighbouring molecules, as has often been observed for alkoxylated molecules adsorbed on surfaces,[2, 5-9] and the molecular arrangement was easily identified. The interdigitation of alkyl-chains was also observed in the solid-state structure of **4** and **14** (see Figure 5.3).

All compounds **4**, **14** and **15** initially formed monolayers. In each case, these comprised multiple domains with similar structures but different orientation.[10] For each compound, three different orientations were observed, reflecting the threefold symmetry of α-graphite.[11, 12]

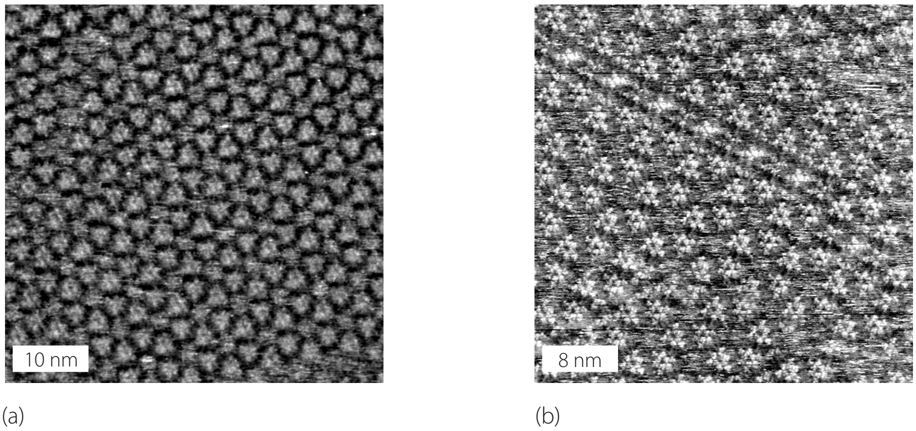

Figure 5.6 Two typical STM images of monolayer of compound (a) **4** (50 nm x 50 nm, $U_b = -700$ mV, $I_t = 30$ pA) and (b) **14** (40 nm x 40 nm, $U_b = -700$ mV, $I_t = 8$ pA).

These domains (Figure 5.6) consisted predominantly of trimeric substructures as previously reported by P. Wu *et al.* for 3,5-bis[(3,5-bis(dodecyloxy)phenyl)methoxy]benzoic acid.[8] However, in contrast to the work of P. Wu *et al.*, additional features were also observed. As can be seen in Figure 5.6(b), rows of embedded dimers were present within the domains of trimers. As expected, the rows of dimers showed three orientations with respect to the surface. The two monolayers of **4** and **14** looked very similar with the same trimeric pattern and the same dimensions. The monolayer of compound **15** also showed a trimeric pattern with similar dimensions as those for the other two compounds.

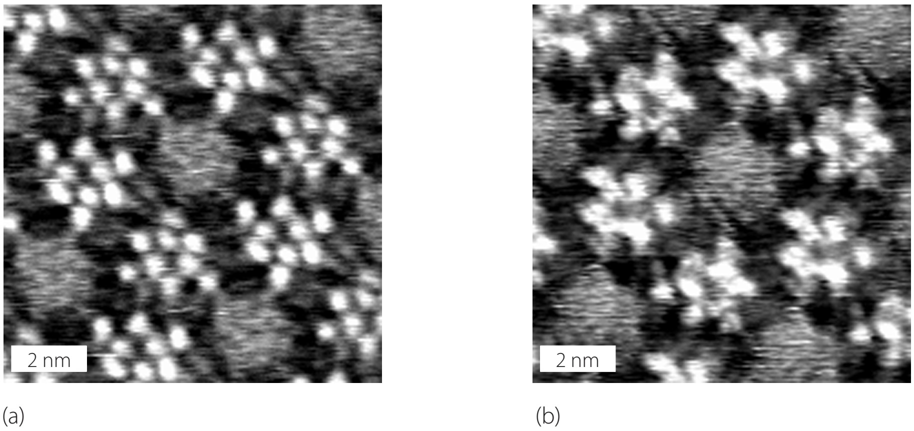

(a) (b)

Figure 5.7 Expanded and averaged STM images of monolayers of (a) compound **4** and (b) compound **14**. Scan parameters: (a) 10 nm x 10 nm, U_b = −700 mV, I_t = 7 pA, averaged over 18 positions; (b) 10 nm x 10 nm, U_b = −700 mV, I_t = 11 pA, averaged over 18 positions.

The biggest difference between the monolayer of **15** and the monolayer obtained from **4** or **14** can be seen by comparing the expanded and averaged images of all three compounds. At the centre of each hexagonal array of trimers of **4** and **14**, an unresolved, noisy centre was observed. Using the averaging procedure described in Chapter 2, the ordered molecules became better resolved, but the noisy centre was smoothed out. The height of the centre in the raw data (Figure 5.6) was roughly the same as for the ordered molecules (see also Figure 5.26(a)). In the averaged image (Figure 5.7), the height of the centre was less than the aromatic parts of the fixed molecules. This indicated random noise, which was generated by mobile molecules. Further proof of the random noise arising from the presence of one molecule confined to an area of roughly 2 nm^2 is given in Section 5.2.2.

STM can resolve and distinguish static and dynamic molecules. The mobile molecule in the centre of the hexagonal array simply had no partners with which to form an interdigitating pattern with its alkyl-chains. At room temperature, the motion of the molecule was faster than the time scale of the STM measurements. Neglecting the randomness of the central molecule, these hexagonal patterns had a unit cell of *seven* molecules with a plane group *p*6. The monolayers of compound **4** and compound **14** were isomorphous, as has already been described for the 3D crystal structures.

Because the images were highly resolved, it was possible to carry out a conformational analysis. A further reduction of noise by using an averaging procedure was helpful, but was not mandatory in order to perform a conformational analysis. Due to the fact that the three aromatic rings showed spots with high intensity, only the angles and distances between the three spots had to be determined. The appropriate conformation for both compounds **4** and **14** was the *anti, anti*-conformation, the same conformation has already been assigned to the second generation compound **11** (see Section 4.3). Since each molecule in crystalline **4** and **14** was near planar and in an *anti, anti*-conformation, the overlaid molecules in Figure 5.8 were directly taken from the crystal structure.

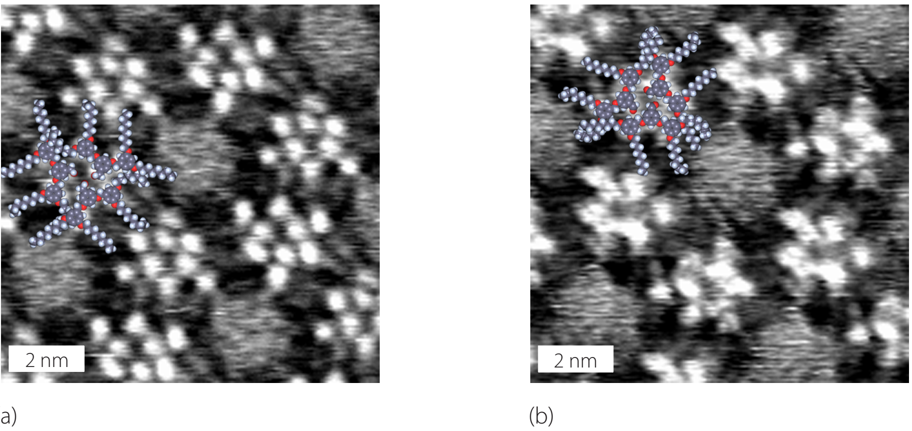

(a) (b)

Figure 5.8 STM image from Figure 5.7 with overlaid molecules. The *anti, anti*-conformation showed the best fit, and therefore the overlaid modelled molecules were taken from the 3D crystal structure (The near planar molecules of the crystal structure were also in an *anti, anti*-conformation). Since the alkyl-chains were not visible on the STM image, they were not modelled.

The alcohol **4** was expected to form a six-membered central ring of hydrogen bonded alcohol groups. The existence of the hydrogen bonds could only be inferred. The distances found between the aromatic moieties were consistent with an arrangement with a central ring of alcohol groups. Perhaps the existence of three hydrogen bonds was the reason for the increased stability of the layers of **4**. The layers of **14** were destroyed by scanning with about 50−100 pA tunnelling current, while the monolayers of **4** were stable up to about 100 pA. It could be concluded that the trimeric structure formed by **4** was slightly more stable than the structure formed by **14** under STM scanning conditions. Additionally, the monolayers of **4** were stable over longer periods of time than layers of the aldehyde.

Another reason for the interest in self-assembled monolayers was the breaking of symmetry that resulted from the interaction with the substrate on only one face.[13-23] Both **4** and **14** are achiral molecules. They become prochiral when they are constrained to a planar conformation. The trimers could be represented as triangles, as shown in Figure 5.9. The trimers formed hexagons. The triangles formed by the trimers did not point towards the centre of the hexagon. A hypothetical substrate-free monolayer of trimers would be correctly described as prochiral – adsorption on the graphite would differentiate the two prochiral faces and result in the formation of a chiral monolayer. Figure 5.9 shows both mirror images of the trimeric pattern. The orientation is called clockwise (Figure 5.9(a)) or counter-clockwise (Figure 5.9(b)), depending on the arrangement of the trimers. Only homochiral domains of this trimeric pattern were observed. Both chiralities were found in equal proportions, but they were separated in different domains. This chiral, trimeric flower pattern was observed for both **4** and **14**.

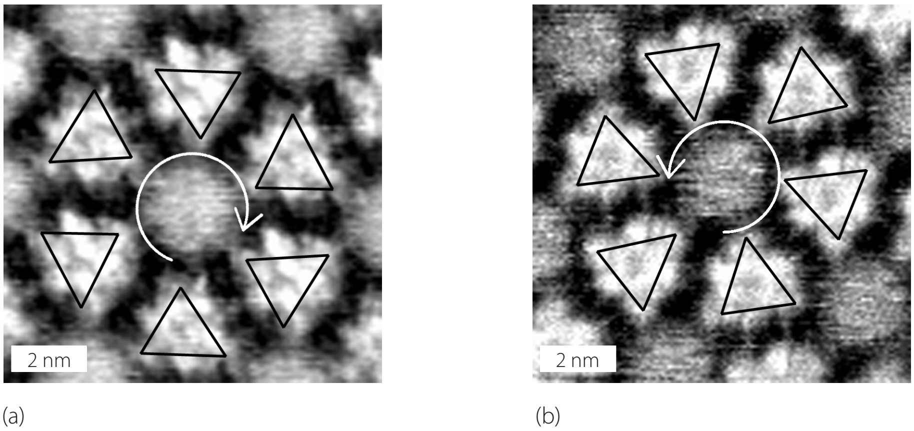

(a) (b)

Figure 5.9 Both mirror images, the trimers formed by **4** were arranged (a) clockwise and (b) counter-clockwise. Scan parameters: (a) 10 nm x 10 nm, $U_b = -500$ mV, $I_t = 30$ pA, averaged over 43 positions; (b) 10 nm x 10 nm, $U_b = -800$ mV, $I_t = 15$ pA, averaged over 28 positions.

The centre of the hexagonal array of compound **15** was better resolved than those for **4** and **14** and a subunit of two different parts could be made out (Figure 5.10). In contrast to the trimeric units of the monolayer of **4** and **14**, the trimeric units of the monolayer of **15** always had a hole in the middle which could be interpreted in terms of looser packing in the region of the three methyl ester groups compared to that in **4** and **14**.

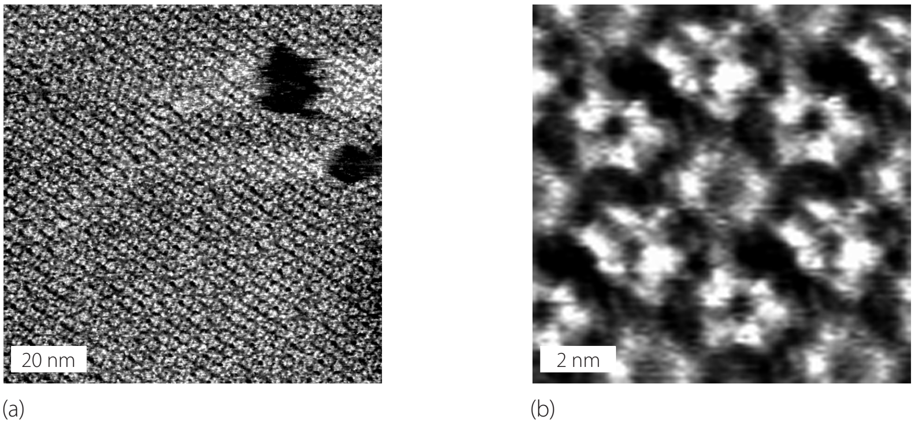

(a) (b)

Figure 5.10 STM image of a monolayer formed from **15**. The flower-like pattern was not very good visible and the trimeric units showed holes in the middle. Scan parameters: 100 nm x 100 nm, $U_b = -700$ mV, $I_t = 10$ pA; (b) an expanded (10 nm x 10 nm) and averaged (over 46 positions) image of (a).

A possible arrangement of the trimeric unit with the *anti, anti*-conformation of compound **15** is shown in Figure 5.11. The molecular model was taken from the crystal structure data of **14**, with the aldehyde group being changed into a methyl ester group. The resolution of the STM images was too low for a conformational assignment of the molecules. However, since the hexagonal pattern was of the same size and similar shape to that of the hexagonal pattern of **4** and **14**, it was assumed that the conformation was the same as the conformation of compounds **4** and **14** in their monolayers.

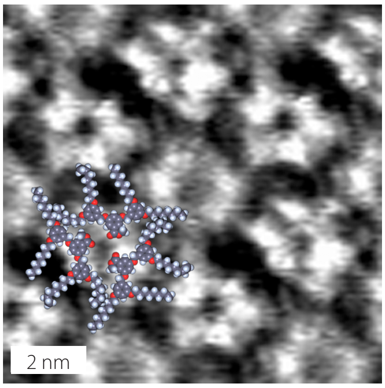

Figure 5.11 STM image from Figure 5.10(b) with overlaid molecules of compound **15** in one trimeric unit.

As already mentioned, the central part of the hexagon was better resolved than in the monolayers of **4** and **14**. Hexagons with embedded rows were observed just as in STM images of monolayers of **4** (compare Figure 5.10(a) with Figure 5.12(a)). This type of row, (as shown in Figure 5.12) was different to the rows that are visible in Figure 5.6(b).

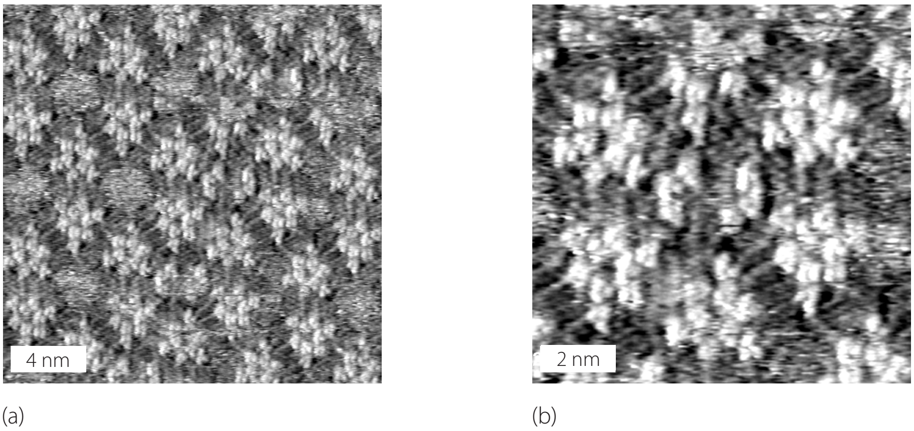

(a) (b)

Figure 5.12 (a) STM image of a monolayer of **4**. A row is embedded in the hexagonal pattern. Scan parameters: 20 nm x 20 nm, U_b = −700 mV, I_t = 10 pA. (b) An expanded image of (a) showing a hexagonal unit with an embedded row.

Both rows had a width of two molecules. However, it is interesting to mention that whereas in the row of Figure 5.6(b) the two molecules had a head to head interaction with alkyl-chains pointing out of the row, the molecules forming the row in Figure 5.12 had a tail to tail interaction with interdigitating octyl-chains in the centre of the row (Figure 5.13). Assuming that the hexagonal structure of **15** was of the same type as the hexagonal structure of compound **4** shown in Figure 5.12(b), it could be concluded that the central part of the hexagons of the monolayer of **15** consisted of *two* molecules and therefore the unit cell contained *eight* molecules, comprising two trimers and one dimer. This was quite remarkable, since the unit cell area of the hexagon of the monolayer of compound **15** was roughly the same as the unit cell area of the hexagon forming the monolayer of compound **4** and **14** but with Z = 8 instead of 7 as for compounds **4** and **14**. This means that compound **15** had a denser packing than compounds **4** and **14**. The rows observed in the monolayers of **4** and **14** could be assigned as defects, where instead of one single molecules, two molecules are placed in the centre of the hexagon.

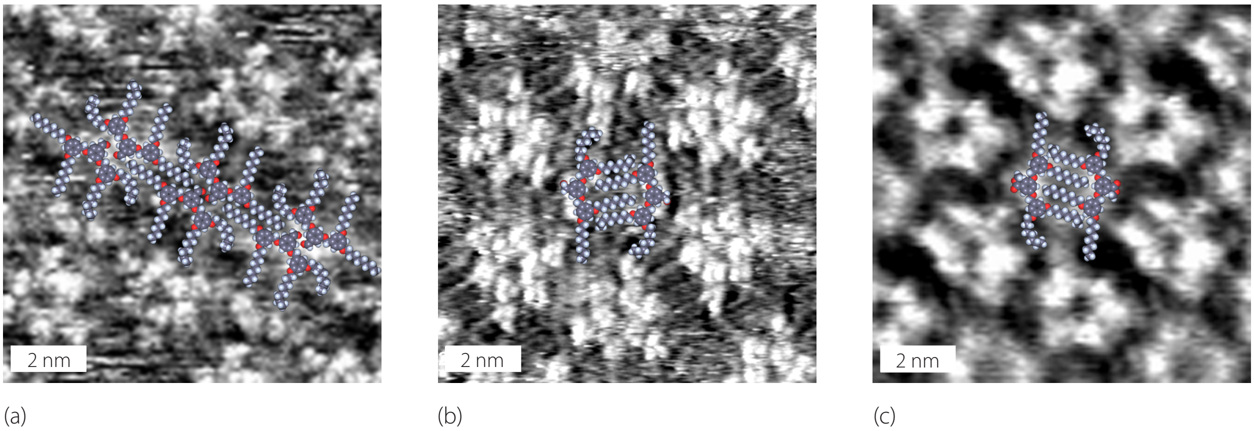

(a) (b) (c)

Figure 5.13 The two types of rows observed embedded in the trimeric pattern of the monolayers of **4** and **14**. (a) Expanded image (10 nm x 10 nm) of Figure 5.6(b) with overlaid molecules of compound **14**. (b) Figure 5.12 with overlaid molecules of compound **4**. (c) Figure 5.10 with overlaid molecules of compound **15**.

5.2.2 Delayed conversion of the trimeric pattern resulting in a supramolecular arrangement of a dimeric pattern

The trimeric patterns observed for **4**, **14** and **15** were not stable over time. After minutes to hours, a conversion into a different assembly started. This conversion could be followed in real time by STM measurements. While measuring the domains of trimers, a domain, consisting of dimers, appeared from outside of the observed window in the measurement and spread over all the observed area. The newly formed dimeric domain was a lamellar phase. One of the observed conversions is shown in Figure 5.14. Similar phenomena were already observed using STM technique.[24-27]

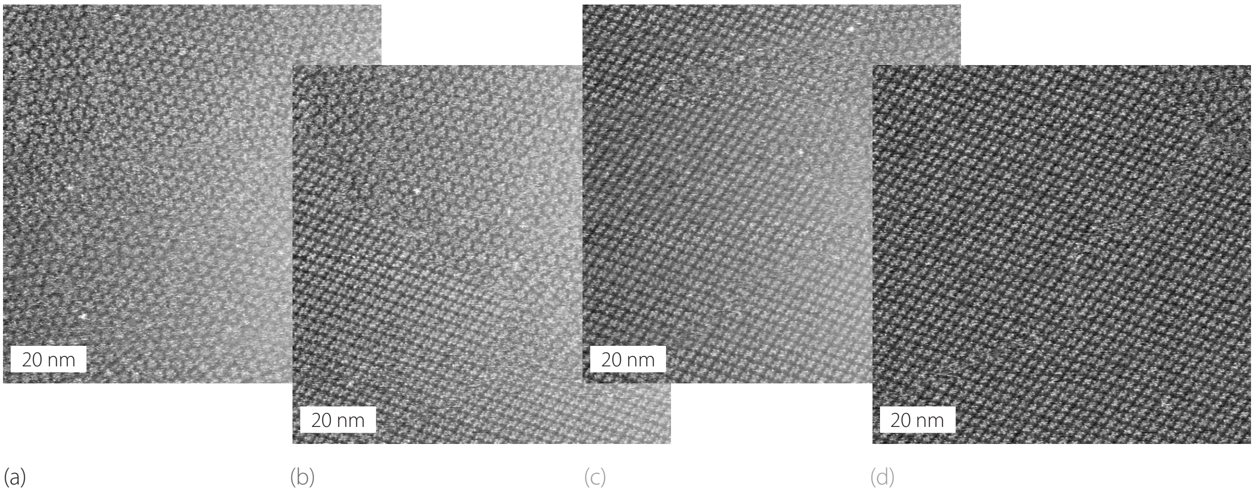

Figure 5.14 A sequence of 100 nm x 100 nm STM images for compound **14**, showing a conversion of the supramolecular arrangement. (b) A domain of dimers appeared at the bottom left of the scan-window. At the top right of the image, several domains of trimers were seen. (c) As the conversion continued, more and more of the trimers rearranged into dimers. (d) The conversion was almost complete. The sample was prepared from hexane. Each image took about 6 min to be recorded. Scan parameters: (100 nm x 100 nm, U_b = −700 mV, I_t = 9 pA).

The newly formed pattern of dimers was stable over days, and no further conversion could be observed. The structural and conformational analysis of this new monolayer is given below. The dimers also formed a chiral pattern, because the two molecules did not face each other directly, but were closer together with a lateral offset. Figure 5.15 shows a highly resolved image of the final lamellar pattern.

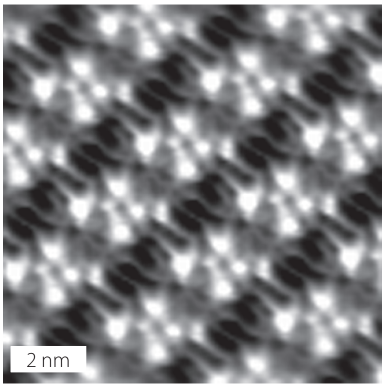

Figure 5.15 Expanded and averaged image of a monolayer of **14** after the conversion. Even the octyl-chains are visible on this highly resolved image. Scan parameters: 10 nm x 10 nm, U_b = −700 mV, I_t = 8.5 pA, averaged over 215 positions.

Both chiralities (offset to the right or offset to the left) were observed, separated in homochiral domains. The domains of dimers were of much larger size than those of the trimers. Again, the pattern was observed in the three equivalent orientations of the graphite surface. These lamellar regions were very well ordered and images of domains up to 400 nm x 400 nm were commonly observed. The software resolution (512 pixels x 512 pixels) precluded the observation of molecular structure within larger windows and it could be merely stated that individual domains were significantly greater than 160 000 nm^2 without defects or vacancies. The structure of the dimeric domains differed from that of the rows of dimers observed in the original trimeric monolayers and *no* isolated dimeric rows were seen in the large dimeric domains. Rarely, two domains were found with either an angle of 120° or a linear offset between them. By thermal annealing (70 °C) of a freshly prepared trimeric sample, a structure with smaller domains consisting of dimers could be prepared. Under these thermal conditions, multiple domains of dimers were observed.

Whereas the conversion of the monolayers of compound **14** started at the latest after 5 hours, the trimeric pattern of **4** was sometimes stable at room temperature over periods of several weeks. As it has already been discussed in Section 5.2.1, this might due to the presence of hydrogen bonds in the trimeric pattern of **4**.

The dimeric pattern of monolayers of both molecules **4** and **14** showed the same unit cell (*p*2, a = 2.9 nm, b = 2.4 nm, α = 77°). Due to the high resolution of the obtained images, the distances and angles between the three aromatic units of each molecule could be measured and the conformation of the molecules could therefore be assigned. The monolayer of **4** was isomorphous and isostructural with the monolayer of **14**. Both compounds **4** and **14** of the dimeric pattern had an *anti, anti*-conformation. This means, that during the conversion from the trimeric into the dimeric pattern, the molecules maintained their conformation. This was expected, since a conformational change of the benzyl unit would imply the rotation not only of one aromatic ring, but of the entire wedge with the two octyl-chains.

Since one layer of the 3D structure of **4** and **14** also showed a lamellar packing with the same plane group and the same unit cell parameters as the monolayer on graphite (Figure 5.3), the monolayer on HOPG could be directly compared with one layer of the crystal structure as shown in Figure 5.16.[11]

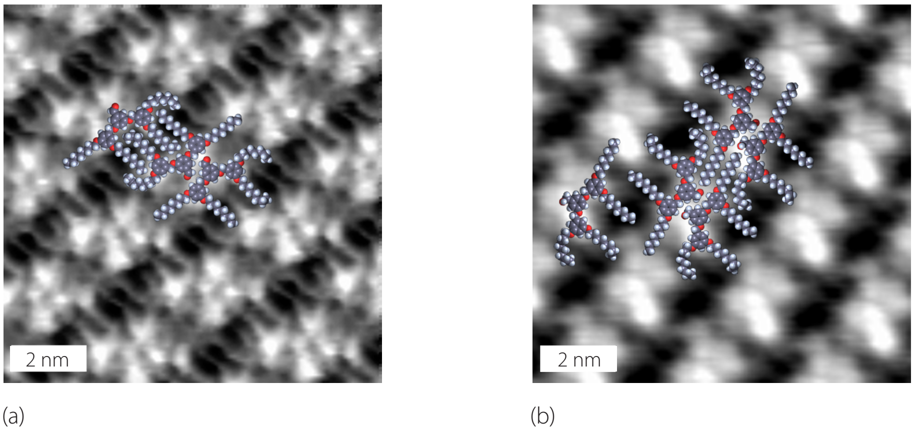

Figure 5.16 (a) STM image of **14** (Figure 5.15) with overlaid layer of the crystal structure of **14**. Even the octyl-chains seemed to have the same conformation in the crystal structure than in the monolayer. (b) STM image of **4** with overlaid crystal structure of **4**. The image is not as well resolved as (a). Scan parameters: 10 nm x 10 nm, U_b = −700 mV, I_t = 8 pA, averaged over 229 positions.

Due to the highly resolved images of the lamellar packing, even the conformation of the octyl-chains in the monolayer on graphite could be compared with one layer of the crystal structure. As shown in Figure 5.16, the overlaid single layer from the crystal X-ray structure fitted perfectly with the underlying STM-image, and also the octyl-chains seemed to have the same conformation. Because of the observed spontaneous conversion of the trimeric to the dimeric arrangement, the question of the nature of the mobile centre of the hexagons could be answered. The surface coverage was determined for both arrangements. Under the assumption that the number of molecules per unit area for a given domain remains constant, it was calculated that *one* molecule must have formed the mobile centre of the hexagons (dimer: 3.3 nm^2/molecule; trimer with *one* central molecule: 3.2 nm^2/molecule; trimer with *two* central molecules: 2.8 nm^2/molecule). The lamellar phase was observed to be stable over several days, and no further change was observed in any case. The next question to be addressed was what triggered the conversion of trimeric to dimeric monolayers and why the trimeric arrangement often appeared metastable.

There was no evidence that the rows of dimers found in the trimeric phase initiated the trimer to dimer conversion. They had a different orientation on the graphite than the dimers of the lamellar pattern, and the embedded rows of dimers proved to be stable over observed times of minutes to days; occasionally, they were even converted into the lamellar domain with a different orientation, as can be seen in the conversion shown in Figure 5.14. A few of the other obvious candidates for the initiation could be excluded as follows. The STM scanning process always has a certain influence on the sample. Sometimes it is deliberately used to inflict an ordering process[28] or to manipulate individual molecules.[26, 29] By using a low current STM with currents below 10 pA, this influence should be minimised. The STM as a possible trigger could be excluded by two clues. Firstly, immediately after the observation of a conversion at a certain position of the graphite sample, a location millimetres away was measured (too far away to be influenced by the previous measurements) – only dimers were observed. If the STM triggered the conversion, one should always observe trimers first, which would then be converted. The actual start of the conversion was observed only once (Figure 5.17). Normally, the rearrangement started outside of the measured range and spread to areas much larger than the observed window. This was directly observed when the scan range was enlarged after the observation of the conversion. Secondly, a sample of **14** that was annealed for half an hour at 70 °C showed only dimers.

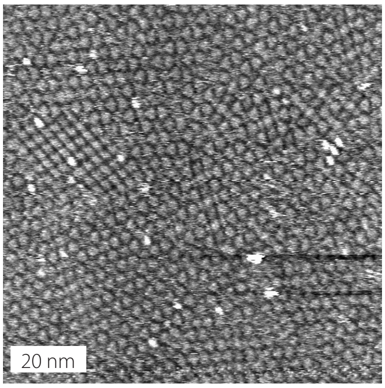

Figure 5.17 An island of a small domain of the dimeric pattern (at the left) inside a domain of trimers. This island, which was the initial point of the rearrangement of the whole domain was observed only once. Scan parameters: 100 nm x 100 nm, $U_b = -1000$ mV, $I_t =$ 10 pA.

It is believed that the trimer to dimer interconversion was thermal in origin. Every sample was slightly cooled by the evaporation of the solvent, and then heated to about 30−40 °C in the STM by the measurement. The image showed very little drift at the time of the trimer–dimer conversion, which indicated that a constant temperature had been attained over the sample and microscope. As already mentioned, the domains were of a very large size and only one or two domains could be observed over a 500 nm x 500 nm area. In contrast, the thermally annealed sample showed dimeric structures in many small domains. These observations were consistent with the conversion having a relatively high activation energy that resulted in only a few initiation events at 30−40 °C.

In contrast to other studies,[30-32] the observed pattern did not change depending on the measurement technique. The images at the liquid–solid interface looked very similar to those of monolayers prepared by evaporation techniques. The domains were of much larger size and no embedded rows or other irregularities could be detected. No conversion could be observed at the liquid–solid interface. An image of the solid–liquid interface is shown in Figure 5.18.

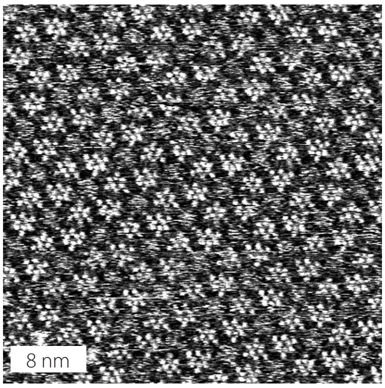

Figure 5.18 A 40 nm x 40 nm image of compound **4** at the solid–liquid interface, measured in a 1-phenyloctane solution. Scanning parameters: $U_b = -700$ mV, $I_t = 8$ pA.

In 3D crystallography, it is well known that metastable crystals can be formed, which are then converted into a more stable form.[33]

Clearly, for the spontanous conversion of the trimers to the dimers, the global Gibbs energy change must be negative. A comparison of the entropy of the dimeric pattern with the trimeric pattern was very difficult. The nomenclature for *dimers* and *trimers* was used more in terms to express the symmetry of the pattern and it was not meant to emphasize that oligomeric formation involves weak interactions. Otherwise, one could conclude that the dimers are entropically more stable than the trimers. But the comparison of the two arrangements in terms of entropy is much more complex. Since the entropy factor for solid materials (as which the monolayer is considered) is small, the negative enthalpy change associated with the rearrangement should be the dominant factor for the negative global Gibbs energy change. Since no conformational change in the molecules occurred during the conversion, the interactions between the molecules should have changed. The most important change when comparing the two patterns was the formation of a lamellar structure in the dimeric pattern with interdigitating octyl-chains (see Figure 5.3). Although, interdigitation between the alkyl groups of adjacent trimers occurred, it can be imagined, that the van der Waals interaction between the parallel octyl-chains in the lamellae is of much larger energy than the van der Waals interaction of the interdigitated octyl-chains of adjacent trimers. It could be concluded, that the dimeric pattern is the *thermodynamic* and the trimeric pattern the *kinetic* arrangement.

The question as to why the kinetic structure was observed first rather than the thermodynamic structure being directly observed was very difficult. Solution casting with the following solvents showed firstly the trimeric pattern: *n*-pentane, *n*-hexane, *n*-decane, toluene, dichloromethane, acetone, or 1:1 dichloromethane:methanol. Apolar, polar and protic polar solvents were investigated. It was thought that the alcohols especially would break possible hydrogen bonds between the central alcohol groups of each dendron. The solubility of the molecules in the solvent was found to be more important than the polarity of the solvents. Fréchet-type dendrimers with octyl-chains are more soluble than Fréchet-type dendrimers with unsubstituted benzylic end groups in all of the solvents mentioned above.[1, 34-36] Because of their spherical shape and their large number of aliphatic end groups, dendrimers with alkyl end groups can be described as inverse micelles.[35] Since the entropic factor in solution can not be neglected, the formation of micelles is favoured to the formation of lamellae in solution, due to the smaller size. The trimeric pattern on graphite can be considered as a direct imprint of a 2D analogue of a micelle in solution. Therefore, the conversion never occurred measuring in solid–liquid interface. Using DMF as a solvent for solution casting, the direct formation of the dimeric pattern could be observed with **4** and **14**. This might be due to the very high solubility of the central part in DMF.

The trimeric pattern of the ester **15** also changed its arrangement after a delay (Figure 5.19). The resulting structure after the conversion showed rows, which were broader than the lamellar stripes in the dimeric pattern of **4** and **14**.

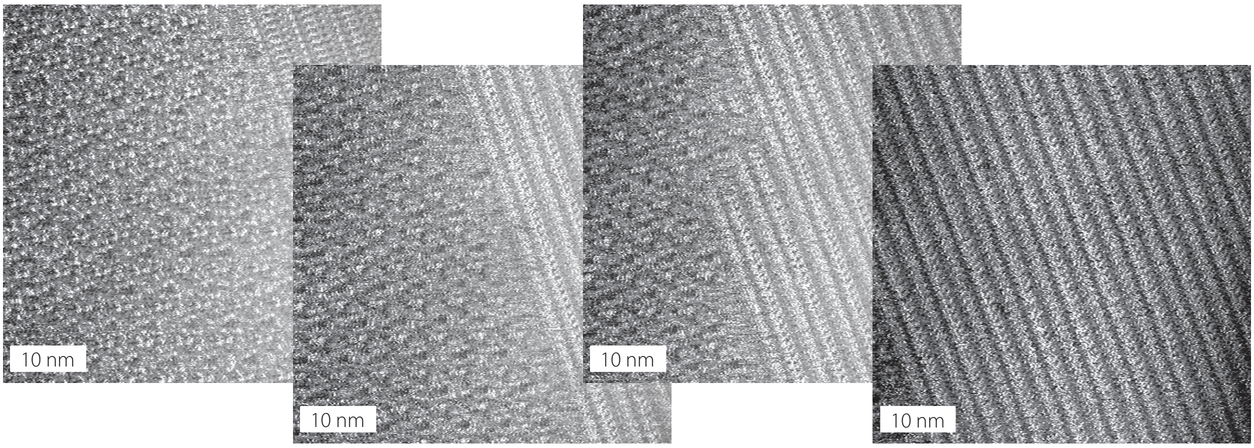

(a) (b) (c) (d)

Figure 5.19 A sequence of 100 nm x 100 nm STM images for compound **15**, showing a conversion of the supramolecular arrangement. (b) A domain of dimers appeared at the top right of the scan-window. At the bottom left of the image, several domains of trimers were seen. (c) As the conversion continued, more and more of the trimers rearranged into dimers. (d) The conversion was almost complete. The sample was prepared from hexane. Each image took about 3 min to be recorded. Scan parameters: 50 nm x 50 nm, $U_b = -700$ mV, $I_t = 10$ pA.

The resolution of the rows of compound **15** was worse than for the corresponding alcohol or aldehyde. No dimeric substructure could be identified. An averaged and expanded STM image after the conversion is shown in Figure 5.20.

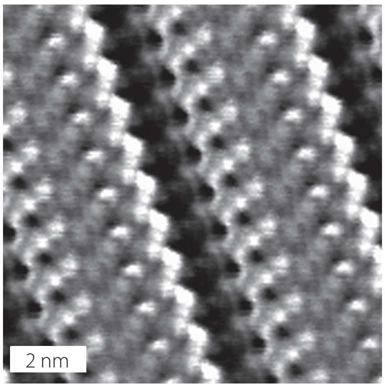

Figure 5.20 An expanded and averaged STM image of compound **15** after the rearrangement to a lamellar structure. Scan parameters: 10 nm x 10 nm, $U_b = -700$ mV, $I_t = 15$ pA, averaged over 75 positions.

The assignment of the packing arrangement and of the conformation was quite demanding because of missing information from the image. The unit cell could be measured (a = 5.3 nm, b = 1.1 nm, α = 82°). Assuming that the pattern at the right border of each stripe is the same pattern as at the left border, but with a rotation of 180° (the different contrast could be a consequence of a different orientation compared with the underlying graphite) the plane group would be *p*2. This assumption would facilitate the assignment of the packing enormously. The resolution was too bad for conformational analysis but it was assumed (as for the trimeric pattern of **15**) that the conformation was the same as for the molecules in the monolayer of **4** and **14**. The molecular model was taken from the crystal structure data of **14** as was done for the trimeric pattern of **15** (see Section 5.2.1). Better resolved STM images have to be obtained in order to make further analysis of the self-assembled monolayer.

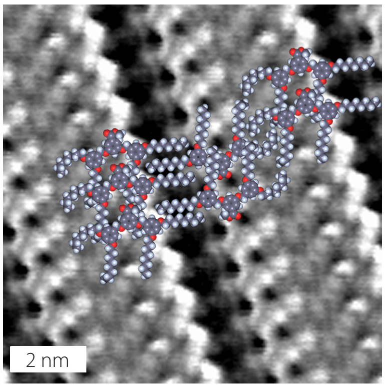

Figure 5.21 STM image from Figure 5.20. The overlaid molecules of compound **15** show a possible arrangement, in which the molecules were not arranged in a dimeric structure as for compounds **4** and **14**.

The positions of the octyl-chains of the overlaid molecule could not be identified, but it was assumed that the darker regions consisted only of octyl-chains, since they are rarely seen in STM images.[37, 38] The packing differed from the dimeric packing of **4** and **14**, as **15** had no head-to-head arrangements of two molecules.

5.3 Exchanging the *seventh molecule* of the trimeric pattern of 4 by a metal complex

In monolayers of **4** and **14** there was a hexagonal pattern of trimers with a mobile molecule in the centre of the hexagon as discussed in Section 5.2.1. When two molecules were placed in the centre of the hexagon, rows were formed through the hexagonal arrangement (see Section 5.2.1). On very rare occasions, the centre of the hexagon remained empty; no noisy centre could be observed. Such a vacancy, where the height of the bare graphite was seen, is shown in Figure 5.22, which further indicated that there was a mobile molecule in most noisy centres.

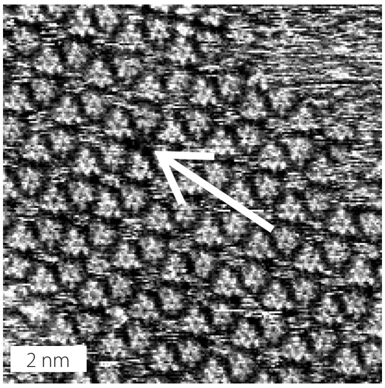

Figure 5.22 A rare 40 nm x 40 nm image (U_b = −700 mV, I_t = 8 pA) of a vacancy in the trimeric pattern (marked with an arrow) for **4**. The monolayer was prepared from a hexane solution. On the top right of the image, the edge of the domain can be seen. The graphite there is covered with highly mobile molecules, leading to streaky noise. The vacancy inside the pattern showed the bare graphite.

Similar phenomena were observed in X-ray analyses of trimesic acid hydrogen-bonded structures that left cavities filled with solvent molecules, which might retain a degree of mobility within a cavity.[39, 40] Recently, the same cavities were detected in self-assembled monolayers of trimesic acid (see Section 1.1.4).[41, 42] As one possible guest, trimesic acid molecules could be sometimes imaged in the cavities.[42] It was then also possible to incorporate coronene into the cavities.[43]

The idea was to replace this mobile molecule in the centre of the hexagon by another guest. The metal complex **16**[44] was chosen to replace this single molecule of compound **4**.

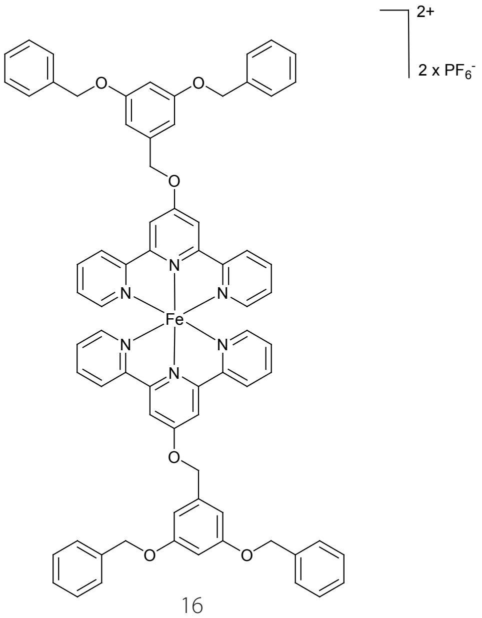

16

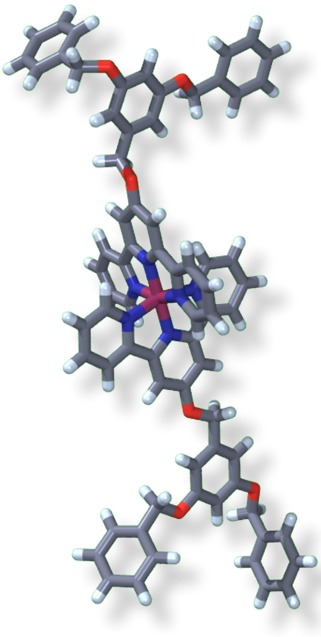

Figure 5.23 The molecular structure of **16**.[44] The solvents and the counter anions are omitted in the representation of the complex cation taken from the crystal structure (right).

The crystal structure of compound **16** was known, and therefore the dimensions of the molecule could be compared with the central part of an STM image of the trimeric pattern of compound **4** (Figure 5.24). In Figure 5.23, the cation of **16** is shown. The cation has a length of ≈3 nm and a width of ≈1.3 nm.

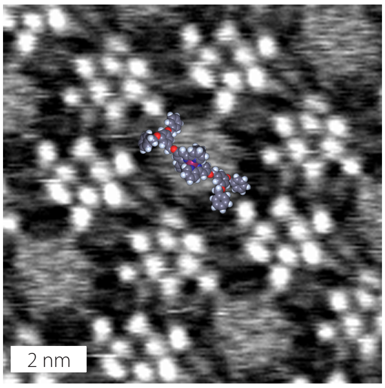

Figure 5.24 Figure 5.7 with an overlaid molecule **16**. The molecular model was taken from the crystal structure.

The complex cation is bigger than a single molecule of **4**. As a consequence, it was hoped that the cation would remain fixed in the lattice.

A mixture of **4** and **16** in a ratio of 6:1 in dichloromethane was placed on graphite and the solvent was evaporated. The so formed monolayer was remained in the STM for 16 hours after which the same hexagonal pattern was observed as for **4** and **14**. At first glance, the raw images of **4** and of the mixture of **4** and **16** looked the same (Figure 5.25).

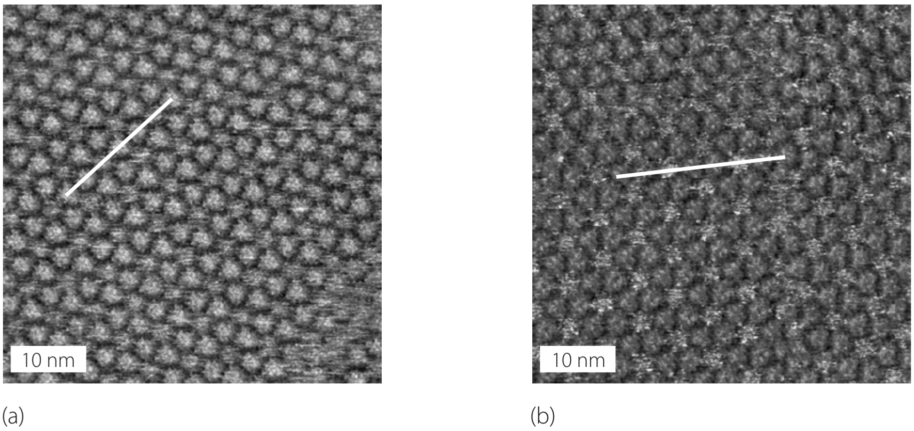

(a) (b)

Figure 5.25 STM images of (a) **4** and (b) of a mixture of **4** and **16** (6:1). Both monolayers have the same hexagonal pattern with the same dimensions. In image (b) of the mixture, the centre of the hexagon appeared with more contrast. The white line indicates the cut made for the profile for Figure 5.26. Scan parameters: (a) 50 nm x 50 nm, $U_b = -350$ mV, $I_t = 30$ pA; (b) 50 nm x 50 nm, $U_b = -800$ mV, $I_t = 8$ pA.

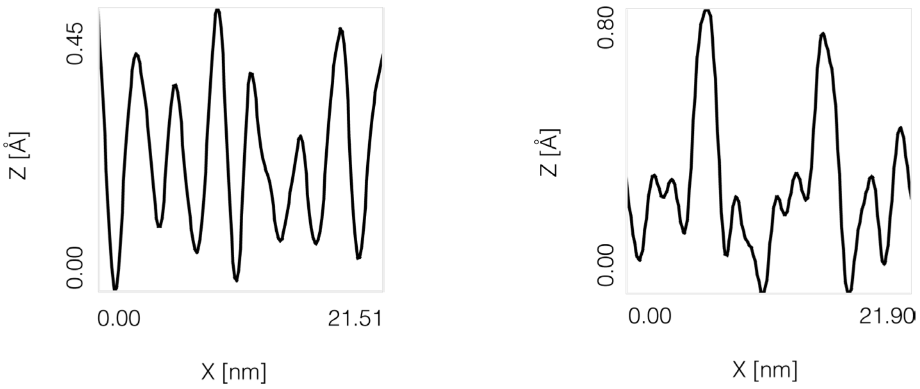

(a)

(b)

Figure 5.26 The profile of the trimeric pattern of a monolayer (a) of **4** and (b) of a mixture of **4** and **16** (6:1). The profile was taken from Figure 5.25 along the white line indicated in the two STM images of Figure 5.25. The trimers appeared sometimes as doublets or broad singlets (as in (b)).

The unit cell dimensions were the same for both monolayers shown in Figure 5.25. The centre of the hexagon of the monolayer from the 6:1 mixture of **4** and **16** appeared with more contrast. This is more clearly visible in the profile along the *z*-axis of the two measurements. In Figure 5.26(a) the height of each peak in the profile is about the same. The two signals arising from the central part of the hexagon are a bit smaller than the other six signals from the trimeric unit. In Figure 5.26(b) the two peaks from the centre are higher than the six signals from the trimeric unit formed from compound **4**.

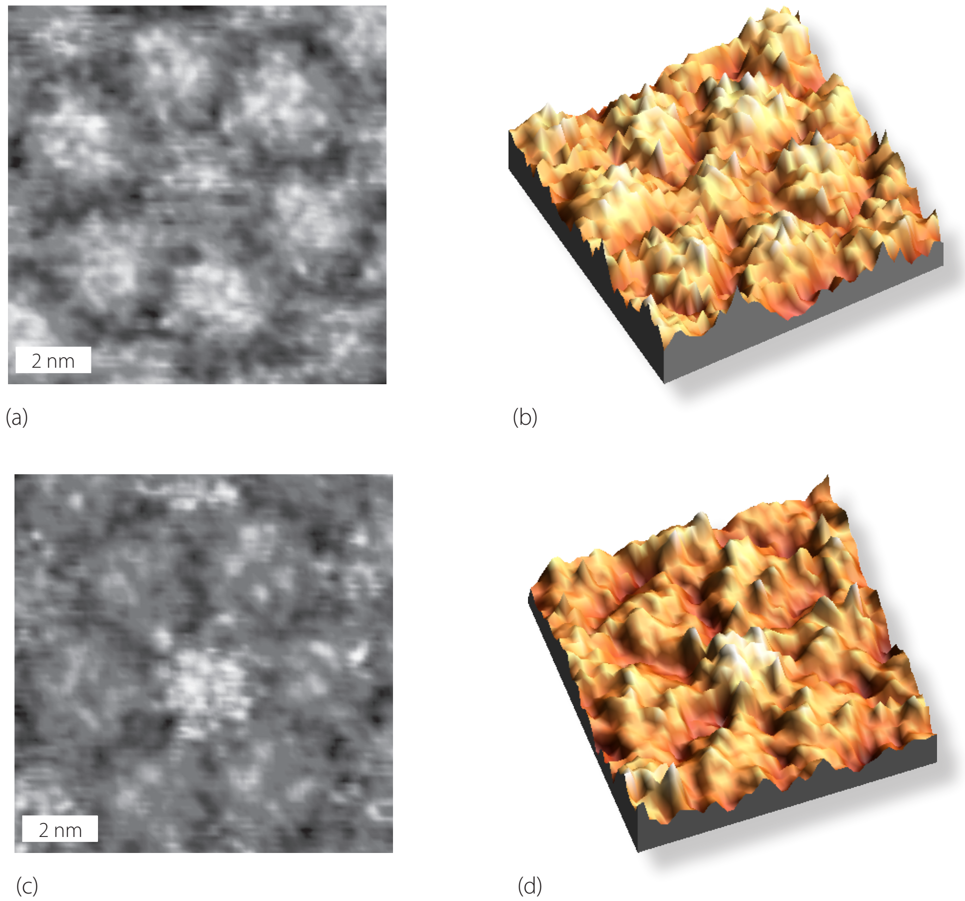

(a) (b)

(c) (d)

Figure 5.27 (a) and (c) show two non-averaged 10 nm x 10 nm expanded images of (a) a monolayer of **4** and (c) a monolayer of **4** and **16**. (b) and (d) are the 3D illustrations referring to (a) and (c) respectively.

In Figure 5.27, expanded images are shown. In the hexagon of **4**, the central part was darker than the outer trimers, whereas in the STM image of the 6:1 mixture of **4** and **16**, the central part appeared with more contrast than the hexagonal border. This can be emphasised with 3D representations.

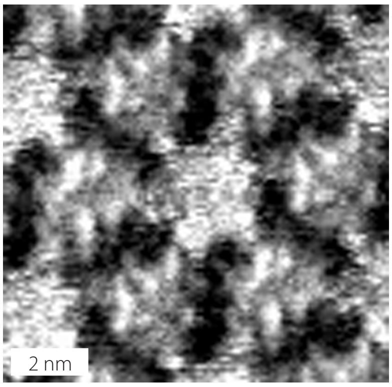

Figure 5.28 Averaged STM image of a monolayer consisting of compounds **4** and **16** in a ratio 6:1. Scan parameters: 10 nm x 10 nm, $U_b = -800$ mV, $I_t = 8$ pA, averaged over 21 positions.

Figure 5.28 shows an averaged image of a monolayer with compounds **4** and **16**. The centre of the hexagon showed also in the averaged images more contrast than the trimeric units.

As was observed later and will be shown in Chapter 6, bis(tpy) iron(II) complexes are not stable under the conditions used for all these measurements. Hence, it is not evident what exactly was in the centre of the hexagonal arrangement obtained from the mixture of **4** and **16**. It would be interesting to see, if more stable metal complexes, as for example the corresponding bis(tpy) ruthenium(II) complex show the same pattern.

5.4 Experimental part

Compound 14: To a dry solution of PCC (16.7 mg, 77.0 μmol) and molecular sieves (3Å, 0.4 g) in dichloromethane (6 mL) was added a dry solution of **3** (64 mg, 76.8 mmol) in dichloromethane (2 mL). The reaction mixture was then allowed to stir at room temperature for 4 hours, filtered through Cellite and the solvent evaporated. Chromatography on silica (ethyl acetate:hexane 1:8) yielded **14** as a white powder (58. mg, 69.8 mmol, 91%). m.p. 34 °C. ^{1}H NMR (500 MHz, $CDCl_3$): δ 9.89 (s, 1H, CHO), 7.09 (d, J = 2.3 Hz, 2H, H^{2A}), 6.85 (t, J = 2.3 Hz, 1H, H^{4A}), 6.55 (d, J = 2.2 Hz, 4H, H^{2B}), 6.41 (t, J = 2.2 Hz, 2H, H^{4B}), 5.00 (s, 4H, H^{OCH_2B}), 3.94 (t, ^3J = 6.6 Hz, 8H, $H^{OCH_2CH_2}$), 1.77 (tt, J = 7.1, 6.7 Hz, 8H, $H^{OCH_2CH_2}$), 1.44 (tt, J = 7.3, 7.3 Hz, 8H, $H^{OCH_2CH_2CH_2}$), 1.25−1.37 (m, 32H, $H^{(CH_2)_4}$), 0.88 ppm (t, J = 7.0 Hz, 12H, H^{CH_3}). ^{13}C NMR (100 MHz, $CHCl_3$): δ 192.01, 160.72, 160.50, 138.51, 138.48, 108.84, 108.42, 105.86, 101.05, 70.54, 68.25, 31.97, 29.51, 29.39, 29.39, 26.20, 22.81, 14.26 ppm. IR (neat): ($\tilde{\nu}$, cm^{-1}) 2924 s, 2854 m, 1705 m, 1597 s, 1458 m, 1165 m, 1057 w, 833 w. MS (MALDI-TOF+): *m/z* 869.7 $[M + K]^+$, 853.7 $[M + Na]^+$. Anal. Calcd for $C_{53}H_{82}O_7$: C, 76.58; H, 9.94; N, 0.0; found: C, 76.23; H, 9.86; N, 0.0 %.

5.5 References

[1] P. B. Rheiner, D. Seebach, *Chem. –Eur. J.* **1999**, *5*, 3221.

[2] X. Qiu, C. Wang, Q. Zeng, B. Xu, S. Yin, C. Wang, S. Xu, C. Bai, *J. Am. Chem. Soc.* **2000**, *122*, 5550.

[3] X. Qiu, C. Wang, S. Yin, Q. Zeng, B. Xu, C. Bai, *J. Phys. Chem. B* **2000**, *104*, 3570.

[4] A. Miura, Z. Cheng, H. Uji-I, S. De Feyter, M. Zdanowska, P. Jonkheijm, A. P. H. J. Schenning, E. W. Meijer, F. Würthner, F. C. De Schryver, *J. Am. Chem. Soc.* **2003**, *125*, 14968.

[5] S. De Feyter, M. M. S. Abdel-Mottaleb, N. Schuurmans, B. J. V. Verkuijl, J. van Esch, B. L. Feringa, F. C. De Schryver, *Chem. –Eur. J.* **2004**, *10*, 1124.

[6] E. C. Constable, B. A. Hermann, C. E. Housecroft, L. Merz, L. J. Scherer, *Chem. Commun.* **2004**, 928.

[7] L. J. Scherer, L. Merz, E. C. Constable, C. E. Housecroft, M. Neuburger, B. A. Hermann, *J. Am. Chem. Soc.* **2005**, *127*, 4033

[8] P. Wu, Q. Fan, G. Deng, Q. Zeng, C. Wang, C. Bai, *Langmuir* **2002**, *18*, 4342.

[9] P. Wu, Q. Fan, Q. Zeng, C. Wang, G. Deng, C. Bai, *ChemPhysChem* **2002**, 633.

[10] W. Mandouh, H. Uji-I, A. E. Dulcey, V. Percec, S. De Feyter, F. C. De Schryver, *Langmuir* **2004**, *18*, 4342.

[11] R. Azumi, G. Götz, T. Debaerdemaeker, P. Bäuerle, *Chem. –Eur. J.* **2000**, *6*, 735.

[12] R. Lim, J. Li, J. Li, Z. Feng, S. Valiaveettil, *Langmuir* **2000**, *16*, 7023.

[13] F. Tao, S. L. Bernasek, *J. Phys. Chem. B* **2005**, *109*, 6233.

[14] S. De Feyter, A. Gesquière, M. M. Abdel-Mottaleb, P. C. M. Grim, F. C. De Schryver, C. Meiners, M. Sieffert, S. Valiyaveettil, K. Müllen, *Acc. Chem. Res.* **2000**, *33*, 520.

[15] C. B. France, B. A. Parkinson, *J. Am. Chem. Soc.* **2003**, *125*, 12712.

[16] M. Böhringer, K. Morgenstern, W.-D. Schneider, R. Berndt, F. Mauri, A. De Vita, R. Car, *Phys. Rev. Lett.* **1999**, *83*, 324.

[17] J. Weckesser, A. De Vita, J. V. Barth, C. Cai, K. Kern, *Phys. Rev. Lett.* **2001**, *87*, 096101/1.

[18] L. Pérez-Garcia, D. B. Amabilino, *Chem. Soc. Rev.* **2002**, *31*, 342.

[19] S. De Feyter, A. Gesquière, K. Wurst, D. B. Amabilino, J. Veciana, F. C. De Schryver, *Angew. Chem. Int. Ed.* **2001**, *40*, 3217.

[20] M. Böhringer, K. Morgenstern, W.-D. Schneider, R. Berndt, *Angew. Chem. Int. Ed.* **1999**, *38*, 821.

[21] J. V. Barth, J. Wedkesser, G. Trimarchi, M. Vladimirova, A. De Vita, C. Cai, H. Brune, P. Günter, K. Kern, *J. Am. Chem. Soc.* **2002**, *124*, 7991.

[22] L. C. Giancarlo, G. W. Flynn, *Acc. Chem. Res.* **2000**, *33*, 491.

[23] G. M. Florio, T. L. Werblowsky, T. Müller, B. J. Berne, G. W. Flynn, *J. Phys. Chem. B* **2005**, *109*, 4520.

[24] J. P. Rabe, S. Buchholz, *Phys. Rev. Lett.* **1991**, *66*, 2096.

[25] S. Buchholz, J. P. Rabe, *J. Vac. Sci. Technol. B.* **1991**, *9*, 1126.

[26] K. Kim, K. E. Plass, A. J. Matzger, *Langmuir* **2003**, *19*, 7149.

[27] A. Stabel, R. Heinz, F. C. De Schryver, J. P. Rabe, *J. Phys. Chem.* **1995**, *99*, 505.

[28] J.-R. Gong, Lei, L.-J. Wan, G. Deng, Q. Fan, C. Bai, *Chem. Mater.* **2003**, *15*, 3098.

[29] A. J. Heinrich, C. P. Lutz, J. A. Gupta, D. M. Eigler, *Science* **2002**, *298*, 1381.

[30] I. Widmer, U. Huber, M. Stöhr, L. Merz, H.-J. Güntherodt, B. A. Hermann, P. Samorí, J. P. Rabe, P. B. Rheiner, G. Creiveldinger, P. Murer, *Helv. Chim. Acta* **2002**, *85*, 4255.

[31] W. Mamdouh, H. Uji-i, J. S. Ladislaw, A. E. Dulcey, V. Percec, F. C. D. Schryver, S. D. Feyter, *J. Am. Chem. Soc.* **2005**, *ASAP*.

[32] S. Graber, oral communication, **2005**.

[33] W. Ostwald, *Z. Phys. Chem. (Leipzig)* **1897**, *22*, 289.

[34] G. R. Newkome, Z.-Q. Yao, G. R. Baker, J. A. Gupta, *J. Org. Chem.* **1985**, *50*, 2003.

[35] S. Stevelmans, J. V. van Hest, J. F. G. A. Jansen, D. A. F. J. van Boxtel, E. M. M. de Brabender-van den Berg, E. W. Meijer, *J. Am. Chem. Soc.* **1996**, *118*, 7398.

[36] L. J. Scherer, *Diploma Work*, University of Birmingham, Birmingham, **2001**.

[37] Y. Cai, S. L. Bernasek, *J. Am. Chem. Soc.* **2004**, *126*, 14234.

[38] J. P. Rabe, S. Buchholz, *Science* **1991**, *253*, 424.

[39] G. R. Desiraju, *Angew. Chem. Int. Ed.* **1995**, *34*, 2311.

[40] F. H. Herbstein, in *Comprehensive Supramolecular Chemistry, Vol. 6* (Eds.: J. L. Atwood, J. E. D. Davies, D. D. MacNicol, F. Vögtle, F. Toda, R. Bishop), Pergamon, Oxford, **1996**, pp. 61.

[41] Z. Li, B. Han, L. J. Wan, T. Wandlowski, *Langmuir* **2005**, *21*, 6915.

[42] S. Griessl, M. Lackinger, M. Edelwirth, M. Hietschols, W. M. Heckl, *Single Mol.* **2002**, *1*, 25.

[43] S. Griessl, M. Lackinger, F. Jamitzky, T. Markert, M. Hietschold, W. M. Heckl, *Langmuir* **2004**, *20*, 9403.

[44] E. C. Constable, C. E. Housecroft, M. Neuburger, S. Schaffner, L. J. Scherer, *Dalton Trans.* **2004**, 2635.

Teach me the glorious lesson that ocassioinally it is possible that I may be mistaken.
„Prayer of an ageing woman“, ascribed to Teresa de Ávila

6 STM Studies of Self-assembled Monolayers of Metal Complexes Decorated with Fréchet-type Dendrimers

The $[M(tpy)_2]^{n+}$ motif (tpy = 2,2':6',2''-terpyridine and its derivatives; n = 2, 3) is a powerful redox and photoactive unit that finds increasing application in metallosupramolecular chemistry, nanoscale chemistry and nanotechnology.[1, 2] Originally selected for the synthesis of diastereomerically pure high nuclearity metallodendrimers[3] the $[M(tpy)_2]^{n+}$ functionality has been combined with a wide variety of other structural components, either to introduce desired redox, optical, photochemical, photophysical, magnetic or magneto-optical properties or as a result of metal-directed self-assembly processes. Recent examples include the combination of $[M(tpy)_2]^{n+}$ motifs with poly(ethylene glycol), poly(styrene), dendrimer, biomolecule or micelle structural units.[1, 4]

The chelated $[M(tpy)_2]^{n+}$ complexes are thermodynamically stable and the rapid kinetics of complexation (at least with first row d-block metal ions)[2] makes them attractive candidates for studies of self-assembly processes and as motifs for self-assembly in unusual environments. Direct static and dynamic imaging of surface-bound species is routinely possible using scanning tunnelling and force microscopy and has been used to monitor different metal-ligand complexes.[5-7] In particular, self-assembly of porphyrin and phtalocyanine metal complexes on surfaces has been widely investigated.[8-18] Supramolecular systems consisting of oligopyridine metal complexes have been explored using STM.[19-24] STM techniques have also been used to monitor the binding of ruthenium(II) and iron(II) at the phase boundary of a solution of a chiral multi-terpyridine dendrimer in CH_2Cl_2 and a freshly cleaved highly ordered pyrolytic graphite (HOPG) surface.[25, 26] The palladation of a self-assembled 2,2'-bipyridine monolayer on HOPG by treatment with solutions of palladium(II) complexes has been directly observed by STM.[27] Combined STM and electrochemical studies of the self-assembly of monolayers of $[Ru(tpy)(ptpy)]^{2+}$ units (ptpy = 4'-(4-pyridyl)-2,2':6',2''-terpyridine) on platinum have been reported.[28] All STM images containing oligopyridine metal complexes lack resolution and therefore detailed analysis of the monolayers could not be carried out.

A synthetic program based on Fréchet-type[29] dendrimer-functionalised ligands has been developed; this system is ideally suited for imaging by tunnelling methods (Chapters 3–5, and 7).[30-35] Aromatic-rich dendrimers show π–π-interactions with the graphite surface and/or neighbouring molecules, and if they bear hydrophobic alkyl substituents, they exhibit strong CH_2–graphite and chain–chain interdigitation interactions. The self-organisation of 2,2':6',2''-terpyridines on HOPG has been described in Chapter 4, and in this Chapter the formation of following self-organised monolayers of two different types of hydrophobic metal complexes will be discussed: ionic bis(2,2':6',2''-terpyridine) metal(II) complexes and neutral platinum bis(alkyne)-bis(triethylphosphine) species, both decorated with first and second generation Fréchet-type dendrons. Pre-formed complexes are delivered to the surface from solution – there are no covalent bonds between the complexes and the surface or between monolayer sub-units. Remarkably high-resolution STM images of the complexes under ambient (room temperature, atmospheric pressure, air) conditions are obtained.

6.1 Compound synthesis

6.1.1 Synthesis and analysis of compounds 16–21

The synthetic strategy used to obtain the *trans*-Pt alkyne complexes **17** and **19** was to couple the alkyne derivative of the Fréchet-type dendrimer without further characterisation with *trans*-$PtI_2(PEt_3)_2$ using catalytic amounts of a transmetallating agent (Cu(I)) and an amine base (Scheme 6.1).[36]

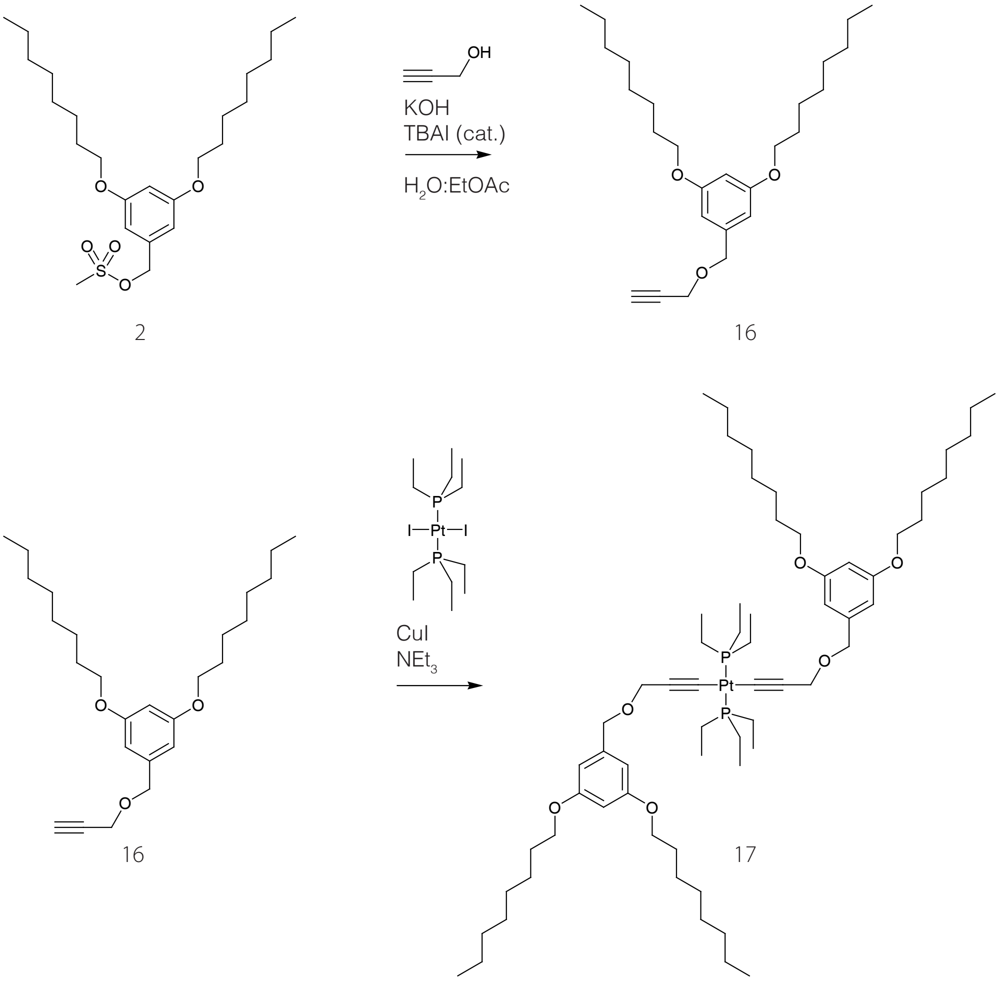

Scheme 6.1 The crude mesylated dendron **2** was subsequently coupled with propargylic alcohol using phase transfer conditions with *n*-Bu_4NI as phase transfer catalyst (yield: 77%). The alkyne derivative **16** was then coupled with *trans*-$PtI_2(PEt_3)_2$ to give **17** using catalytic amounts of CuI as transmetallating agent. Yield: 66%.

The first generation alkyne compound **16** (Scheme 6.1) could be prepared in good yield using phase transfer conditions. *n*-Bu_4NI (10%) was used as phase transfer catalyst, and KOH turned out to be basic enough to deprotonate propargylic alcohol under these conditions. *trans*-$PtI_2(PEt_3)_2$ was produced starting from *cis*-$PtCl_2(PEt_3)_2$ by sonicating the starting material with KI for 5 minutes in an ethanol:water solution. The *cis*-$PtI_2(PEt_3)_2$ so-obtained was heated at 145 °C until all of the solid was melted, after cooling down, the thermodynamically more stable *trans*-$PtI_2(PEt_3)_2$ was obtained.[37] The *trans*-$PtI_2(PEt_3)_2$ was reacted with the alkyne **16** and CuI (0.2%, purified with water and acetone before use) in a degased solution of triethylamine.[36] The $[Et_3NH]I$ precipitated out of the reaction mixture. After about one day of stirring, compound **17** was formed, which was stable enough to be purified by chromatography.

The platinum compound with pendant benzylic groups (**19**) was prepared in 48% yield by the same methodology as compound **17** (Scheme 6.2). Alkyne **18** was obtained in good yields using phase transfer conditions with 10% 18-crown-6 as phase transfer catalyst and KOH as base.

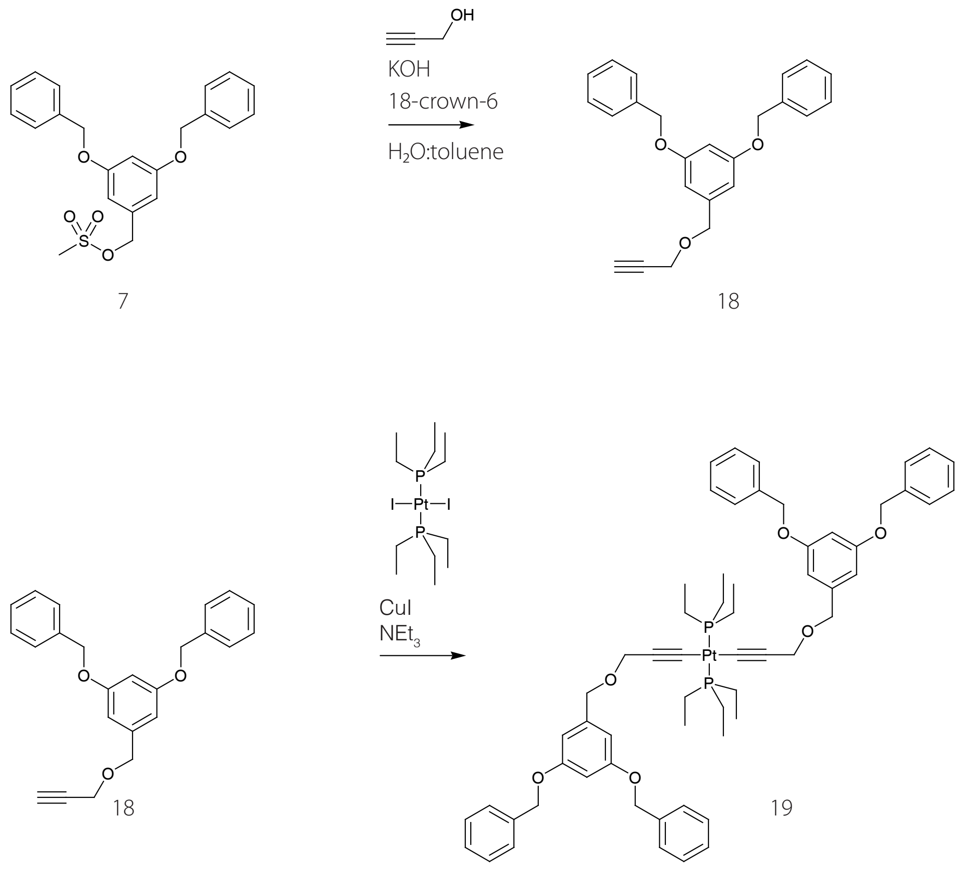

Scheme 6.2 The mesylate **7** was reacted with propargylic alcohol to form compound **18** (68% yield) using 18-crown-6 as phase transfer catalyst. **18** was then coupled with *trans*-$PtI_2(PEt_3)_2$ to obtain **19** in 48% yield.

Although different phase transfer conditions were tried out, compound **20** could not be obtained using phase transfer conditions. Finally, the coupling was carried out using classical conditions (NaH as base in dry THF) in 34% yield (Scheme 6.3). For the complexation with *trans*-$PtI_2(PEt_3)_2$, the same conditions were chosen as for the first generation products. The yield was 63% after purification with chromatography.

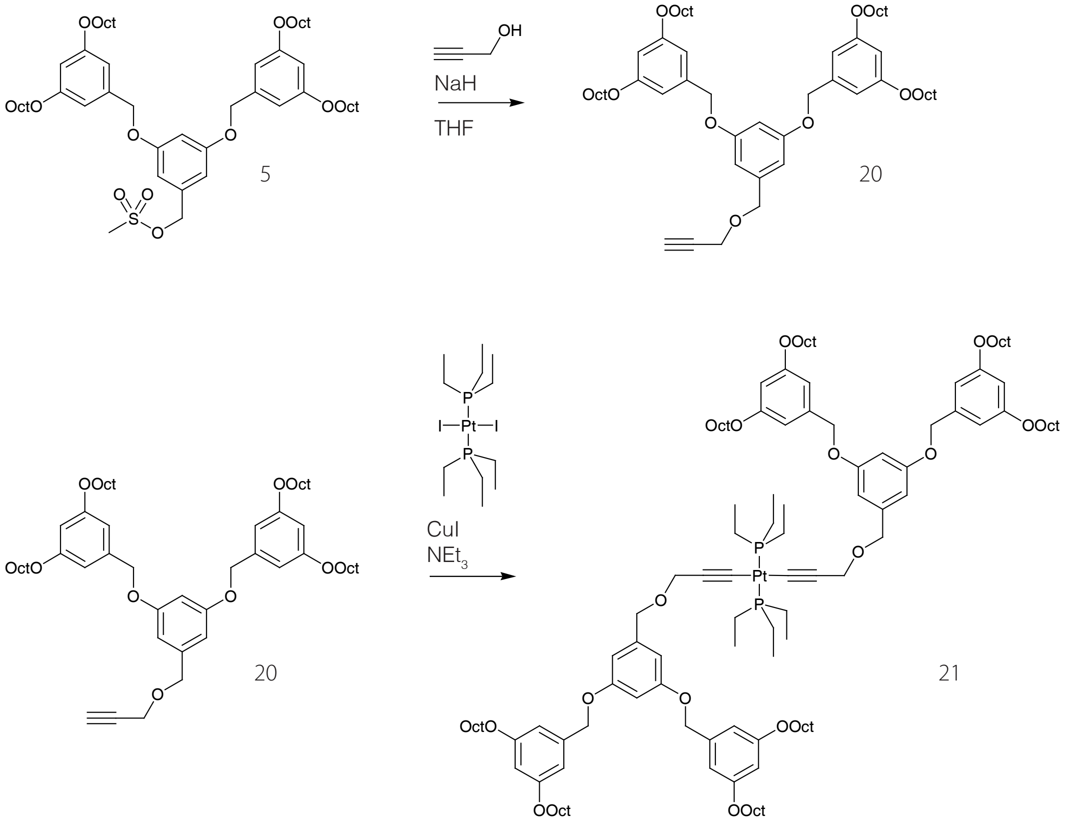

Scheme 6.3 Compound **20** was prepared using NaH as base in THF in 34% yield. The complex **21** was obtained in 63% yield.

In addition to the routine characterisation techniques, ^{31}P and ^{195}Pt NMR spectroscopic data were obtained for the platinum complexes **17** and **21**. Platinum-195, with a spin of ½, is the only NMR-active platinum isotope. With a natural abundance of 33.8% it has a receptivity of 19.1 compared to ^{13}C and is easily detected.[38] K_2PtCl_6 was always used as reference with $\delta(PtCl_6^{2-})$ 4533 ppm.[39] ^{195}Pt NMR spectroscopy was especially useful to verify that *trans*-isomers were obtained for all three platinum complexes. The coupling constant of 2407 Hz for $J(^{195}Pt^{31}P)$ obtained for compound **17** is characteristic for platinum complexes having two PEt_3 and two alkynyl ligands at mutual *trans*-positions.[40, 41] The coupling constants for **21** and **19** are 2399 and 2379 Hz, respectively. ^{195}Pt NMR spectra of compounds **17** and **21** are shown in Figure 6.1. This shift difference of about 6 Hz (δ −340 ppm for **17** versus δ −346 ppm for **21**) is negligible given the huge shift range and the large temperature effect of ^{195}Pt NMR.[38]

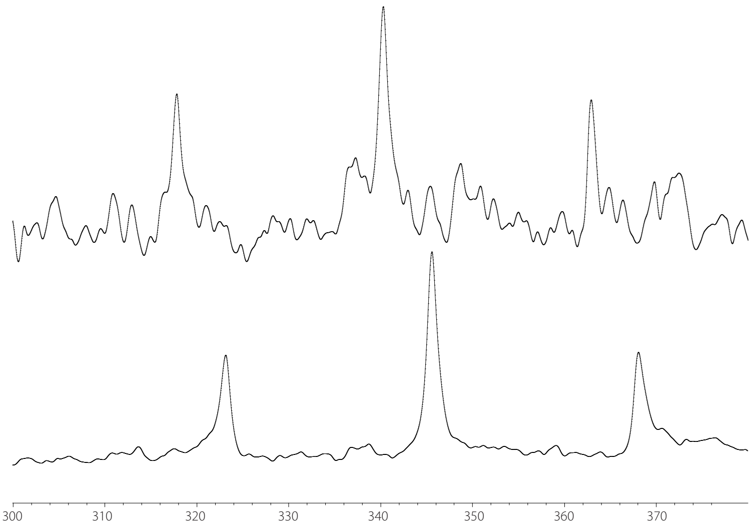

Figure 6.1 Two ^{195}Pt NMR spectra of compounds **17** (above) and **21.**

The ^{13}C NMR signals of the alkynyl groups also exhibit coupling with ^{195}Pt and ^{31}P nuclei (Figure 6.2). The $J(^{195}Pt^{13}C)$ values of α- and β-carbons (**17**, 950 and 266 Hz; **21**, 954 and 266 Hz) are in the same range than those of the phenylethynyl coordinated analogue.[40] The presence of a binomial triplet for the α-carbon at 101.8 ppm (J = 14.6 Hz) for **17** (102.1 ppm for **21** (J = 14.4 Hz)) arising up from the coupling between the ^{13}C and the ^{31}P nuclei also was consistent with *trans*-coordination. The value of $J(^{31}P^{13}C)$ between the phosphorus nuclei and the α-carbons of the ethyl chain (**17**, 17.5 Hz; **21**, 17.3 Hz) is characteristic for this kind of $[Pt(PEt_3)_2]$ complex, as are the corresponding chemical shifts (**17**, δ 16.9 ($H^{PCH_2CH_3}$) and 8.5 ppm ($H^{PCH_2CH_3}$) ; **21**, δ 16.7 and 8.5 ppm).[36] These signals from the ethyl groups showed broad shoulders at the base of the peaks, which is consistent with coupling to the ^{195}Pt nuclei, similar to those shown in Figure 6.3 for the proton signals. The assignment of the peaks was done using DEPT, HMBC and HMQC techniques.

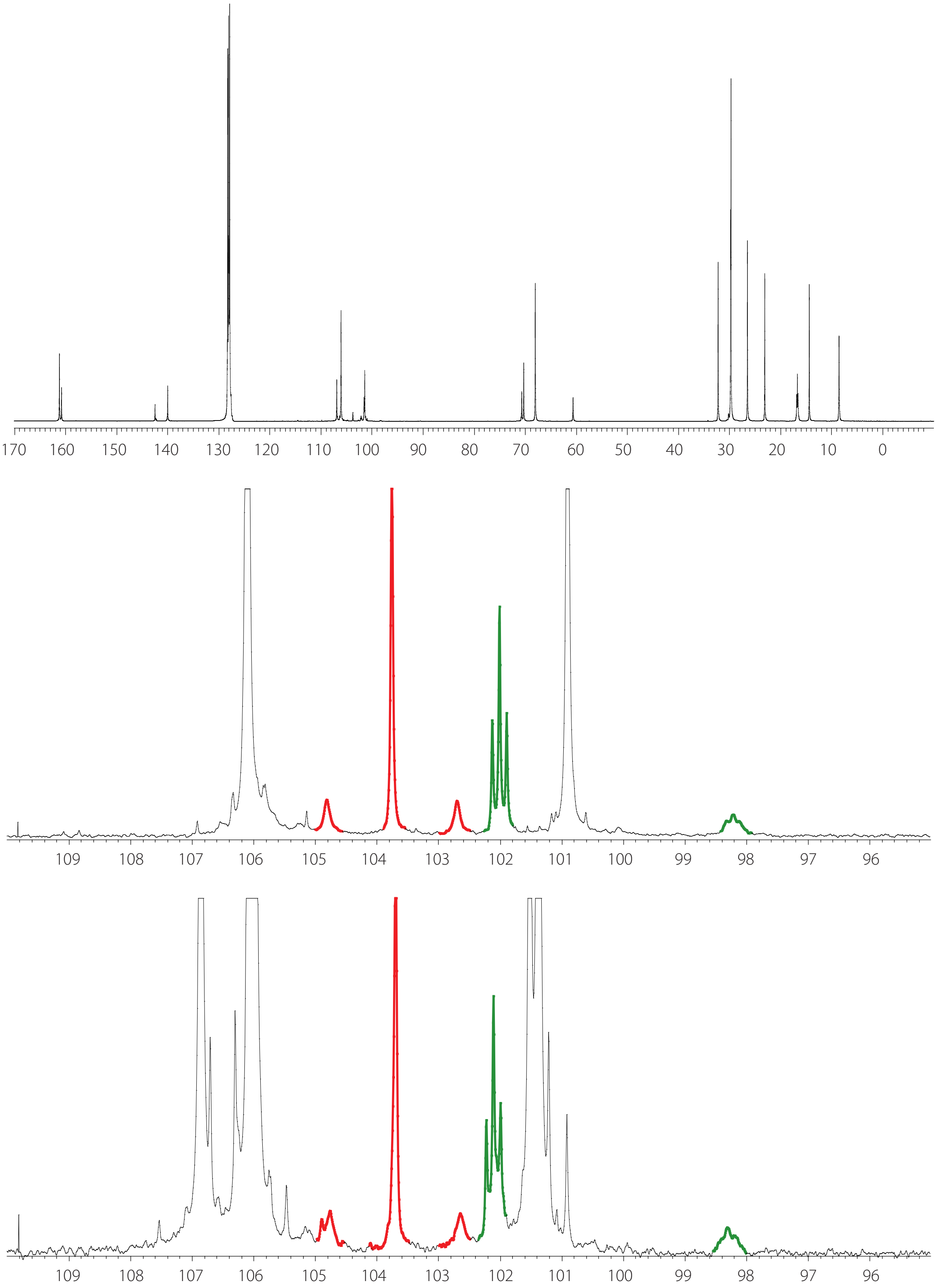

Figure 6.2 ^{13}C NMR spectra of compounds **17** (middle) and **21**(up and down) measured in d_6-benzene. The expanded spectra of **17** and **21** show the range between 95 and 110 ppm. The signals for the α-carbon atoms are shown in green and those belonging to the β-carbons of the alkynyl group are shown in red. The satellite at $\delta \approx 106$ ppm from the α-carbon is covered by the signal of C^{2C} for **17**and C^{2D} for **21**, respectively.

For each of the complexes, a singlet was observed in the ^{31}P NMR spectrum. This was in the range of δ 10 ppm with two satellites originating from a doublet due to coupling with the ^{195}Pt nucleus (integration of the two satellites amount 50% of the singlet, as expected since the natural abundance of the ^{195}Pt nuclei is 33.8%).

The ^{1}H NMR spectrum looked similar to that of a mixture of the two uncoordinated ligands, and no significant shifts of signals occurred. The doublet of HC≡CCH_2O in the free ligands **16**, **18** and **20** appeared as a triplet in the complex. The source of the triplet was the coupling with the ^{31}P nuclei as it could be demonstrated by ^{31}P decoupled ^{1}H NMR measurements (Figure 6.3). As can be seen in Figure 6.4, the signal shows a broadened base which was originated from the coupling with the ^{195}Pt nuclei.

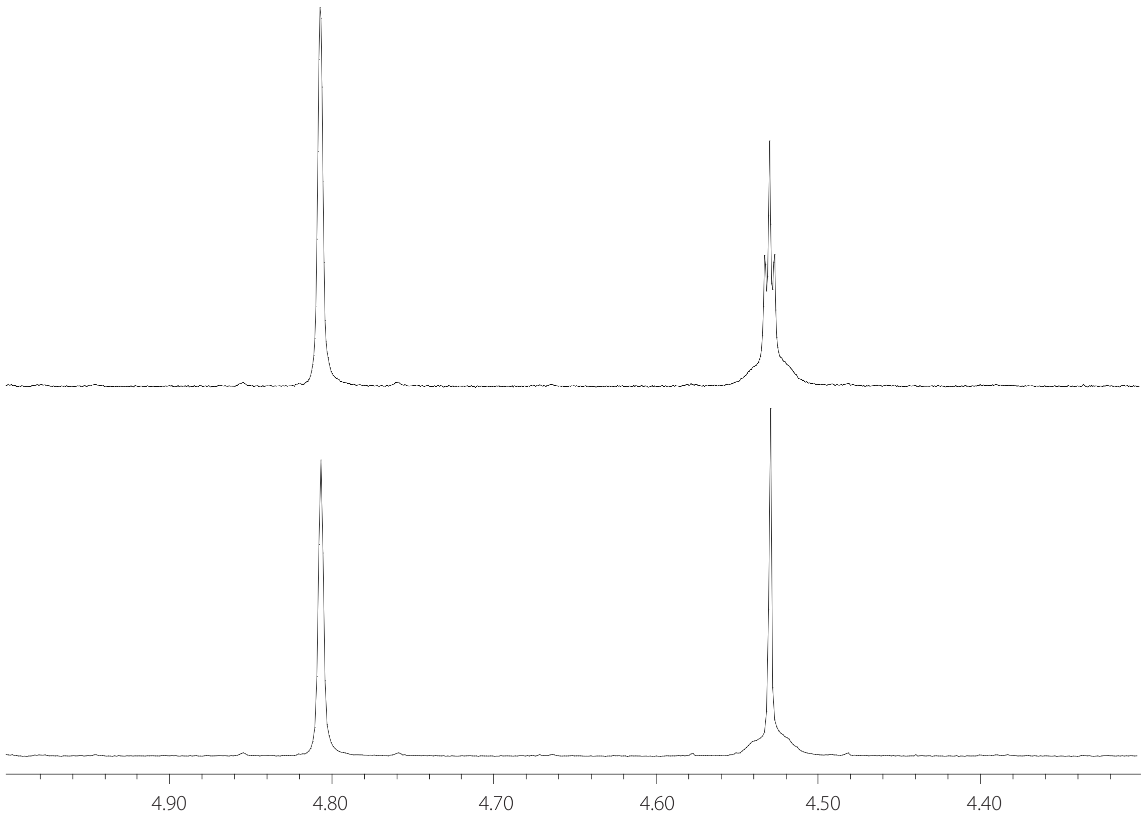

Figure 6.3 ^{1}H NMR spectrum of compound **17** in the range of 4–5 ppm showed the two CH_2 protons of the CH_2–O–CH_2 unit. The spectrum below is a ^{31}P decoupled measurement. The signal at δ 4.53 ppm no longer appeared as a triplet. The broad base of the signal originated from the coupling with the ^{195}Pt nuclei.

Mass spectrometric data were obtained for all the complexes. Whereas the first generation octyl-decorated compound **17** could be measured using ESI-MS, the second generation dendrimer **21** and compound **19** had to be measured with MALDI-TOF MS.

6.1.2 Synthesis and analysis of bis(tpy) metal complexes

The preparation of the tpy ligands used in this Chapter was previously discussed in Chapter 4. These ligands were complexed with Fe(II), Co(II), Co(III) and Ru(II) metal ions. The low-spin bis(tpy) Co(II) complexes are paramagnetic, while the analogous Fe(II), Ru(II) and Co(III) complexes are diamagnetic. Whereas the Fe(II) and Co(II) bis(tpy) complexes are obtained by simply mixing two equivalents of tpy with one equivalent of an appropriate metal(II)-salt, the creation of the Co(III) and Ru(II) complexes is more demanding, in particular for the Fréchet-type functionalised tpy ligands **10**, **11** and **13**. Ring labels used for NMR spectroscopic assignments are the same as those used for the free ligands (Chapter 4).

6.1.2.1 Synthesis and analysis of bis(tpy) iron(II) complexes

The complex **[Fe(10)$_2$]Cl$_2$** was obtained by stirring 2 equivalents of ligand **10** with one equivalent of $FeCl_2·4H_2O$ in ethanol:dichloromethane (2:1) at room temperature. The complex was apolar enough to be purified by chromatography with standard organic solvents. A similar procedure was used to isolate the $[BF_4]^-$ salt. Therefore, ligand **10** was treated with $Fe(BF_4)_2·6H_2O$ in ethanol:dichloromethane (3:1) (Scheme 6.4).

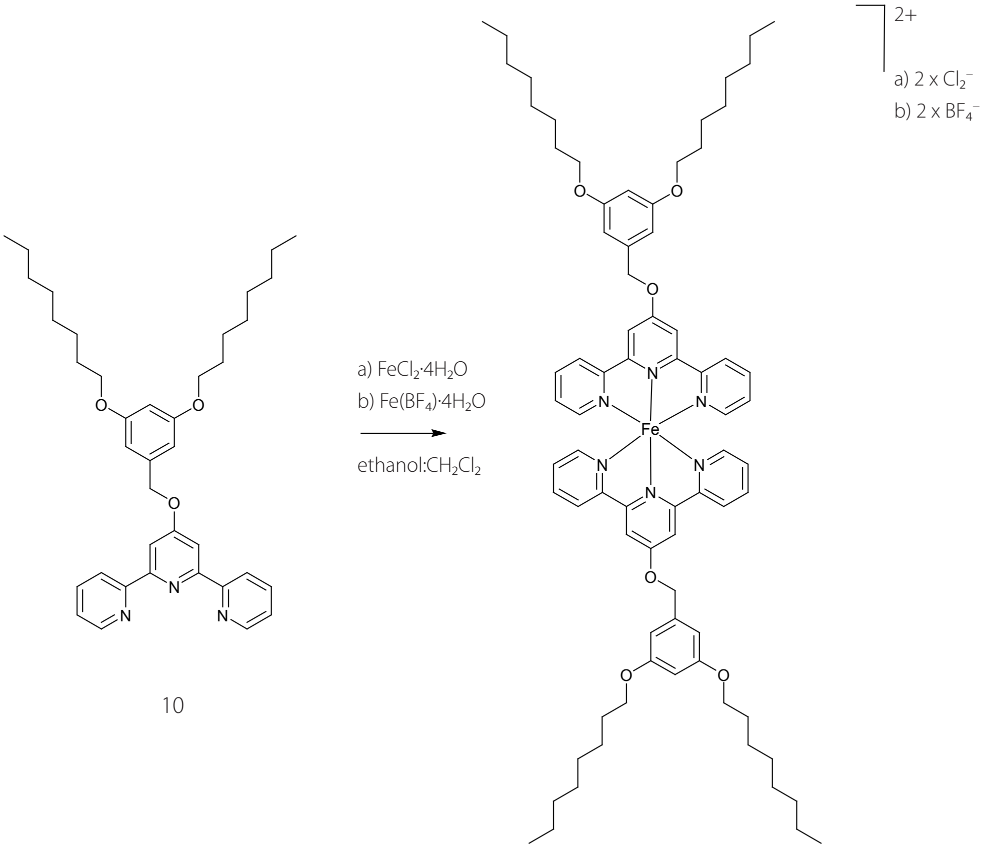

Scheme 6.4 Synthesis of complexes **[Fe(10)$_2$]Cl$_2$** and **[Fe(10)$_2$][BF$_4$]$_2$**.

The complex **[Fe(10)$_2$]Cl$_2$** was soluble in methanol. Thus, anionic exchange reactions could be carried out with this complex in methanol using more apolar anions. A precipitate was collected by ion exchange with NH_4PF_6, $Na[BPh_4]_2$, and Na_4[TPPSA] affording the corresponding complexes **[Fe(10)$_2$][PF$_6$]$_2$**, **[Fe(10)$_2$][BPh$_4$]$_2$** and **[Fe(10)$_2$]$_2$[TPPSA]** (Scheme 6.5). With these complexes, the effect of the counter-ions concerning the self-assembling process in 2D and 3D were investigated. Except of compound **[Fe(10)$_2$]$_2$[TPPSA]**, all other complexes were very soluble in dichloromethane and could be purified by standard chromatography methods. Compound **[Fe(10)$_2$]$_2$[TPPSA]** was only soluble in DMF and slightly soluble in methanol. Therefore the purification was done by washing the crude material with dichloromethane, water and ethanol.

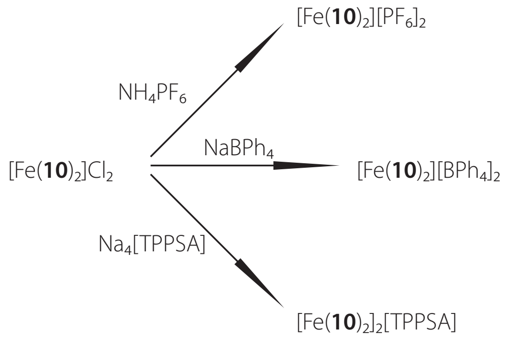
[Fe(**10**)$_2$][PF$_6$]$_2$
NH_4PF_6
NaBPh$_4$
[Fe(**10**)$_2$]Cl$_2$
[Fe(**10**)$_2$][BPh$_4$]$_2$
Na$_4$[TPPSA]
[Fe(**10**)$_2$]$_2$[TPPSA]

Scheme 6.5 Counter-ion exchange starting from complex **[Fe(10)$_2$]Cl$_2$**.

The ^{1}H NMR spectra of the complexes may be compared with the ^{1}H NMR spectrum of the free ligand **10**. In Figure 6.4, the ^{1}H-NMR spectra of ligand **10** and **[Fe(10)$_2$][PF$_6$]$_2$** are shown. The spectrum of the complex is consistent with the formation of a symmetrical species. Compared to the ligand, however, the signals for H^{3C} and H^{5C} of **[Fe(10)$_2$][PF$_6$]$_2$** were broadened, which can be rationalised as arising from the poor solubility of the apolar dendritic complex in d_3-acetonitrile (Figure 6.4). The doublet of H^{3A} shifted by 1.50 ppm to higher field during the complexation as well as H^{4A} ($\Delta\delta$ −0.81 ppm) and H^{6A} ($\Delta\delta$ −0.29 ppm). The remarkable change in chemical shift for H^{3A} can be explained in terms of the conformational change of tpy unit from *trans, trans* to *cis, cis*.[2, 42] The same effect was observed for the complexation of the bpy-ligand **3** during the complexation with Pd(II) (see Section 3.1.1). It is also noteworthy that H^{OCH_2C} shifted by 0.34 ppm to lower shift. This effect has already been observed for other work on tpy decorated Fréchet-type dendrimers.[43]

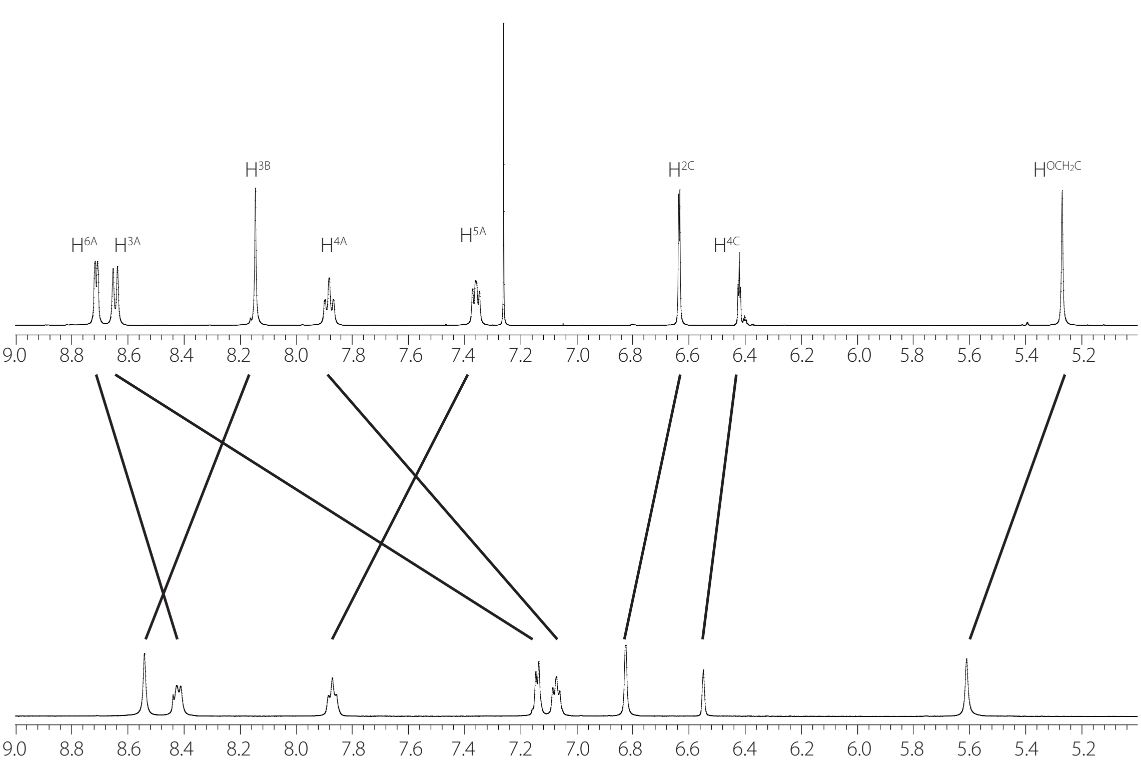

Figure 6.4 ^{1}H-NMR spectra of ligand **10** (upper) and **$[Fe(10)_2][PF_6]_2$** (lower) are shown.

The ^{1}H NMR spectra of the complexes with the different counter-ions did not differ significantly from each other, with the exception of signals arising from the anions. The ^{1}H NMR spectrum of a d_6-DMSO solution of $[$**Fe(10)$_2$**$]_2$[**TPPSA**] exhibited the lowest field peak at δ 9.04 ppm assigned to H^{3B} and also H^{6A} was low-field shifted (δ 8.80 ppm) compared to the spectra of the other [**Fe(10)$_2$**] complexes (Figure 6.5). This may be the result of using d_6-DMSO instead of d_3-acetonitrile as the NMR solvent. The two protons of the NH-group of the porphyrin unit were at very high field (δ −2.97 ppm) due to the magnetic anisotropy of the porphyrin-ring. The integration of the TPPSA signals compared to the integration of the cation signals confirmed the cation:anion ratio of 2:1.

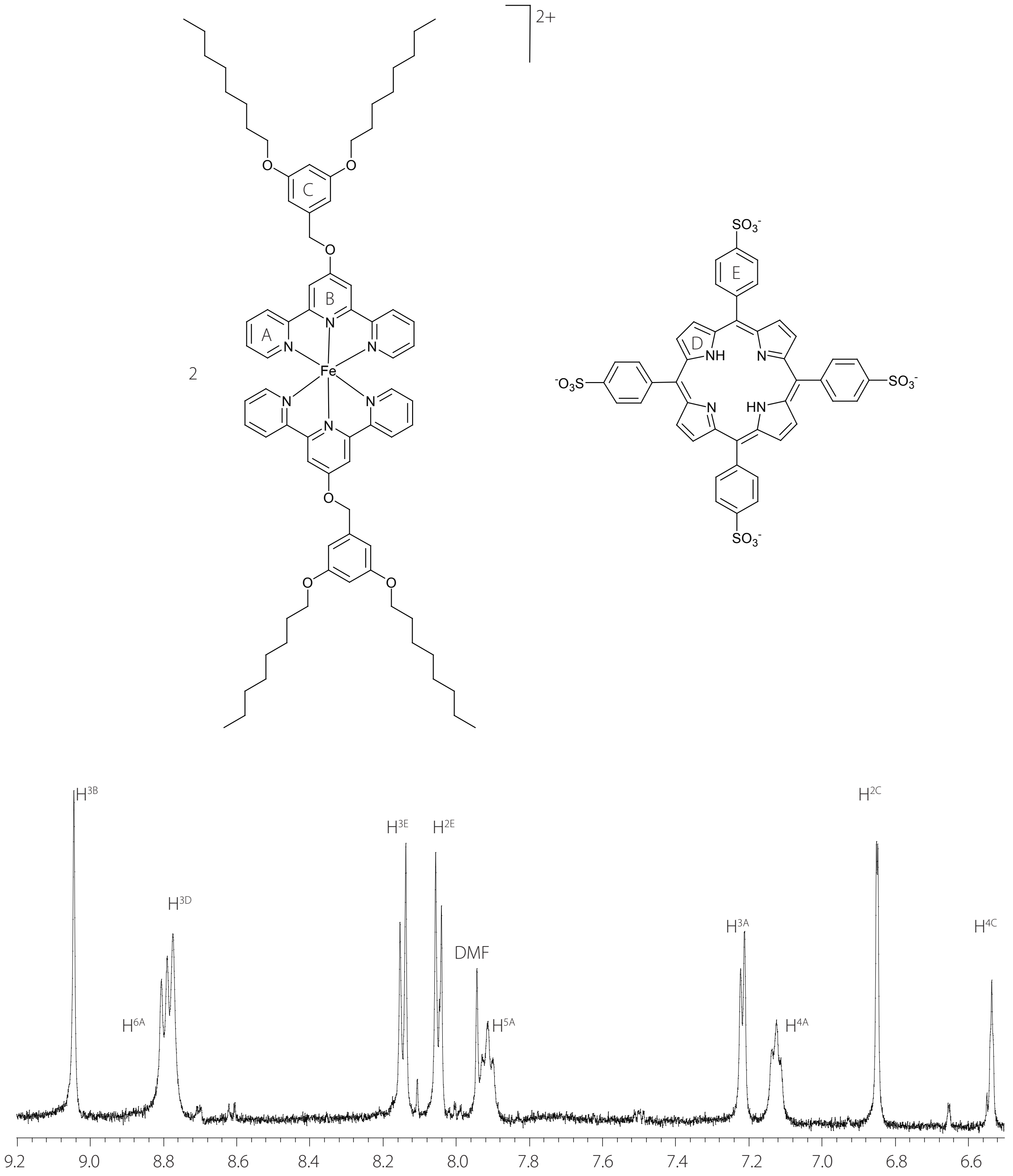

Figure 6.5 ^{1}H-NMR spectrum of **[Fe(10)$_2$]$_2$[TPPSA]**. The signals H^{3B} and H^{6A} are low-field shifted compared to the ^{1}H-NMR spectrum of other **[Fe(10)$_2$]$^{2+}$** complexes. Ring labels are used for NMR spectroscopic assignments.

In the ESI-MS of all the [Fe(**10**)$_2$]$^{2+}$ salts, peaks at *m/z* 623 were the most intense, and corresponded to [M − 2X]$^{2+}$ (X = counter-ion). For all peaks, the observed isotope distributions matched those simulated.[44] Since no [M − X]$^+$ or [M] signal could be detected in the ESI-MS, and the NMR measurements showed no significant differences (except for [Fe(**10**)$_2$][BPh$_4$]$_2$ and [Fe(**10**)$_2$]$_2$[TPPSA]), the only clear proof for the counter-ion exchange was from elemental analytical data.

All single crystals obtained from these complexes were too small to be measured using single crystal X-ray techniques. The single crystal of complex [Fe(**10**)$_2$][PF$_6$]$_2$ was obtained by recrystallisation in ethanol (Figure 6.6). The data were very poor in quality, but nonetheless confirmed the gross structural features of the complex.

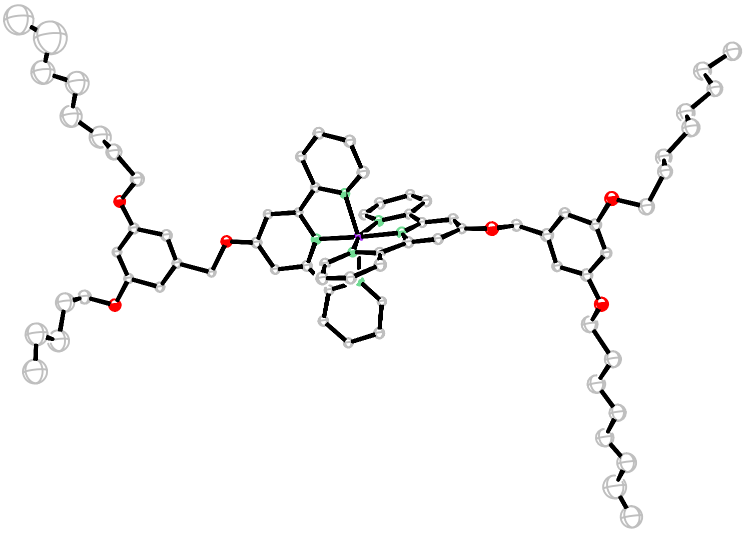

Figure 6.6 The molecular structure of the cation in **[Fe(10)$_2$][PF$_6$]$_2$** obtained by slowly cooling an ethanolic solution of **[Fe(10)$_2$][PF$_6$]$_2$**. One octyl-chain, the solvents and the counter-ions could not be refined.

The iron(II) complex of the second generation Fréchet-type ligand **11** was synthesised by an analogous method. Two equivalents of ligand **11** were stirred in a dichloromethane:methanol 4:1 solution with FeCl$_2$·4H$_2$O at room temperature (Scheme 6.6). The obtained complex [Fe(**10**)$_2$]Cl$_2$ was very soluble in most common organic solvents and therefore no counter-ion exchange was performed. The compound was fully characterised.

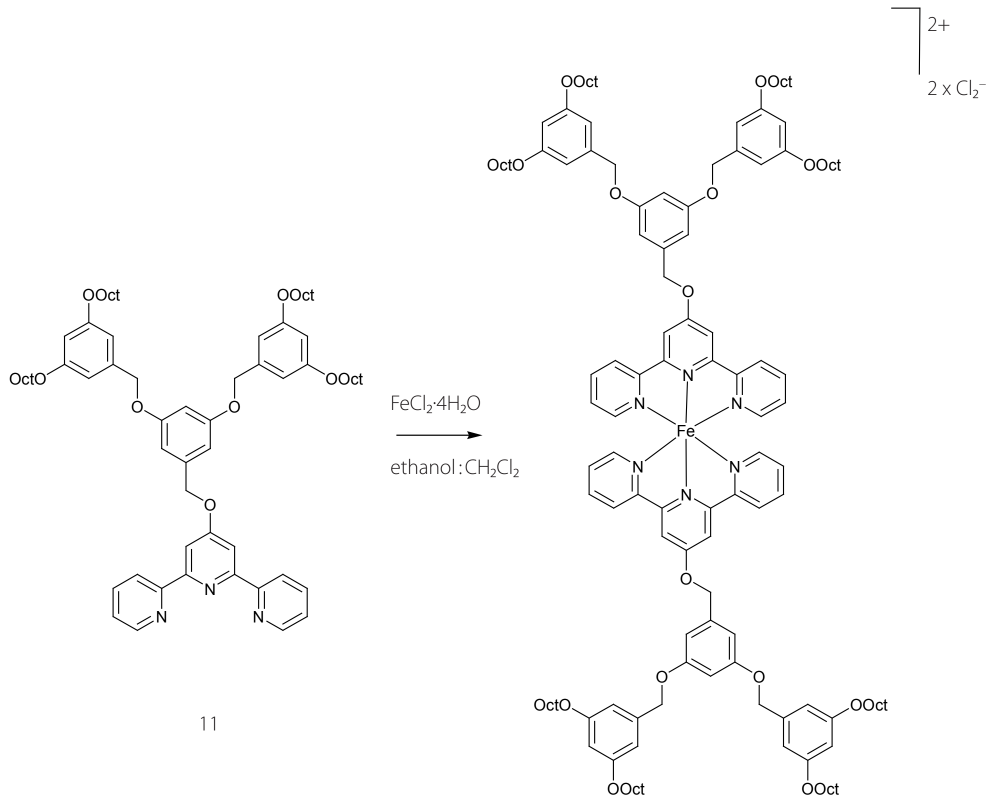

Scheme 6.6 Synthesis of complex **[Fe(11)$_2$]Cl$_2$**.

The iron complexes [**Fe**(**10**)$_2$][**PF**$_6$]$_2$ and [**Fe**(**11**)$_2$]**Cl**$_2$ are purple and exhibit an MLCT absorption at ≈555 nm, typical of a [Fe(tpy)$_2$]$^{2+}$ chromophore.[2] Within experimental error, the two complexes have identical absorption maxima and molar extinction coefficients indicating that no significant perturbation of the metal–ligand interaction occurs with increasing generations of the dendritic substituents.

6.1.2.2 Synthesis and analysis of bis(tpy) cobalt(II) and cobalt(III) complexes

The complex [**Co**(**10**)$_2$][**BF**$_4$]$_2$ was obtained by stirring 2 equivalents of ligand **10** with one equivalent of Co(BF$_4$)$_2$·6H$_2$O in ethanol:dichloromethane 3:1 at room temperature (Scheme 6.7). The solvent from the deep-orange solution was removed *in vacuo* and the remaining compound [**Co**(**10**)$_2$][**BF**$_4$]$_2$ was very pure as it could be verified by elemental analysis.

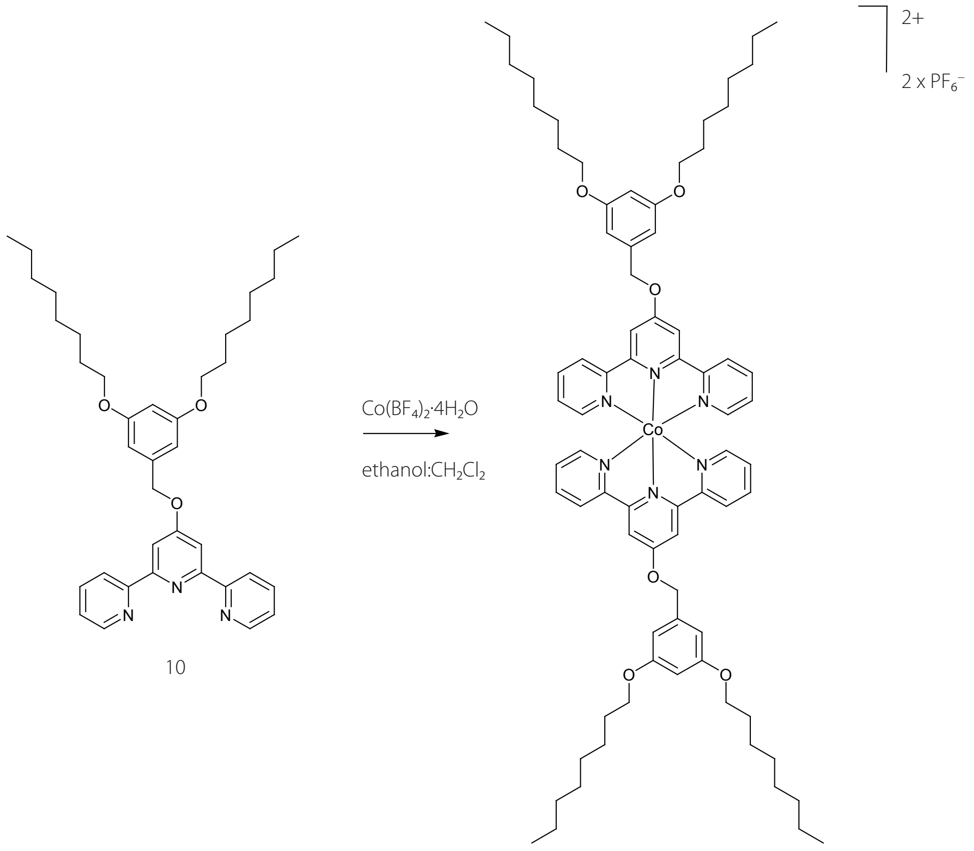

Scheme 6.7 Synthesis of complex **$[Co(10)_2][BF_4]_2$**.

As for the iron(II) complex, the ESI-MS showed a very intense peak for $[M - 2PF_6]^{2+}$ at *m/z* 625. No other signals could be seen. The isotopic pattern matched that simulated.[44]

The paramagnetically shifted ^1H NMR spectra of Co(II) bis(tpy) complexes are, although broadened, usually well resolved.[43, 45-47] The spectra of the present complex were no exception. The ^1H NMR signals that are the most affected by the presence of the paramagnetic d^7 cobalt(II) centre are those belonging to the tpy protons. These signals were assigned by comparison with those for Co(II) complexes of other Fréchet-type dendrimers substituted at 4'-position of the tpy unit.[43] The signal for the H^{6A} proton appeared at δ 113.8 ppm in acetonitrile solution of **$[Co(10)_2][BF_4]_2$**. Since H^{6A} is in closest proximity to the Co(II) centre, the corresponding signal experiences the greatest shift to higher frequency of any proton in these complexes. Signals at δ 77.2, 71.9, 35.1 and 6.25 ppm were assigned to H^{3B}, H^{3A}, H^{5A} and H^{4A}, respectively. The broadened signals assigned to H^{2C} and H^{4C} appeared at δ 12.2 and 8.37 ppm compared to δ 6.63 and 6.42 ppm in the free ligand, while the signals for the protons in the octyl chain were relatively sharp and come at δ 5.85 ($H^{OC\mathit{H}_2CH_2}$), 2.85 ($H^{OCH_2C\mathit{H}_2}$), 2.27 ($H^{OCH_2CH_2C\mathit{H}_2}$), 1.80 ($H^{O(C\mathit{H}_2)_3C\mathit{H}_2}$), 1.56 ($H^{O(C\mathit{H}_2)_4C\mathit{H}_2}$), 1.36 ($H^{(C\mathit{H}_2)_2}$) and 0.91 ($H^{C\mathit{H}_3}$) compared to δ 3.95 ($H^{OC\mathit{H}_2CH_2}$), 1.77 ($H^{OCH_2C\mathit{H}_2}$), 1.46 ($H^{OCH_2CH_2C\mathit{H}_2}$), 1.25–1.37 ($H^{(C\mathit{H}_2)_4}$) and 0.89 ppm ($H^{C\mathit{H}_3}$) in the free ligand (Figure 6.7). The assignment was done with COSY experiments.

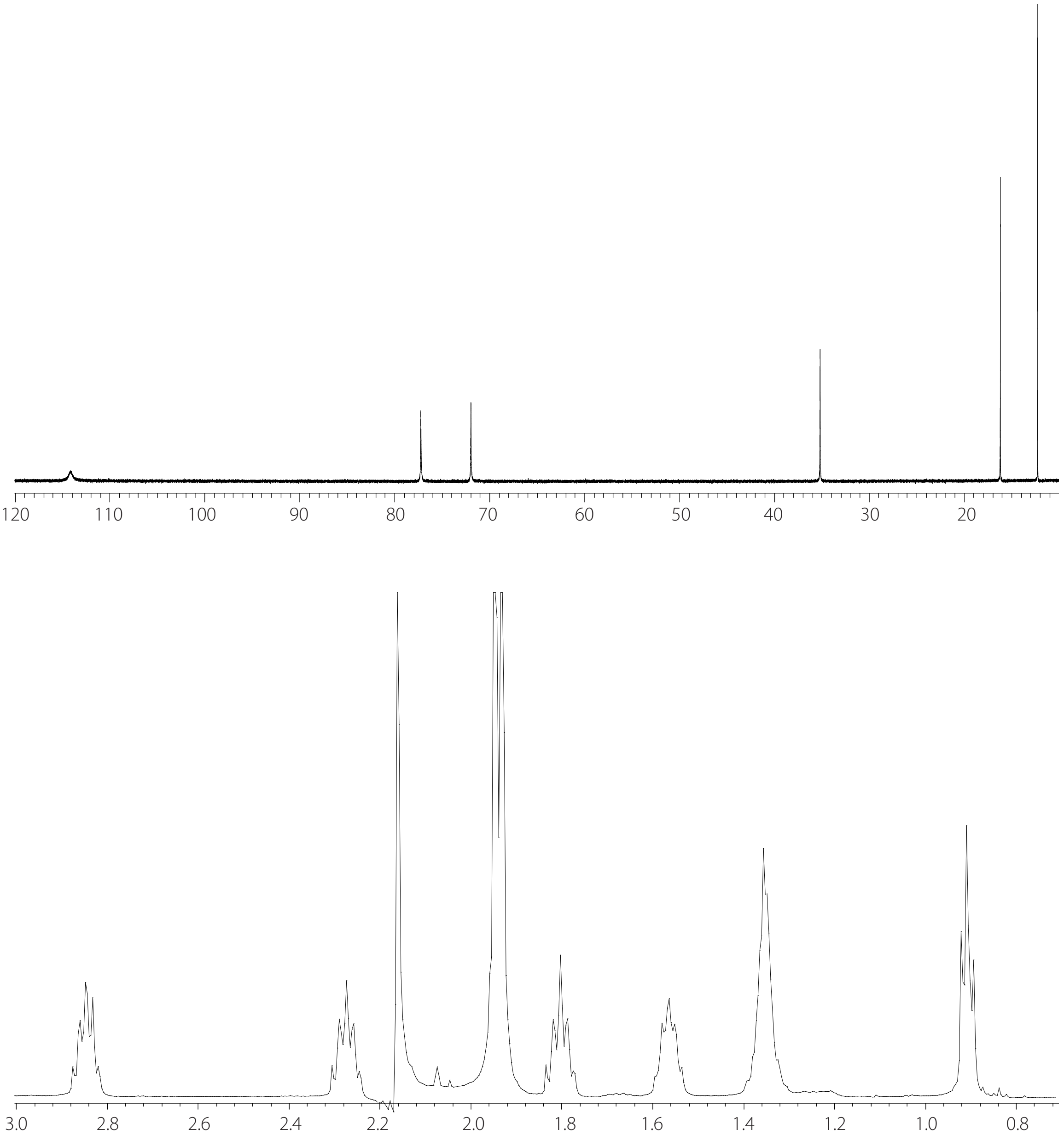

Figure 6.7 ^{1}H NMR spectra of **$[Co(10)_2][BF_4]_2$** in the range of 120 and 10 ppm measured in acetonitrile. Below, an expanded spectrum shows the range between 3.0 and 0.7 ppm. The signals corresponding to the CH_2-protons of octyl chains are well separated.

The cobalt(II) complex was then oxidised to the $[\mathbf{Co(10)_2}]^{3+}$ complex. This oxidation turned out to be quite demanding, since the tpy–O–CH_2 unit is sensitive to Lewis acids and the electrophilic bromine (used for the cobalt(II) oxidation) attacks the aromatic-rich phenyl-group from the dendrimers unit. Acid (HOAc, HBF_4) in the presence of oxygen was not strong enough to oxidise the Co(II) centre, not even by addition of aqueous H_2O_2 and charcoal. $Pb(OAc)_4$ in dichloromethane was finally chosen as an appropriate oxidising agent. The oxidation occurred immediately as it could be followed by the colour change of the solution from deep-orange to bright-yellow. **$[Co(10)_2][PF_6]_3$** was precipitated upon treatment with ammonium hexafluorophosphate in methanol.

Surprisingly, the ESI-MS spectrum resembled the spectrum obtained from [**Co**(**10**)$_2$][**BF**$_4$]$_2$. No signal from a Co(III) complex could be detected, although no reductive solvent was used (acetonitrile). Elemental analysis, UV-vis and NMR spectroscopy revealed clearly the formation of [**Co**(**10**)$_2$][**PF**$_6$]$_3$ (Figure 6.8).

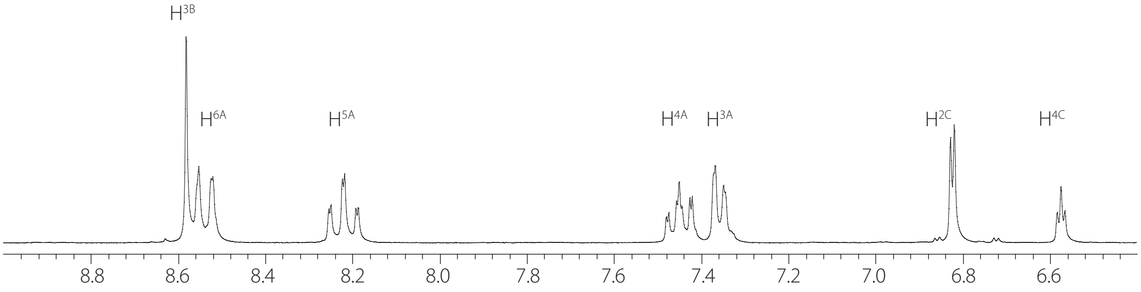

Figure 6.8 ^{1}H NMR spectrum of **[Co(10)$_2$][PF$_6$]$_3$**.

The chemical shifts of the tpy-protons in the ^{1}H NMR of the diamagnetic low-spin complex [**Co**(**10**)$_2$][**PF**$_6$]$_3$ were similar to those for compound [**Fe**(**10**)$_2$][**PF**$_6$]$_2$ with the exception of the H^{4A} and H^{5A} signals, which were both shifted to higher field in the cobalt(III) complex by 0.38 ppm for H^{4A} and by 0.65 ppm for H^{5A} respectively.

6.1.2.3 Synthesis and analysis of bis(tpy) ruthenium(II) complexes

Ruthenium(II)-complexes of ligands **10**, **11** and **13** were prepared. Bis(tpy) Ru(II) complexes are kinetically more stable than the corresponding iron(II) and cobalt(II/III) complexes. The complexation does not occur as spontaneously as with cobalt(II) or iron(II) salts.[2] Bis(tpy) Ru(II) complexes are normally obtained via a two-step synthesis procedure. Firstly, one equivalent of tpy ligand is reacted with one equivalent of $RuCl_3{\cdot}3H_2O$ to produce the Ru(tpy)Cl_3 complex. A second equivalent of tpy ligand then reacts with this complex in the presence of a reducing agent to obtain the desired bis(tpy) Ru(II) complex. In this way, both homo- and heteroleptic bis(tpy) complexes can be obtained. Another useful strategy is to react two equivalents of tpy ligands directly with one equivalent of $RuCl_3{\cdot}3H_2O$ in ethylene glycol in a microwave oven[48] (600 W).[49, 50] When using this second method for the synthesis of [**Ru**(**10**)$_2$][**PF**$_6$]$_2$, the yield was very low (8%), which was explained by the high Lewis acidity of ruthenium(III) which results in cleavage of the tpy−O−CH_2 unit. Ru(DMSO)$_4$$Cl_2$ was chosen as the appropriate ruthenium(II) source. Ru(DMSO)$_4$$Cl_2$ is a yellow powder which can be prepared by simply heating $RuCl_3{\cdot}3H_2O$ in DMSO,[51] furthermore it is air-stable. Since the Ru−Cl bond is strong, precipitation of an insoluble halide metal salt was necessary to force the equilibrium to the product side. In such cases, Ag^+ is often used.[52, 53] Due to the fact that Ag^+ can form complexes with olygopyridine ligands (Section 3.1.1), $TlPF_6$ was used. TlCl is not soluble in any common solvent and thallium(I) is known not to form metal complexes with oligopyridine ligands.[2] The complexation reactions were carried out in refluxing ethanol (Scheme 6.8).

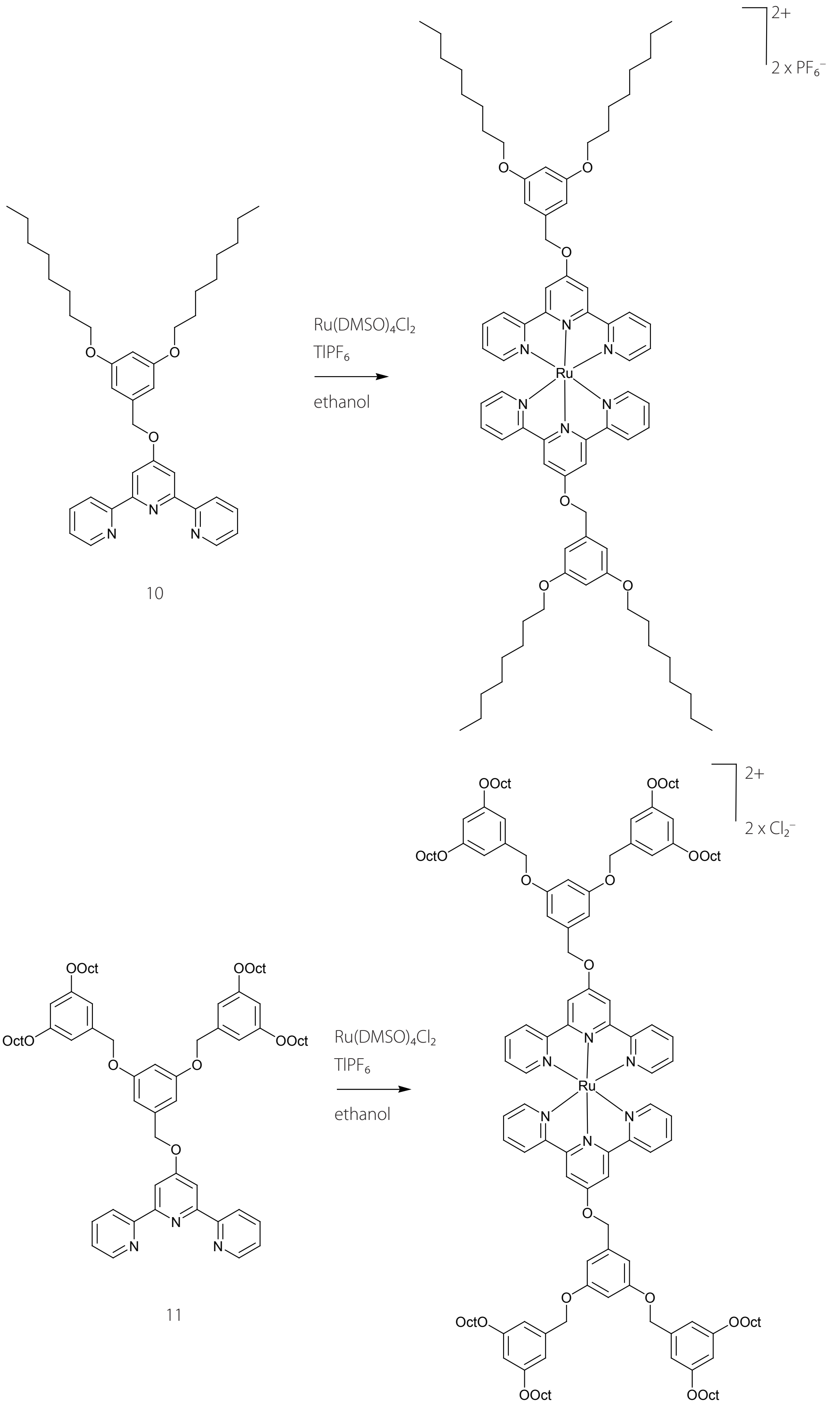
2+
2 x PF_6^-
O
N
Ru(DMSO)$_4$Cl$_2$
TlPF$_6$
ethanol
Ru
10
2+
2 x Cl_2^-
OOct
OctO
11

Scheme 6.8 Synthesis of the two ruthenium(II) complexes **[Ru(10)$_2$][PF$_6$]$_2$** and **[Ru(11)$_2$]Cl$_2$**.

By the same procedure complex **[Ru(13)$_2$][PF$_6$]$_2$** was prepared (Scheme 6.9). The corresponding iron(II) and cobalt(II) complexes of ligand **13** are already known.[43]

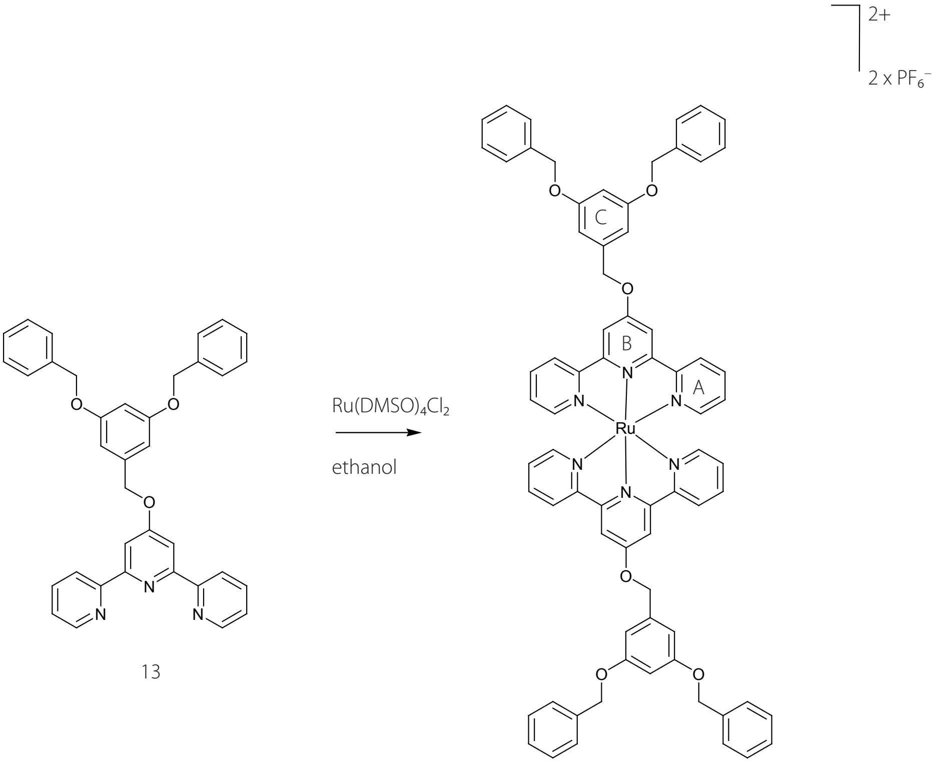

Scheme 6.9 Synthesis of **[Ru(13)$_2$][PF$_6$]$_2$**. Ring labels are used for NMR spectroscopic assignments.

As for the iron(II) and cobalt(II) complexes, the ESI-MS for **[Ru(10)$_2$][PF$_6$]$_2$** showed only a signal for $[M - 2PF_6]^{2+}$ at *m/z* 646. The isotopic pattern matched that simulated.[44] For **[Ru(11)$_2$]Cl$_2$** and **[Ru(13)$_2$][PF$_6$]$_2$** the doubly charged cation was the most intense signal in the ESI-MS spectrum.

The ^{1}H NMR spectra of the ruthenium(II) complexes had similar chemical shifts observed in the spectra of the iron(II) complexes with the only remarkable difference of the signal at lowest field, which was for the ruthenium complexes the doublet from the proton H^{6A}. The three signals for H^{6A} ($\Delta\delta$ 0.40 ppm), H^{3B} ($\Delta\delta$ 0.44 ppm) and H^{3A} ($\Delta\delta$ 0.40 ppm) were significantly at lower field in the second generation complex than in the first generation complex (Figure 6.9). This observation has neither been made in other studies where classical Fréchet-type dendrimers were attached in the 4'-position of bis(tpy) metal complexes,[43] nor with the corresponding iron(II) complexes **[Fe(10)$_2$][PF$_6$]$_2$** and **[Fe(11)$_2$]Cl$_2$** (see Section 6.1.2.1). Nevertheless, one must emphasise that different solvents were used for the two ^{1}H NMR spectra. **[Ru(10)$_2$][PF$_6$]$_2$** was measured in d_3-acetonitrile, while the **[Ru(11)$_2$]Cl$_2$** spectrum was recorded in d_6-acetone. It is supposed, that the solvent was responsible for these observed differences in the chemical shifts, as discussed for compound **[Fe(10)$_2$]$_2$[TPPSA]** in Section 6.1.2.1.

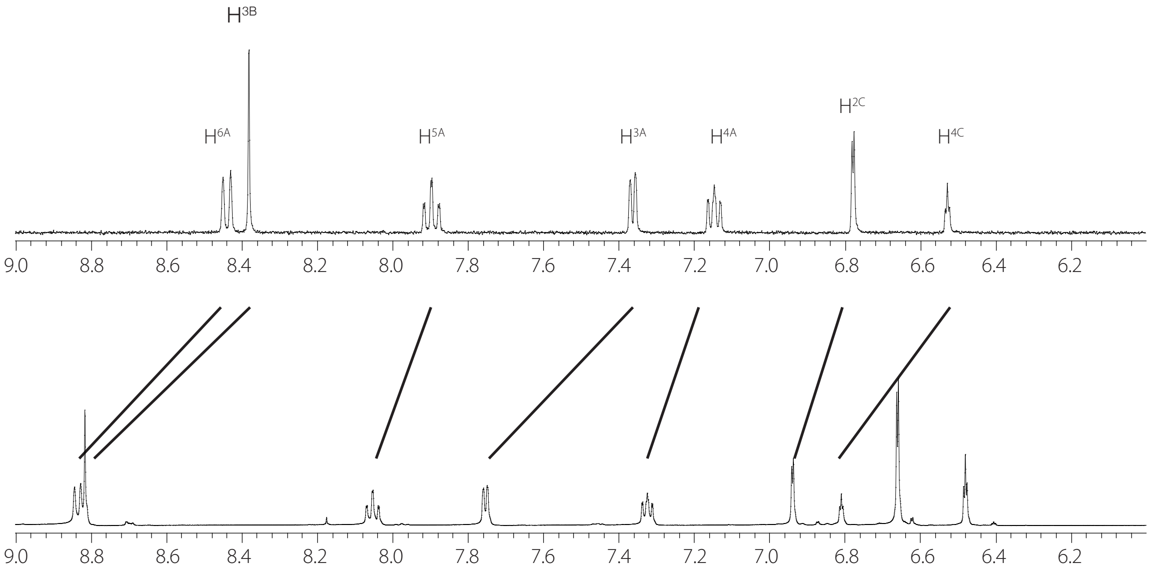

Figure 6.9 ^{1}H NMR spectrum of **[Ru(10)$_2$][PF$_6$]$_2$** measured in d_3-acetonitrile (above) and of **[Ru(11)$_2$]Cl$_2$** from a d_6-acetone solution.

The ruthenium complexes were orange and exhibited an MLCT absorption at ≈485 nm, typical of a $[Ru(tpy)_2]^{2+}$ chromophore.[2] Within experimental error, the three complexes had identical absorption maxima and molar extinction coefficients indicating that no significant perturbation of the metal–ligand interaction occured with increasing generation of the dendritic substituent.

6.2 Study of self-assembled monolayers of metal complexes

6.2.1 Self-assembled monolayers of bis(tpy) metal complexes

The self-assembling of two different types of metallated hydrophobic complexes are discussed: ionic metal bis(tpy) complexes and neutral platinum species. Pre-formed complexes were introduced to the surface from solution under ambient (room temperature, atmospheric pressure, air) conditions are obtained in remarkably high resolution STM images.

Compound **[Fe(10)$_2$][PF$_6$]$_2$** was firstly measured and formed very reproducible and stable self-assembled monolayers by solution casting, with a 0.2 mM acetonitrile solution (Figure 6.10). Although good quality images were obtained, it was not obvious how the molecules were organised on the surface. The rows were an indication of a lamellar packing with interdigitating octyl-chains in the darker region. Every second row showed a different contrast which was important to notice before averaging.

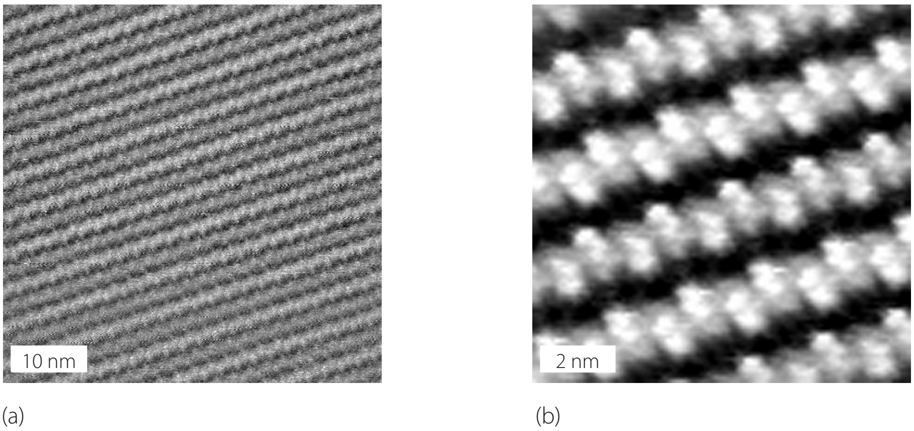

Figure 6.10 (a) A typical STM image of compound **$[Fe(10)_2][PF_6]_2$** (50 nm x 50 nm, $U_b = -700$mV, $I_t = 10$ pA). (b) Expanded image (10 nm x 10 nm, $U_b = -700$mV, $I_t = 15$ pA) averaged over 67 positions.

STM images were overlaid by models of the cation. The fitting seemed reasonable, although it was not clear, where the counter-ions were placed on the surface (Figure 6.11).

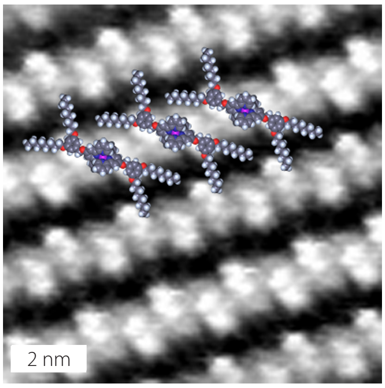

Figure 6.11 STM image of **$[Fe(10)_2][PF_6]_2$** taken from Figure 6.10 with overlaid cations.

To answer the question of the counter-ions, the self-assembled monolayers of $[Fe(\mathbf{10})_2]^{2+}$ with different counter-ions were studied. Compounds **$[Fe(10)_2]Cl_2$**, **$[Fe(10)_2][BF_4]_2$**, **$[Fe(10)_2][BPh_4]_2$** and **$[Fe(10)_2]_2[TPPSA]$** were chosen. BF_4^-, BPh_4^-, $TPPSA^{4-}$ and BPh_4^- are different in size and therefore it was expected that this would influence the 2D packing. Furthermore, the cation:anion ratio of **$[Fe(10)_2]_2[TPPSA]$** is different and $TPPSA^{4-}$ is anticipated to interact well with the graphite surface.

All of these complexes formed very stable monolayers and the pattern could be observed immediately after approaching the tip. The resulting STM images are shown in Figure 6.12–Figure 6.15.

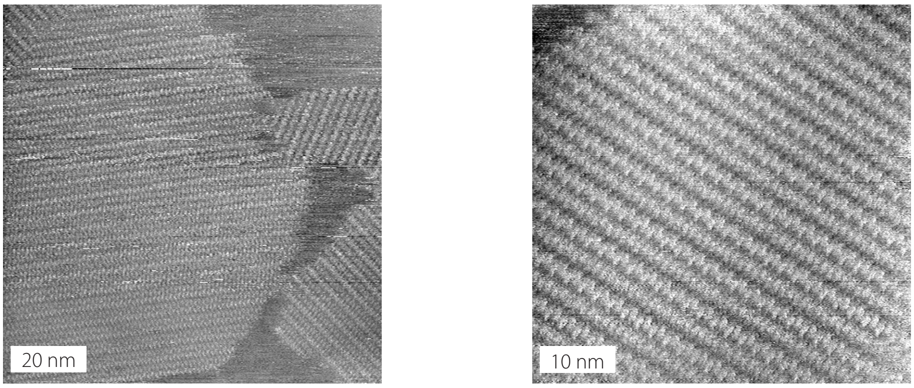

(a) (b)

Figure 6.12 Two STM images of **[Fe(10)$_2$][BF$_4$]$_2$**. Scan parameters: (a) 100 nm x 100 nm, $U_b = -700$mV, $I_t = 8$ pA; (b) 50 nm x 50 nm, $U_b = -700$mV, $I_t = 10$ pA.

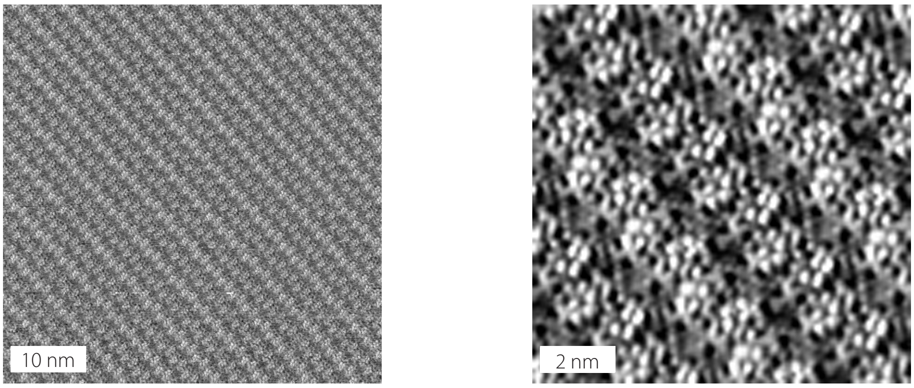

(a) (b)

Figure 6.13 Two STM images of compound **[Fe(10)$_2$]Cl$_2$**. Scan parameters: (a) 50 nm x 50 nm, $U_b = -700$mV, $I_t = 12$ pA; (b) 10 nm x 10 nm, $U_b = -700$mV, $I_t = 40$ pA, averaged over 164 points.

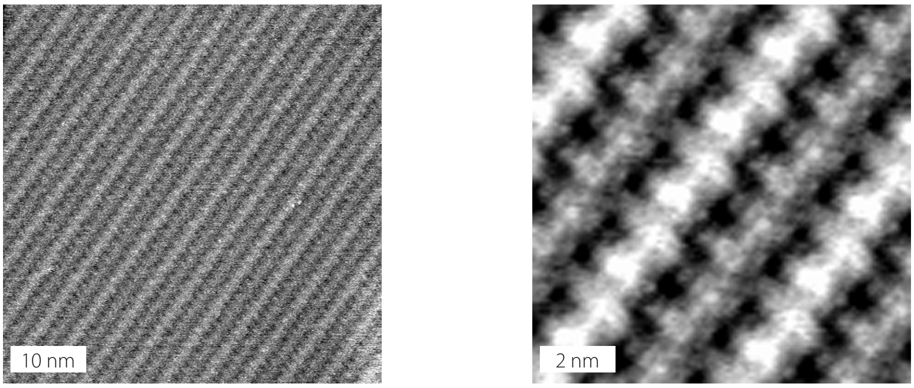

(a) (b)

Figure 6.14 STM image of a monolayer formed from **[Fe(10)$_2$][BPh$_4$]$_2$**. Scan parameters: 50 nm x 50 nm, $U_b = -700$ mV, $I_t = 8$ pA; (b) an expanded (10 nm x 10 nm) and averaged (over 101 positions) image of (a).

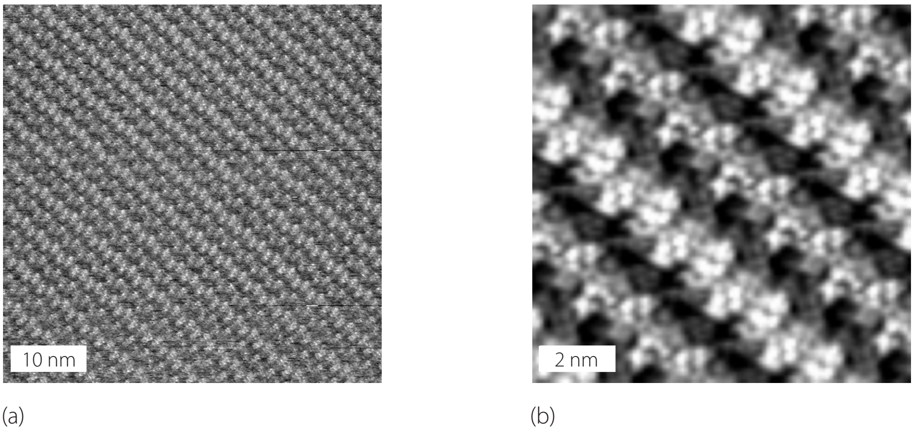

Figure 6.15 STM image of a monolayer formed from a 0.2 mM DMF solution of **$[Fe(10)_2]_2[TPPSA]$**. Scan parameters: 50 nm x 50 nm, U_b = −1200 mV, I_t = 10 pA; (b) an expanded (10 nm x 10 nm) and averaged (over 133 positions) image (10 nm x 10 nm, U_b = −700 mV, I_t = 18 pA).

The STM images of compounds $[Fe(\mathbf{10})_2][PF_6]_2$, $[Fe(\mathbf{10})_2]Cl_2$, $[Fe(\mathbf{10})_2][BF_4]_2$, $[Fe(\mathbf{10})_2][BPh_4]_2$ and $[Fe(\mathbf{10})_2]_2[TPPSA]$ did not differ from each other. Only the resolution differed, which can be explained with tips of different quality or with the different scanning parameters. The counter-ion did not influence the 2D pattern, which is remarkable, especially for compound $[Fe(\mathbf{10})_2]_2[TPPSA]$, hence it could be followed that the counter-ions do *not* take part in the self-assembled monolayer. To further examine what could have happened to the counter-ion, the metal was varied. The 2D self-assembling of the corresponding cobalt(II) complex is shown in Figure 6.16.

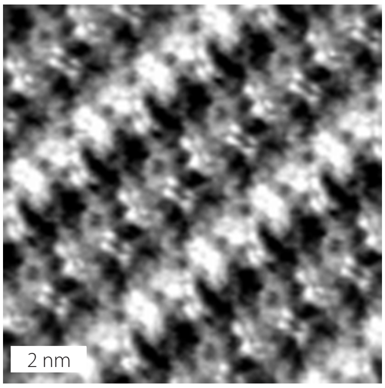

Figure 6.16 An averaged (over 67 points) and expanded STM image of a monolayer formed from **$[Co(10)_2][PF_6]_2$**. Scan parameters: 10 nm x 10 nm, U_b = −700 mV, I_t = 10 pA. Scan parameters: 50 nm x 50 nm, U_b = −1200 mV, I_t = 10 pA.

The ordering of the cobalt(II) complex cations was the same as for the analogous iron(II) complex. Since the cobalt(III) complex was also stable, the influence of the charge was investigated (Figure 6.17).

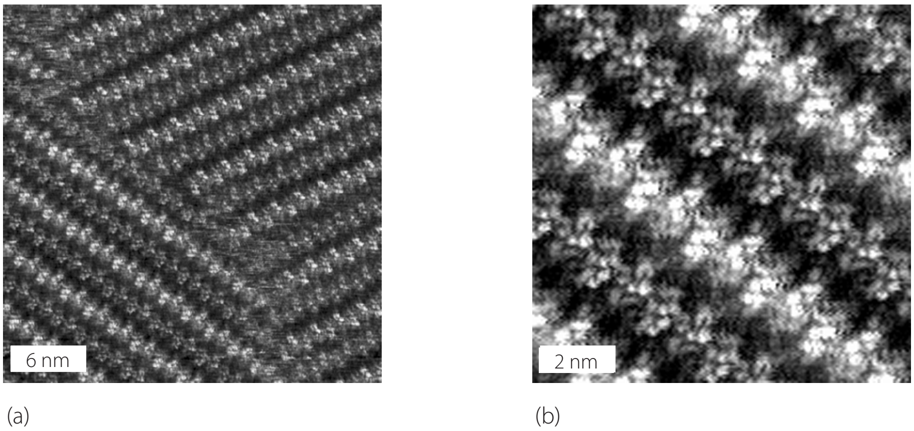

(a) (b)

Figure 6.17 STM image of a monolayer formed from **$[Co(10)_2][PF_6]_3$**. Scan parameters: 30 nm x 30 nm, U_b = −200 mV, I_t = 10 pA, averaged over 12 points.

The cobalt(III) complex **$[Co(10)_2][PF_6]_3$** showed the same pattern as the cobalt(II) **$[Co(10)_2][PF_6]_2$** complex. This observation confirmed the conclusion that the counter-ions do not take part in the self-assembly of the monolayer.

Some STM images obtained from the metal complex were of very high resolution (e. g. Figure 6.13(b)). Nevertheless it was not clear how the molecules would lie on the graphite surface and especially what happened to the counter-ions. When the counter-ions are not present, the surface must be charged, what appeared to be unlikely.

Every second row had a different pattern. By analysing well resolved images (e. g. image of Figure 6.13 (b)), it could be observed that two adjacent rows are mirrored glide planes from each other. Therefore, the plane group could be determined as *p*2*gg*; the same plane group has already been detected in the self-assembled monolayer of ligand **10**. The unit cell parameters for all monolayers showed in Figure 6.10–Figure 6.17 are a = 2.2 nm, b = 4.6 nm and α = 90°, the same parameters have already been observed for compound **10** in the 2D packing. In Figure 6.18, the monolayer of the free ligand **10** is compared with the monolayer of **$[Fe(10)_2]Cl_2$**.

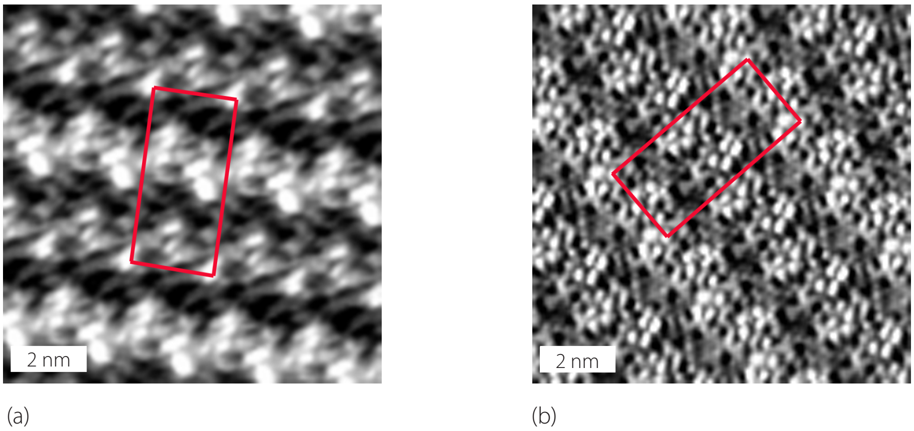

(a) (b)

Figure 6.18 Unit cells (marked in red) and STM images are compared of (a) **10** (from Figure 4.13) and (b) **$[Fe(10)_2]Cl_2$** (Figure 6.13). The unit cell parameters are identical.

Since the resolution varies in each STM measurement, the resolution can mislead the interpretation of the monolayer. It seems improbable that compounds **10** and **[Fe(10)$_2$]Cl$_2$** self-assemble with the same plane group and unit cell parameters. Therefore, it was assumed that the complexes are not stable under the scanning conditions, and the observed monolayer consisted only of the free ligand. The resolution in Figure 6.13 (b) is good enough to compare it with one layer of the crystal structure of compound **10**. Even the octyl-chains are visible, and they could be evaluated with the orientation of the octyl-chains in one layer of the crystal structure of compound **10** (Figure 6.19). Thus, the hypothesis made in Section 4.2 that the molecular packing of the monolayer on graphite is the same as in one layer of the crystal structure could be confirmed.

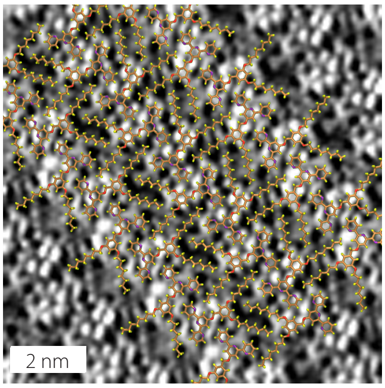

Figure 6.19 STM-image of **[Fe(10)$_2$]Cl$_2$** with overlaid layer of the crystal structure of **10**. The alkyl-chains are visible in this STM image and their orientation could therefore be compared with the alkyl-chains of the molecules in the crystal structure.

The other iron(II) and cobalt(II) complexes were not stable either under STM measurement conditions. Figure 6.20 compares a monolayer of the free ligand **13** with the two complexes **[Fe(13)$_2$][PF$_6$]$_2$** and **[Co(13)$_2$][PF$_6$]$_2$**.[43]

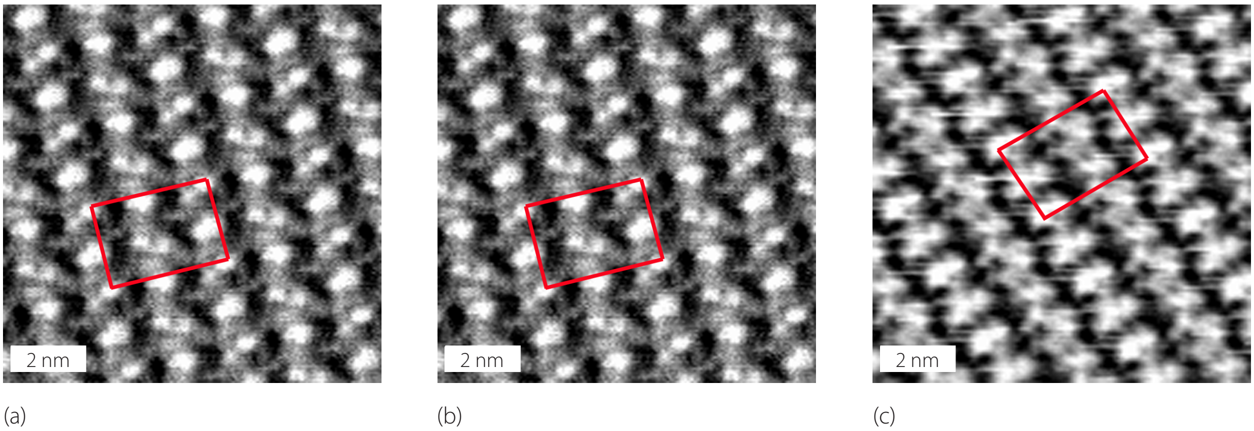

(a) (b) (c)

Figure 6.20 STM images of (a) compound **13** (Figure 4.24); (b) of **[Fe(13)$_2$][PF$_6$]$_2$**, (10 nm x 10 nm, U_b = −700 mV, I_t = 10 pA, averaged over 63 positions); and (c) of **[Co(13)$_2$][PF$_6$]$_2$**, (10 nm x 10 nm, U_b = −700 mV, I_t = 8 pA, averaged over 84 positions).

The unit cell parameters are nearly equivalent (**13**: a = 3.2 nm, b = 2.2 nm, α = 91°; **[Fe(13)$_2$][PF$_6$]$_2$**: a = 3.3 nm, b = 2.2 nm, α = 95°; and **[Co(13)$_2$][PF$_6$]$_2$**: a = 3.2 nm, b = 2.1 nm, α = 93°) with the identical plane group *pg*.

A comparison was also done between compounds **11** and **[Fe(11)$_2$]Cl$_2$**. Unfortunately, the STM images obtained from **[Fe(11)$_2$]Cl$_2$** were poor in quality. No details were visible, but since the "brick-like" pattern of the monolayer of compound **11** (Section 4.3) is unique, the detailed information were not necessary to compare the two images. As expected, **[Fe(11)$_2$]Cl$_2$** showed the same pattern (Figure 6.21) as the free ligand **11**.

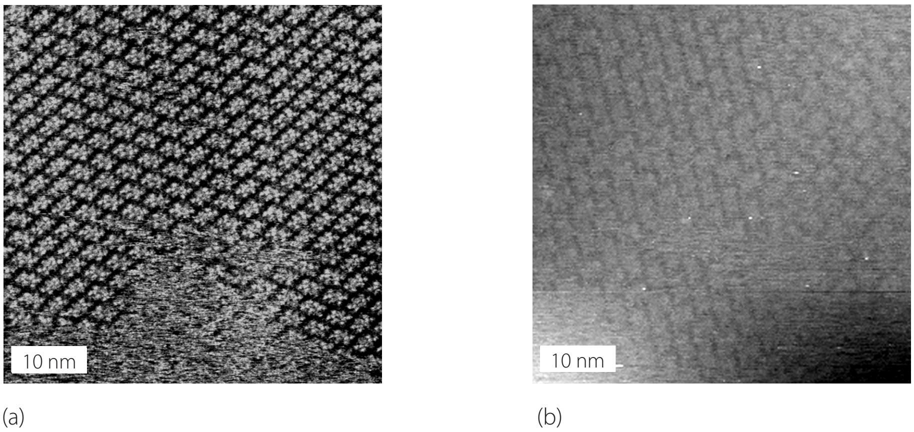

(a) (b)

Figure 6.21 STM images of (a) compound **11** (Figure 4.19); (b) of **[Fe(11)$_2$]Cl$_2$**, (50 nm x 50 nm, U_b = −700 mV, I_t = 8 pA).

Very seldom, other patterns are observed for the iron(II) complexes. In Figure 6.22, such an image resulting from a monolayer of **[Fe(10)$_2$][BPh$_4$]$_2$** is shown.

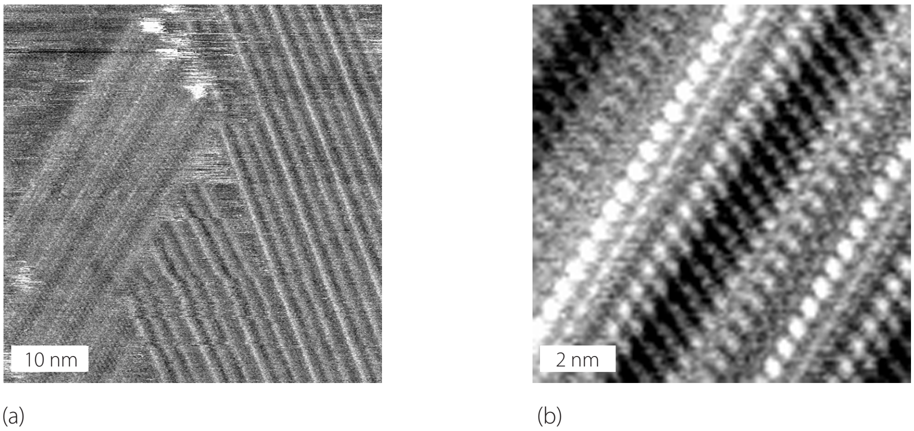

(a) (b)

Figure 6.22 STM image of a monolayer of **[Fe(10)$_2$][BPh$_4$]$_2$**. Scan parameters: (a) 50 nm x 50 nm, U_b = −700 mV, I_t = 8 pA. (b) shows an expanded (19 nm x 10 nm) and averaged (over 61 positions) image of the left domain of (a).

Drift in the images made it impossible to record images of the quality used for the conformational analysis.

The aim of the study was to assemble monolayers of the complexes on the surface which survive the STM conditions. Ruthenium(II) bis(tpy) compounds are kinetically more stable than the corresponding iron(II) or cobalt(II) complexes.[2] Images of a similar pattern as in Figure 6.22 were observed when the monolayer was formed from an acetonitril solution of $[\mathbf{Ru}(\mathbf{10})_2][\mathbf{PF}_6]_2$ side by side to the pattern of the free ligand **10** (Figure 6.23).

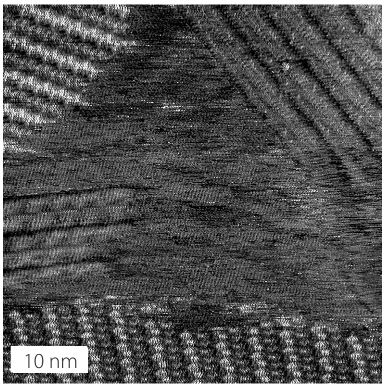

Figure 6.23 At the lower half of the image and at the upper left corner the pattern of the free ligand **10** is observable. At the upper right corner a domain of a lamellar pattern similar to the pattern observed in Figure 6.22 is visible. Scan parameters: 50 nm x 50 nm, $U_b = -200$ mV, $I_t = 8$ pA.

It was anticipated that the octyl chains are in an extended conformation parallel to the graphite surface, with adjacent chains lying parallel to one another with a periodicity of 0.30 nm.[54] Models were constructed using standard chemical modelling packages in which the benzyl and octyl-groups of the compound are constrained to lie as close to coplanar as possible. Intermolecular contacts were determined by van der Waals dimensions and maximising interdigitation of the octyl groups. Single-crystal X-ray structural data (Figure 6.6) were used as a starting point for modelling intermolecular interactions.

More detailed analysis came from high-resolution averaged, dislocation free images; an example of a 10 nm x 10 nm image of the lamellar domains is shown in Figure 6.24.

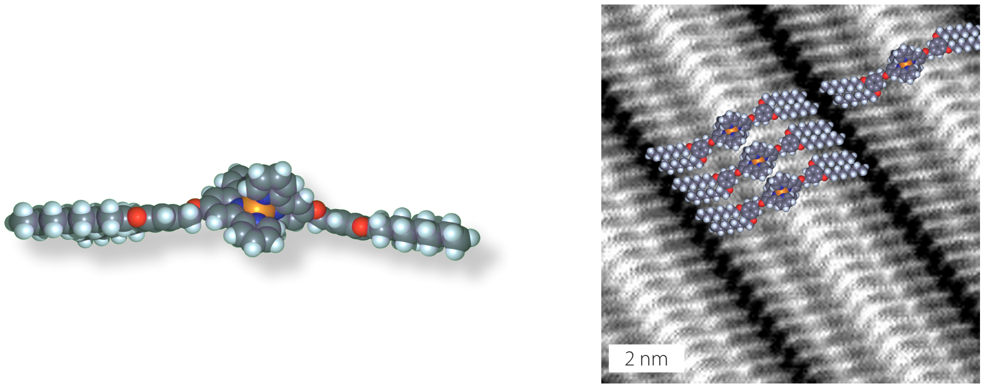

(a) (b)

Figure 6.24 (a) side-view of the molecular model for $\mathbf{[Ru(10)_2]^{2+}}$ used for superimposing the STM image. (b) An averaged (over 17 positions) and expanded STM image of the lamellar arrangement of $\mathbf{[Ru(10)_2][PF_6]_2}$ with a suggested model of the molecular arrangement. (10 nm x 10 nm, $U_b = -200$ mV, $I_t = 10$ pA).

The contrast in the STM image was dominated by the interdigitated octyl chains, whilst in the other work (Chapter 3–Chapter 5) of Fréchet dendrons, the aromatic residues dominated. In the case of $\mathbf{[Ru(10)_2][PF_6]_2}$, one of the Fréchet phenyl rings showed brighter contrast than the other. Generally, contrast in a STM image is caused by interference effects between frontier orbitals (as well as other orbitals close to the Fermi level) of the particular part of the molecule and the through-space electronic current between the tip and the substrate. In the case of self-assembled monolayers of planar molecules lying parallel to the surface, the latter effect is not relevant, but $\mathbf{[Ru(10)_2][PF_6]_2}$ is a three-dimensional molecular structure in which the two tpy ligand domains are orthogonal and even if one were to lie parallel to the graphite, the other would be orthogonal (Figure 6.24(a)). In such cases, both the electronic structure and the distance between a particular part of the molecule and the surface is crucial in determining the tunnelling current and hence the contrast in the image.

The periodicity within a row (and consequently the distance between the ruthenium centres of adjacent molecules) in the lamellar phases was approximately 1.0 nm. It was assumed that the tunnelling current and images only arised from the $\mathbf{[Ru(10)_2]}^{2+}$; as soon as the Ru^{2+} was close to the substrate, electrostatic charge induction in the graphite surface would compensate for the di-cation, regardless of the absolute bias of the graphite. Thus, the molecule could move on the surface acting close to being neutrally charged (the compensating charge in the graphite moved along with the molecule). This resulted in alternating layers of cations and anions. The binding of the dendritic wedges to the surface (through π–π- and methylene-graphite interactions) would be much stronger than those of the PF_6^- counter ions, and so the first layer would be cationic. It was suggested that when the STM tip, with its strong inhomogeneous electric field was close to the surface, the second (anionic) layer was repelled. Assuming an extended conformation for the octyl-chains, $\mathbf{[Ru(10)_2][PF_6]_2}$ had remarkably little conformational freedom: the $\mathbf{[Ru(10)_2]}^{2+}$ unit was conformationally locked and only rotational freedom about the ether units was possible. Although it was possible to dock the $\mathbf{[Ru(10)_2]}^{2+}$ unit or the surface in such a way that the two dendrons were equidistant from the surface, the graphite-phenyl and graphite-methylene distances are not optimised. The model used in Figure 6.24 was tilted in such a way that the interactions of one dendron with the graphite were optimised; as a consequence, the second dendritic wedge was further from the surface. This model predicted that half the molecule, the aromatics would show a brighter contrast (many states for tunnelling, close to the surface) and for the other they would be rather dark (few states for tunnelling, further from the surface), exactly as seen in the image with the superimposed model in Figure 6.24.

The periodicity of the layer could be determined by examination of the domain borders (Figure 6.25). In Figure 6.25, the domain borders are also visible. The ends of the rows are linked together with the ends of the rows of the next domain and therefore the ends of the domains are quite sharp and the domains quite rigid.

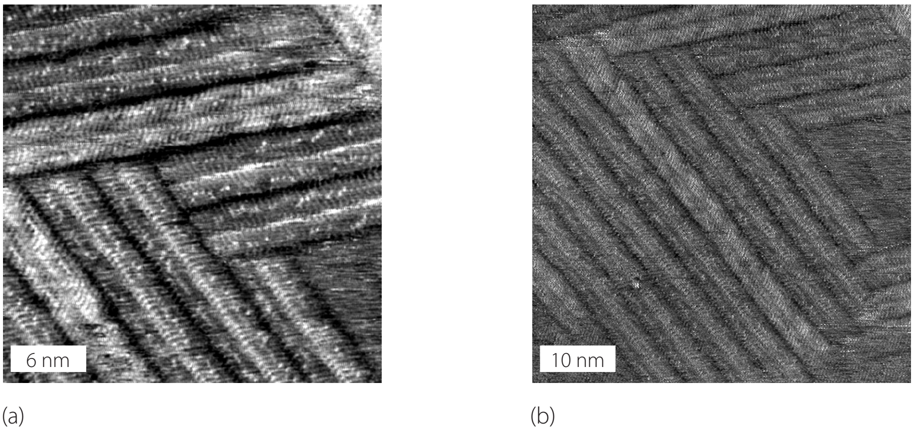

(a)

(b)

Figure 6.25 Two different images of domain borders. The rows of neighbouring domains are linked together. Scan parameters: (a) 30 nm x 30 nm, $U_b = -200$ mV, $I_t = 10$ pA; (b) 50 nm x 50 nm, $U_b = -200$ mV, $I_t = 9$ pA.

In Figure 6.25, dislocated rows are visible. In Figure 6.26, the dislocated row of the lamellar phase was modelled and appeared to arise from the presence of rows of complex cations with mirrored orientations on the graphite surface.

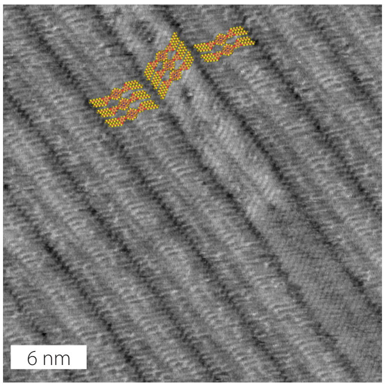

Figure 6.26 STM image with a dislocated row arising from cations having a mirrored orientation on the surface.

The fact that there was no statistical arrangement (1:1) of the two orientations could show that the orientation of each row is influenced by the orientation of the adjacent row.

The self-assembled monolayer of the ruthenium(II) complex of ligand **13** was investigated with the expectation that another pattern than that shown in Figure 6.20 of the free ligand would be visible. In fact, apart of domains with the pattern of the free ligand **13** (Figure 6.27) an additional pattern was observed.

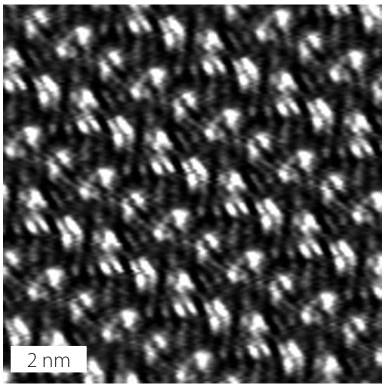

Figure 6.27 The pattern of the free ligand was also observed in the monolayer of **[Ru(13)$_2$][PF$_6$]$_2$**.

The new pattern resembled the monolayer of **[Ru(10)$_2$][PF$_6$]$_2$**. An image showing two different domains is displayed in Figure 6.28.

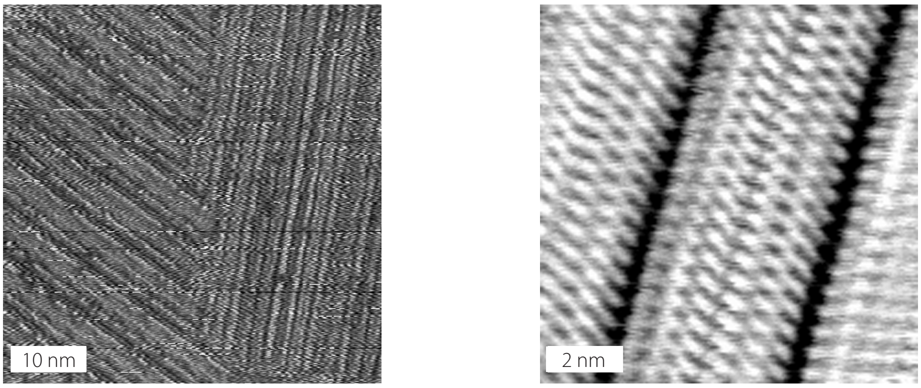

(a) (b)

Figure 6.28 An STM image of a monolayer of **[Ru(13)$_2$][PF$_6$]$_2$**. Scan parameters: (a) 50 nm x 50 nm, $U_b = -800$ mV, $I_t = 7$ pA; (b) an averaged (over 23 positions) and expanded image (10 nm x 10 nm, $U_b = -700$ mV, $I_t = 8$ pA).

The analysis of the image was quite demanding and it has not been completed. However, a preliminary molecular arrangement was suggested and is shown in Figure 6.29.

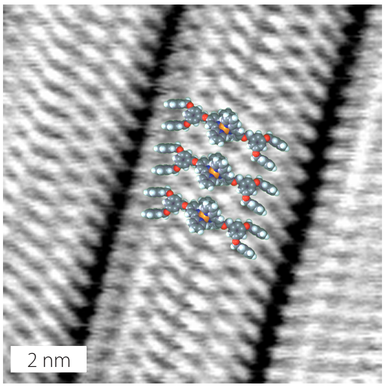

Figure 6.29 The STM image of Figure 6.28(b) with overlaid molecules. The thermal drift of the domain spread the whole image and therefore the molecules appear too small.

In this arrangement, the terminal phenyl groups are orthogonal to the graphite surface and are stabilised through π-stacking interactions. Drift of the domains could not be avoided ant therefore the dimensions in Figure 6.29 are not correct. More images of domains without drift are necessary to complete the analysis of the packing arrangement.

Furthermore, the 2D molecular assembly of $[\mathbf{Ru}(\mathbf{11})_2]\mathbf{Cl_2}$ has to be studied to get more information about the arrangement of bis(tpy) ruthenium(II) complexes on graphite.

6.2.2 Self-assembled monolayers of bis(alkyne) platinum(II) complexes

In addition to the studies of bis(tpy) metal complexes on surface, the 2D ordering of the organometallic species **17** and **21** (Scheme 6.10) were investigated using STM.

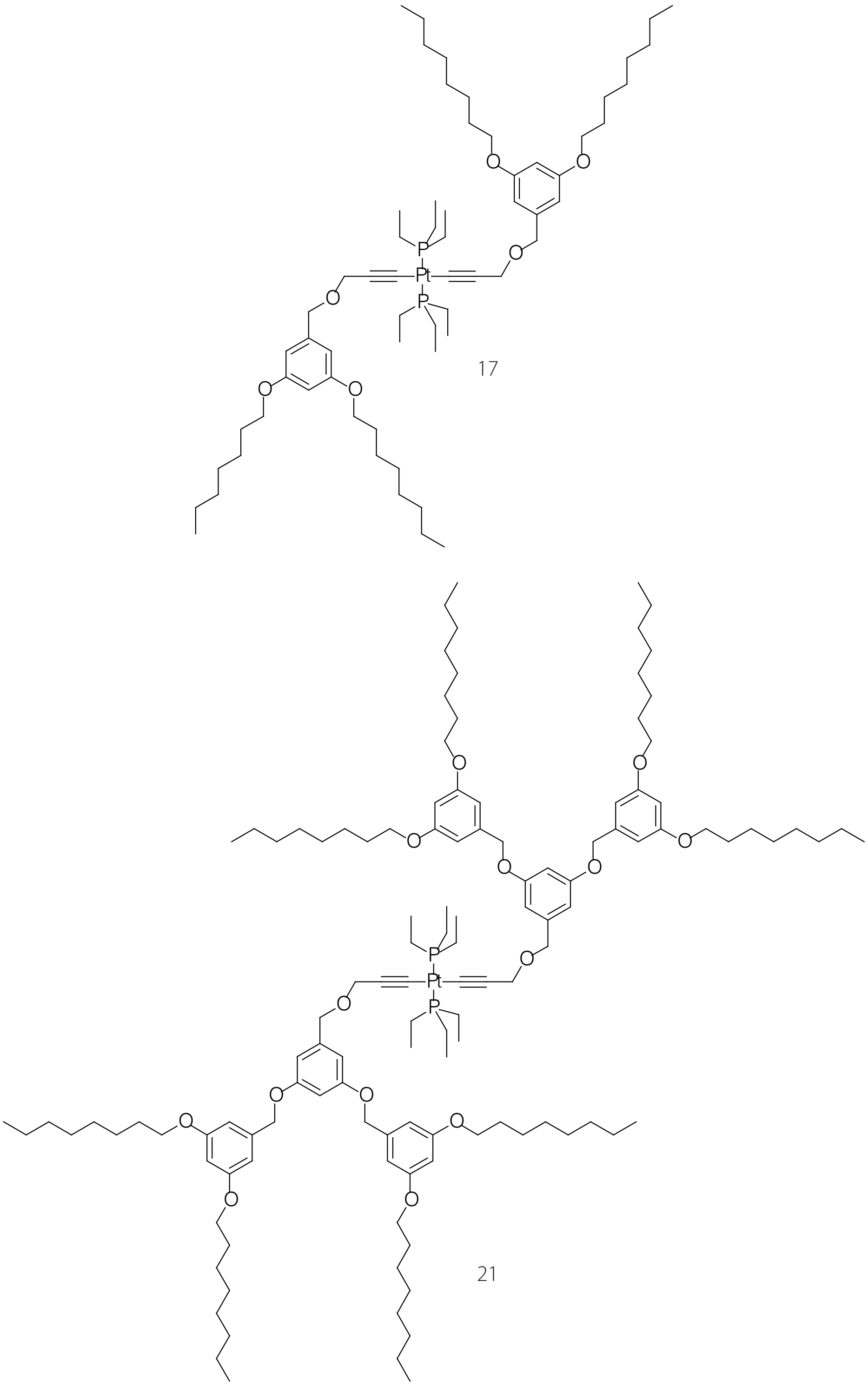

17

21

Scheme 6.10 The two *trans*-bis(alkynyl) platinum(II) compounds **17** and **21**.

Evaporation of a droplet of a solution of the platinum(II) species **17** in hexane gave self-assembled monolayers with primarily lamellar domains (Figure 6.30) with dimensions in the range 20 nm x 20 nm up to 100 nm x 100 nm.

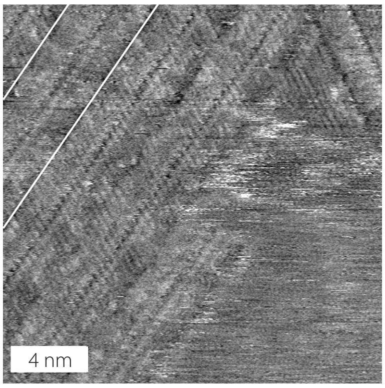

Figure 6.30 This STM image of a monolayer of **17** shows a border of a domain with a dislocated row (marked in white). Scan parameters: 20 nm x 20 nm, $U_b = -800$ mV, $I_t = 8$ pA.

As seen before, the rows reflect the threefold symmetry of the underlying graphite surface. As for $[\mathbf{Ru(11)_2}][\mathbf{PF_6}]_2$, rotational dislocation rows were observed (see Figure 6.30 top left corner). In contrast to the core of $[\mathbf{Ru(11)_2}][\mathbf{PF_6}]_2$, the C≡C−Pt−C≡C unit states available for tunnelling and is easily visible as a symmetric unit in the STM images. A superimposition of the best-fit modelled arrangement based upon a planar monolayer with the C≡C−Pt−C≡C unit coplanar with the surface is presented in Fig. 6.31.

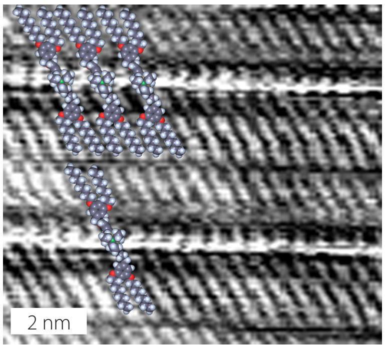

Figure 6.31 An expanded and averaged STM image of **17** with superimposed molecular models. 20 nm x 20 nm, $U_b = -800$ mV, $I_t = 8$ pA, averaged over 25 positions.

As has already been observed for other bis(triethylphosphine) platinum(II) species on HOPG,[6] the square-planar platinum(II) complexes did not lie parallel but orthogonal to the surface on the ethyl chains of one phosphine ligand.

Repeated imaging of the same region of monolayers of **17** revealed that over time larger domains grow at the cost of smaller domains and that kink imperfections in the lamellar phase become less common. This observation indicated that the self-assembly is not only defect intolerant, but that they are also to some extend self-repairable.

To obtain self-assembled monolayers of compound **21** was more demanding. No regular pattern of a monolayer could be observed by simple solution casting method (evaporate one drop of a 0.2 mM hexane solution on the surface). Annealing over a period of 1 hour in 90 °C was necessary to get an ordered monolayer. An expanded image is shown in Figure 6.32.

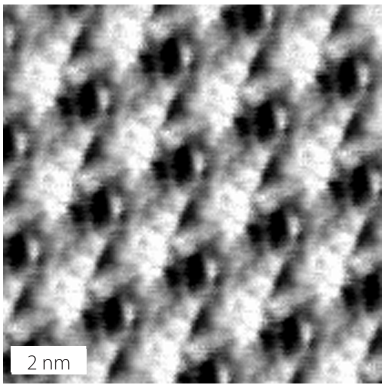

Figure 6.32 An expanded and averaged STM image of the pattern observed by annealing **21** on HOPG. Scan parameters: 10 nm x 10 nm, $U_b = -1000$ mV, $I_t = 12$ pA, averaged over 60 positions.

The STM images were not too well resolved. The $p1$ plane group with $Z = 1$ revealed that the molecules always had the same conformation and orientation. It was suggested that the square-planar complex was placed orthogonal to the graphite surface.[6] Many different molecular arrangements were superimposed the image. The best fit is shown in Figure 6.33.

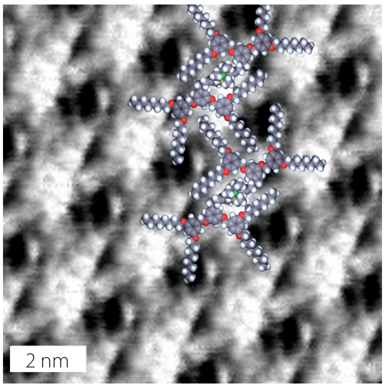

Figure 6.33 One possible molecular arrangement is superimposed the STM image of Figure 6.32.

Unfortunately, due to time limitations, the 2D self-assembling of compound **19** could not be studied during the course of this thesis. The self-assembly of **19** with the peripheral benzyl groups could give further information about the molecular arrangements of this type of organometallic compounds on HOPG.

6.3 Experimental part

Compound 17: Crude **2** (500 mg, ca. 80% pure, 1.10 mmol), propargylic alcohol (84.1 mg, 1.50 mmol), KOH (400 mg, 7.10 mmol) and n-$\mathrm{Bu_4NI}$ (35 mg, 100 µmol) were stirred vigorously in ethyl acetate (500 µL) and water (600 µL) at room temperature for 16 hours. Water (20 mL) was added and the mixture extracted three times with dichloromethane (30 mL). The combined organic layers were dried ($\mathrm{Na_2SO_4}$) and evaporated. Chromatography on silica (hexane:ethyl acetate 20:1) yielded **16** as a yellow oil (340 mg, 844 µmol, 77%). To a degassed suspension of *trans*-$\mathrm{PtI_2(PEt_3)_2}$ (68.7 mg, 100 µmol) and compound **16** (150 mg, 370 µmol) in $\mathrm{NEt_3}$ (3 mL), CuI (0.1 mg, 0.5 µmol; purified with water and acetone before use) was added and stirred at room temperature under a nitrogen atmosphere for 30 hours. $\mathrm{NEt_3}$ (10 mL) was added and the precipitate filtered off and washed with hexane. The solvent of the filtrate was removed *in vacuo*. Chromatography on silica (dichloromethane:methanol: triethylamine 99:0.5:0.5 → 99:3:0.5) afforded **17** as a yellow oil (113 mg, 91.5 µmol, 92%). ^{1}H NMR (500 MHz, d_6-benzene): δ 6.86 (d, J = 2.3 Hz, 4H, $\mathrm{H}^{2\mathrm{A}}$), 6.66 (t, J = 2.3 Hz, 2H, $\mathrm{H}^{4\mathrm{A}}$), 4.81 (s, 4H, $\mathrm{H}^{\mathrm{OC}\mathit{H}_2\mathrm{A}}$), 4.53 (t, $J^{H,P}$ = 1.4 Hz, 4H, $\mathrm{H}^{\text{alkyne-}\mathrm{C}\mathit{H}_2\mathrm{O}}$), 3.79 (t, J = 6.5 Hz, 8H, $\mathrm{H}^{\mathrm{OC}\mathit{H}_2\mathrm{CH}_2}$), 2.03 (qd, J = 7.6, $J^{H,P}$ = 7.6 Hz, 4H, $\mathrm{H}^{\mathrm{PC}\mathit{H}_2\mathrm{CH}_3}$), 1.66 (tt, J = 6.6, 6.5 Hz, 8H, $\mathrm{H}^{\mathrm{OCH}_2\mathrm{C}\mathit{H}_2}$), 1.36 (tt, J = 6.6, 6.5 Hz, 8H, $\mathrm{H}^{\mathrm{OCH}_2\mathrm{CH}_2\mathrm{C}\mathit{H}_2}$), 1.20−1.30 (m, 32H, $\mathrm{H}^{(\mathrm{C}\mathit{H}_2)_4}$), 1.11 (td, J = 7.6, $J^{H,P}$ =7.6 Hz, 6H, $\mathrm{H}^{\mathrm{PCH}_2\mathrm{C}\mathit{H}_3}$), 0.88 ppm (t, J = 7.0 Hz, 12H, $\mathrm{H}^{\mathrm{C}\mathit{H}_3}$). ^{13}C NMR (125 MHz, d_6-benzene): δ 160.8, 141.9, 105.9, 103.5 ($J^{C,Pt}$ = 266 Hz), 101.8 ($J^{C,Pt}$ = 950 Hz, $J^{C,P}$ = 14.6 Hz), 100.6, 70.5, 67.6, 60.3, 32.2, 29.8 (2 overlapping signals), 29.7, 26.5, 23.0, 16.9 ($J^{C,P}$ = 17.5 Hz), 14.3, 8.5 ppm. ^{31}P NMR (202 MHz, d_6-benzene): δ 11.8 (s+d, $J^{P,Pt}$ = 2409 Hz). ^{195}Pt NMR (108 MHz, d_6-benzene): δ −340 ppm (t, $J^{Pt,P}$ = 2407 Hz). IR (neat): ($\tilde{\nu}$, $\mathrm{cm^{-1}}$) 2924 s, 2854 m, 2114 m, 1589 s, 1458 s, 1381 m, 1342 m, 1157 s, 1057 m, 1034 m, 833 w, 734 m. MS (ESI+): *m/z* 1258 $[\mathrm{M + Na}]^+$. Anal. Calcd for $\mathrm{C_{64}H_{112}O_6P_2Pt}$: C, 62.62; H, 9.14; N, 0.00; found: C, 62.52; H, 9.10; N, 0.0%.

Compound 19: Compound 7 (239 mg, 600 µmol), propargylic alcohol (29.1 mg, 519 µmol), KOH (247 mg, 4.40 mmol) and 18-crown-6 (13.2 mg, 50 µmol) were stirred vigorously in toluene (1 mL) and water (1 mL) at room temperature for 20 hours. Water (50 mL) was added and the mixture extracted three times with ethyl acetate (30 mL). The combined organic layers were dried ($\mathrm{Na_2SO_4}$) and evaporated. Chromatography on silica (hexane:ethyl acetate 3:1) yielded **18** as a yellow oil (122 mg, 340 µmol, 66%). To a degassed suspension of *trans*-$\mathrm{PtI_2(PEt_3)_2}$ (68.7 mg, 100 µmol) and compound **18** (122 mg, 340 µmol) in $\mathrm{NEt_3}$ (3 mL), CuI (0.05 mg, 0.25 µmol; purified with water and acetone before use) was added and stirred at room temperature under a nitrogen atmosphere for 10 hours. $\mathrm{NEt_3}$ (15 mL) was added and the precipitate filtered off and washed with hexane. The solvent of the filtrate was removed *in vacuo*. Chromatography on silica (dichloromethane:methanol 100:0 → 96:4) afforded **19** as a yellow oil (55 mg, 47.9 µmol, 48%). ^{1}H NMR (250 MHz, $\mathrm{CDCl_3}$): δ 7.31−7.44 (m, 20H, $\mathrm{H^{Ph}}$), 6.62 (d, J = 2.4 Hz, 4H, $\mathrm{H^{2A}}$), 6.52 (t, J = 2.2 Hz, 2H, $\mathrm{H^{4A}}$), 5.02 (s, 8H, $\mathrm{H}^{\mathrm{OC}H_2\mathrm{Ph}}$), 4.56 (s, 4H, $\mathrm{H}^{\mathrm{OC}H_2\mathrm{A}}$), 4.56 (t, $J^{H,P}$ = 1.5 Hz, 4H, $\mathrm{H}^{\mathrm{alkyne\text{-}C}H_2\mathrm{O}}$), 2.07 (qd, J = 7.6, $J^{H,P}$ = 7.6 Hz, 4H, $\mathrm{H}^{\mathrm{PC}H_2\mathrm{CH_3}}$), 1.13 (td, J = 7.8, $J^{H,P}$ =7.8 Hz, 6H, $\mathrm{H}^{\mathrm{PCH_2C}H_3}$). ^{13}C NMR (125 MHz, d_6-benzene): δ. ^{31}P NMR (101 MHz, $\mathrm{CD_2Cl_2}$): δ 11.8 (s+d, $J^{P,Pt}$ = 2379 Hz). IR (neat): ($\tilde{\nu}$, cm^{-1}) 2924 s, 2870 m, 2114 m, 1589 s, 1450 m, 1373 m, 1342 m, 1150 s, 1057 m, 1034 s, 833 w, 733 s, 694 m. MS (ESI+): *m/z* 1169 $[\mathrm{M + Na}]^+$.

Compound 21: NaH (12.0 mg, 55%, 275 µmol) was added at 0 °C to a solution of propargylic alcohol (16.2 mg, 289 µmol) in dry THF (20 mL). The suspension was allowed to warm up to room temperature and stirred for 3 hours. Crude **5** (350 mg, ca. 80% pure, 307 µmol) was added and stirred for additional 14 hours at room temperature. Water (2 mL) was added, followed by conc. aqueous HCl (1 mL). The solvents were removed *in vacuo*. Chromatography on silica (hexane:ethyl acetate 7:1) yielded **20** as a yellow oil (112 mg, 128 µmol, 47%). To a degassed suspension of *trans*-$\mathrm{PtI_2(PEt_3)_2}$ (34.3 mg, 50.0 µmol) and compound **20** (110 mg, 127 µmol) in $\mathrm{NEt_3}$ (1.5 mL), CuI (0.05 mg, 0.025 µmol; purified with water and acetone before use) was added and stirred at room temperature under a nitrogen atmosphere for 15 hours. The solvent was removed *in vacuo*. Chromatography on silica (dichloromethane:methanol:triethylamine 99:0:0.5 → 99:3:0.5) afforded **21** as a yellow oil (86.0 mg, 39.6 µmol, 79%). ^{1}H NMR (500 MHz, d_6-benzene): δ 6.94 (d, J = 2.2 Hz, 4H, $\mathrm{H^{2A}}$), 6.77 (t, J = 2.2 Hz, 2H, $\mathrm{H^{4A}}$), 6.72 (d, J = 2.2 Hz, 8H, $\mathrm{H^{2B}}$), 6.64 (t, J = 2.2 Hz, 4H, $\mathrm{H^{4B}}$), 4.82 (s, 8H,$\mathrm{H}^{\mathrm{OC}H_2\mathrm{B}}$), 4.76 (s, 4H, $\mathrm{H}^{\mathrm{OC}H_2\mathrm{A}}$), 4.50 (s, 4H, $\mathrm{H}^{\mathrm{alkyne\text{-}C}H_2\mathrm{O}}$), 3.71 (t, J = 6.5 Hz, 16H, $\mathrm{H}^{\mathrm{OC}H_2\mathrm{CH_2}}$), 2.00 (qd, J = 7.6, $J^{H,P}$ = 7.6 Hz, 4H, $\mathrm{H}^{\mathrm{PC}H_2\mathrm{CH_3}}$), 1.63 (tt, J = 6.6, 6.5 Hz, 16H, $\mathrm{H}^{\mathrm{OCH_2C}H_2}$), 1.33 (tt, J = 6.6, 6.5 Hz, 16H, $\mathrm{H}^{\mathrm{OCH_2CH_2C}H_2}$), 1.19−1.29 (m, 64H, $\mathrm{H}^{(\mathrm{C}H_2)_4}$), 1.08 (td, J = 8.0, $J^{H,P}$ =8.0 Hz, 6H, $\mathrm{H}^{\mathrm{PCH_2C}H_3}$), 0.88 ppm (t, J = 7.0 Hz, 24H, $\mathrm{H}^{\mathrm{C}H_3}$). ^{13}C NMR (125 MHz, d_6-benzene): δ 161.2, 160.7, 142.4, 140.0, 106.9, 106.0, 103.7 ($J^{C,Pt}$ = 266 Hz), 102.1 ($J^{C,Pt}$ = 954 Hz, $J^{C,P}$ = 14.4 Hz), 101.5, 101.4, 70.6, 70.2, 68.0, 60.6, 32.2, 29.7, 29.7 (2 overlapping signals), 26.4, 23.1, 16.7 ($J^{C,P}$ = 17.5 Hz), 14.3, 8.5 ppm. ^{31}P NMR (101 MHz, d_6-benzene): δ 11.8 (s+d, $J^{P,Pt}$ = 2410 Hz). ^{195}Pt NMR (108 MHz, d_6-benzene): δ −346 ppm (t, $J^{Pt,P}$ = 2399 Hz). IR (neat): ($\tilde{\nu}$, cm^{-1}) 2924 s, 2854 m, 2114 w, 1597 s, 1450 m, 1342 m, 1157 s, 1049 m, 833 w, 609 m. MS (MALDI-TOF+): *m/z* 2194 $[\mathrm{M + Na}]^+$, 2210 $[\mathrm{M + K}]^+$. Anal. Calcd for $\mathrm{C_{124}H_{200}O_{14}P_2Pt}$: C, 68.57; H, 9.28; N, 0.00; found: C, 68.38; H, 9.16; N, 0.0%.

[Fe(10)$_2$]Cl$_2$: Ligand **10** (248 mg, 416 µmol) and $FeCl_2·4H_2O$ (41.2 mg, 208 µmol) were stirred in ethanol:dichloromethane (2:1, 5 mL) at room temperature for 8 hours. The colour of the solution turned immediately purple. The solvent was then removed *in vacuo*. Chromatography on silica (dichloromethane:methanol 85:15) afforded **[Fe(10)$_2$]Cl$_2$** as a purple solid (230 mg, 175 µmol, 84%). ^{1}H NMR (400 MHz, CD_3CN): δ 8.63 (s, 4H, H^{3B}), 8.50 (d, J = 7.6 Hz, 4H, H^{6A}), 7.86 (dd, J = 7.6, 5.6 Hz, 4H, H^{5A}), 7.14 (d, J = 5.6 Hz, 4H, H^{3A}), 7.06 (dd, J = 7.2, 5.1 Hz, 4H, H^{4A}), 6.84 (d, J = 2.0 Hz, 4H, H^{2C}), 6.54 (t, J = 2.0 Hz, 2H, H^{4C}), 5.65 (s, 4H, $H^{\mathrm{OC}\mathit{H}_2\mathrm{C}}$), 4.05 (t, J = 6.6 Hz, 8H, $H^{\mathrm{OC}\mathit{H}_2\mathrm{CH}_2}$), 1.79 (tt, J = 7.0, 6.6 Hz, 8H, $H^{\mathrm{OCH}_2\mathrm{C}\mathit{H}_2}$), 1.47 (tt, J = 7.0, 7.0 Hz, 8H, $H^{\mathrm{OCH}_2\mathrm{CH}_2\mathrm{C}\mathit{H}_2}$), 1.21–1.39 (m, 32H, $H^{(\mathrm{C}\mathit{H}_2)_4}$), 0.88 ppm (t, J = 6.8 Hz, 12H, $H^{\mathrm{C}\mathit{H}_3}$). IR (neat): ($\tilde{\nu}$, cm^{-1}) 2924 s, 2854 m, 1605 s, 1466 m, 1358 m, 1296 w, 1211 m, 1157 s, 1066 m, 987 m, 833 m. MS (ESI+): *m/z* 623 $[M - 2Cl]^{2+}$. UV-vis (CH_3CN): λ/nm (ε/M^{-1} cm^{-1}) 556 (24000), 358 (13000), 272 (130000), 241 (110000). Anal. Calcd for $C_{76}H_{98}N_6O_6Cl_2Fe·3H_2O$: C, 66.51; H, 7.64; N, 6.12; found: C, 66.45; H, 7.47; N, 6.12%.

[Fe(10)$_2$][BF$_4$]$_2$: To a solution of ligand **10** (37.0 mg, 62.1 µmol) in ethanol:dichloromethane (3:1, 5 mL), a solution of $Fe(BF_4)_2·6H_2O$ (10.5 mg, 31.0 µmol) in ethanol (2 mL) was added at room temperature. The colour of the solution turned purple. The reaction mixture was stirred at room temperature for another hour. The solvent was then removed *in vacuo*. Chromatography on silica (dichloromethane:methanol 97:3) afforded **[Fe(10)$_2$][BF$_4$]$_2$** as a purple solid (86.0 mg, 39.6 µmol, 79%). ^{1}H NMR (400 MHz, CD_3CN): δ 8.54 (s, 4H, H^{3B}), 8.42 (d, J = 7.6 Hz, 4H, H^{6A}), 7.87 (dd, J = 7.6, 5.6 Hz, 4H, H^{5A}), 7.13 (d, J = 5.6 Hz, 4H, H^{3A}), 7.07 (dd, J = 7.6, 5.6 Hz, 4H, H^{4A}), 6.82 (d, J = 2.2 Hz, 4H, H^{2C}), 6.55 (t, J = 2.2 Hz, 2H, H^{4C}), 5.61 (s, 4H, $H^{\mathrm{OC}\mathit{H}_2\mathrm{C}}$), 4.05 (t, J = 6.6 Hz, 8H, $H^{\mathrm{OC}\mathit{H}_2\mathrm{CH}_2}$), 1.79 (tt, J = 7.0, 6.6 Hz, 8H, $H^{\mathrm{OCH}_2\mathrm{C}\mathit{H}_2}$), 1.47 (tt, J = 7.0, 7.0 Hz, 8H, $H^{\mathrm{OCH}_2\mathrm{CH}_2\mathrm{C}\mathit{H}_2}$), 1.25–1.39 (m, 32H, $H^{(\mathrm{C}\mathit{H}_2)_4}$), 0.88 ppm (t, J = 6.8 Hz, 12H, $H^{\mathrm{C}\mathit{H}_3}$). ^{13}C NMR (100 MHz, CD_3CN): δ 168.6, 161.8, 161.8, 158.9, 154.3, 139.4, 138.6, 128.1, 124.4, 112.5, 107.3, 101.9, 72.7, 69.0, 32.5, 30.0, 29.9, 29.9, 26.7, 23.3, 14.3 ppm. IR (neat): ($\tilde{\nu}$, cm^{-1}) 2924 s, 2854 m, 1605 s, 1466 m, 1389 w, 1358 w, 1296 w, 1211 m, 1165 s, 1057 s, 987 m, 833 m. MS (ESI+): *m/z* 623 $[M - 2BF_4]^{2+}$. Anal. Calcd for $C_{76}H_{98}N_6O_6B_2F_8Fe$: C, 64.23; H, 6.95; N, 5.91; found: C, 64.05; H, 7.02; N, 5.82%.

[Fe(10)$_2$][PF$_6$]$_2$: Ligand **10** (62.0 mg, 104 µmol) and $FeCl_2·4H_2O$ (10.3 mg, 52 µmol) were refluxed in ethanol (30 mL) for 30 minutes. The colour of the solution turned immediately purple. The solvent was concentrated to ≈10 mL and NH_4PF_6 (35.0 mg, 215 µmol) in methanol (5 mL) was added. The so-formed precipitate was collected by filtration and washed with methanol (10 mL) affording **[Fe(10)$_2$][PF$_6$]$_2$** (55.0 mg, 38.6 µmol, 74%). ^{1}H NMR (500 MHz, CD_3CN): δ 8.54 (s, 4H, H^{3B}), 8.42 (d, J = 7.2 Hz, 4H, H^{6A}), 7.87 (dd, J = 7.2, 5.1 Hz, 4H, H^{5A}), 7.14 (d, J = 5.1 Hz, 4H, H^{3A}), 7.07 (dd, J = 7.2, 5.1 Hz, 4H, H^{4A}), 6.82 (d, J = 2.2 Hz, 4H, H^{2C}), 6.55 (t, J = 2.2 Hz, 2H, H^{4C}), 5.61 (s, 4H, H^{OCH_2C}), 4.06 (t, *J* = 6.5 Hz, 8H, $H^{OCH_2CH_2}$), 1.79 (tt, *J* = 6.8, 6.5 Hz, 8H, $H^{OCH_2CH_2}$), 1.47 (tt, *J* = 6.8, 6.8 Hz, 8H, $H^{OCH_2CH_2CH_2}$), 1.25–1.39 (m, 32H, $H^{(CH_2)_4}$), 0.88 ppm (t, *J* = 7.0 Hz, 12H, H^{CH_3}). ^{13}C NMR (125 MHz, CD_3CN): δ 168.6, 161.9, 161.8, 159.0, 154.4, 139.5, 138.6, 128.2, 124.5, 112.6, 107.4, 102.0, 72.8, 69.1, 32.6, 30.1, 30.0, 29.9, 26.8, 23.4, 14.4 ppm. IR (neat): ($\tilde{\nu}$, cm^{-1}) 2924 s, 2854 m, 1605 s, 1466 m, 1358 m, 1211 m, 1157 s, 1057 m, 987 m, 825 s, 787 m. MS (ESI+): *m/z* 623 $[M - 2PF_6]^{2+}$. UV-vis (CH_3CN): λ/nm (ε/M^{-1} cm^{-1}) 555 (20000), 359 (8000). Anal. Calcd for $C_{76}H_{98}N_6O_6P_2F_6Fe{\cdot}1H_2O$: C, 58.69; H, 6.48; N, 5.40; found: C, 58.87; H, 6.25; N, 5.54%.

[Fe(10)$_2$][BPh$_4$]$_2$: To a solution of **[Fe(10)$_2$]Cl$_2$** (53.0 mg, 104 μmol) in ethanol (10 mL), a solution of $Na(BPh_4)_2$ (66.0 mg, 99.8 μmol) in ethanol (6 mL) was added. A purple precipitate was formed. After standing for 1 hour, the precipitate was collected by filtration and washed with methanol (20 mL) affording **[Fe(10)$_2$][BPh$_4$]$_2$** (66.0 mg, 34.3 μmol, 33%). ^{1}H NMR (250 MHz, CD_3CN): δ 8.51 (s, 4H, H^{3B}), 8.38 (d, *J* = 7.7 Hz, 4H, H^{6A}), 7.83 (dd, *J* = 7.7, 4.7 Hz, 4H, H^{5A}), 7.22–7.29 (m, 16H, H^{2Ph}), 7.11 (d, *J* = 4.7 Hz, 4H, H^{3A}), 7.02 (dd, *J* = 7.7, 4.7 Hz, 4H, H^{4A}), 6.97 (t, 16H, H^{3Ph}), 6.78–6.58 (m, 12H, H^{2C+4Ph}), 6.55 (t, *J* = 2.2 Hz, 2H, H^{4C}), 5.59 (s, 4H, H^{OCH_2C}), 4.05 (t, *J* = 6.5 Hz, 8H, $H^{OCH_2CH_2}$), 1.79 (tt, *J* = 7.0, 6.5 Hz, 8H, $H^{OCH_2CH_2}$), 1.47 (tt, *J* = 7.0, 7.0 Hz, 8H, $H^{OCH_2CH_2CH_2}$), 1.25–1.39 (m, 32H, $H^{(CH_2)_4}$), 0.88 ppm (t, *J* = 6.7 Hz, 12H, H^{CH_3}). IR (neat): ($\tilde{\nu}$, cm^{-1}) 2924 m, 2854 m, 1605 s, 1466 m, 1420 m, 1358 m, 1211 m, 1157 s, 1057 w, 987 m, 840 m, 787 m, 702 s. MS (ESI+): *m/z* 623 $[M - 2BPh_4]^{2+}$. Anal. Calcd for $C_{124}H_{138}N_6O_6B_2Fe{\cdot}2H_2O$: C, 77.49; H, 7.45; N, 4.37; found: C, 77.53; H, 7.14; N, 4.36%.

[Fe(10)$_2$]$_2$TPPSA: **[Fe(10)$_2$]Cl$_2$** (50.0 mg, 37.9 μmol) and Na$_4$TPPSA (23.5 mg, 19.0 μmol) were refluxed in methanol (100 mL) for 1 hour. After cooling down, the formed precipitate was collected by filtration and washed with water (100 mL) and ethanol (25 mL) affording **[Fe(10)$_2$]$_2$TPPSA** (53.2 mg, 15.4 μmol, 81%). ^{1}H NMR (500 MHz, d_3-DMSO): δ 9.04 (s, 8H, H^{3B}), 8.80 (d, *J* = 7.8 Hz, 8H, H^{6A}), 8.77 (s, 8H, H^{3D}), 8.15 (d, *J* = 8.0 Hz, 8H, H^{3E}), 8.05 (d, *J* = 8.0 Hz, 8H, H^{2E}), 7.91 (dd, *J* = 7.8, 5.6 Hz, 8H, H^{5A}), 7.22 (d, *J* = 5.6 Hz, 8H, H^{3A}), 7.12 (dd, *J* = 7.8, 5.6 Hz, 8H, H^{4A}), 6.85 (d, *J* = 1.8 Hz, 8H, H^{2C}), 6.54 (t, *J* = 1.8 Hz, 4H, H^{4C}), 5.64 (s, 8H, H^{OCH_2C}), 3.98 (t, *J* = 6.4 Hz, 16H, $H^{OCH_2CH_2}$), 1.67 (tt, *J* = 6.8, 6.4 Hz, 16H, $H^{OCH_2CH_2}$), 1.35 (tt, *J* = 6.8, 6.8 Hz, 16H, $H^{OCH_2CH_2CH_2}$), 1.15–1.27 (m, 64H, $H^{(CH_2)_4}$), 0.81 (t, *J* = 6.8 Hz, 24H, H^{CH_3}), −2.97 ppm (s, 2H, H^{NH}). ^{13}C NMR (125 MHz, d_3-DMSO): δ 167.4, 160.4, 160.1, 153.1, 149.0, 147.9, 141.4, 138.5, 137.5, 133.7, 127.4, 124.2, 123.7, 119.6, 111.9, 106.8, 100.9, 71.6, 67.6, 31.2, 28.6, 28.6 (2 overlapping signals), 25.5, 22.1, 13.9 ppm (2 signals from the TPPSA unit could not be detected). IR (neat): ($\tilde{\nu}$, cm^{-1}) 3425 br, 3063 w, 2924 m, 2854 m, 1605 s, 1466 m, 1358 m, 1196 s, 1157 s, 1119 m, 1034 m, 1011 m, 849 m, 733 m, 633 m. MS (ESI+): *m/z* 623 **[Fe(10)$_2$]$^{2+}$**. MS (ESI−): *m/z* 933 $[TPPSA + 3H]^-$. UV-vis (DMF): λ/nm (ε/M^{-1} cm^{-1}) 550 (10200), 516 (12000), 417 (190000), 368 (13000), 314 (32000).

Anal. Calcd for $C_{196}H_{222}N_{16}O_{24}S_4Fe_2$: C, 68.72; H, 6.53; N, 6.54; found: C, 60.00; H, 5.79; N, 6.89% (better elemental analysis could not be made).

[Fe(11)$_2$]Cl$_2$: To ligand **11** (66.0 g, 62.0 µmol) in dichloromethane:methanol (4:1, 5 mL), $FeCl_2·4H_2O$ (6.16 mg, 31.0 µmol) in methanol (1.5 mL) was added and stirred at room temperature for 3 hours. The colour of the solution turned immediately purple. The solvent was then removed *in vacuo*. Chromatography on silica (dichloromethane:methanol 95:5) afforded **[Fe(11)$_2$]Cl$_2$** as a purple solid (53.2 mg, 23.6 µmol, 76%). ^1H NMR (400 MHz, CD_3CN): δ 8.12 (s, 4H, H^{3B}), 8.46 (d, J = 7.6 Hz, 4H, H^{6A}), 7.86 (dd, J = 7.6, 5.7 Hz, 4H, H^{5A}), 8.63 (d, J = 5.7 Hz, 4H, H^{3A}), 7.05 (dd, J = 7.6, 5.7 Hz, 4H, H^{4A}), 6.93 (d, J = 2.2 Hz, 4H, H^{2C}), 6.70 (t, J = 2.2 Hz, 2H, H^{4C}), 6.59 (d, J = 2.2 Hz, 8H, H^{2D}), 6.40 (t, J = 2.2 Hz, 4H, H^{4D}), 5.63 (s, 4H, H^{OCH_2C}), 5.10 (s, 8H, H^{OCH_2D}), 3.95 (t, J = 6.6 Hz, 16H, $H^{OCH_2CH_2}$), 1.70 (tt, J = 6.8, 6.6 Hz, 16H, $H^{OCH_2CH_2}$), 1.40 (tt, J = 6.8, 6.7 Hz, 16H, $H^{OCH_2CH_2CH_2}$), 1.22−1.34 (m, 32H, $H^{(CH_2)_4}$), 0.86 ppm (t, J = 7.2 Hz, 24H, H^{CH_3}). ^{13}C NMR (125 MHz, CD_3CN): δ 166.0, 161.8, 161.4, 161.1, 158.9, 154.2, 140.4, 139.4, 128.1, 124.6, 112.6, 108.0, 106.7, 102.9, 101.1, 72.6, 70.6, 68.8, 32.5, 29.9, 29.9, 29.8, 26.6, 23.3, 14.3 ppm. IR (neat): ($\tilde{\nu}$, cm^{-1}) 2924 m, 2854 m, 1597 s, 1450 m, 1358 w, 1296 w, 1211 w, 1157 s, 1049 m, 995 m, 833 m. MS (ESI+): *m/z* 1092 $[M - 2PF_6]^{2+}$. UV-vis (CH_3CN): λ/nm (ε/M^{-1} cm^{-1}) 557 (14000), 362 (5700), 315 (51000). Anal. Calcd for $C_{136}H_{186}N_6O_{14}Cl_2Fe·2H_2O$: C, 72.41; H, 8.31; N, 3.73; found: C, 71.28; H, 8.36; N, 3.67%.

[Co(10)$_2$][BF$_4$]$_2$: To a solution of ligand **10** (200 mg, 335 µmol) in ethanol:dichloromethane (2:1, 15 mL), a solution of $CoBF_4·6H_2O$ (57.2 mg, 168 µmol) in ethanol (5 mL) was added. The colour of the solution turned immediately orange. The reaction mixture was stirred for 1 hour. The solvent was removed a vacuo affording **[Co(10)$_2$][BF$_4$]$_2$** as an orange residue (239 mg, 168 µmol, quant.). ^1H NMR (500 MHz, CD_3CN): δ 114.0 (br s, 4H, H^{6A}), 77.2 (br s, 4H, H^{3B}), 71.9 (br s, 4H, H^{3A}), 35.2 (br s, 4H, H^{5A}), 16.2 (br s, 4H, H^{OCH_2C}), 12.2 (br s, 4H, H^{2C}), 8.37 (br s, 2H, H^{4C}), 6.25 (br s, 4H, H4A), 5.85 (t, J = 6.6 Hz, 8H, $H^{OCH_2CH_2}$), 2.85 (tt, J = 7.4, 6.6 Hz, 8H, $H^{OCH_2CH_2}$), 2.27 (tt, J = 7.4, 7.4 Hz, 8H, $H^{OCH_2CH_2CH_2}$), 1.80 (tt, J = 7.4, 7.4 Hz, 8H, $H^{O(CH_2)_3CH_2}$),1.56 (tt, J = 7.4, 7.4 Hz, 8H, $H^{O(CH_2)_4CH_2}$),1.31−1.39 (m, 16H, $H^{(CH_2)_2}$), 0.89 ppm (t, J = 6.8 Hz, 12H, H^{CH_3}). IR (neat): ($\tilde{\nu}$, cm^{-1}) 2924 m, 2854 m, 1612 s, 1566 w, 1481 m, 1434 m, 1366 w, 1219 m, 1034 s, 849 m, 787 m. MS (ESI+): *m/z* 625 $[M - 2PF_6]^{2+}$. UV-vis (CH_3CN): λ/nm (ε/M^{-1} cm^{-1}) 454 (970), 305 (32000). Anal. Calcd for $C_{76}H_{98}N_6O_6B_2F_8Co$: C, 64.10; H, 6.94; N, 5.90; found: C, 63.74; H, 6.68; N, 5.85%.

[Co(10)$_2$][PF$_6$]$_3$: **[Co(10)$_2$][BF$_4$]$_2$** (12.5 mg, 8.78 µmol) and $Pb(OAc)_4$ (26.6 mg, 60.0 µmol) were stirred at room temperature in dichloromethane (3 mL). The colour of the solution turned immediately bright orange. The reaction mixture was stirred for 1 hour. Water (20 mL) was added and the mixture extracted three times with dichloromethane (20 mL). The combined organic layers were dried (Na_2SO_4) and evaporated. The residue was disolved in methanol (3 mL) and NH_4PF_6 (20.0 mg, 123 µmol) in methanol (5 mL) was added. The formed precipitate was collected by filtration yielding **[Co(10)₂][PF₆]₃** as a yellow powder (13.8 mg, 8.1 µmol, 92%). ^{1}H NMR (250 MHz, CD_3CN): δ 8.58 (s, 4H, H^{3B}), 8.54 (d, J = 7.0 Hz, 4H, H^{6A}), 8.22 (dd, J = 7.0, 4.7 Hz, 4H, H^{5A}), 7.45 (dd, J = 7.0, 4.7 Hz, 4H, H^{4A}), 7.36 (d, J = 4.7 Hz, 4H, H^{3A}), 6.82 (d, J = 2.1 Hz, 4H, H^{2C}), 6.58 (t, J = 2.1 Hz, 2H, H^{4C}), 5.65 (s, 4H, H^{OCH_2C}), 4.06 (t, J = 6.7 Hz, 8H, $H^{OCH_2CH_2}$), 1.80 (tt, J = 7.6, 6.7 Hz, 8H, $H^{OCH_2CH_2}$), 1.49 (tt, J = 6.7, 6.7 Hz, 8H, $H^{OCH_2CH_2CH_2}$), 1.25−1.42 (m, 32H, $H^{(CH_2)_4}$), 0.90 ppm (t, J = 7.0 Hz, 12H, H^{CH_3}). ^{13}C NMR (125 MHz, CD_3CN): δ 173.2, 161.8, 157.8, 157.0, 153.2, 143.9, 137.4, 131.6, 127.6, 115.7, 107.5, 102.0, 74.1, 69.0, 32.5, 30.0, 29.9, 29.8, 26.7, 23.3, 14.3 ppm. IR (neat): ($\tilde{\nu}$, cm^{-1}) 2924 m, 2854 m, 1612 s, 1566 w, 1481 m, 1442 m, 1357 m, 1219 m, 1165 s, 1057 w, 987 m, 825 s, 787 m. MS (ESI+): *m/z* 625 $[M - 3PF_6]^{2+}$. UV-vis (CH_3CN): λ/nm (ε/M^{-1} cm^{-1}) 455 (470), 321 (23000). Anal. Calcd for $C_{76}H_{98}N_6O_6P_3F_{18}Co\cdot 1H_2O$: C, 53.59; H, 5.92; N, 4.99; found: C, 53.65; H, 5.85; N, 5.05%.

[Ru(10)₂][PF₆]₂: Ligand **10** (12.5 g, 21.0 µmol), $Ru(DMSO)_4Cl_2$ (5.07 mg, 10.5 µmol) and $TlPF_6$ (7.30 mg, 21.0 µmol) were refluxed in ethanol (30 mL) for 3 hours. The colour of the solution turned from yellow to orange. The solvent was then removed *in vacuo*. Chromatography on silica (dichloromethane:methanol 10:1) afforded **[Ru(10)₂][PF₆]₂** as an orange powder (12.0 mg, 7.58 µmol, 72%). ^{1}H NMR (400 MHz, CD_3CN): δ 8.44 (d, J = 8.1 Hz, 4H, H^{6A}), 8.38 (s, 4H, H^{3B}), 7.90 (dd, J = 8.1, 5.6 Hz, 4H, H^{5A}), 7.36 (d, J = 5.6 Hz, 4H, H^{3A}), 7.15 (dd, J = 8.1, 5.6 Hz, 4H, H^{4A}), 6.78 (d, J = 2.0 Hz, 4H, H^{2C}), 6.53 (t, J = 2.0 Hz, 2H, H^{4C}), 5.53 (s, 4H, H^{OCH_2C}), 4.04 (t, J = 6.6 Hz, 8H, $H^{OCH_2CH_2}$), 1.77 (tt, J = 7.6, 6.6 Hz, 8H, $H^{OCH_2CH_2}$), 1.46 (tt, J = 7.6, 7.6 Hz, 8H, $H^{OCH_2CH_2CH_2}$), 1.25−1.39 (m, 32H, $H^{(CH_2)_4}$), 0.88 ppm (t, J = 6.8 Hz, 12H, H^{CH_3}). ^{13}C NMR (125 MHz, CD_3CN): δ 166.5, 161.7, 159.1, 157.3, 153.4, 138.7, 138.6, 128.3, 125.1, 112.1, 107.2, 101.8, 72.4, 69.0, 32.5, 30.0, 29.9, 29.8, 26.6, 23.3, 14.3 ppm. IR (neat): ($\tilde{\nu}$, cm^{-1}) 2924 m, 2854 m, 1605 s, 1466 m, 1381 m, 1350 w, 1203 m, 1165 s, 1049 m, 987 m, 833 s, 787 m. MS (ESI+): *m/z* 646 $[M - 2PF_6]^{2+}$. UV-vis (CH_3CN): λ/nm (ε/M^{-1} cm^{-1}) 485 (19000), 362 (57000), 303 (65000), 267 (63000), 240 (57000). Anal. Calcd for $C_{76}H_{98}N_6O_6P_2F_{12}Ru$: C, 57.68; H, 6.24; N, 5.31; found: C, 57.64; H, 6.29; N, 5.43%.

[Ru(11)₂][PF₆]₂: Ligand **11** (73.0 g, 68.6 µmol), $Ru(DMSO)_4Cl_2$ (16.6 mg, 34.3 µmol) and $TlPF_6$ (23.8 mg, 68.6 µmol) were refluxed in ethanol:dichloromethane (4:1, 5 mL) for 4 hours. The colour of the solution turned from yellow to orange. The solvent was then removed *in vacuo*. Chromatography on silica (dichloromethane:methanol 20:1) afforded **[Ru(10)₂][PF₆]₂** as an orange powder (55.0 mg, 21.4 µmol, 62%). ^{1}H NMR (500 MHz, d_3-acetone): δ 8.84 (d, J = 8.2 Hz, 4H, H^{6A}), 8.82 (s, 4H, H^{3B}), 8.05 (dd, J = 8.2, 5.4 Hz, 4H, H^{5A}), 7.76 (d, J = 5.4 Hz, 4H, H^{3A}), 7.32 (dd, J = 8.2, 5.4 Hz, 4H, H^{4A}), 6.94 (d, J = 2.2 Hz, 4H, H^{2C}), 6.81 (t, J = 2.2 Hz, 2H, H^{4C}), 6.66 (d, J = 2.2 Hz, 8H, H^{2D}), 6.48 (t, J = 2.2 Hz, 4H, H^{4D}), 5.64 (s, 4H, H$^{\mathrm{OC}\mathit{H}_2\mathrm{C}}$), 5.14 (s, 8H, H$^{\mathrm{OC}\mathit{H}_2\mathrm{D}}$), 4.01 (t, J = 6.5 Hz, 16H, H$^{\mathrm{OC}\mathit{H}_2\mathrm{CH}_2}$), 1.77 (tt, J = 7.3, 6.5 Hz, 16H, H$^{\mathrm{OCH}_2\mathrm{C}\mathit{H}_2}$), 1.47 (tt, J = 7.3, 7.3 Hz, 16H, H$^{\mathrm{OCH}_2\mathrm{CH}_2\mathrm{C}\mathit{H}_2}$), 1.25–1.39 (m, 32H, H$^{(\mathrm{C}\mathit{H}_2)_4}$), 0.87 ppm (t, J = 6.9 Hz, 24H, H$^{\mathrm{C}\mathit{H}_3}$). ^{13}C NMR (125 MHz, d_3-acetone): δ 167.8, 162.5, 162.3, 160.5, 158.6, 154.6, 141.3, 139.8, 139.7, 129.6, 126.4, 113.2, 109.1, 107.7, 103.5, 102.1, 73.4, 71.6, 69.6, 33.6, 29.5, 29.4, 29.4, 27.8, 24.3, 15.4 ppm. IR (neat): ($\tilde{\nu}$, cm^{-1}) 2924 m, 2854 m, 1597 s, 1458 m, 1350 w, 1157 s, 1049 m, 825 s, 586 m. MS (ESI+): *m/z* 1114 [M − 2Cl]$^{2+}$. UV-vis (CH$_3$CN): λ/nm (ε/M^{-1} cm^{-1}) 485 (21000), 302 (140000), 269 (160000). Anal. Calcd for $C_{136}H_{186}N_6O_{14}P_2F_{12}Ru{\cdot}3H_2O$: C, 63.46; H, 7.52; N, 3.26; found: C, 63.46; H, 7.36; N, 3.33%.

[Ru(13)$_2$][PF$_6$]$_2$: Ligand **13** (30.0 g, 54.4 µmol) and Ru(DMSO)$_4$Cl$_2$ (13.2 mg, 27.2 µmol) were refluxed in ethanol (30 mL) for 3 hours. The colour of the solution turned from yellow to orange. The solvent was then removed *in vacuo*. The residue was disolved in methanol (30 mL) and NH$_4$PF$_6$ (80.0 mg, 492 µmol) was added. The formed precipitate was collected by filtration yielding **[Ru(13)$_2$][PF$_6$]$_3$** as a yellow powder (21.6 mg, 14.5 µmol, 53%). ^{1}H NMR (500 MHz, CD$_3$CN): δ 8.44 (d, J = 8.2 Hz, 4H, H^{6A}), 8.37 (s, 4H, H^{3B}), 7.90 (dd, J = 8.2, 6.3 Hz, 4H, H^{5A}), 7.49 (d, J = 7.3 Hz, 8H, H^{2D}), 7.42 (dd, J = 7.3, 5.0 Hz, 8H, H^{3D}), 7.37 (m, 8H, H^{4D+3A}), 7.15 (dd, J = 8.2, 6.3 Hz, 4H, H^{4A}), 6.92 (d, J = 2.2 Hz, 4H, H^{2C}), 6.72 (t, J = 2.2 Hz, 2H, H^{4C}), 5.34 (s, 4H, H$^{\mathrm{OC}\mathit{H}_2\mathrm{C}}$), 5.17 (s, 8H, H$^{\mathrm{OC}\mathit{H}_2\mathrm{D}}$). ^{13}C NMR (125 MHz, CD$_3$CN): δ 168.5, 161.8, 161.3, 158.9, 154.3, 139.4, 138.8, 138.0, 129.5, 129.0, 128.7, 128.1, 124.4, 112.5, 108.0, 102.9, 72.6, 70.9 ppm. IR (neat): ($\tilde{\nu}$, cm^{-1}) 3086 w, 3032 w, 2924 m, 2870 m, 1597 s, 1450 m, 1358 m, 1211 m, 1150 s, 995 m, 825 s, 694 m. MS (ESI+): *m/z* 602 [M − 2PF$_6$]$^{2+}$. UV-vis (CH$_3$CN): λ/nm (ε/M^{-1} cm^{-1}) 486 (20000), 302 (66000), 267 (72000), 238 (68000) .

6.4 References

[1] H. Hofmeier, U. S. Schubert, *Chem. Soc. Rev.* **2004**, *33*, 373.

[2] E. C. Constable, *Adv. Inorg. Chem. Radiochem.* **1986**, *30*, 69.

[3] E. C. Constable, in *Comprehensive Coordination Chemistry II* (Eds.: J. A. McCleverty, T. J. Meyer), Elsevier, Amsterdam, **2003**.

[4] P. R. Anders, U. S. Schubert, *Adv. Mater.* **2004**, *16*, 1043.

[5] Z. Wang, Q. Zeng, Y. Luan, X. Wu, L. Wan, C. Wang, G. U. Lee, S. Yin, J. Yang, C. Bai, *J. Phys. Chem. B* **2003**, *107*, 13384.

[6] J.-R. Gong, L.-J. Wan, Q.-H. Yuan, C. Bai, H. Jude, P. J. Stang, *PNAS* **2005**, *102*, 971.

[7] K. Miyamura, M. Kimura, A. Okumura, Y. Gohshi, *J. Vac. Sci. Technol. B.* **1994**, *12*, 1930.

[8] T. Yokoyama, S. Yokoyama, T. Kamikado, Y. Okuno, S. Mashiko, *Nature* **2001**, *413*, 619.

[9] K. W. Hipps, L. Scudiero, D. E. Barlow, M. P. Cooke Jr., *J. Am. Chem. Soc.* **2002**, *124*, 2126.

[10] L. Scudiero, K. W. Hipps, D. E. Barlow, *J. Phys. Chem. B* **2003**, *107*, 2903.

[11] X. Lu, K. W. Hipps, X. D. Wang, U. Mazur, *J. Am. Chem. Soc.* **1996**, *118*, 7197.

[12] K. W. Hipps, X. Lu, X. D. Wang, U. Mazur, *J. Phys. Chem.* **1996**, *100*, 11207.

[13] X. Lu, K. W. Hipps, *J. Phys. Chem. B* **1996**, *101*, 5391.

[14] L. Scudiero, D. E. Barlow, K. W. Hipps, *J. Phys. Chem. B* **2000**, *104*, 11899.

[15] L. Scudiero, D. E. Barlow, U. Mazur, K. W. Hipps, *J. Am. Chem. Soc.* **2001**, *123*, 4073.

[16] M. de Wild, S. Berner, H. Suzuki, H. Yanagi, D. Schlettwein, S. Ivan, A. Baratoff, H.-J. Güntherodt, T. A. Jung, *ChemPhysChem* **2002**, *3*, 881.

[17] J. A. A. W. Elemans, M. C. Lensen, J. W. Gerritsen, H. Kerpen, S. Speller, R. J. M. Nolte, A. E. Rowan, *Adv. Mater.* **2003**, *15*, 2070.

[18] S. Yoshimoto, N. Higa, K. Itaya, *J. Am. Chem. Soc.* **2004**, *126*, 8540.

[19] L. Latterini, G. Pourtois, C. Moucheron, R. Lazzaroni, J.-L. Brédas, A. Kirsch-De Mesmaeker, F. C. De Schryver, *Chem. –Eur. J.* **2000**, *6*, 1331.

[20] M. Ruben, J. Rojo, F. J. Romero-Salguero, L. H. Uppadine, J.-M. Lehn, *Angew. Chem.* **2004**, *116*, 3728.

[21] M. S. Alam, S. Strömsdörfer, V. Dremow, P. Müller, J. Kortus, M. Ruben, J.-M. Lehn, *Angew. Chem. Int. Ed.* **2005**, *44*, 7896.

[22] U. Ziener, J.-M. Lehn, A. Mourran, M. Möller, *Chem. –Eur. J.* **2002**, *8*, 951.

[23] A. Semenov, J. P. Spatz, M. Möller, J.-M. Lehn, B. Sell, D. Schubert, C. H. Weidl, U. S. Schubert, *Angew. Chem. Int. Ed.* **1999**, *38*, 2547.

[24] A. Semenov, J. P. Spatz, J.-M. Lehn, C. H. Weidl, U. S. Schubert, M. Möller, *Appl. Surf. Sci.* **1999**, *144–145*, 456.

[25] D. J. Díaz, G. D. Storrier, S. Bernhard, K. Takada, H. D. Abruña, *Langmuir* **1999**, *15*, 7351.

[26] D. J. Díaz, S. Bernhard, G. D. Storrier, H. D. Abruña, *J. Phys. Chem. B* **2001**, *105*, 8746.

[27] M. M. S. Abdel-Mottaleb, N. Schuurmans, S. De Feyter, J. van Esch, B. L. Feringa, F. C. De Schryver, *Chem. Commun.* **2002**, 1894.

[28] E. Figgemeier, L. Merz, B. A. Hermann, Y. C. Zimmermann, C. E. Housecroft, H.-J. Güntherodt, E. C. Constable, *J. Phys. Chem. B* **2003**, *107*, 1157.

[29] C. J. Hawker, J. M. J. Fréchet, *J. Am. Chem. Soc.* **1990**, *112*, 7638.

[30] I. Widmer, U. Huber, M. Stöhr, L. Merz, H.-J. Güntherodt, B. A. Hermann, P. Samorí, J. P. Rabe, P. B. Rheiner, G. Creiveldinger, P. Murer, *Helv. Chim. Acta* **2002**, *85*, 4255.

[31] P. Wu, Q. Fan, G. Deng, Q. Zeng, C. Wang, C. Bai, *Langmuir* **2002**, *18*, 4342.

[32] S. A. Prokhorova, S. S. Sheiko, A. Mourran, R. Azumi, U. Beginn, G. Zipp, C. H. Ahn, M. N. Holerca, V. Percec, M. Möller, *Langmuir* **2000**, *16*, 6862.

[33] L. J. Scherer, L. Merz, E. C. Constable, C. E. Housecroft, M. Neuburger, B. A. Hermann, *J. Am. Chem. Soc.* **2005**, *127*, 4033

[34] L. Merz, H.-J. Güntherodt, L. J. Scherer, E. C. Constable, C. E. Housecroft, B. A. Hermann, *Chem. –Eur. J.* **2005**, *11*, 2307.

[35] B. A. Hermann, L. J. Scherer, C. E. Housecroft, E. C. Constable, *Adv. Funct. Mater.* **2006**, *16*, 221.

[36] K. Osakada, M. Hamada, T. Yamamoto, *Organometallics* **2000**, *19*, 458.

[37] K. A. Jensen, *Z. Anorg. Chem.* **1936**, 235.

[38] P. Granger, in *NMR of Newly Accessible Nuclei* (Ed.: P. Laszlo), Academic Press, New York, **1983**.

[39] P. S. Pregosin, *Coord. Chem. Rev.* **1982**, *44*, 247.

[40] A. Sebald, C. Stader, B. Wrackmeyer, W. Bensch, *J. Organomet. Chem.* **1986**, *311*, 233.

[41] A. Sebald, B. Wrackmeyer, C. R. Theocharis, W. Jones, *J. Chem. Soc., Dalton Trans.* **1984**, 747.

[42] E. C. Constable, A. M. W. Cargill Thompson, *J. Chem. Soc., Dalton Trans.* **1992**, 2947.

[43] E. C. Constable, C. E. Housecroft, M. Neuburger, S. Schaffner, L. J. Scherer, *Dalton Trans.* **2004**, 2635.

[44] F. Antolasic, *Isotope Version 1.0* **2003**.

[45] E. C. Constable, C. P. Hart, C. E. Housecroft, *Appl. Organomet. Chem.* **2003**, *17*, 383.

[46] E. C. Constable, C. E. Housecroft, T. Kulke, C. Lazzarini, E. Schofield, Y. Zimmermann, *J. Chem. Soc., Dalton Trans.* **2001**, 2864.

[47] E. C. Constable, C. E. Housecroft, Y. Tao, *Synthesis* **2004**, 869.

[48] A. de la Hoz, Á. Díaz-Ortiz, A. Moreno, *Chem. Soc. Rev.* **2005**, *34*, 164.

[49] S. Encinas, L. Flamigni, F. Barigelletti, E. C. Constable, C. E. Housecroft, E. Schofield, E. Figgemeier, D. Fenske, M. Neuburger, J. G. Vos, M. Zehnder, *Chem. –Eur. J.* **2002**, *8*, 137.

[50] E. C. Constable, R. Handel, C. E. Housecroft, M. Neuburger, E. Schofield, M. Zehnder, *Polyhedron* **2004**, *23*, 135.

[51] E. Dulière, M. Devillers, J. Marchand-Brynaert, *Organometallics* **2003**, *22*, 804.
[52] Z. Qin, M. C. Jennings, R. J. Puddephatt, *Inorg. Chem.* **2003**, *42*, 1956.
[53] Z. Qin, M. C. Jennings, R. J. Puddephatt, *Inorg. Chem.* **2002**, *41*, 3967.
[54] M. Lupkowski, J. F. Maguire, *Composite Interf.* **1994**, *2*, 1.

Ich bin überzeugt, dass auch die abstrakteste theoretische Forschung einfach erklärt werden kann, vorausgesetzt, dass sie wirklich Sinn macht.

R. R. Ernst

7. Octyl-decorated Fréchet-type Dendrons: What have we learnt?

As has been demonstrated in Chapters 3−6, Fréchet-type dendrons with peripheral octyl groups are ideally suited for visualisation by tunnelling methods. This molecular unit is not only interesting for the study of self-assembled monolayers, but also the 3D packing shows appealing features and sometimes the 3D organisation could be compared with the 2D packing (see Sections 4.2 and 5.2.2). In supramolecular chemistry, interactions between molecules are studied (see Chapter 1). The most commonly used tools to investigate the intermolecular contacts are X-ray diffraction techniques. STM is a novel method to examine the behaviour of molecules on surfaces. In this Chapter, the advantages and disadvantages of STM as instrument to probe intermolecular interactions are discussed. Areas in which STM can supplement X-ray techniques in supramolecular chemistry and limitations of this approach are discussed.

The results of Chapters 3−6 will be summarised and the properties of octyl-decorated Fréchet-type dendrons will be analysed and possible reasons why octyl-decorated Fréchet-type dendrons are useful STM chromophores will be discussed.

7.1 Investigating intermolecular forces: STM versus X-ray diffraction

Supramolecular chemistry in which intermolecular interactions are studied is a growing field in chemical science (Chapter 1).[1] Since intermolecular contacts are, in particular, investigated in the solid state, X-ray diffraction is the most widely used technique to examine these intermolecular interactions.

The direct imaging of species of chemical interest at the molecular and submolecular levels using STM has revolutionised possibilities for the visualisation and control of self-organised systems.[2, 3] Certainly, with STM, molecular orientations can only be studied in two dimensions; usually monolayers on conducting surfaces are explored. Intermolecular, as well as intramolecular, structural questions of chemical interest can be investigated with STM. Not only static properties of the monolayer can be researched, as with X-ray crystallography, but also dynamic behaviours of monolayers. Conventional methods such as single crystal X-ray crystallography or NMR spectroscopic methods for determining molecular conformations and metrical parameters, give structures averaged over some 10^{15} molecules. With STM, individual molecules can be studied, and since no averaging is necessary (although it is possible, see therefore Section 2.3.2), STM is particularly useful for characterising surfaces with non-periodic properties, visualising irregularities or non-systematic defects.[4, 5] Whereas for STM, irregularities as shown in Figure 7.1 can give important indications about the self-assembly processes, such defects would enormously disturb the refinement of X-ray crystallography data.

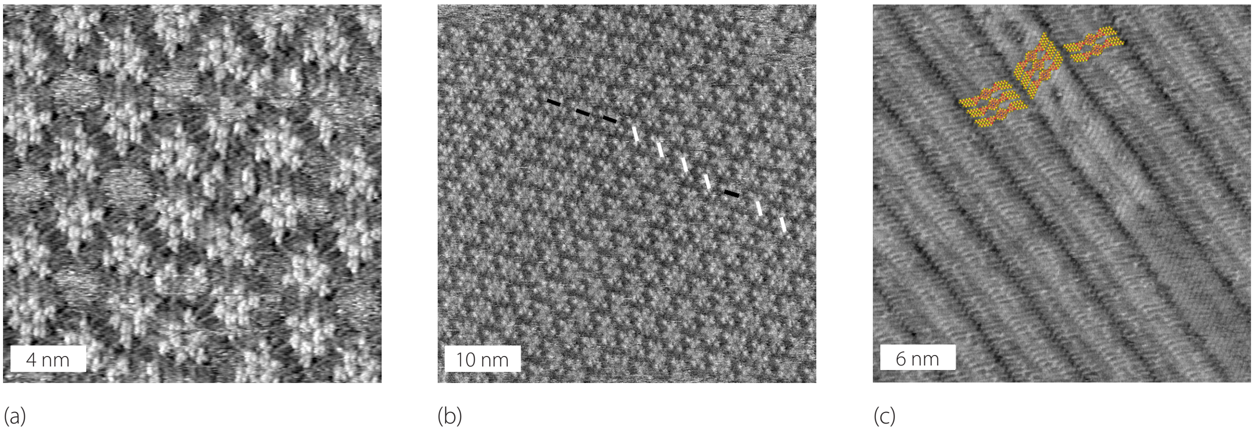

Figure 7.1 Three images showing irregularities in the self-assembly pattern. Images are taken from (a) Figure 5.12(a), (b) Figure 4.23 and (c) from Figure 6.26.

It is not only possible to monitor both the extent and detailed structure of surface-bound monolayers, but it is also possible to move single atoms[6] or molecules[7] or to initiate and to monitor chemical reactions of adsorbed molecules.[8, 9] Molecular manipulation by means of STM or AFM represents the ultimate in size reduction for the fabrication and operation of nanodevices (see Section 1.1.5) and therefore has applications as an analysing tool.

At room temperature, isolated molecules are generally mobile on surfaces, and such a mobility during a lateral scan with the STM tip is thought to prevent collection of reproducible STM images. One approach to obviate this problem is measuring at very low temperatures in an ultra high vacuum. Another approach to circumvent this problem is to form overlayer combinations that spontaneously assemble in domains of well-defined monolayers. In this fashion, the same molecular structure can be reliably prepared and observed experimentally over a variety of trials. The same approach of fixing the molecules in a lattice is used in X-ray crystallography, where the molecules are ordered in a well-defined 3D assembly as a single crystal. It can be quite challenging to find the appropriate conditions where the molecules spontaneously crystallise in a periodic arrangement of a size of some hundreds of micrometers, as it is necessary for single crystal X-ray crystallography.

Thermal movements of parts of the molecule can lead to poor quality X-ray structures. The same problem is often observed for monolayers, even when the formed domains are large in size, the whole domain can have thermal drift which often makes conformational and structural analysis impossible (see Section 2.2.2.4). Furthermore, the quality of the tip influences the resolution of the images enormously. Since only the macroscopic shape of the tip can be influenced, resolutions are often not reproducible, even by using the same monolayer. This problem of reproducibility does normally not exist in X-ray crystallography when measuring the same single crystal. Furthermore, a prerequisite for high resolution STM images is a stable assembly that is not perturbed during the scanning process by the STM tip.

Whereas for X-ray crystallography, the quality of the refinement can be quantified with different *R*-

values, and software programs for refinements are reasonably developed, the interpretation of the STM data can not be evaluated and the whole analysis has to be done manually (see Section 2.3.2). The main problem is that it has not been fully understood how different aspects of the adsorbate and the experimental conditions combine together to create the observed image. It is thus of great theoretical and experimental interest to understand, in a systematic fashion, the factors that control the spatial image contrast in a molecular-resolution image.[10] Several theories have already been developed to predict and explain STM images.[11]

Molecules, which tend to assemble in a 2D fashion on surfaces, often possess peripheral alkyl-chains which are very flexible. Due to this flexibility, they often do not tend to form spontaneously single crystals which can be measured with X-ray diffraction techniques. On the other hand, rigid molecules which have a propensity to be very crystalline in solid state do normally not form self-assembled monolayers on surfaces. Therefore, these two techniques complement one another and are therefore very useful when combined together.

7.2 Special features of octyl-decorated Fréchet-type dendrimers for STM studies

As discussed above, STM is a powerful tool to investigate 2D self-assembly properties of specific compounds. In Chapters 3–6, the power of Fréchet-type dendrimers for different kind of STM investigations was demonstrated. Whereas different compounds decorated with Fréchet-type dendrons showed interesting static assembly motifs in three dimensions which could be investigated using X-ray crystallography,[12-14] not only the static but also the dynamic behaviours of self-assembled monolayers were explored with STM (Chapter 5) and furthermore the changes of an organised pattern by treating the assembly with gaseous HCl were visualised (Section 3.4). X-ray diffraction and STM were used together to investigate different molecules functionalised with Fréchet-type dendrons. Whereas the Fréchet-type dendrons with peripheral benzyl-groups were obtained in crystalline form and therefore their assembly properties were primarily investigated using single crystal X-ray crystallography,[12-17] compounds decorated with Fréchet-type dendrons possessing pendant alkyl-chains showed a high tendency to self-assemble in layers (either in single crystals or as monolayers on graphite surface).[18-24] Due to this predisposition to form monolayers, the assumption was made that all compounds with Fréchet-type dendrons could have liquid crystalline properties.[25] This proposal was corroborated by the fact that similar Fréchet-type dendrimers showed liquid-crystalline properties.[26, 27] The compounds were tested for liquid-crystalline properties using differential scanning calorimetry (DSC) and optical polarised microscopy. Although the melting processes of compounds **4** and $[\mathbf{Pd(3)_2}][\mathbf{PF_6}]_2$ (Scheme 7.1) were atypical – the DSC spectrum of compound **4** showed two peaks during the melting, and the signal in the DSC for the melting point of $[\mathbf{Pd(3)_2}][\mathbf{PF_6}]_2$ was extraordinarily broad – no compound discussed in this thesis showed clear liquid-crystalline properties.

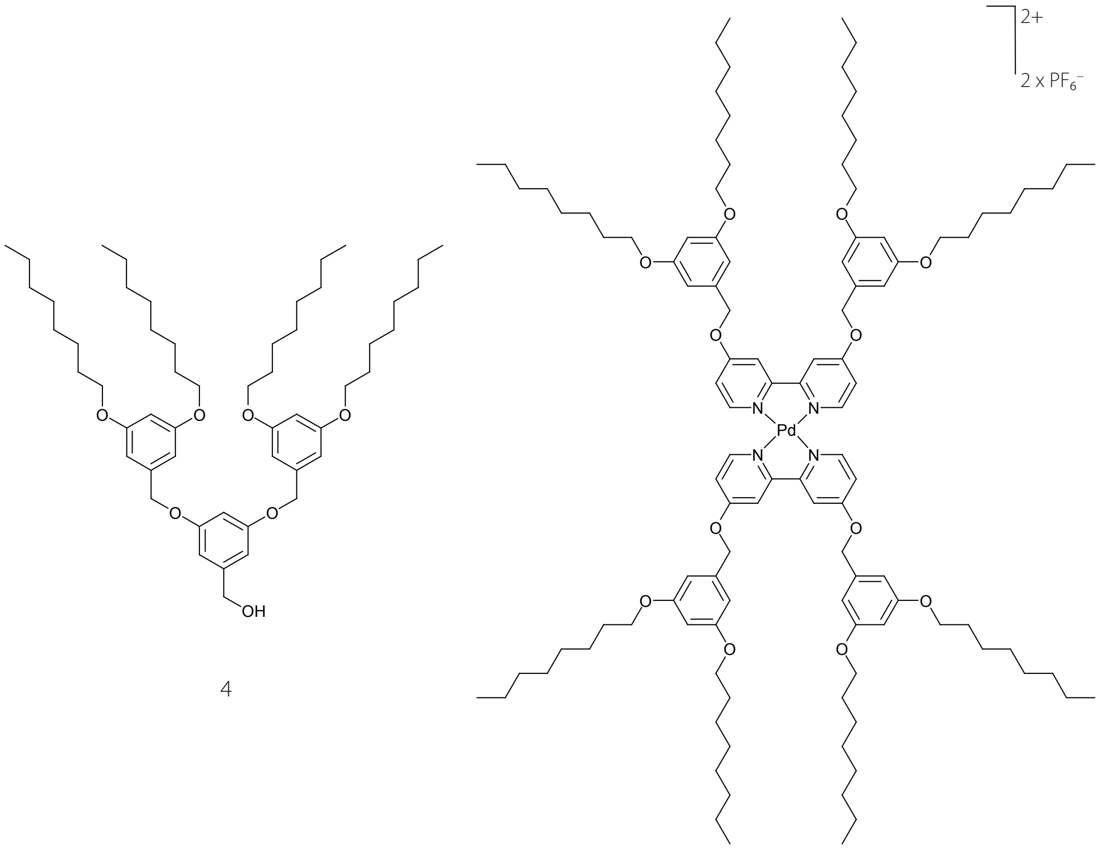

4

Scheme 7.1 The chemical structures of **4** and **$[Pd(3)_2][PF_6]_2$**.

The general use of long-chain alkyl-decorated Fréchet-type dendrons as *STM chromophores* has been demonstrated in the preceding Chapters. Now, an attempt to explain why these dendrons act as *chromophores* in STM measurements will be done.

The first and second generation dendritic wedges are illustrated in Scheme 7.2.

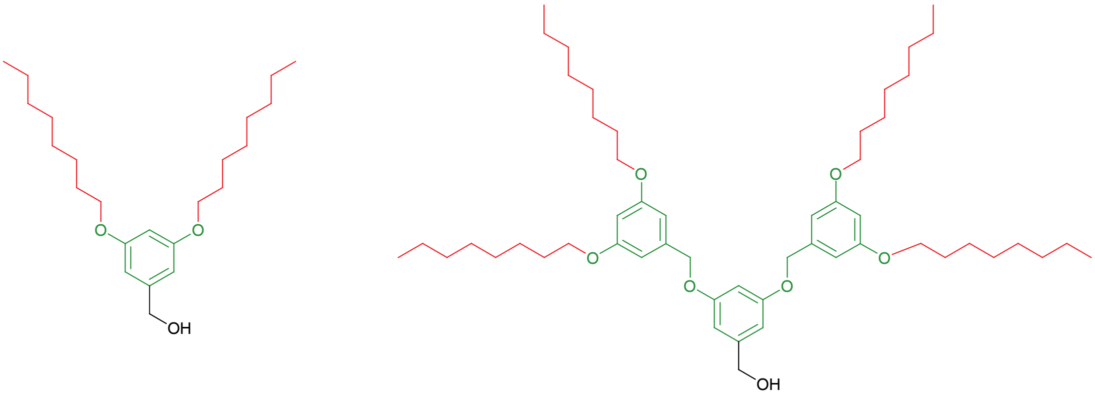

Scheme 7.2 The first and second generation octyl-functionalised Fréchet-type dendritic wedges. The dendritic wedge can be divided in two parts: the peripheral octyl-chains (marked in red) and the electron-rich aromatic part (marked in green).

The dendron functionalisation serves two purposes; visualisation and self-assembly. The dendritic wedge can be split in two parts; firstly the peripheral alkyl chains and secondly the aromatic-rich core (Scheme 7.2).

Each phenyl-ring is functionalised with two ether units what make them very electron-rich. The resulting lower ionisation potential of this electron-rich phenyl rings compared with unsubstituted ones corresponds to more favourable coupling between the orbitals of the molecules and those of the substrate and, thus, stronger interaction between the adsorbate electronic levels and the surface Fermi level are obtained.[10, 28, 29] This leads to enhanced tunnelling probability (topographic protrusions) in STM images and therefore these groups stand out in STM images. Heavy atoms have been used to elucidate 3D crystal structures by X-ray crystallography. Similarly, *chemical marker groups* have been used to assist the identification of both specific groups within a 2D assembly and the pattern of self-organisation.[30-37] The second generation dendron with three aromatic residues per wedge makes visualisation facile (Figure 7.2).

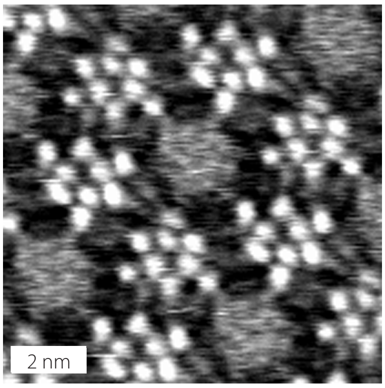

Figure 7.2 The electron-rich aromatic rings stand out as single plots in the STM image as in the image taken from Figure 5.7(a).

The central part of the dendritic wedge (marked in green in Scheme 7.1) acts as STM-marker, but this is not the only feature of this aromatic-rich part. The dendritic compound provides mechanical freedom to rotate about the interannular C−C and C−O bonds. The aromatic-rich central part is highly flexible and was therefore not seen to be appropriate for molecules which should lie flat on the surface, since compounds used so far for STM studies were mainly rigid and flat (e. g. porphyrins, polyphenylenes and phthalocyanines[36, 38-50]).

In parallel with the studies of monolayers, 3D solid state investigations have been performed in this thesis for molecules possessing Fréchet-type dendrons, since the number of structural determinations of these systems was remarkably small.[12-17, 51] Somewhat surprisingly, a survey of all aromatic ethers of the Fréchet-type dendrons in all single crystal X-ray studies of this thesis and in the Cambridge Crystallographic Data Base revealed a strong preference for the C−O−CH_2−C residue to lie in plane of the attached aromatic ring. Three examples are shown in Figure 7.3.

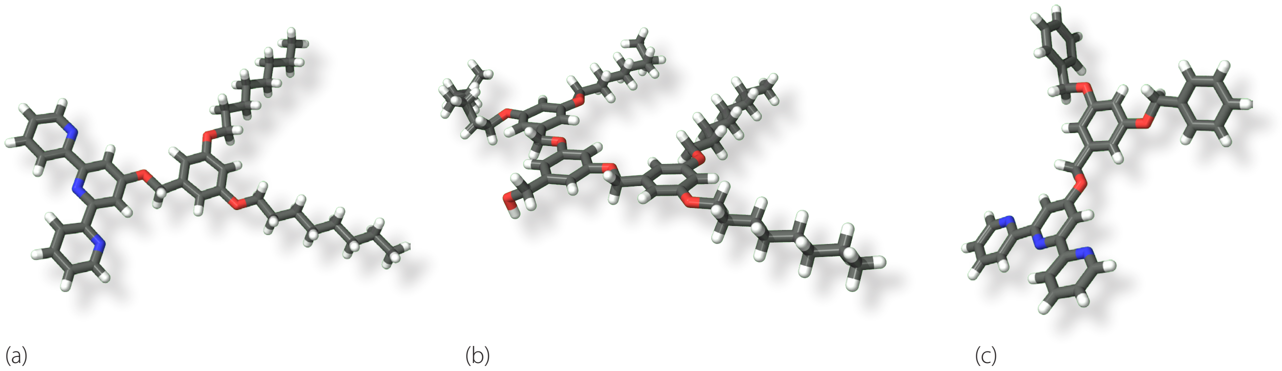
(a) (b) (c)

Figure 7.3 Three examples of compounds possessing Fréchet-type dendrons. The molecular structures of (a) **10**, (b) **4** and (c) **13** are taken from the single crystal X-ray crystallography data. The $C^{Ar}–O–CH_2–C^{Ar}$ unit lies in all of these structures in the plane of the attached aromatic ring.

The phenol ether C–O bond lengths were all in the range between 1.35–1.39 Å and the $C^{Ar}–O–CH_2$ angles were ≈116° for the pyridine ether and between 116–118° for the outer phenol ethers. The short $C^{Ar}–O$ bonds and the angles close to 120° reflect the sp²-character of the oxygens where the non-bonding p-orbital of the oxygens forms part of a delocalised system involving the π-system of the phenyl-ring. Thus the $C^{Ar}–C^{Ar}–O–CH_2$ unit lies in plane. The fact that also the $C^{Ar}–O–CH_2–C$ unit are mostly in plane can be explained with hyperconjugation between the non-bonding p-orbital of the oxygens and the 1s orbitals of the protons of the adjacent CH_2 group. The same reason is assumed for the phenyl groups being in plane with the adjacent $CH_2–O–C^{Ar}$ unit. This was often but not always observed (Figure 7.4).

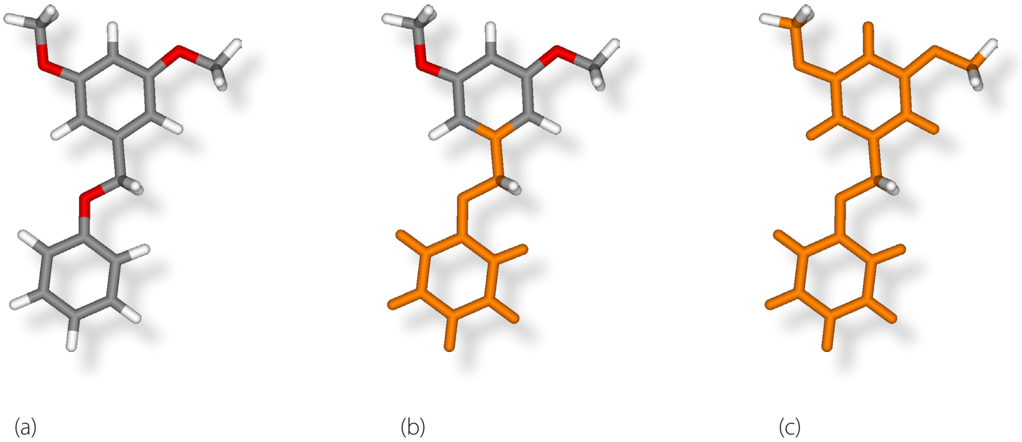
(a) (b) (c)

Figure 7.4 (a) A representation of the $Ar^1–O–CH_2–Ar^2$ group. (b) The $Ar^1–O–CH_2$ unit (marked in orange) lies mostly in plane in the known solid state structures of Fréchet-type dendrimers. (c) In many cases, the whole $Ar^1–O–CH_2–Ar^2$ unit lies in plane.

With the assumption of planarity, each ether unit can adopt a *syn*- or *anti*-conformation (defined with respect of the C^4 proton) (Section 3.1). A search of the Cambridge Structural Database for 1,3-

bis(benzyloxy)benzene derivatives gave a total of 18 hits with a total of 31 $C^{Ar}–O–CH_2–C$ torsion angles; this revealed an overwhelming preference for the adoption of the *syn,anti*-conformation (22 hits) over the *anti, anti*-conformation (7 hits) with just a single example of a *syn,syn*-conformation. There appears to be no obvious stereoelectronic or steric reason for the adoption of the *syn,anti*-conformation.

The outer alkyl-chains of the dendritic unit (Scheme 7.1) are important for the self-assembly process. Alkyl-decorated molecules are often used to form self-assembled monolayers.[10, 11, 52] Alkyl-alkyl interactions are considered as important *supramolecular synthon* for self-assembled monolayers.[53] The alkyl chains show predominantly the all-*trans*-conformation.[10, 11, 52] Exceptions have been observed in the 3D and 2D packing of compounds **4** and **14** (Chapter 5). There has been some debate about whether the alkane adsorption is driven by adsorbate–substrate interactions or by lateral intermolecular interactions. It was reported that some alkylated planar molecules (phtalocyanine, porphyrin) could be imaged with high stability and immobility by STM in ambient conditions, whereas for unsubstituted molecules uniform domains could not be observed by STM under similar circumstances.[54, 55] Similar annotations were done with the molecules measured during this thesis. For the molecules where available both peripheral alkyl and peripheral benzyl groups, the monolayers formed from the molecules with pendant alkyl-chain self-assembled better on the surface and were therefore better to measure by STM.

Two different configurations of alkanes on graphite are possible; a flat orientation, where the carbon skeleton is oriented parallel to the graphite surface and a vertical orientation, where the carbon skeleton is oriented perpendicular to the graphite surface. In both flat and vertical orientations the methylene hydrogens are located above the hollow site of the graphite hexagon. The distance between the zigzag carbon and the basal plane of graphite is 3.8 Å in flat orientations and 3.7 and 4.5 Å in vertical orientations.[52] The contribution of electrostatic interactions is very small compared with the short-range van der Waals interactions.[10, 52] This shows that the van der Waals interactions play the primary role in substrate–molecule interactions. It is noted that the adsorption energy of the flat orientation is lower than that of the vertical orientation, the adsorption energies per CH_2 are -12.1 and -10.4 kJ mol^{-1} for the flat and vertical orientations, respectively.[52] Molecular mechanics calculations revealed that the distance between the adjacent alkane molecules is 4.5 Å for the flat orientations and 4.1 Å for the vertical orientations.[52] These distances are close to those observed experimentally in STM images of alkanes adsorbed on graphite. However, up to now it has not been possible to distinguish the flat and vertical orientations by means of highly resolved STM images.

Similar to the substrate–molecule interactions, van der Waals interactions are the primary contributor to the molecule–molecule interactions. Valence force field calculations revealed, per methylene unit for C_8H_{18}, -4.56 and -5.65 kJ mol^{-1} for the flat and vertical orientations, respectively.[52] Comparing the adsorption energies with the 2D crystallisation energies, it can be seen that the adsorption energies are lower than the two-dimensional crystallisation energy, regardless of the alkane orientation. This comparison implies that the relatively strong substrate–molecule interactions are the major factor to determine the adsorption site of alkane molecules in the close-packing assembly. At the same time, the molecule–molecule interactions also play an important role in achieving the close packing assembly. The lateral molecule–molecule interactions drive the molecules into a close packing configuration; the more the alkyl-chains overlap the more stable the system will be.

The alkyl-chains do not interact only with parallel alkyl-chains but there is also a contact between the end-groups of alkyl-chains of adjacent rows as shown in Section 6.2.1 and Section 6.2.2. Moreover, the chain length can have major influences on the pattern.[56]

Another feature of pendant alkyl-groups is the increase in solubility of the compound in apolar solvents. Due to the increased solubility, a larger diversity of solvents can be used for the formation of monolayers which is important for the solution casting method and for STM measurements in the solid–liquid interface.

High-resolution images with sub-molecular resolution can be obtained for self-assembled monolayers of a variety of cores functionalised with octyl-decorated Fréchet dendrons. Therefore, the idea of suggesting the general use of long chain alkyl-decorated Fréchet-type dendrons as *chromophores* for STM has been introduced.

7.3 References

[1] J.-M. Lehn, *Supramolecular Chemistry*, VCH, Weinheim, **1995**.

[2] G. Binnig, H. Rohrer, *Helv. Phys. Acta* **1982**, *55*, 726.

[3] G. Binnig, H. Rohrer, C. Gerber, E. Weibel, *Phys. Rev. Lett.* **1982**, *49*, 57.

[4] S. Chiang, *Chem. Rev.* **1997**, *97*, 1083.

[5] F. Rosei, M. Schunack, Y. Naitoh, P. Jiang, A. Gourdon, E. Laegsgaard, I. Stensgaard, C. Joachim, F. Besenbacher, *Prog. Surf. Sci.* **2003**, *71*, 95.

[6] D. M. Eigler, E. K. Schweizer, *Nature* **1990**, *344*, 524.

[7] G. Meyer, B. Neu, K.-H. Rieder, *Appl. Phys. A* **1995**, *60*, 343.

[8] S.-W. Hla, L. Bartels, G. Meyer, R. K.-H., *Phys. Rev. Lett.* **2000**, *85*, 2777.

[9] J. R. Hahn, W. Ho, *J. Phys. Chem. B* **2005**, *109*, 20350.

[10] C. Claypool, F. Faglioni, W. A. Goddard III, H. B. Gray, N. S. Lewis, R. A. Marcus, *J. Phys. Chem. B* **1997**, *101*, 5978.

[11] F. Faglioni, C. Claypool, N. S. Lewis, W. A. Goddard III, *J. Phys. Chem. B* **1997**, *101*, 5996.

[12] E. C. Constable, C. E. Housecroft, M. Neuburger, S. Schaffner, L. J. Scherer, *Dalton Trans.* **2004**, 2635.

[13] M. Brewis, G. J. Clarkson, V. Goddard, M. Helliwell, A. M. Holder, N. B. McKeown, *Angew. Chem. Int. Ed.* **1998**, *37*, 1092.

[14] M. Brewis, G. J. Clarkson, M. Helliwell, A. M. Holder, N. B. McKeown, *Chem. –Eur. J.* **2000**, *6*, 4630.

[15] P. B. Rheiner, D. Seebach, *Chem. –Eur. J.* **1999**, *5*, 3221.

[16] F. Vögtle, M. Plevoets, M. Nieger, G. C. Azzelini, A. Credi, L. De Cola, V. De Marchis, M. Venturi, V. Balzani, *J. Am. Chem. Soc.* **1999**, *121*, 6290.

[17] R. E. Marsh, *Acta Crystallogr.,Sect.B* **1999**, *55*, 931.

[18] I. Widmer, U. Huber, M. Stöhr, L. Merz, H.-J. Güntherodt, B. A. Hermann, P. Samorí, J. P. Rabe, P. B. Rheiner, G. Creiveldinger, P. Murer, *Helv. Chim. Acta* **2002**, *85*, 4255.

[19] P. Wu, Q. Fan, G. Deng, Q. Zeng, C. Wang, C. Bai, *Langmuir* **2002**, *18*, 4342.

[20] P. Wu, Q. Fan, Q. Zeng, C. Wang, G. Deng, C. Bai, *ChemPhysChem* **2002**, 633.

[21] S. A. Prokhorova, S. S. Sheiko, A. Mourran, R. Azumi, U. Beginn, G. Zipp, C. H. Ahn, M. N. Holerca, V. Percec, M. Möller, *Langmuir* **2000**, *16*, 6862.

[22] L. Merz, H.-J. Güntherodt, L. J. Scherer, E. C. Constable, C. E. Housecroft, B. A. Hermann, *Chem. –Eur. J.* **2005**, *11*, 2307.

[23] L. J. Scherer, L. Merz, E. C. Constable, C. E. Housecroft, M. Neuburger, B. A. Hermann, *J. Am. Chem. Soc.* **2005**, *127*, 4033

[24] E. C. Constable, B. A. Hermann, C. E. Housecroft, L. Merz, L. J. Scherer, *Chem. Commun.* **2004**, 928.

[25] N. Katsonis, A. Marchenko, D. Fichou, *J. Am. Chem. Soc.* **2003**, *125*, 13682.

[26] V. Percec, T. K. Bera, M. Glidde, Q. Fu, V. S. K. Balagurusamy, P. A. Heiney, *Chem. –Eur. J.* **2003**, *9*, 921.

[27] X. Zeng, G. Ungar, Y. Liu, V. Percec, A. E. Dulcey, J. K. Hobbs, *Nature* **2004**, *428*, 157.

[28] L. C. Giancarlo, G. W. Flynn, *Acc. Chem. Res.* **2000**, *33*, 491.

[29] R. Lazzaroni, A. Calderone, J. L. Bredas, J. P. Rabe, *J. Chem. Phys.* **1997**, *107*, 99.

[30] R. Harners, J. Hovis, S. Lee, H. Liu, J. Shan, *J. Phys. Chem. B* **1997**, *101*, 1489.

[31] J. Hovis, S. Lee, L. Liu, R. Harners, *J. Vac. Sci. Technol. B.* **1997**, *15*, 1153.

[32] B. C. Stipe, M. A. Rezaei, W. Ho, *Science* **1998**, *280*, 1732.

[33] J. Gaudioso, H. J. Lee, W. Ho, *J. Am. Chem. Soc.* **1999**, *121*, 8479.

[34] J. Shan, Y. J. Wang, R. J. Hamers, *J. Phys. Chem.* **1996**, *100*, 4961.

[35] P. S. Weiss, D. M. Eigler, *Phys. Rev. Lett.* **1993**, *71*, 3139.

[36] X. Lu, K. W. Hipps, *J. Phys. Chem. B* **1997**, *101*, 5391.

[37] N. J. Tao, *Phys. Rev. Lett.* **1996**, *76*, 4066.

[38] K. W. Hipps, X. Lu, X. D. Wang, U. Mazur, *J. Phys. Chem.* **1996**, *100*, 11207.

[39] X. Lu, K. W. Hipps, X. D. Wang, U. Mazur, *J. Am. Chem. Soc.* **1996**, *118*, 7197.

[40] L. Scudiero, D. E. Barlow, K. W. Hipps, *J. Phys. Chem. B* **2000**, *104*, 11899.

[41] L. Scudiero, D. E. Barlow, U. Mazur, K. W. Hipps, *J. Am. Chem. Soc.* **2001**, *123*, 4073.

[42] L. Scudiero, K. W. Hipps, D. E. Barlow, *J. Phys. Chem. B* **2003**, *107*, 2903.

[43] K. W. Hipps, L. Scudiero, D. E. Barlow, M. P. Cooke Jr., *J. Am. Chem. Soc.* **2002**, *124*, 2126.

[44] T. Yokoyama, S. Yokoyama, T. Kamikado, Y. Okuno, S. Mashiko, *Nature* **2001**, *413*, 619.

[45] M. de Wild, S. Berner, H. Suzuki, H. Yanagi, D. Schlettwein, S. Ivan, A. Baratoff, H.-J. Güntherodt, T. A. Jung, *ChemPhysChem* **2002**, *3*, 881.

[46] J. A. A. W. Elemans, M. C. Lensen, J. W. Gerritsen, H. Kerpen, S. Speller, R. J. M. Nolte, A. E. Rowan, *Adv. Mater.* **2003**, *15*, 2070.

[47] S. Yoshimoto, N. Higa, K. Itaya, *J. Am. Chem. Soc.* **2004**, *126*, 8540.

[48] F. Jäckel, W. D. Watson, K. Müllen, J. P. Rabe, *Phys. Rev. Lett.* **2004**, *92*, 188303.

[49] L. Plot, A. Marchenko, J. Wu, K. Müllen, D. Fichou, *J. Am. Chem. Soc.* **2005**, *127*, 6245.

[50] K. Ding, D. Grebel-Köhler, R. Berger, K. Müllen, H.-J. Butt, *J. Mater. Chem.* **2005**, *15*, 3431.

[51] B. Karakaya, W. Claussen, K. Gessler, W. Saenger, A.-D. Schluter, *J. Am. Chem. Soc.* **1997**, *119*, 3296.

[52] S. Yin, C. Wang, X. Qiu, B. Xu, C. Bai, *Surf. Interface Anal.* **2001**, *32*, 248.

[53] G. R. Desiraju, *Angew. Chem. Int. Ed.* **1995**, *34*, 2311.

[54] X. Qiu, C. Wang, Q. Zeng, B. Xu, S. Yin, C. Wang, S. Xu, C. Bai, *J. Am. Chem. Soc.* **2000**, *122*, 5550.

[55] X. Qiu, C. Wang, S. Yin, Q. Zeng, B. Xu, C. Bai, *J. Phys. Chem. B* **2000**, *104*, 3570.

[56] Y. Wei, K. Kannappan, G. W. Flynn, M. B. Zimmt, *J. Am. Chem. Soc.* **2004**, *126*, 5318.

The difference between a chemist and a crystallographer can be compared to two people who try to ascertain what furniture is present in a darkened room; one probes around in the dark breaking the china, the other stays by the door and switches on the light!

J. D. Dunitz

8. Formation of metallomacrocycles with tpy metal-binding domains

Metallosupramolecular chemistry is concerned with the construction of complex structures using the interaction of specific metal-binding domains with appropriate metal centres.[1-3] Increasingly, the 2,2':6',2''-terpyridine (tpy) metal-binding domain is being used as an assembly motif; in part this is because tpy forms stable complexes with almost every metal centre in the periodic table,[4] and partly because of the stereogenic properties of [M(tpy)$_2$] motifs compared to the more commonly encountered [M(bpy)$_3$] or [M(phen)$_3$] (bpy = 2,2'-bipyridine, phen = 1,10-phenanthroline) motifs.[5, 6] Complexes of the type [M(tpy)$_2$] are thermodynamically stable, but may be kinetically inert or labile, allowing, respectively, for self-assembly strategies involving the interaction of tpy metal-binding domains with metal centres or the use of building blocks containing [M(tpy)$_2$].

The advantage of metal-orientated approaches to self-assembly is the range of metals available for experimentation, their sensitivity to subtle changes in ligand properties, and the defined geometry at the metal centre, which allows significant structural predetermination. Additionally, transition metals can adopt a number of easily accessible oxidation states, the properties of which differ dramatically.

The self-assembly of metallomacrocycles from metal centres and di- or polytopic ligands with varying degrees of pre-organisation is currently an area of intense interest.[7-12] Tpy–metal binding domains have been utilised for the formation of metallomacrocycles with both highly pre-organised and flexible spacers.[13-26]

In this Chapter, two novel homoditopic ligands are presented, which spontaneously form macrocycles by reacting with metal(II) salts. The two tpy units of the first ligand are linked by a short disulfide bridge and the second ligand has a long and flexible alkyl-chain between the two tpy units.

8.1 Synthesis and solid-state characterisation of a pre-organised homoditopic disulfide 22 and a metallomacrocycle out of 22

8.1.1 Synthesis and crystal structure analysis of compound 22

The formation of compound **9** has been discussed in Section 4.1.1. In the course of characterising compound **9**, it was noted that solutions were air sensitive and over a period of time a new tpy containing species was observed in the ^{1}H NMR spectrum. Since the new compound was colourless and showed tpy signals in the ^{1}H NMR spectrum that were indicative of a symmetrical species, it was assumed that the product was the oxidised disulfide compound **22** (Scheme 8.1). To confirm this hypothesis, disulfide **22** was synthesised from compound **9** by oxidation with iodine under aqueous alkaline conditions (Scheme 8.1). Since compound **9** is soluble in basic aqueous solution and the disulfide product **22** was not soluble in water, the resulting white precipitate could be isolated by filtration in 63% yield after washing with water, ethanol and diethyl ether.

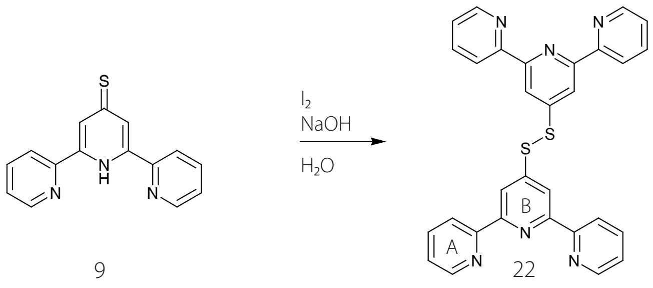

Scheme 8.1 Synthesis of compound **22** by oxidation of **9** with iodine in 63% yield. Ring labels are used for NMR spectroscopic assignments.

The ^{1}H NMR spectrum of compound **22** showed it to be highly symmetrical, with the terminal rings of each tpy ring equivalent and the two tpy moieties equivalent on the NMR timescale. The ^{13}C NMR spectrum showing 8 signals (3 quarternary carbons) and with ESI-MS experiments showing at *m/z* 529 the mass of $[M + H]^+$.

Furthermore, single crystals were obtained from an ethanolic solution as white needles. The X-ray determination of compound **22** confirmed the proposed structure (Figure 8.1).

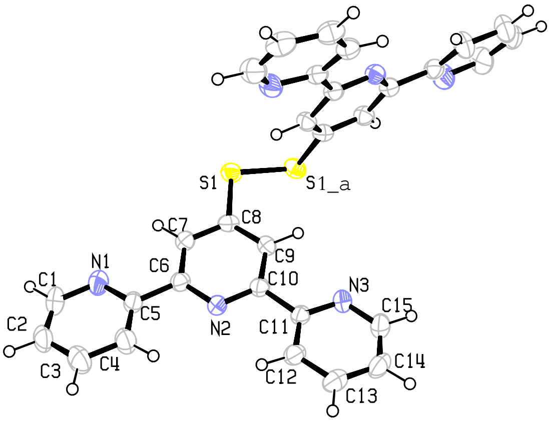

Figure 8.1 The molecular structure of compound **22**. The two halves of the molecule are symmetry related. Important bond lengths and angles: S1–S1_a = 2.0281(12), S1–C8 = 1.774(2), N1–C1 = 1.344(3), N1–C5 = 1.339(3), N2–C6 = 1.345(3), N2–C10 = 1.342(3), N3–C11 = 1.346(3), N3–C15 = 1.338(3), C1–C2 = 1.363(4), C2–C3 = 1.378(4), C3–C4 = 1.385(3), C4–C5 = 1.382(3), C5–C6 = 1.491(3), C6–C7 = 1.391(3), C7–C8 = 1.391(3), C8–C9 = 1.394(3) Å; S1_a–S1–C8 = 105.41(8), S1–C8–C7 = 116.43(17), S1–C8–C9 = 124.11(16), C4–C5–C6 = 121.5(2), C1–N1–C5 = 117.1(2), C6–N28–C10 = 117.81(18), N1–C5–C4 = 122.4(2), N2–C6–C7 = 123.0(2), N3–C11–C10 = 116.2(2), N1–C5–C6 = 116.2(2)°.

The structure revealed a number of interesting features. Firstly, the tpy domains adopt the expected *trans, trans*-conformation although they are not completely planar with the angles between the least squares planes of the terminal and central rings of 9.1 and 10.0°. Bond lengths and angles were typical of tpy ligands. The S–S bond length was 2.0281(12) Å. The angle between the least squares planes of the two central pyridine rings is 78.1° and the C–S–S–C torsion angle is 90.8° (Figure 8.2). This near orthogonal torsion angle made this ligand ideally preorganised to act as homoditopic ligand.

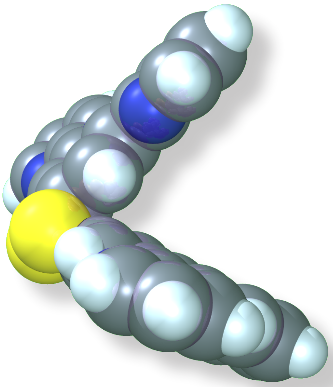

Figure 8.2 Side-view of ligand **22**. The two tpy units are near to being orthogonal to each other.

The packing of molecules of **22** showed extensive coplanarity with interplanar distances of 3.4 Å between the least squares planes of adjacent tpy moieties (Figure 8.3). However, no π-stacking interactions between pyridine units were observed in the crystal structure.

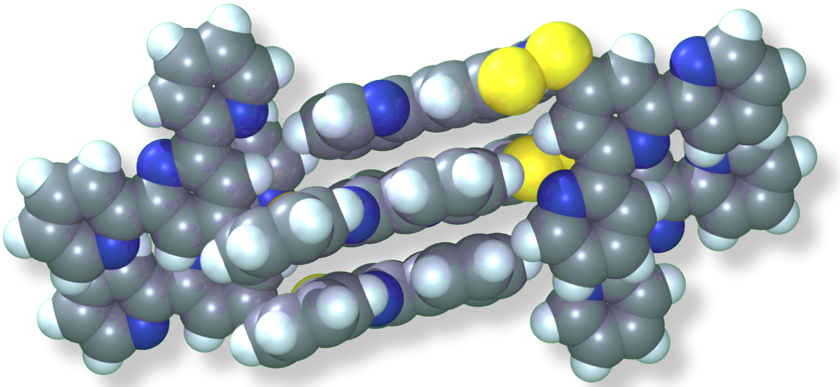

Figure 8.3 The molecules of **22** were coplanar to each other in the crystal structure.

8.1.2 Formation of a metallomacrocycle from preorganised homoditopic ligand 22

The reaction of **22** with $Fe(BF_4)_2{\cdot}6H_2O$ in a 5.4 mM solution of methanol:dichloromethane (2:1) resulted in the formation of a purple solution typical of a $[Fe(tpy)_2]^{2+}$ chromophore. No TLC system in which the obtained iron complexes would moved from the bottom could be found. The ESI-MS of an acetonitrile solution of this solid only exhibited fragments containing one ligand and one iron atom. The ^1H NMR spectrum of a CD_3CN solution of the purple solid showed a single tpy environment and was slightly broadened (Figure 8.4), although not as broad as typical $[Fe(tpy)_2]^{2+}$ metallopolymers. Furthermore, the so-obtained solid was soluble in acetonitrile which was a strong indication of the formation of a macrocycle and not of polymeric material.

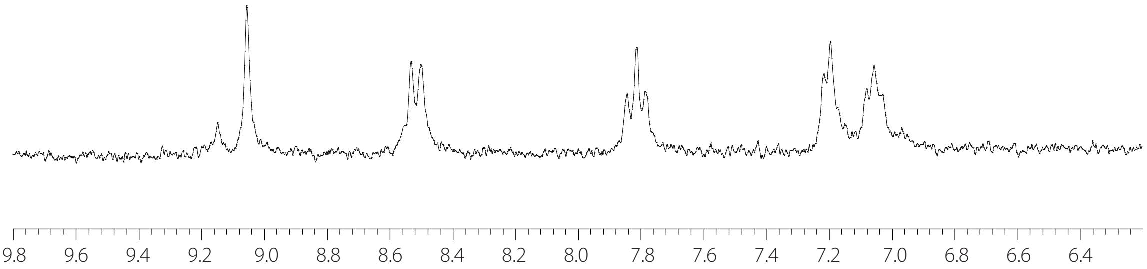

Figure 8.4 The ^1H NMR spectrum of the macrocyclic complex obtained after recrystallisation in acetonitrile:diethyl ether. Only one set of tpy signals was observed.

After ESI-MS and ^1H NMR spectroscopic experiments, it was not possible to confirme which macrocycle was present in solution. Therefore, crystallisations were carried out in order to get single crystals. Finally, a single, very thin, deep purple plate crystallised out of a acetonitrile:diethyl ether solution. The crystal structure was determined by single crystal X-ray analysis. Since the NMR spectra of the recrystallised material and the crude material were similar, it was assumed that the compound measured in solid-state using X-ray difraction was the same macrocycle as in solution. In addition, the rate of ligand exchange for $[Fe(tpy)_2]^{2+}$ complexes is in the order of days to weeks, as it was observed in the study presented in Section 8.2.2.

The quality of the data did not allow refinement to a reasonable level and the structure must be regarded as preliminary, although the macrocyclic part could be refined reasonably well. Data for the solid-state structure of $[\mathbf{Fe_4(22)_4}][\mathbf{BF_4}]_8$ were collected at 153 K and were refined to $R = 0.1621$. As the electron density distribution did not indicate any more clearly identifiable features, the refinement was left at this stage knowing that there were more solvent molecules present in this structure.

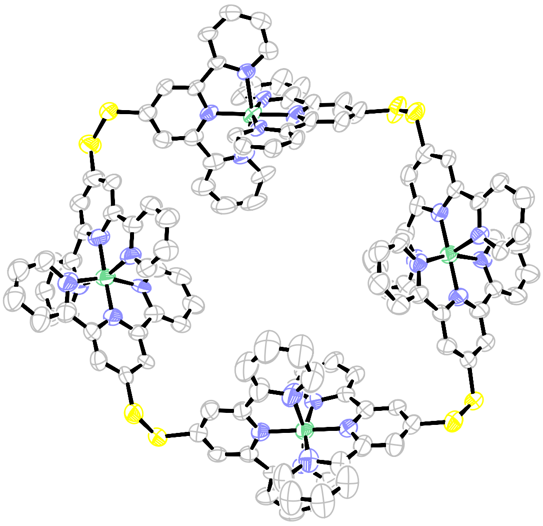

Figure 8.5 ORTEP presentation of the partial structure of the $\mathbf{[Fe_4(22)_4]}^{8+}$ cation in $\mathbf{[Fe_4(22)_4][BF_4]_8}$. Due to the poor structure quality, bond lengths and angles are not given.

The structure of the cation (Figure 8.5) revealed the formation of a [4+4] metallomacrocycle of formula $[\mathbf{Fe_4(22)_4}]^{8+}$. The tetrafluoroborate counterions were ordered and exhibited no close contacts with the octacation. There were considerable amounts of disordered solvent in the lattice, modelled incompletely with 5½ acetonitrile, 1½ diethyl ether, one methanol and 4½ water molecules. The presence of so many solvent molecules was compatible with the elemental analysis data of the bulk microcrystalline material which showed a total of 14 water molecules per tetranuclear formula unit. Figure 8.6 shows the molecular structure of the cation along with the anions and the resolved solvents molecules.

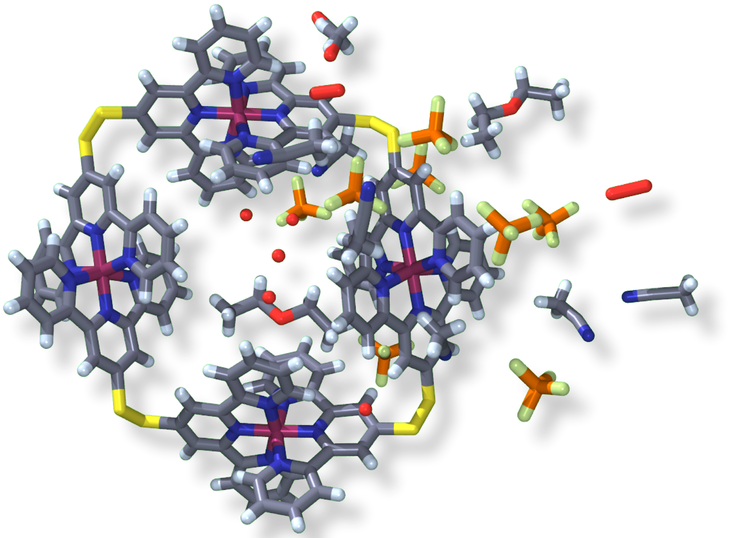

Figure 8.6 The molecular structure of **[Fe$_4$(22)$_4$][BF$_4$]$_8$**. None of the counter-ions was trapped within the cavity.

The four iron(II) atoms lie approximately in a plane, with none of the atoms being more than 0.24 Å from the least squares plane of the four centres. The Fe···Fe distances were between 9.7 and 11.0 Å and the [Fe$_4$(**22**)$_4$]$^{8+}$ coordination domains had typical metrical parameters. The C–S–S–C torsion angles lay between 80 and 99°, indicating a significant degree of flexibility within the ligand, and highlighting the danger of predicting the nuclearity of metallocycles formed with relatively conformationally free ligands.[9] Views from the metallocyclic cation from above and from the side are presented in Figure 8.7 and Figure 8.8. The macrocyles are chiral, as can be recognised in both Figures; the disulfide–tpy units had always the same handedness with respect to the centre of the cycle.

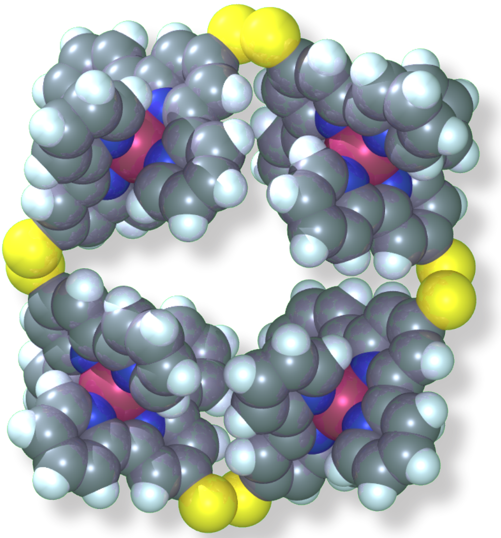

Figure 8.7 Space-filling representation of the metallocyclic cation **[Fe$_4$(22)$_4$]$^{8+}$** from above.

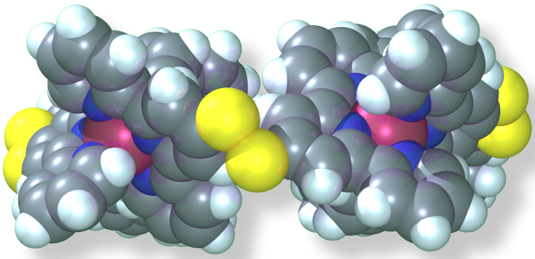

Figure 8.8 A side-view form the metallocycle **[Fe_4(22)$_4$]$^{8+}$**. The iron(II) atoms centres lie approximately in a plane.

The macrocycles [Fe_4(**22**)$_4$]$^{8+}$ were packed in layers. S···S interactions between adjacent molecules in one direction were observed with short S···S distances of 3.59 Å (Figure 8.9), and therefore shorter than the van der Waals distance of 3.70 Å.

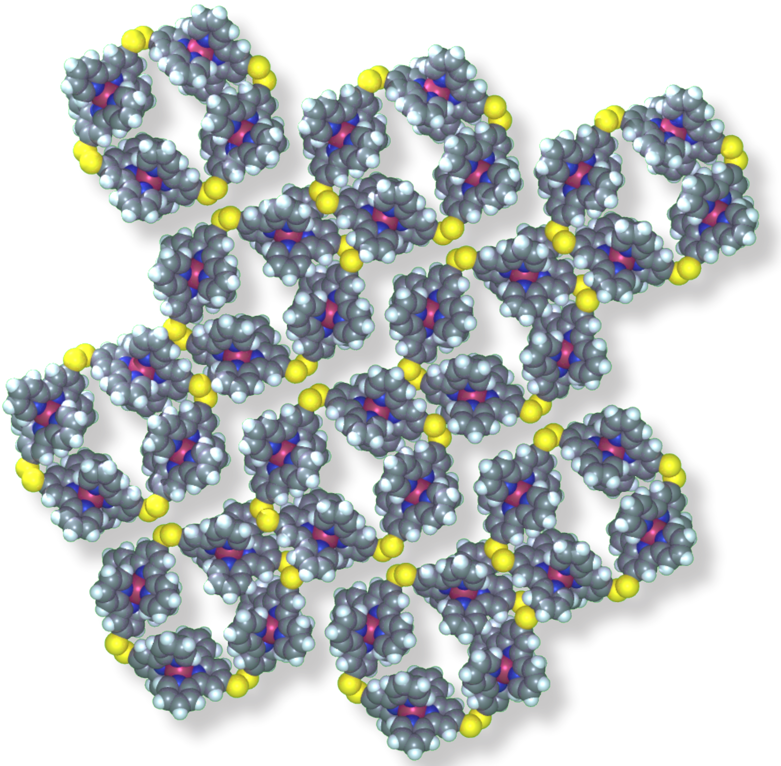

Figure 8.9 One layer from the packing of molecules of cation **[Fe_4(22)$_4$]$^{8+}$**. The chirality of the metallomacrocycles alters within one row from molecule to molecule. The counter-ions and solvent molecules are omitted for clarity.

The counter-ions and most solvent molecules were placed between the layers, thus no short contacts between cations of adjacent layers are possible (Figure 8.10).

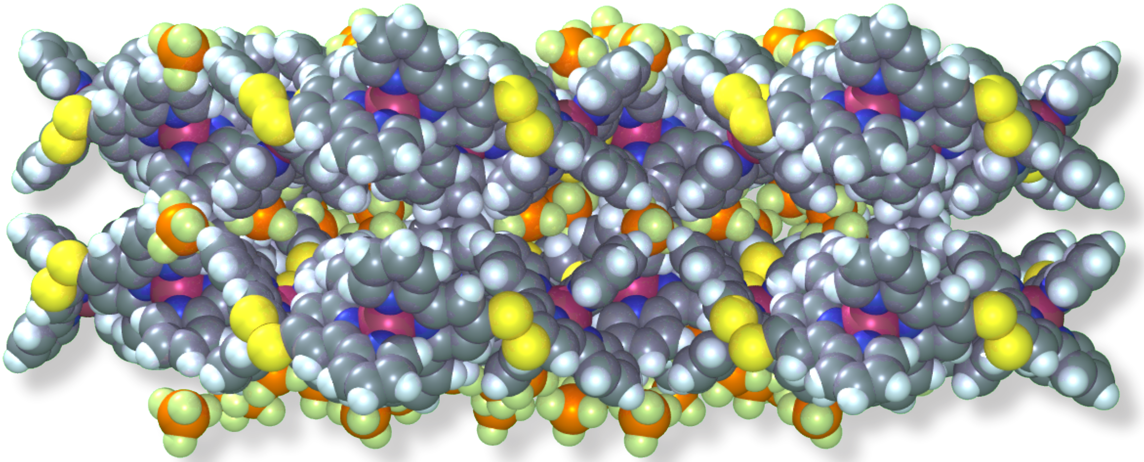

Figure 8.10 Two layers of cations $\mathbf{[Fe_4(22)_4]^{8+}}$. The $[BF_4]^-$ anions are placed between the layers. The solvent molecules are omitted for clarity.

8.2 Studies of macrocycles containing homoditopic tpy ligands with alkyl-chain linkers

In Section 8.1, the formation of a [4+4] macrocycle was discussed using a homoditopic tpy ligand with a short disulfide linker. In this section, a hexadecyl unit was used as a linker to study the possible formation of macrocycles. Homoditopic tpy ligands with long-chained polyethyleneoxy linkers are known and form [2+2] macrocycles either by complexation with a ruthenium(II) salt in a two-step process[16, 17]

In this Section, metallomacrocycle studies were conducted with iron(II), cobalt(II) and ruthenium(II) metal centres.

8.2.1 Synthesis, crystal structure and monolayer analysis of compound 23

Ditopic ligand **23** was synthesised by coupling hexadecane-1,16-diol with 4'-chloro-2,2':6',2''-terpyridine[27] using potassium hydroxide as base in DMSO (Scheme 8.2).[28, 29] The crude material was purified by recrystallisation from methanol yielding **23** in 93.5% as a white powder.

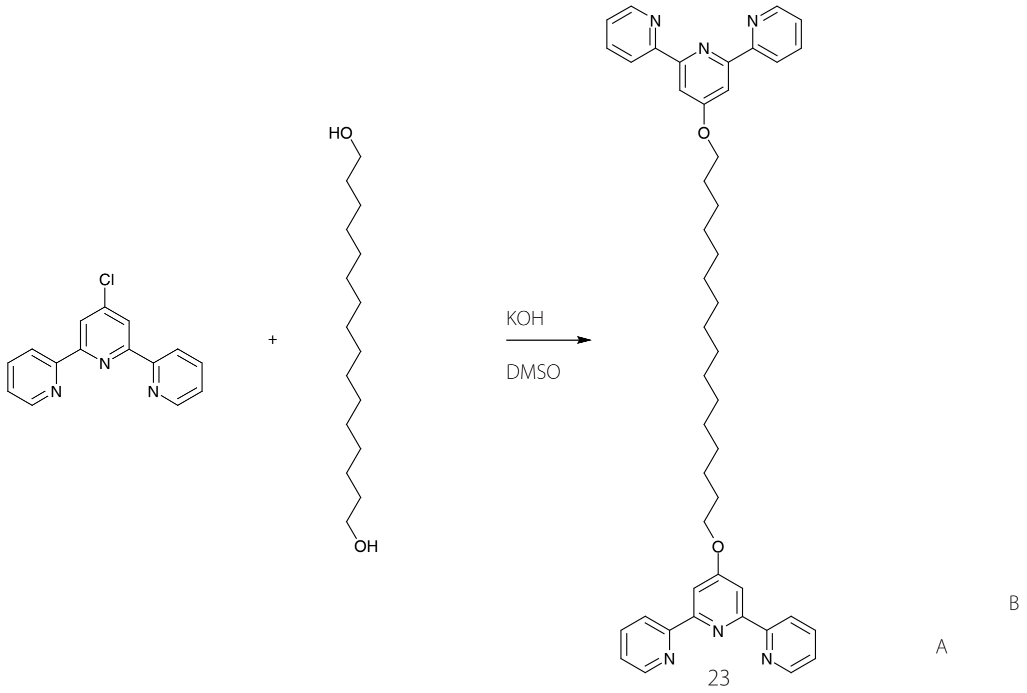

Scheme 8.2 Synthesis of compound **23**. Ring labels are used for NMR spectroscopic assignments.

The ^{1}H NMR spectrum of compound **23** showed it to be highly symmetrical, with five signals for the tpy rings and the characteristic signal for $\mathrm{H}^{\mathrm{OC}H_2\mathrm{CH}_2}$ as a triplet at δ 4.22 ppm. The major peaks at *m/z* 723 and 745 in the MALDI-TOF mass spectrum were assigned to $[\mathrm{M} + 2\mathrm{H}]^+$ and $[\mathrm{M} + \mathrm{Na} + \mathrm{H}]^+$ respectively.

By slowly evaporating a chloroform solution of compound **23**, colourless needles were obtained, which were analysed using X-ray crystallography (Figure 8.11).

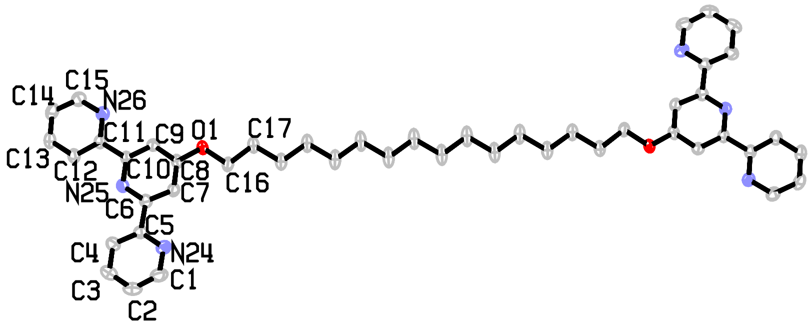

Figure 8.11 Molecular structure of compound **23**. For clarity, hydrogen atoms are omitted and selected atoms only are numbered. Atoms on right hand side are related to left hand side by centre of symmetry. Important bond lengths and angles: O(1)–C(8) = 1.359(3), O(1)–C(16) = 1.443(3), C(16)–C(17) = 1.506(4), C(7)–C(8) = 1.383(4), C(6)–C(7) = 1.394(3), C(5)–C(6) = 1.502(3), N(24)–C(5) = 1.343(4), N(24)–C(1) = 1.336(4), N(25)–C(6) = 1.338(3), N(25)–C(10) = 1.345(3), N(26)–C(11) = 1.340(3), N(26)–C(15) = 1.346(4) Å; C(8)–O(1)–C(16) = 117.2(2), O(1)–C(16)–C(17) = 108.2(2), O(1)–C(8)–C(7) = 124.4(2), O(1)–C(8)–C(9) = 116.0(2), C(10)–N(25)–C(6) = 117.7(2), C(1)–N(24)–C(5) = 116.8(3), C(11)–N(26)–C(15) = 116.8(2), C(11)–C(10)–N(25) = 115.9(2), C(5)–C(6)–N(25) = 115.8(2)°.

The centrosymmetric structure of **23** revealed some interesting features. The most remarkable characteristic was the observation of a planar arrangement of the molecule with the hexadecyl-chain in an all-*trans*-conformation (Figure 8.12). The tpy domains adopted a *trans, trans*-conformation, they were nearly planar with least squares planes angles between terminal and central rings of 8.1 and 4.9°. The C(8)–O(1)–C(16) angle of 117.2(2)° exhibited the sp^2-character of the oxygen.

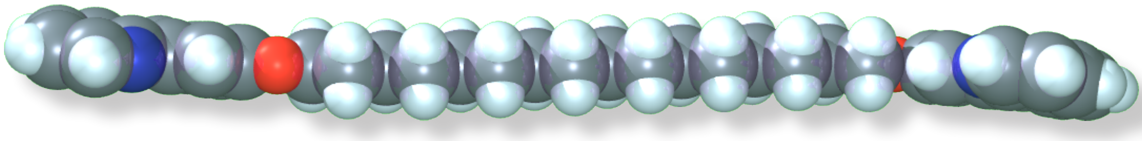

Figure 8.12 Side-view of compound **23**. The molecule has a flat arrangement.

Although the single molecules were shown to be flat, there was not layered structure within the packing as has been observed during the course of this thesis for flat molecular structures of Fréchet-type dendrimers with octyl end-groups (planar arrangement of molecules are discussed in Chapter 4 and Chapter 5, respectively). The molecules were arranged in rows of stacked molecules (Figure 8.13). Within one row of molecules, the shortest contact between protons of the alkyl-chains of adjacent molecules is 2.6 Å. No classical π–π stacking interactions between aromatic rings were detected due to an offset of pyridine rings of adjacent molecules.

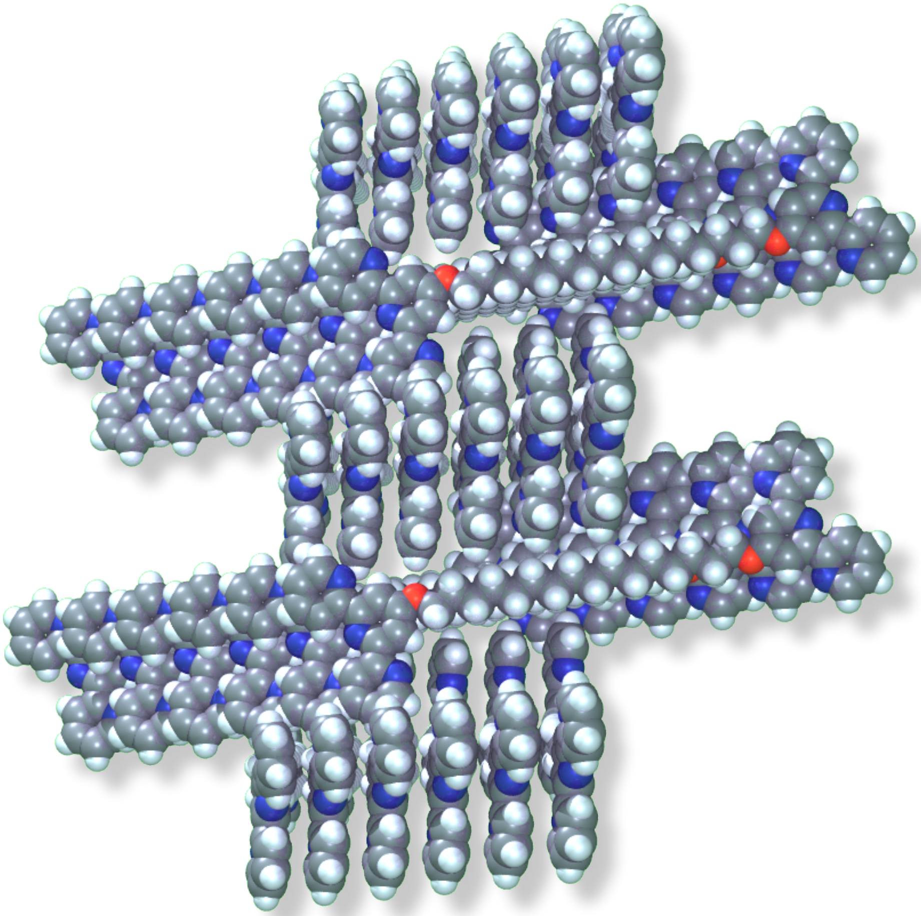

Figure 8.13 Molecular packing of compound **23**. The flat molecules did not exhibit a layered arrangement, but showed rows with parallel molecules.

In the course of STM studies, the 2D self-assembly properties of compound **23** on a graphite surface were examined. Good quality and extensive self-assembled monolayers of **23** were obtained upon allowing hexane solutions to evaporate under ambient conditions. In STM images of self-organised monolayers of molecule **23**, multiple domain formation was observed with a lamellar arrangement of **23.** The rows were an indication of a lamellar packing with the hexadecyl-chains in the darker region (Figure 8.14).

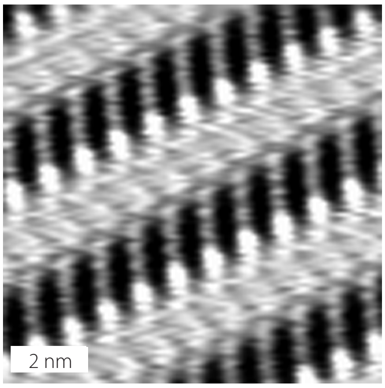

Figure 8.14 An averaged STM image of a monolayer of compound **23** on HOPG. The dodecyl-chains are situated in the darker regions and could be seen. Scan parameters: 10 nm x 10 nm, $U_b = -700$ mV, $I_t = 8$ pA, averaged over 78 points.

The analysis of the monolayer was facilitated by the fact that the hexadecyl-chains were visible. They showed the expected all-*trans*-conformation. The STM image indicated that all overlaid molecules possessed the same orientation since the structure was assigned to a *p*1 plane group. Unfortunately, the solid state structure did not possess a layered arrangement which could be compared with the monolayer on graphite as has been done previously in Chapter 4 and Chapter 5. However, as the single molecules in the crystal structure were flat, they were taken as a model to superimpose the STM image. A possible arrangement is shown in Figure 8.15.

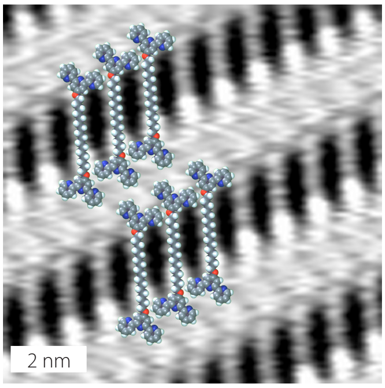

Figure 8.15 STM image from Figure 8.14 with overlaid molecules taken from the single crystal structure.

8.2.2 Ligand lability in Fe(II) complexes of tpy

The macrocycles presented in this Section involve ruthenium(II), cobalt(II) and iron(II) salts. Ruthenium(II) bis(tpy) complexes are known to be kinetically stable in contrast with cobalt(II) bis(tpy) complexes, which are kinetically labile.[30] This Section deals with a preliminary study of the kinetic lability of iron(II) bis(tpy) complexes. In order to study the lability of iron(II) bis(tpy) complexes, the heteroleptic complex **[Fe(10)(tpy)][BF$_4$]$_2$** was prepared by mixing two ligands (tpy and **10**) with Fe(BF$_4$)$_2$·6H$_2$O (Scheme 8.3). Crude ^{1}H NMR spectroscopy revealed the statistical ratio 1:2:1 of the three possible complexes. Spot TLC showed the presence of three purple compounds. 2D spot TLC proved the stability of each of these three compounds over chromatography on silica. A complex with ligand **10** has been chosen since it could be shown that complexes bearing Fréchet-type dendrimers with pendant octyl-groups can be purified by chromatography over silica using conventional solvents (Chapter 6). The three complexes had very different polarities, they were separated by column chromatography using dichloromethane:methanol (10:1) as eluent. The compound of the first fraction was consistent with the complex **[Fe(10)$_2$][BF$_4$]$_2$** discussed in Chapter 6. The second fraction contained the heteroleptic complex **[Fe(10)(tpy)][BF$_4$]$_2$**. The last purple fraction which was assumed to contain [Fe(tpy)$_2$][BF$_4$]$_2$ did not move on the column using this solvent system.

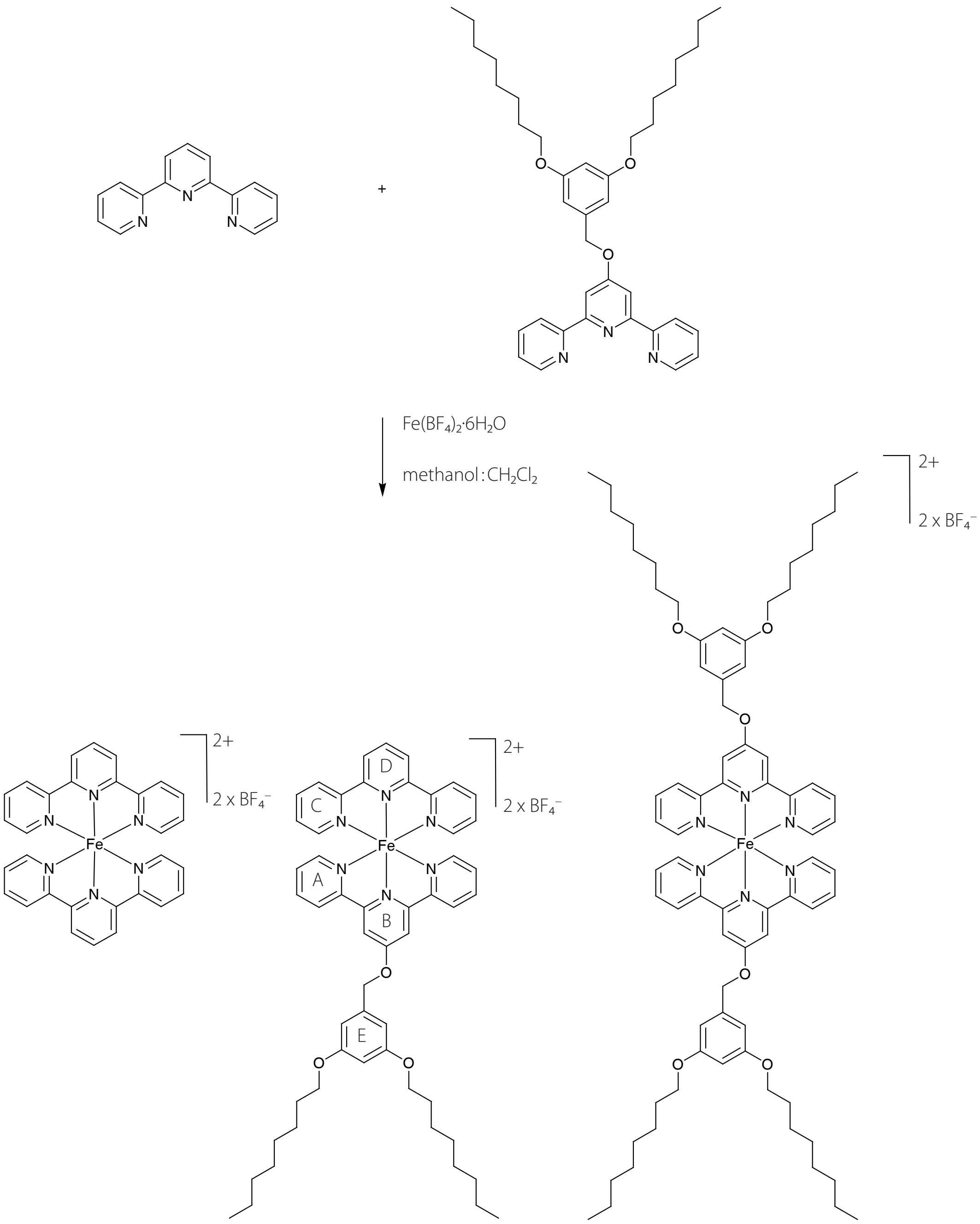

Scheme 8.3 Formation of heteroleptic compound **[Fe(10)(tpy)][BF$_4$]$_2$** by mixing the two ligands with Fe(BF$_4$)$_2$·6H$_2$O. A statistical ratio of 1:2:1 of these three possible complexes was obtained. Ring labels are used for NMR spectroscopic assignments.

Compound **[Fe(10)$_2$][BF$_4$]$_2$** was characterised using standard methods. The ESI-MS spectra showed the most intense peak at *m/z* 442 which was assigned as $[M - 2BF_4]^{2+}$.

To study the lability of this complex, ^{1}H NMR spectroscopic studies were carried out in *d*$_3$-acetonitrile. The expected equilibrium of 1:2:1 was achieved after ≈30 days as it can be seen in Figure 8.16.

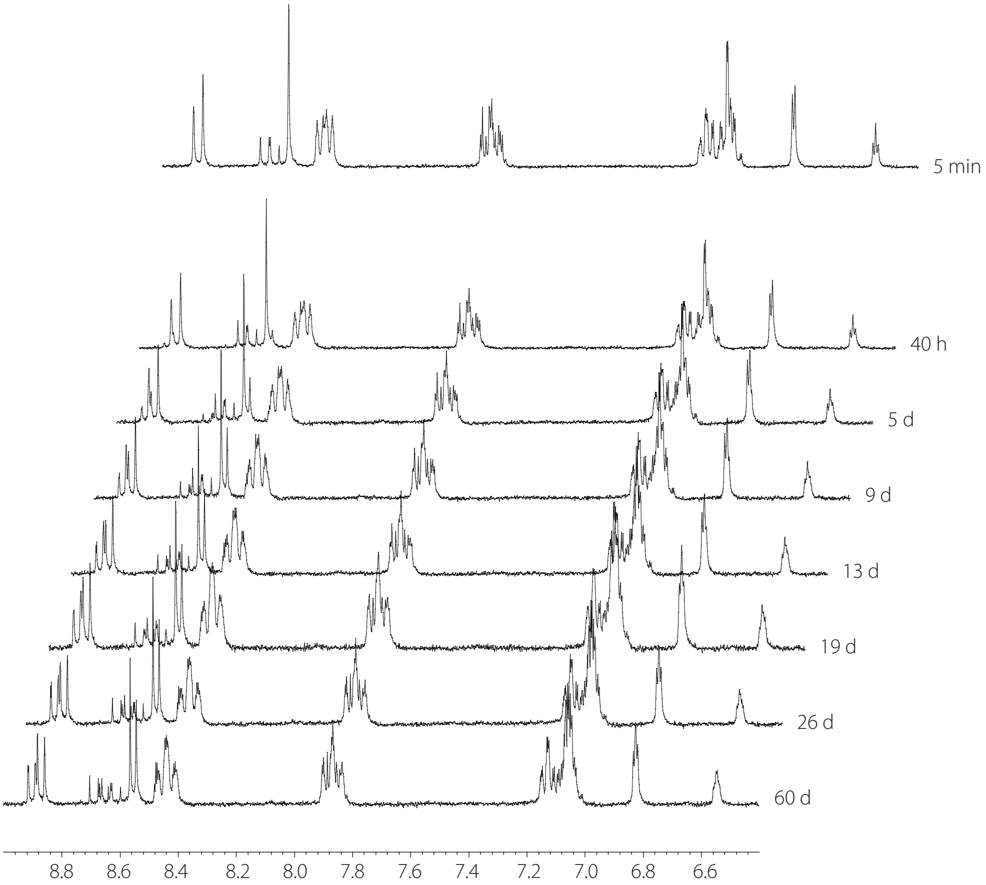

Figure 8.16 ^{1}H NMR spectroscopic studies of compound **[Fe(10)(tpy)][BF$_4$]$_2$**. The equilibrium shown in Scheme 8.3 of 1:2:1 was achieved after ≈30 days.

The information that Fe(II) bis(tpy) complexes are kinetically stable over hours in solution was important when it comes to studying the metallomacrocyclisation of ligand **23** with iron(II) salts studied in the next Section.

8.2.3 Formation of metallomacrocycles using 23 and Fe(II), Co(II) and Ru(II) salts

It was envisaged that metallomacrocycles could be formed from ligand **23** by using a one-step methodology. The reactions were performed in 3–5 mM solution; these conditions are not so dilute as in other metallomacrocycle synthesis.[13, 16] All experiments were carried out on a small scale, and therefore the macrocycles were only characterised by ^1H NMR spectroscopic experiments (ring labels as for the free ligand) and by ESI-MS spectrometry. Further experiments (especially COSY and NOSY) have to be conducted on the metallomacrocyclic products.

8.2.4 Metalomacrocycles containing 23 and ruthenium(II) metal centres

Ruthenium(II) bis(tpy) macrocycles are well known.[16, 17, 20-24] All published macrocycles containing ruthenium(II) bis(tpy) were prepared following a two-step process; the first step involves the reaction of the ligand with two equivalents of ruthenium trichloride in ethanol to form an isolable, dinuclear ruthenium(III) complex $[Cl_3Ru(L)RuCl_3]$ (L = ditopic tpy ligand). This was reacted further with an equimolar amount of the same or another ditopic tpy ligand in the presence of a reducing agent (*N*-ethylmorpholine) affording ruthenium(II) metallomacrocycles or metallopolymers. This two-step methodology to form complexes containing $[Ru(tpy)_2]^{2+}$ motifs has been widely used.[31-36]

[1+1] Metallomacrocycles are not producible using the two-step approach since any macrocycles prepared with the two-step synthetic route possesses an odd number of ligand and metal centres. As shown in Section 6.1.2.3, there are other ways to obtain $[Ru(tpy)_2]^{2+}$ motifs. Whereas the two-step approach is suitable for the construction of heteroleptic ruthenium(II) bis(tpy) complexes, the one-step procedure is generally more efficient. As already mentioned in Section 6.1.2.3, there are two principal ways to obtain $[Ru(tpy)_2]^{2+}$ motifs in one step; firstly, by irradiating two equivalents of tpy ligand with $RuCl_3{\cdot}3H_2O$ in ethylene glycol in a microwave oven, or secondly, by reacting a Ru(II) salt with tpy ligands (Scheme 8.4). For these studies using ligand **23**, both methods were tried out and different results were obtained.

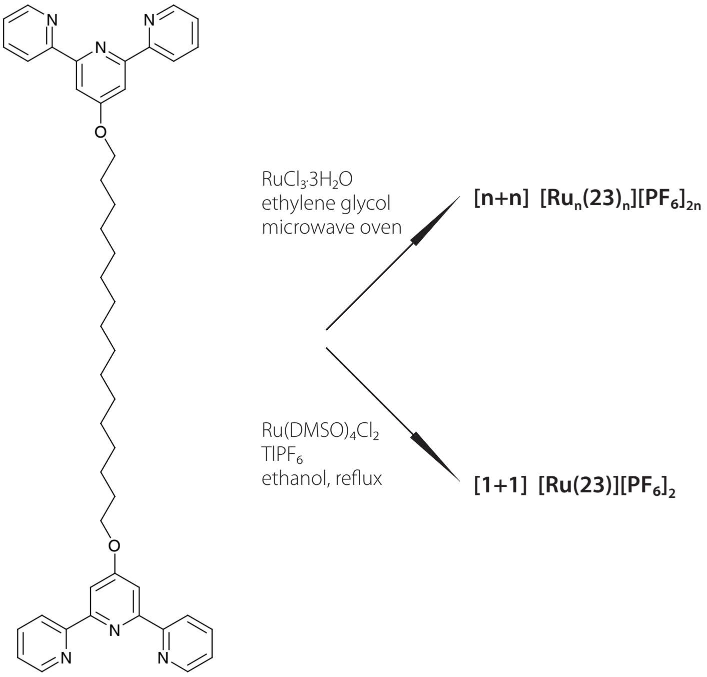

Scheme 8.4 Schematic representation of the two possible routes obtaining **[Ru(23)]$_n$[PF$_6$]$_{2n}$** macrocycles.

By irradiating compound **23** with $RuCl_3{\cdot}3H_2O$ in ethylene glycol (10 mM solution) in a microwave oven for 4 minutes (600 W), an orange suspension was obtained. After addition of water, the insoluble material was separated by filtration and the filtrate treated with NH_4PF_6 afforded a deep orange precipitate. Spot TLC indicated the presence of one product. The ^1H NMR spectrum showed one set of tpy signals with the terminal rings of each tpy ring equivalent. The $H^{OC\mathit{H}_2CH_2}$ signal was a sharp triplet (Figure 8.19). The solubility and the high symmetry revealed by ^1H NMR spectroscopy exposed the presence of *one* metallomacrocyclic product. The size of the macrocycle could not be identified, since no $[\mathbf{Ru}_n(\mathbf{23})_n]^{m+}$ peak could be detected using ESI-MS spectrometry. MALDI-TOF mass spectrometry showed two peaks in the mass range above *m/z* 700; the signal at *m/z* 824 was attributed to [Ru + **23**]$^+$, and at *m/z* 1073 ascribed to [2Ru + **23** + PF$_6$]$^+$. Since MALDI-TOF often fragments molecules, the data were not helpful in the interpretation of the macrocyclic product.

Since Ru(II) bis(tpy) complexes remain stable under STM conditions (see Chapter 6), the self-assembly behaviour on HOPG was studied using STM in order to visualise the macrocycle and thus obtain information about the size of the macrocycle.

Indeed, the compound formed a very stable 2D self-assembly pattern by evaporating a droplet of 0.2 mM solution of the macrocyclic product in acetonitrile on a graphite surface (Figure 8.17).

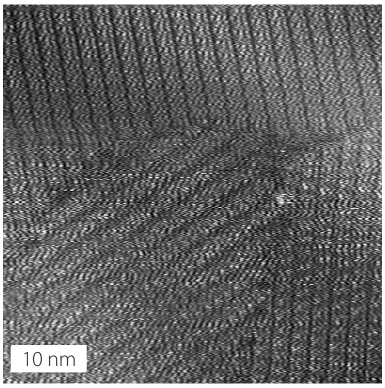

Figure 8.17 An STM image of a monolayer formed from the metallomacrocyclic product formed from $RuCl_3 \cdot 3H_2O$ and **23** by irradiating in a microwave oven. The self-assembled monolayer was formed spontaneously by solution casting using acetonitrile as solvent. Scan parameters: 50 nm x 50 nm, $U_b = -700$ mV, $I_t = 8$ pA.

By expanding and averaging the obtained raw data, high resolved images were obtained (Figure 8.18). Nevertheless, no information could be gained about the obtained ring-size.

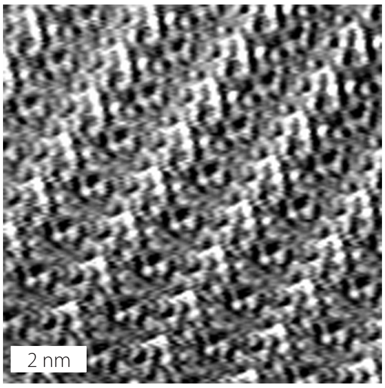

Figure 8.18 Expanded and averaged STM image of a monolayer formed from the metallomacrocyclic product formed from $RuCl_3 \cdot 3H_2O$ and **23** by irradiating in a microwave oven. Although details were visible and unit cells could be determined, no information about the ring-size could be gained. Scan parameters: 10 nm x 10 nm, $U_b = -200$ mV, $I_t = 8$ pA, averaged over 22 positions.

In the second route used to synthesise $[\mathbf{Ru(23)}]_n[\mathbf{PF_6}]_{2n}$, compound **23** was refluxed with $Ru(DMSO)_4Cl_2$ and two equivalents of $TlPF_6$ in ethanol for 18 hours (see Section 6.1.2.3). The yellow solution turned orange after several hours. Spot TLC showed two products, in which the major complex was the first fraction. The two products were separated with chromatography over silica using acetonitrile:sat.aq.KNO_3:water 7:1:0.5 as eluent. ESI-MS revealed clearly the formation of a [1+1] metallomacrocycle as the major product in 50% yield. The most intense signal at *m/z* 411 was assigned to $[Ru + \mathbf{23}]^{2+}$ and the isotopic pattern of a high resolved ESI-MS spectrum matched that simulated.[37] The signal at *m/z* 967 for $[Ru + \mathbf{23} + PF_6]^+$ was less intense. No other signals with a ruthenium isotopic pattern were detected.

The ^1H NMR spectrum showed only two sharp signals in the tpy region, which were assigned to the singlet of H^{3B} and the doublet of H^{6A} (Figure 8.19). The remaining peaks were broadened. In addition, the signal for $H^{OC\mathit{H}_2CH_2}$ was splitted in two broad signals, whereas in the free ligand they appeared as a well-resolved triplet. NOESY and COSY experiments have to be conducted in order to attribute the signals.

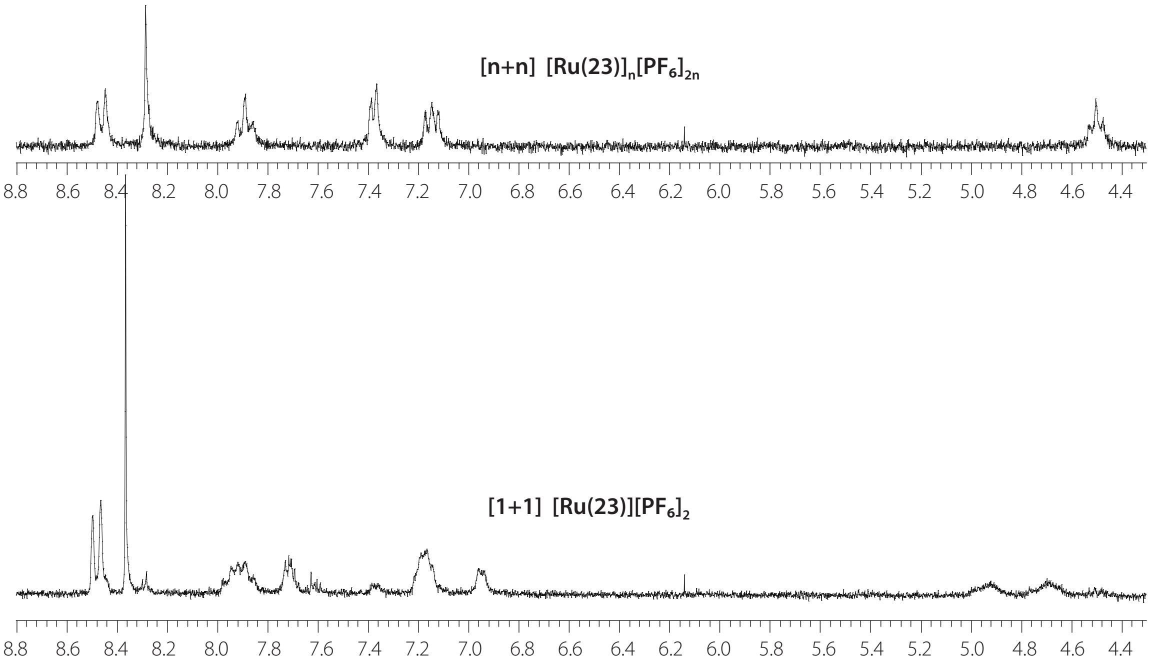

Figure 8.19 ^1H NMR spectra of the $[\mathbf{Ru(23)}]_n[\mathbf{PF_6}]_{2n}$ macrocycles obtained from the microwave reaction (upper spectrum) and from the reaction of **23** with $Ru(DMSO)_4Cl_2$ (lower spectrum).

An attempt to grow crystals suitable for X-ray diffraction studies failed. Semi-empirical modelling at the PM3 level of the [**Ru**(**23**)]$^{2+}$ cationic macrocycle showed a conformationally restricted [1+1] complex in which the alkyl unit was locked into a cleft between the two tpy ligands (Figure 8.20). The short spacer means that the alkyl was locked on one side of the complex in such a way that the tpy terminal rings are non-equivalent.[19]

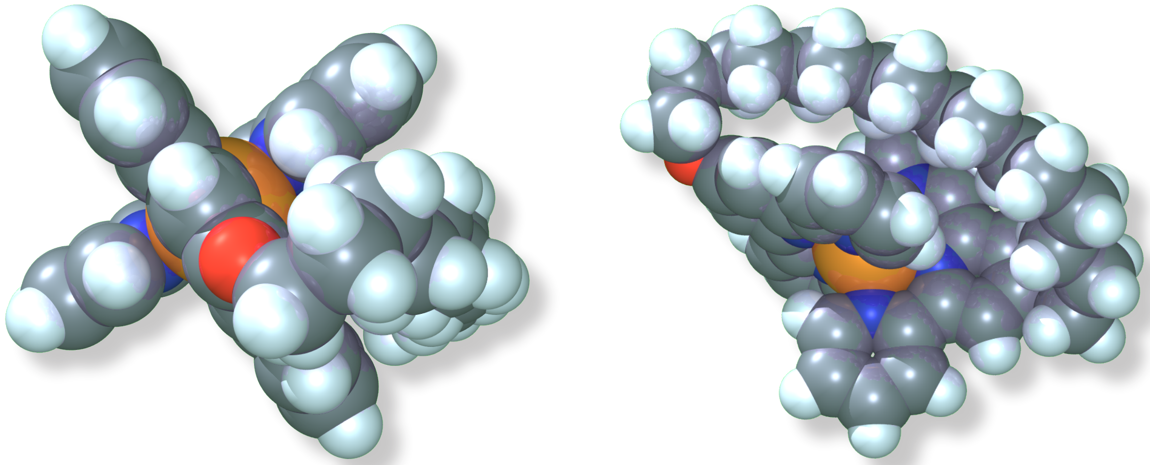
(a) (b)

Figure 8.20 (a) Front-view and (b) side-view of a molecular model of the **[Ru(23)]**$^{2+}$ cationic macrocycle. The alkyl unit was locked into a cleft between the two tpy ligands and this makes the macrocycle chiral.[19]

The locked alkyl-chain makes the macrocycle chiral;[19] this loss in symmetry was proven by the splitting of some signals in the ^{1}H NMR. Although the [1+1] macrocycle was the *kinetic* product – the *thermodynamic* product was the [2+2] macrocycle, as will be shown later – it remained stable over months in solution. This gives support for the kinetic stability of [Ru(tpy)$_2$]$^{2+}$ motifs.

The solid-state properties of the [1+1] metallomacrocyclic product could not be investigated by X-ray crystallography because single crystals could not be obtained. Since the ruthenium(II) metallomacrocycle obtained from microwave conditions showed spontaneous formation of self-assembled monolayers on graphite, STM studies of monolayer formed from the [1+1] macrocycle were conducted. The monolayers on HOPG were formed by solution casting using acetonitrile as solvent. Figure 8.21 shows a typical STM image obtained.

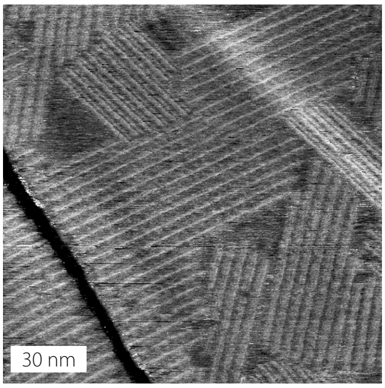

Figure 8.21 An STM image of a monolayer of the macrocyclic product **[Ru(23)][PF$_6$]$_2$** formed from Ru(DMSO$_2$Cl$_2$ and **23** by refluxing in ethanol. On the left, an irregularity from the graphite is visible. Scan parameters: 150 nm x 150 nm, U_b = −300 mV, I_t = 13 pA.

Domains consisting of rows were formed of a size between 20 nm x 20 nm and 100 nm x 100 nm. The monolayer could only be visualised by measuring with bias voltages under −400 mV. By expanding and averaging STM images, good quality images were obtained (Figure 8.22).

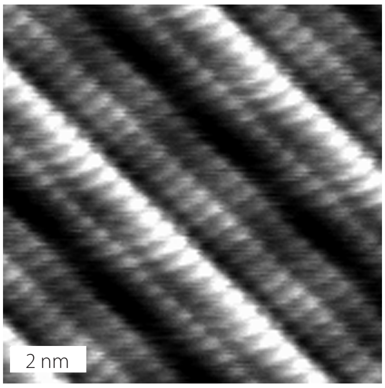

Figure 8.22 An expanded and averaged STM image of the macrocyclic product **[Ru(23)][PF$_6$]$_2$** formed from Ru(DMSO$_2$Cl$_2$ and **23** by refluxing in ethanol. Different intensities of protrusions were visible within a row. Scan parameters: 10 nm x 10 nm, U_b = −180 mV, I_t = 15 pA, averaged over 33 positions.

The analysis of the monolayered arrangement has not been satisfactory solved so far. The minimised models shown in Figure 8.20 were taken to superpose the STM image. One possible molecular ordering is shown in Figure 8.23. In this arrangement, the macrocycles form rows consisting of only one enantiomer. The molecular chirality of each row alternates having final racemic domains.

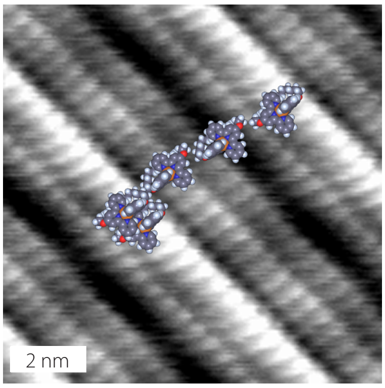

Figure 8.23 Molecular models presented in Figure 8.20 of the [1+1] macrocyclic product formed from Ru(DMSO$_2$Cl$_2$ and **23** by refluxing in ethanol are superimposed to the STM image of Figure 8.22. In this ordering, each row consists of a different enantiomer.

8.2.5 Metallomacrocycles containing 23 and iron(II) metal centres

Iron(II) salts react much faster with tpy ligands than ruthenium(II) salts.[4] As shown in Section 8.2.2, the iron(II) bis(tpy) complexes are kinetically stable. No fast ligand exchange occurred in the study presented in Section 8.2.2. Since the reaction time was only 30 minutes at room temperature, no ligand exchange was expected during the reaction time. However, it was not clear how the kinetic lability of the [Fe(tpy)$_2$] unit behaves in strained systems, e. g. in a [1+1] macrocycle as shown in Figure 8.20.[19] Furthermore, it appears as though chloride ions have an effect on the ligand lability.[30]

Metallomacrocycles containing [Fe(tpy)$_2$]$^{2+}$ motifs are known.[15, 19, 20] In one case,[15] the macrocycle changed during the reaction from a polymeric material to a [4+4] or [3+3] macrocycle which remained stable in solution over many days.

The synthesis of [Fe(tpy)$_2$]$^{2+}$ complexes was quite straightforward. Ligand **23** was stirred at room temperature with one equivalent of $FeCl_2 \cdot 4H_2O$ in methanol:dichloromethane (5:1). The concentration (5 mM) was similar to that used for the ruthenium(II) macrocycle (Section 8.2.4). Mixing resulted in the immediate formation of a purple solution, characteristic of the [Fe(tpy)$_2$]-chromophore formation. After stirring for 30 minutes at room temperature, NH_4PF_6 was added, which gave rise to the formation of a purple precipitate. This was collected by filtration. Figure 8.24 shows the ^{1}H NMR spectrum of the crude material. The ^{1}H NMR spectrum of this compound showed it to be highly symmetrical, with the terminal tpy rings being equivalent. The presence of a small amount of impurity was visible in the spectrum. The compound was purified by column chromatography (Figure 8.24).

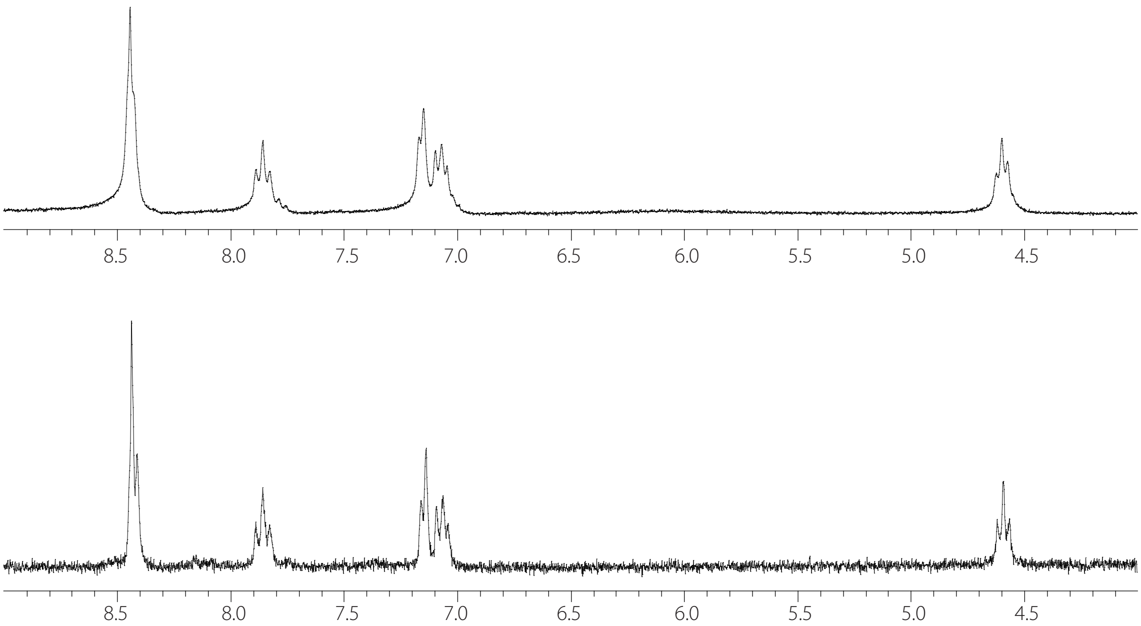

Figure 8.24 The upper ^{1}H NMR spectrum was taken just after the isolation of the PF$_6^-$ salt without any further purification. The impurities observed at the base of some signals could be removed by column chromatography (down). The lower resolution of the upper spectrum was due to worse shimming.

To determine the macrocyclic size of the cation, ESI-MS spectrometry of an acetonitrile solution of the metallomacrocycle was conducted. The triply charged ion at *m/z* 585 was attributed to [2x**23** + 2Fe + PF$_6$ +F + K]$^{3+}$.

The spectrum could not be ascribed to a specific species; ESI-MS experiments carried out at lower temperature did not change significantly the spectrum. It is assumed that a [2+2] metallomacrocycle was formed, due to the symmetrical tpy units confirmed in the ^{1}H NMR spectrum. Further proof of the existence of the [2+2] metallomacrocycle has to be found.

The complex maintained its structural integrity in acetonitrile solution with no evidence of redistribution or equilibration to any other cyclic species over many days, in sharp contrast to the previously reported example of [3+3] and [4+4] iron(II) bis(tpy) metallomacrocycles.[20]

8.2.6 Metallomacrocycles containing 23 and cobalt(II+III) metal centres

Cobalt(II) bis(tpy) complexes are the most labile of the three studied metal(II) complexes. [Co(tpy)$_2$] complexes showed to change their ligands within seconds to minutes.[30] Therefore, the thermodynamic product was expected to be the only present species. Due to the paramagnetic low-spin d^7 metal centre of cobalt(II) complexes, the signals are dispersed more widely in the ^{1}H NMR spectrum.[38-41] The number of different species can hence be assigned more easily using ^{1}H NMR spectroscopy.

After adding compound **23** to a 3 mM methanolic solution of $CoAc_2 \cdot 4H_2O$, the solution immediately turned deep orange. The so-obtained complex was precipitated by anion exchange with NH_4PF_6. A solution of the precipitate indicated the presence of a single compound in the ^{1}H NMR spectrum (Figure 8.25).

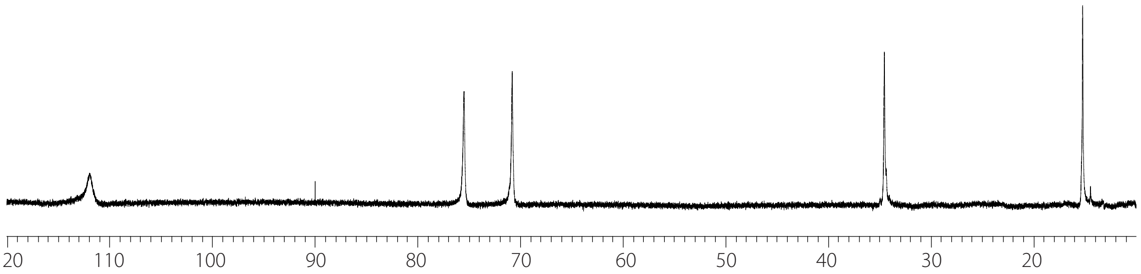

Figure 8.25 ^{1}H NMR spectrum of the cobalt(II) macrocycle. The spectrum shows the range between δ 10 and 120 ppm containing four tpy signals and the H^{OCH_2} signal.

The ^{1}H NMR spectrum of this compound showed the presence of a symmetrical species, with the terminal rings of each tpy ring equivalent and the two tpy moieties equivalent. All signals appeared as singlets. ESI-MS analysis of the product in acetonitrile solution provided strong evidence for metallomacrocycle formation. The metallomacrocyclic product gave a very clean mass spectrum which showed a peak that could be assigned to a doubly charged ion at *m/z* 924 for **[Co$_2$(23)$_2$]$^{2+}$**. The resulting macrocycle is shown in Figure 8.26.

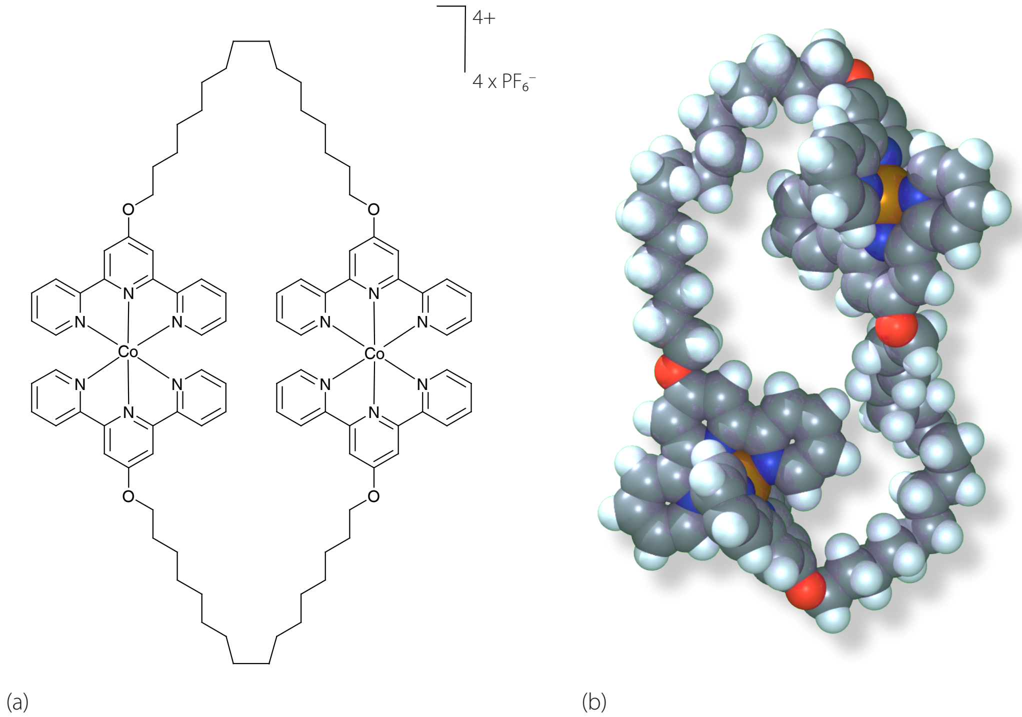

(a) (b)

Figure 8.26 The [2+2] metallomacrocyclic cation. (a) schematic representation and (b) a semi-empirical minimised model at PM3 level of the cationic metallomacrocycle.

The [2+2] macrocyclic product was stable over weeks in acetonitrile solution. After several months, the colour changed from orange to yellow, which was a sign of the oxidation of the metal centres to cobalt(III) (see Section 6.1.2.2). The existence of diamagnetic cobalt(III) metal could be evidenced from ^{1}H NMR spectroscopy; the spectrum was no longer broadened (Figure 8.27.

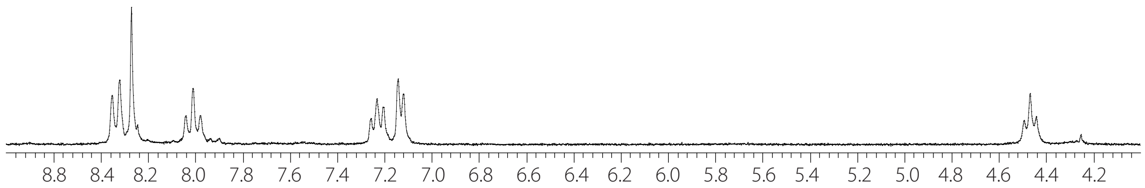

Figure 8.27 ^{1}H NMR spectrum of the oxidised metallomacrocyclic compound **$[Co_2(23)_2][PF_6]_4$**.

The ESI-MS of an acetonitrile solution of this cobalt(III) species exhibited peaks that could be assigned to a [2+2] $[\mathbf{Co_2(23)_2}]^{6+}$ species: $[M - 3PF_6]^{3+}$, *m/z* 664; $[M - 4PF_6]^{4+}$, *m/z* 462.

During the oxidation, the metallomacrocycle did not change its metal:ligand composition and ESI-MS proved that both metal centres were oxidised.

Since cobalt(II) salts formed [2+2] macrocycles with ligand **23**, it was assumed that this is the *thermodynamic* product, due to the ligand lability of cobalt(II) bis(tpy) complexes. This seems reasonable, since entropy dictates the formation of metallomacrocycles as small as possible in order to obtain the largest amount of species; and the [1+1] species seems energetically not favourable due to the tensioned alkyl-group and the sterical hindrance between the alkyl-chain and the metal(II) bis(tpy) unit (Figure 8.21).

Since the intramolecular ring-closure is kinetically favoured to the reaction with another tpy ligand – even at higher concentration (5 mM) – and the complexation of tpy ligands with $Ru(DMSO)_4Cl_2$ at room temperature or even under reflux is a very slow process, the *kinetically* favoured [1+1] metallomacrocycle is formed when $Ru(DMSO)_4Cl_2$ is used. If the irreversibility of Ru(II) bis(tpy) complexes was the reason for the formation of the [1+1] cycle, it would be expected that iron(II) also formed [1+1] macrocycles, assuming that the ligand lability for the **[Fe(23)]**$^{2+}$ macrocycle is the same as for conventional $[Fe(tpy)_2]^{2+}$ complexes.[18] However, the [1+1] metallomacrocycle could not be detected by ESI-MS and the ^1H NMR spectrum showed a symmetrical spectrum.

8.3 Experimental part

Compound 22: Compound **9** (70.0 mg, 0.264mmol), NaOH (12.0 mg (0.300 mmol) and iodine (38.1 mg, 0.150 mmol) were stirred vigorously in water (5 mL) at room temperature for 16 hours. The off-white precipitate was filtered off and washed with water (10 mL), ethanol (2 mL) and diethyl ether (2 mL) and dried over P_2O_5 affording 44 mg (63%) of **22**. m.p. 197 °C; ^1H NMR (500 MHz, $CDCl_3$): δ 8.67 (dd, J = 4.7, 1.6 Hz, 4H, H^{6A}), 8.66 (s, 4H, H^{3B}) , 8.55 (dd, J = 7.8, 1.0 Hz, 4H, H^{3A}), 7.82 (dd, J = 7.9, 7.7 Hz, 4H, H^{4A}), 7.31 ppm (dd, J = 7.7, 4.8 Hz, 4H, H^{5A}). ^{13}C NMR (125 MHz, $CDCl_3$): δ 155.7, 155.4, 149.3, 149.2, 136.8, 124.0, 121.4, 117.3 ppm. IR (neat): ($\tilde{\nu}$, cm^{-1}) 3055 w, 2916 m, 2854 m, 1551 s, 1458 m, 1381 s, 987 m 872 m, 787 s, 733 m. MS (ESI+): *m/z* 551 $[M + Na]^+$, 529 $[M + H]^+$. Anal. Calcd for $C_{30}H_{20}N_6S_2$: C, 68.16; H, 3.78; N, 15.90; found: C, 67.77; H, 3.78; N, 15.51%.

$[Fe_4(22)_4][BF_4]_8$: A solution of ligand **22** (14.5 mg, 27.4 μmol) and $Fe(BF_4)_2{\cdot}6H_2O$ (9.25 mg, 27.4 μmol) in methanol:dichloromethane (2:1, 5 mL) was heated to reflux for 1 hour to give a deep purple solution. The solvent was then removed *in vacuo* and the residue resolved in acetonitrile (5 mL) and the solution filtered over cotton wool. The solvent of the filtrate was then removed *in vacuo* to give **$[Fe(10)_2][BF_4]_2$** as a purple solid (21.9 mg, 26.7 μmol, 97.4%). ^1H NMR (250 MHz, CD_3CN): δ 9.05 (s, 16H, H^{3B}), 8.52 (d, J = 7.7 Hz, 16H, H^{6A}), 7.81 (dd, J = 7.7, 7.0 Hz, 16H, H^{5A}), 7.21 (d, J = 5.0 Hz, 16H, H^{3A}), 7.06 ppm (dd, J = 7.0, 5.0 Hz, 16H, H^{4A}). IR (neat): ($\tilde{\nu}$, cm^{-1}) 2922 m, 2853 w, 1717 m, 1595 m, 1533 w, 1466 m, 1423 s, 1394 m, 1285 w, 1244 w, 1026 s, 787 s, 752 s, 729 m. MS (ESI+): *m/z* 848 [**22** + Fe + 3H + $3BF_4$]$^+$, 694 [**22** + Fe + Na + BF_4]$^{2+}$, 641 [**22** + 2Fe + H]$^+$, 610 [**22** + Fe + Na + 3H]$^+$, 584 [**22** + Fe]$^+$, 556 [2x**22** + Fe]$^{2+}$. UV-vis (CH_3CN): λ/nm (ε/M^{-1} cm^{-1}) 569 (56000), 315 (150000), 276 (180000), 237 (120000). Anal. Calcd for $C_{120}H_{80}N_{24}B_8F_{32}S_8Fe_4{\cdot}14H_2O$: C, 43.88; H, 3.31; N, 10.23; found: C, 43.71; H, 2.96; N, 10.23%.

Compound 23: Dodecane-1,12-diol (24.2 mg, 93.5 µmol) were stirred vigorously in DMSO (1 mL) at 80 °C for 30 minutes. 4'-chloro-2,2':6',2''-terpyridine[26] (100 mg, 375 µmol) was added and stirred for an additional 16 hours at 80 °C. Saturated aqueous NaCl (20 mL) was added and extracted (3x) with dichloromethane. The combined dichloromethane layers were dried (Na_2SO_4) and evaporated to give an oil. Recrystallisation from a methanolic solution afforded **23** as a white powder (2.00 g, 87.4 µmol, 93.5%). m.p. 102 °C. ^{1}H NMR (500 MHz, $CDCl_3$): δ 8.69 (d, *J* = 4.7 Hz, 4H, H^{6A}), 8.60 (d, *J* = 7.6 Hz, 4H, H^{3A}), 8.00 (s, 4H, H^{3B}), 7.86 (dd, *J* = 8.0, 7.7 Hz, 4H, H^{4A}), 7.33 (dd, *J* = 7.7, 4.2 Hz, 2H, H^{5A}), 4.22 (t, *J* = 6.3 Hz, 4H, $H^{\mathrm{OC}\mathit{H}_2\mathrm{CH}_2}$), 1.85 (tt, *J* = 7.2, 6.3 Hz, 4H, $H^{\mathrm{OCH}_2\mathrm{C}\mathit{H}_2}$), 1.50 (tt, *J* = 7.2, 7.2 Hz, 4H, $H^{\mathrm{OCH}_2\mathrm{CH}_2\mathrm{C}\mathit{H}_2}$), 1.38 (tt, *J* = 7.2, 7.2 Hz, 4H, $H^{\mathrm{O(CH}_2)_3\mathrm{C}\mathit{H}_2}$), 1.25−1.32 (m, 16H, $H^{(\mathrm{C}\mathit{H}_2)_4}$. ^{13}C NMR (125 MHz, $CHCl_3$): δ 167.8, 155.3, 155.0, 148.0, 138.1, 124.2, 122.0, 108.3, 68.8, 32.0, 29.6 (2 overlapping signals), 29.6, 29.5, 29.3, 29.0, 25.9 ppm. IR (neat): ($\tilde{\nu}$, cm^{-1}) 2917 s, 2847 m, 1558 s, 1466 m, 1443 m, 1404 m, 1358 m, 1204 s, 1026 s, 864 w, 787 s, 733 m, 617 s. MS (MALDI-TOF+): *m/z* 723 [M + 2H]$^+$, 745 [M + Na + H]$^+$, 761 [M + K + H]$^+$. Anal. Calcd for $C_{46}H_{52}N_6O_2$: C, 75.88; H, 6.67; N, 12.64; found: C, 75.38; H, 7.27; N, 10.95%.

[Fe(10)(tpy)][BF$_4$]$_2$: A solution of ligand **10** (64.0 mg, 113 µmol), tpy (24.6 mg, 113 µmol) and $Fe(BF_4)_2{\cdot}6H_2O$ (18.8 mg, 56.0 µmol) in methanol:dichloromethane (2:1, 10 mL) was stirred at room temperature for 10 hours to give a deep purple solution. The solvent was removed *in vacuo*. Chromatography over silica (dichloromethane:methanol 12:1 → 10:1) afforded two purple fractions. The second fraction containing **[Fe(10)(tpy)][BF$_4$]$_2$** was collected (32.0 mg, 25.1 µmol, 44.7%). ^{1}H NMR (250 MHz, CD_3CN): δ 8.88 (d, *J* = 7.7 Hz, 2H, H^{3D}), 8.63 (t, *J* = 7.7 Hz, 1H, H^{4D}), 8.57 (s, 2H, H^{3B}), 8.46 (d, *J* = 4.7 Hz, 2H, H^{6A}), 8.42 (d, *J* = 5.0 Hz, 2H, H^{3D}), 7.87 (m, 4H, H^{5A+5C}), 7.01−7.16 (m, 8H, $H^{3A+4A+3C+4C}$), 6.83 (d, *J* = 2.3 Hz, 2H, H^{2E}), 6.55 (t, *J* = 2.2 Hz, 1H, H^{4E}), 5.62 (s, 4H, $H^{\mathrm{OC}\mathit{H}_2\mathrm{E}}$), 4.06 (t, *J* = 6.5 Hz, 4H, $H^{\mathrm{OC}\mathit{H}_2\mathrm{CH}_2}$), 1.79 (tt, *J* = 7.2, 6.5 Hz, 4H, $H^{\mathrm{OCH}_2\mathrm{C}\mathit{H}_2}$), 1.47 (tt, *J* = 7.2, 7.2 Hz, 4H, $H^{\mathrm{OCH}_2\mathrm{CH}_2\mathrm{C}\mathit{H}_2}$), 1.25−1.39 (m, 16H, $H^{(\mathrm{C}\mathit{H}_2)_4}$), 0.88 ppm (t, *J* = 7.0 Hz, 6H, $H^{\mathrm{C}\mathit{H}_3}$). IR (neat): ($\tilde{\nu}$, cm^{-1}) 2924 m, 2854 w, 1604 s, 1450 m, 1358 w, 1219 m, 1157 m, 1026 s, 764 m. MS (ESI+): *m/z* 442 [M − $2BF_4$]$^{2+}$. Anal. Calcd for $C_{53}H_{44}N_6O_3B_2F_8Fe{\cdot}2CH_2Cl_2{\cdot}6H_2O$: C, 50.03; H, 4.58; N, 6.36; found: C, 49.98; H, 4.82; N, 6.82%.

[Ru(23)]$_n$[PF$_6$]$_{2n}$ with RuCl$_3$·3H$_2$O: Ligand **23** (7.0 mg, 9.7 µmol) and RuCl$_3$·3H$_2$O (2.5 mg, 10 µmol) were suspended in ethylene glycol (1 mL) and heated in a microwave oven (600 W) for 2 x 2 minutes. A red solution resulted, after addition of water (5 mL), the solution was filtered and NH$_4$PF$_6$ (6.5 mg, 0.04 mmol) was added. The product was precipitated and collected on Cellite and removed by dissolution in acetonitrile.The solvent was removed *in vacuo* affording **[Ru(23)]$_n$[PF$_6$]$_{2n}$** (6.0 mg, 5.4 µmol, 56%) as a red solid. ^{1}H NMR (250 MHz, CD$_3$CN): δ 8.46 (d, J = 8.0 Hz, 4H, H^{6A}), 8.29 (s, 4H, H^{3B}), 7.89 (dd, J = 8.0, 5.0 Hz, 4H, H^{5A}), 7.38 (d, J = 5.0 Hz, 4H, H^{3A}), 7.15 (dd, J = 8.0, 5.0 Hz, 4H, H^{4A}), 4.50 (t, J = 7.4 Hz, 4H, H$^{\mathrm{OC}H_2\mathrm{CH}_2}$), 1.15−1.43 (m, 28H, H$^{(CH_2)_{14}}$).

[Ru(23)][PF$_6$]$_2$ with Ru(DMSO)$_4$Cl$_2$: Ligand **23** (23 g, 32 µmol), Ru(DMSO)$_2$Cl$_2$ (15 mg, 32 µmol) and TlPF$_6$ (22 mg, 64 µmol) were refluxed in ethanol (20 mL) for 15 hours. The colour of the solution turned from yellow to orange. The solvent was then removed *in vacuo*. Chromatography over silica (acetonitrile:sat.aq.KNO$_3$:water 7:1:0.5) yielded **11** as red solid (18 mg, 16 µmol, 50%). ^{1}H NMR (250 MHz, CD$_3$CN): δ 8.48 (d, J = 8.0 Hz, 4H, H^{6A}), 8.37 (s, 4H, H^{3B}), 7.9 (m, 4H, H^{5A}), 7.2 (m, 4H, H^{3A}), 6.9 (m, 2H, H^{4A}), 4.9 (m, 2H, H$^{\mathrm{OC}H_2\mathrm{CH}_2}$), 4.7 (m, 2H, H$^{\mathrm{OC}H_2\mathrm{CH}_2}$),1.15−1.43 (m, 28H, H$^{(CH_2)_{14}}$). MS (ESI+): *m/z* 411 [M − 2PF$_6$]$^{2+}$, 967 [M − PF$_6$]$^+$.

[Fe(23)]$_n$[PF$_6$]$_{2n}$: Ligand **23** (22 g, 31 µmol) and FeCl$_2$·4H$_2$O (6.1 mg, 31 µmol) were stirred at room temperature in methanol:dichloromethane (5:1, 6 mL) for 30 minutes. The colour of the solution turned immediately deep purple. The solvent was concentrated to ≈3 mL and NH$_4$PF$_6$ (20 mg, 120 µmol) was added. The formed precipitate was collected by filtration and washed with water (5 mL) affording **[Fe(23)]$_n$[PF$_6$]$_{2n}$**, which was purified by chromatography over silica (acetonitrile:sat. aq.KNO$_3$:water 7:1:0.5). ^{1}H NMR (250 MHz, CD$_3$CN): δ 8.44 (s, 4H, H^{3B}), 8.42 (d, J = 6.0 Hz, 4H, H^{6A}), 7.87 (dd, J = 6.0, 5.7 Hz, 4H, H^{5A}), 7.15 (d, J = 5.7 Hz, 4H, H^{3A}), 7.06 (dd, J = 6.0, 5.7 Hz, 4H, H^{4A}), 4.59 (t, J = 6.6 Hz, 4H, H$^{\mathrm{OC}H_2\mathrm{CH}_2}$), 1.26−1.57 (m, 28H, H$^{(CH_2)_{14}}$). MS (ESI+): *m/z* 585 [2x**23** + 2Fe + PF6$^-$ + F$^-$ + K]$^{3+}$.

[Co(23)]$_2$[PF$_6$]$_4$: Ligand **23** (10 mg, 14 µmol) and CoAc$_2$·4H$_2$O (3.5 mg, 14 µmol) were stirred at room temperature in methanol:dichloromethane (2:1, 6 mL) for 4 days. The colour of the solution turned immediately deep orange. The solvent was concentrated to ≈3 mL and NH$_4$PF$_6$ (10 mg, 60 µmol) was added. The formed precipitate was collected by filtration and washed with water (2 mL) affording **[Co(23)]$_2$[PF$_6$]$_4$** (14.3 mg, 7 µmol). ^{1}H NMR (500 MHz, CD$_3$CN): δ 112 (br s, 8H, H^{6A}), 75.5 (br s, 8H, H^{3B}), 70.8 (br s, 8H, H^{3A}), 34.5 (br s, 8H, H^{5A}), 15.2 (br s, 8H, H$^{\mathrm{OC}H_2\mathrm{C}}$), 8.5−1.0 ppm (br m, 64H, H^{2C}). MS (ESI+): *m/z* 924 [M − 2PF$_6$]$^{2+}$.

[Co(23)]$_2$[PF$_6$]$_4$ was oxidised in a d_3-acetonitrile solution over a period of three months obtaining a

$[\mathbf{Co(23)}]_{\mathbf{2}}^{\mathbf{6+}}$ macrocycle. ^{1}H NMR (250 MHz, CD_3CN): δ 8.54 (d, J = 8.0 Hz, 4H, H^{6A}), 8.47 (s, 4H, H^{3B}), 8.21 (dd, J = 8.0, 5.4 Hz, 4H, H^{5A}), 7.43 (dd, J = 8.0, 5.4 Hz, 4H, H^{4A}), 7.33 (d, J = 5.4 Hz, 4H, H^{3A}), 4.67 (t, J = 6.4 Hz, 4H, $H^{OCH_2CH_2}$), 1.26–1.59 (m, 28H, $H^{(CH_2)_{14}}$). MS (ESI+): *m/z* 664 [M – $3PF_6]^{3+}$, 462 [M – $4PF_6]^{4+}$.

8.4 References

[1] E. C. Constable, *Chem. Ind.* **1994**, 56.

[2] V. G. Machado, P. N. W. Baxter, J.-M. Lehn, *J. Braz. Chem. Soc.* **2001**, *12*, 431.

[3] Y. Tor, *Synlett* **2002**, 1043.

[4] E. C. Constable, *Adv. Inorg. Chem. Radiochem.* **1986**, *30*, 69.

[5] E. C. Constable, in *Education in Advanced Chemistry, Perspectives in Coordonation Chemistry Vol. 7* (Eds.: A. M. Trzeciak, P. Sobota, J. J. Ziolkowski), University Publishing House, **2000**.

[6] E. C. Constable, A. M. W. Cargill Thompson, D. A. Tocher, in *Supramolecular Chemistry* (Eds.: V. Balzani, L. De Cola), Kluwer Academic Press, Dordrecht, **1992**.

[7] S. Leininger, B. Olenyuk, P. J. Stang, *Chem. Rev.* **2000**, *100*, 853.

[8] M. Fujita, *Chem. Soc. Rev.* **1998**, *27*, 417.

[9] G. F. Swiegers, T. J. Malefetse, *Chem. Rev.* **2000**, *100*, 3483.

[10] B. J. Holliday, C. A. Mirkin, *Angew. Chem. Int. Ed.* **2001**, *40*, 2022.

[11] P. J. Stang, B. Olenyuk, *Acc. Chem. Res.* **1997**, *30*, 502.

[12] F. Würthner, C.-C. You, C. R. Saha-Möller, *Chem. Soc. Rev.* **2004**, *33*, 133.

[13] E. C. Constable, E. Schofield, *Chem. Commun.* **1998**, 403.

[14] C. B. Smith, E. C. Constable, C. E. Housecroft, B. Kariuki, *Chem. Commun.* **2002**, 2068.

[15] E. C. Constable, C. E. Housecroft, C. B. Smith, *Inorg. Chem. Comm.* **2003**, *6*, 1011.

[16] E. C. Constable, C. E. Housecroft, M. Neuburger, S. Schaffner, C. B. Smith, *Dalton Trans.* **2005**, 2259.

[17] H. S. Chow, E. C. Constable, C. E. Housecroft, M. Neuburger, S. Schaffner, *Polyhedron*, in press.

[18] E. C. Constable, C. E. Housecroft, M. Neuburger, S. Schaffner, E. J. Shardlow, *Dalton Trans.* **2005**, 234.

[19] H. S. Chow, E. C. Constable, C. E. Housecroft, M. Neuburger, *Dalton Trans.* **2003**, 4568.

[20] F. M. Romero, R. Ziessel, A. Dupont-Gervais, A. Van Dorsselaer, *Chem. Commun.* **1996**, 551.

[21] G. R. Newkome, T. J. Cho, C. N. Moorefield, G. R. Baker, C. R., P. S. Russo, *Angew. Chem. Int. Ed.* **1999**, *38*, 3717.

[22] G. R. Newkome, T. J. Cho, C. N. Moorefield, R. Cush, P. S. Russo, L. A. Godínez, S. M. J., P. Mohapatra, *Chem. –Eur. J.* **2002**, *8*, 2946.

[23] G. R. Newkome, T. J. Cho, C. N. Moorefield, *Chem. Commun.* **2002**, 2164.

[24] P. Wang, C. N. Moorefield, G. R. Newkome, *Org. Lett.* **2004**, *6*, 1197.

[25] G. R. Newkome, T. J. Cho, C. N. Moorefield, P. P. Mohapatra, L. A. Godínez, *Chem. –Eur. J.* **2004**, *10*, 1493.

[26] G. U. Priimov, P. Moore, P. K. Maritim, P. K. Butalanyi, N. W. Alcock, *J. Chem. Soc., Dalton Trans.* **2000**, 445.

[27] E. C. Constable, A. M. W. Cargill Thompson, *J. Chem. Soc., Dalton Trans.* **1992**, 2947.

[28] H. Hofmeier, U. S. Schubert, *Chem. Soc. Rev.* **2004**, *33*, 373.

[29] U. S. Schubert, C. Eschbaumer, O. Hien, P. R. Anders, *Tetrahedron Letters* **2001**, *42*, 4705.

[30] E. Schofield, *PhD Thesis*, University of Basel, Basel, **1999**.

[31] E. C. Constable, A. M. W. Cargill Thompson, *J. Chem. Soc., Dalton Trans.* **1994**, 1409.

[32] E. C. Constable, P. Harverson, *Polyhedron* **1999**, *18*, 3093.

[33] E. C. Constable, A. M. W. Cargill Thompson, *New J. Chem.* **1992**, 855.

[34] M. Beley, J. P. Collin, R. Louis, B. Metz, J.-P. Sauvage, *J. Am. Chem. Soc.* **1991**, *113*, 8521.

[35] E. C. Constable, C. E. Housecroft, M. Cattalini, D. Phillips, *New J. Chem.* **1998**, 193.

[36] E. C. Constable, D. Phillips, *Chem. Commun.* **1997**, 827.

[37] F. Antolasic, *Isotope Version 1.0* **2003**.

[38] E. C. Constable, C. E. Housecroft, M. Neuburger, S. Schaffner, L. J. Scherer, *Dalton Trans.* **2004**, 2635.

[39] E. C. Constable, C. P. Hart, C. E. Housecroft, *Appl. Organomet. Chem.* **2003**, *17*, 383.

[40] E. C. Constable, C. E. Housecroft, T. Kulke, C. Lazzarini, E. Schofield, Y. Zimmermann, *J. Chem. Soc., Dalton Trans.* **2001**, 2864.

[41] E. C. Constable, C. E. Housecroft, Y. Tao, *Synthesis* **2004**, 869.

Thus for chemists have learnt to spell words, now we need to learn to construct sentences from those words.

J. F. Stoddart

9. Additional and Further Work

In this Chapter additional work, which follows naturally from the studies presented in Chapters 3–8 will be briefly discussed. Most of the work discussed in this Chapter has not been finished in the period of this thesis and therefore experimental details are not given.

Additionally, further work related to the studies presented so far will be shortly discussed.

9.1 Building of [Ru(tpy)$_2$] arrays with pendant octyl-decorated Fréchet-type dendrons

The idea was to construct molecules with various metal(II) centres, which are decorated with octyl-decorated Fréchet-type dendrons. The properties of self-assembled monolayers of these compounds were considered to study. 2D assemblies of metal(II) bis(tpy) complexes are presented in Chapter 6, but only interesting compounds possessing one metal centre were investigated in Chapter 6.

Two molecules will be shown with 2 and 3 metal centres. Since the kinetic stability of metal complexes seems to be crucial for STM studies (see Chapter 6), These metal(II) bis(tpy) arrays were constructed with ruthenium(II) metal centres, due to the kinetic stability of [Ru(tpy)$_2$]-motifs. Scheme 9.1 shows the synthetic pathway to construct compound [(**10**)**Ru**(**23**)**Ru**(**10**)][PF$_6$]$_4$.

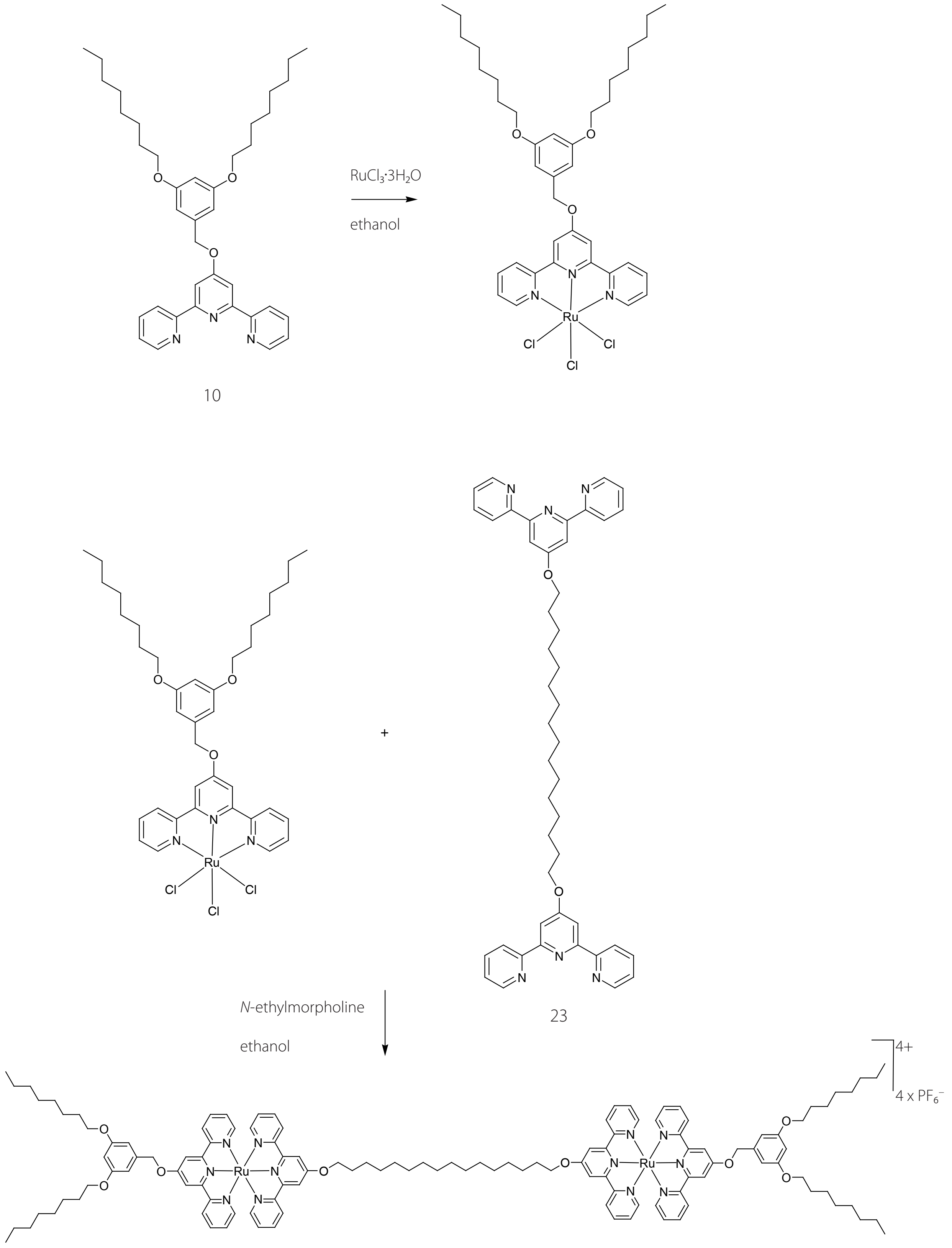
$RuCl_3{\cdot}3H_2O$
ethanol
N
Ru
Cl
O
+
N-ethylmorpholine
ethanol
4+
4 x PF_6^-

10

23

Scheme 9.1 Synthesis of compound **[(10)Ru(23)Ru(10)][PF$_6$]$_4$**.

The compound was synthesised with a two-step methodology. Compound **10** was reacted with a stoichiometric amount of $RuCl_3 \cdot 3H_2O$ in refluxing ethanol forming [(**10**)**RuCl$_3$**] as a brown solid.[1-5] [(**10**)**RuCl$_3$**] was used in the subsequent reaction without further purification. [(**10**)**RuCl$_3$**] was refluxed with compound **23** in ethanol in the presence of *N*-ethylmorpholine. Additional counter-ion exchange with NH_4PF_6 afforded [(**10**)**Ru**(**23**)**Ru**(**10**)][**PF$_6$**]$_4$ as an orange precipitate, which was collected by filtration. Spot TLC and ^{1}H NMR spectroscopy verified the presence of only one ruthenium(II) species, which was fully characterised. ESI-MS spectrometry showed one signal at *m/z* 529 which was assigned to $[M - 4PF_6]^{4+}$ and the isotopic pattern matched that simulated.[6] ^{1}H NMR shows two sets of tpy signals, which were assigned using the COSY spectrum. UV-vis spectroscopy of the bis-complex exhibited an MLCT absorption at 486 nm, typical of a $[Ru(tpy)_2]^{2+}$ chromophore.

Monolayers of [(**10**)**Ru**(**23**)**Ru**(**10**)][**PF$_6$**]$_4$ were obtained upon evaporation of an acetonirile solution under ambient conditions. A typical STM image obtained is shown in Figure 9.1.

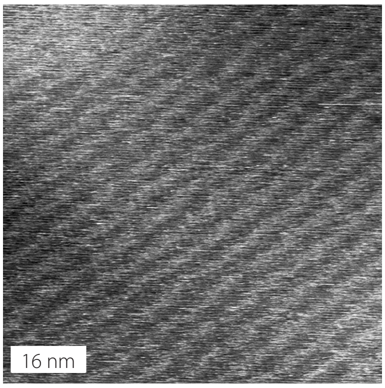

Figure 9.1 An STM image taken after solution casting of **[(10)Ru(23)Ru(10)][PF$_6$]$_4$** in acetonitrile. The unresolved pattern was reproducibly observed. Scan parameters: 80 nm x 80 nm, U_b = −400 mV, I_t = 8 pA.

The STM image showed rows which could not be well resolved. Artefacts could be excluded since the same pattern was observed in each measurement. The rows had a distance of ≈5 nm and the darker regions were ≈2 nm wide. This width is consistent with the length of the hexadecyl-spacer of the molecule.

For the analysis of the monolayer, better resolved images are necessary.

The second compound possessed three $[M(tpy)_2]$ centres and was also linear with ligand **10** at both ends. Scheme 9.2 shows the desired compound [(**10**)**Ru**(**tpyStpy**)**Ru**(**10**)][**PF$_6$**]$_6$.

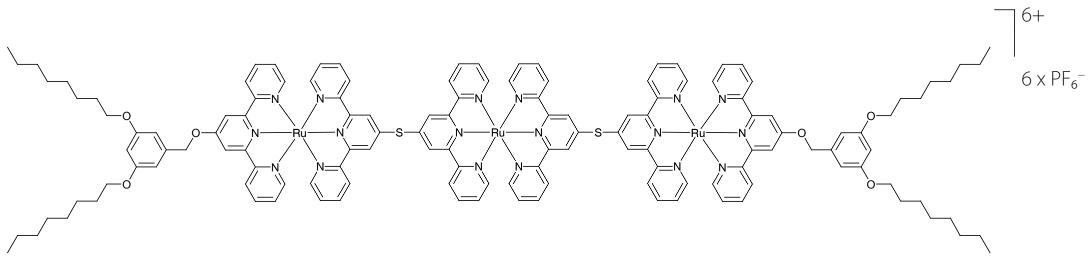

Scheme 9.2 Compound **[(10)Ru(tpyStpy)Ru(10)][PF$_6$]$_6$**.

The two Fréchet-type dendrons at the periphery serve the purpose to spontaneously self-assemble on HOPG. Compound [(**10**)**Ru**(**tpyStpy**)**Ru**(**10**)][**PF$_6$**]$_6$ could not be synthesised in the course of this thesis. Only the model system [(**tpy**)**Ru**(**tpyStpy**)**Ru**(**tpy**)][**PF$_6$**]$_6$ shown in Scheme 9.3 was prepared. Instead of ligand **10** at both ends, the molecule possessed terminal unsubstituted tpy units.

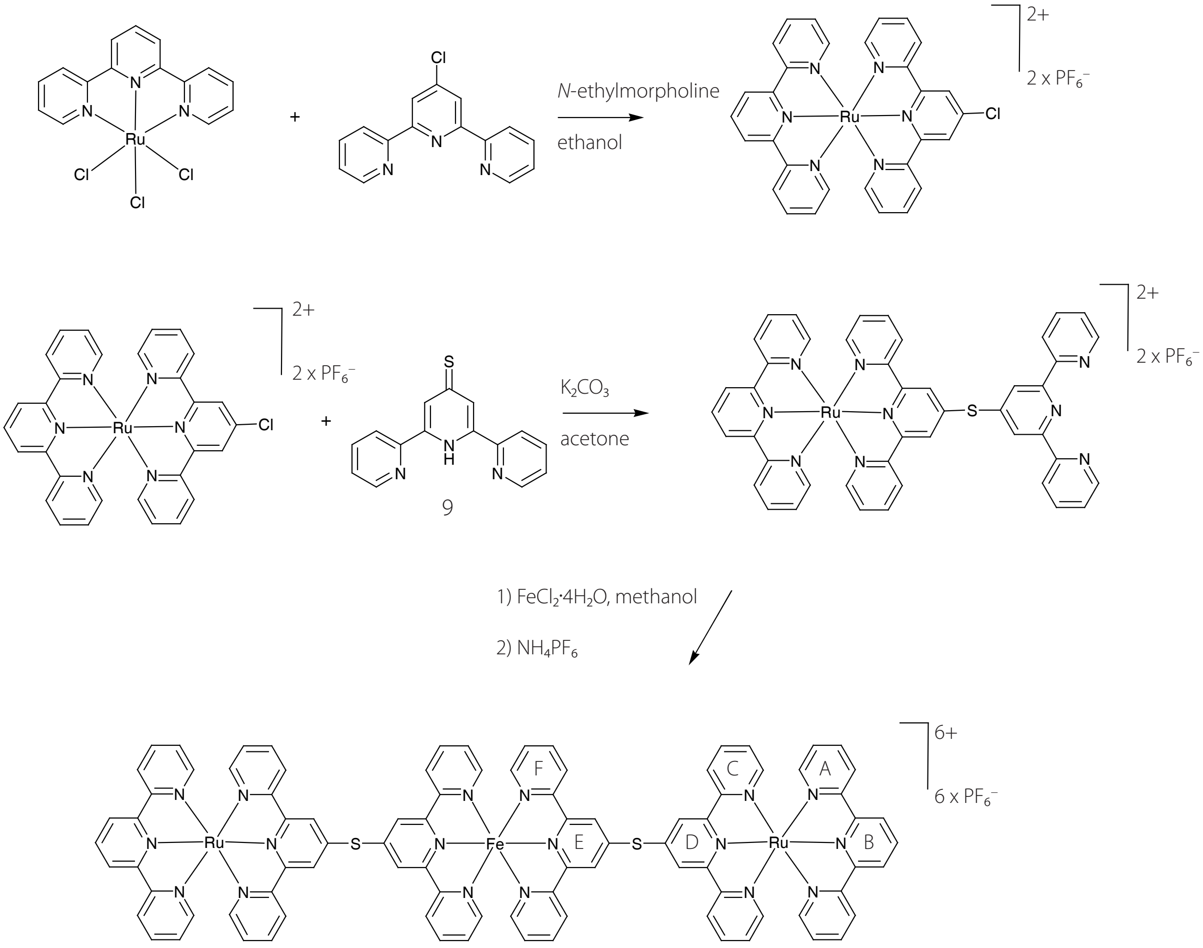
+
N-ethylmorpholine
ethanol
2+
2 x PF$_6^-$
2+
2 x PF$_6^-$
+
9
K$_2$CO$_3$
acetone
2+
2 x PF$_6^-$
1) FeCl$_2$·4H$_2$O, methanol
2) NH$_4$PF$_6$
6+
6 x PF$_6^-$
A
B
C
D
E
F

Scheme 9.3 Synthesis of **[(tpy)Ru(tpyStpy)Ru(tpy)][PF$_6$]$_6$**. Ring labels are used for NMR spectroscopic assignments (for Figure 9.2).

Scheme 9.3 shows the synthetic pathway. The heteroleptic ruthenium compound with one 4'-chloro-2,2':6',2''-terpyridine unit (4'-Cl-tpy) was electrophilic enough to react with compound **9** at room temperature using K_2CO_3 as base. The final complexation worked smoothly with $FeCl_2{\cdot}4H_20$. ESI-MS spectrometry showed two significant signals at *m/z* 717 and 1148 which were attributed to $[M - 3PF_6]^{3+}$ and $[M - 2PF_6]^{2+}$ respectively. The isotopic pattern of both signals matched that simulated.[6]

The ^1H NMR spectrum showed three sets of tpy signals (Figure 9.2). The assignment was done with additional COSY and NOSY experiments.

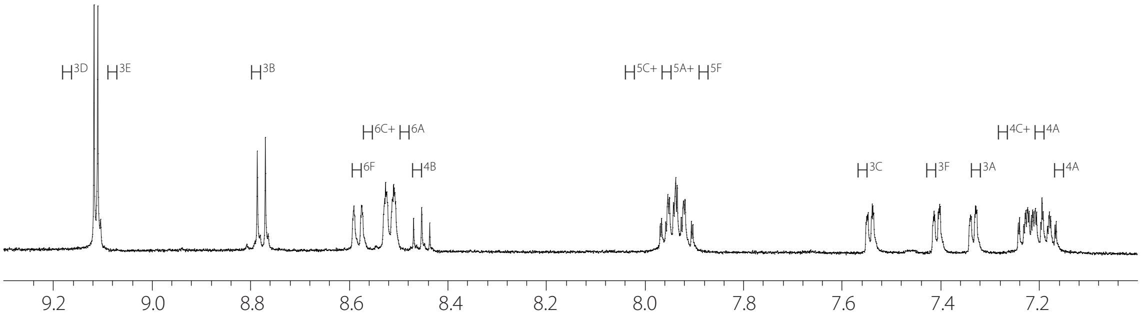

Figure 9.2 The ^1H NMR spectrum showed three sets of tpy signals, which could be assigned with additional COSY and NOSY experiments.

The desired compound shown in Scheme 9.2 could not be prepared using the same synthetic strategy. The aromatic nucleophilic substitution of **9** to the **[Ru(4'-Cl-tpy)(10)][PF$_6$]$_2$** complex did not work under the same conditions used for the preparation of **[(tpy)Ru(tpyStpy)Ru(tpy)][PF$_6$]$_6$**. The apolar octyl-chains might influence the substitution negatively.

9.2 Synthesis of a Fujita-square with peripheral octyl-decorated Fréchet-type dendrons

In the course of the studies with Fréchet type metal-complex arrays decorated with Fréchet-type dendrons, the synthesis of a Fujita-square possessing four palladium(II) centres was studied.[7-12] The synthetic strategy was to react **[Pd(3)Cl$_2$]** (see Chapter 3 for the preparation) with 4,4'-bipyridine (**24**) in the presence of $TlPF_6$ under the same conditions used for the synthesis of **[Pd(3)$_2$][PF$_6$]$_2$** (Chapter 3). The only difference was the long reaction time of 3 days in order to get the thermodynamic equilibrium. The synthesis is shown in Scheme 9.4.

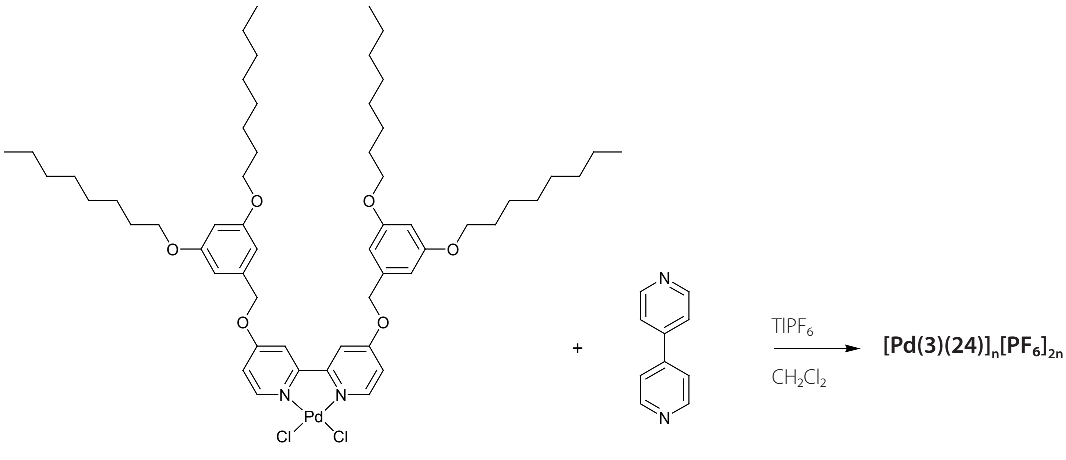

24

Scheme 9.4 By reacting **[Pd(3)Cl$_2$]** with one mol equivalent of **24** in the presence of TlPF$_6$, the formation of a metallomacrocycle is anticipated.

ESI-MS spectrometry showed only fragments with a major signal at *m/z* 1179 which was attributed to [Pd + Cl + **3** + **24**]$^+$. The ^{1}H NMR spectrum revealed the formation of a macrocycle since five pyridine signals were detected. The signals were broadened (Figure 9.3).

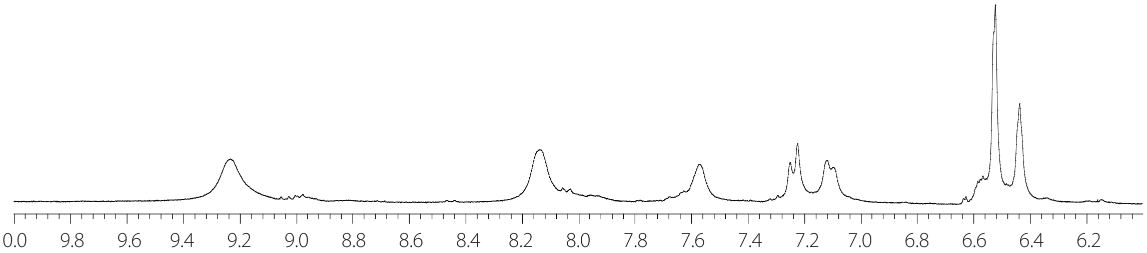

Figure 9.3 ^{1}H NMR spectrum of the formed macrocycle obtained by reacting **24** with **[Pd(3)Cl$_2$]**.

The ^{1}H NMR spectrum showed the presence of impurities. Since the product decomposed on silica, purification could not be done with chromatography. The impurities may arise from other macrocycles. One possible solution to get only one product would be to let equilibrate the mixture in solution for a longer period of time.

9.3 Study of the effect of apolar anions for the formation of self-assembled monolayers

In Chapter 6, the effect of different counter-ions for the cationic complex [**Fe**(**10**)$_2$]$^{2+}$ (Scheme 9.5) for the formation of 2D assemblies on HOPG were studied. All compounds possessing different anions showed the same monolayered pattern. The anions differed mainly in size, but no compound with apolar counter-ions has been tested. Therefore, the cationic complex [**Fe**(**10**)$_2$]$^{2+}$ was prepared with two apolar docyl-sulfate anions. It is expected that the anion is more likely to interact with the graphite surface than the cationic complex; thus, the cations would form the second layer after the anionic layer and the anions may therefore not be repelled by the STM tip while scanning. The compound has been prepared but no STM studies have been conducted so far.

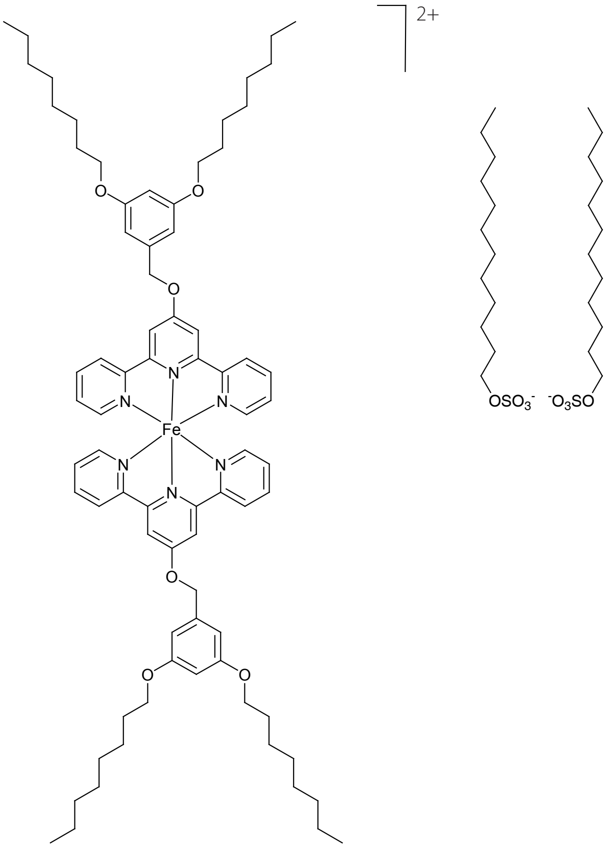

Scheme 9.5 Molecular structure of **[Fe(10)$_2$]$^{2+}$** with the two dodecyl sulfonate counter-ion.

9.4 Related work by other group members

Since Fréchet-type dendrons are useful STM-markers, other investigations are in progress in our research group.

S. Graber is synthesising chiral Frechet-type dendrons which are then attached to the bpy unit at 4- and 4'-position (see Chapter 3). With this chirality, the goal is to fix the molecular conformation on the surface.

M. Malarek investigates the influence of the length of the alkyl-chain of second generation Fréchet-type dendrimers on the self-assembly.

M. Häusler and D. Malarek functionalise biomolecules with Fréchet-type dendrons in order to study their self-organisation properties.

9.5 References

[1] E. C. Constable, A. M. W. Cargill Thompson, *J. Chem. Soc., Dalton Trans.* **1994**, 1409.

[2] E. C. Constable, P. Harverson, *Polyhedron* **1999**, *18*, 3093.

[3] E. C. Constable, A. M. W. Cargill Thompson, *New J. Chem.* **1992**, 855.

[4] E. C. Constable, C. E. Housecroft, M. Neuburger, S. Schaffner, C. B. Smith, *Dalton Trans.* **2005**, 2259.

[5] M. Beley, J. P. Collin, R. Louis, B. Metz, J.-P. Sauvage, *J. Am. Chem. Soc.* **1991**, *113*, 8521.

[6] F. Antolasic, *Isotope Version 1.0* **2003**.

[7] M. Fujita, J. Yazaki, K. Ogura, *J. Am. Chem. Soc.* **1990**, *112*, 5645.

[8] M. Fujita, J. Yazaki, K. Ogura, *Chem. Lett.* **1991**, 1031.

[9] P. J. Stang, D. H. Cao, S. Saito, A. M. Arif, *J. Am. Chem. Soc.* **1995**, *117*, 6273.

[10] C. A. Schalley, T. Müller, P. Linnartz, M. Witt, M. Schäfer, A. Lützen, *Chem. Eur. J.* **2002**, *8*, 3538.

[11] S. Leininger, B. Olenyuk, P. J. Stang, *Chem. Rev.* **2000**, *100*, 853.

[12] M. Fujita, K. Umemoto, M. Yoshizawa, N. Fujita, T. Kusukawa, K.Biradha, *Chem. Commun.* **2001**, 509.

Publications

1. *Monitoring conformational diversity in self-organised monolayers with scanning tunnelling microscopy at near atomic resolution*
   Edwin C. Constable, Bianca A. Hermann, Catherine E. Housecroft, Leo Merz, Lukas J. Scherer, *Chem. Commun.*, **2004**, *8*, 928–929.

2. *Preparation and structural characterisation of terpy-cored dendrimers and dendriplexes*
   Edwin C. Constable, Catherine E. Housecroft, Markus Neuburger, Silvia Schaffner, Lukas J. Scherer, *Dalton Trans.*, **2004**, *17*, 2635–2642.

3. *Conformational Analysis of Self-organized Monolayers with Scanning Tunneling Microscopy at Near Atomic Resolution*
   Lukas J. Scherer, Leo Merz, Edwin C. Constable, Catherine E. Housecroft, Markus Neubuger, Bianca A. Hermann, *J. Am. Chem. Soc.*, **2005**, *127*, 4033–4041.

4. *Octyl-decorated Fréchet-type dendrons: a general motif for visualisation of static and dynamic behaviour using scanning tunnelling microscopy?*
   Leo Merz, H.-J. Güntherodt, Lukas J. Scherer, Edwin C. Constable, Catherine E. Housecroft, Bianca A. Hermann, *Chem. –Eur. J.*, **2005**, *11*, 2307–2318.

5. *Self-Organised Monolayers – a Route for Switching and Read-out of Functional Supra molecular Assemblies by Scanning Probe Methods*
   B. A. Hermann, L. J. Scherer, C. E. Housecroft, E. C. Constable, *Advanced Functional Materials* **2006**, *16*, 221–235

6. *2',2':6',2''-Terpyridine-4(1H)-thione: a missing link in metallosupramolecular chemistry*
   Edwin C. Constable, B. A. Hermann, Catherine E. Housecroft, Markus Neuburger, Silvia Schaffner, Lukas J. Scherer, *New J. Chem.* , **2005**, *29*, 1475–1481.

7. *Self-Organised Monolayers of 2',2':6',2''-Terpyridines substituted with Fréchet-type dendrimers studied with Scanning Tunnelling Microscopy*
   Edwin C. Constable, B. A. Hermann, Catherine E. Housecroft, Markus Neuburger, Silvia Schaffner, Lukas J. Scherer, in prep.

Curriculum Vitae

Lukas Jaime Scherer

St. Galler-Ring 19
CH-4055 Basel
Switzerland
Home Phone (+41) 061 322 1591
Work Phone (+41) 061 267 1035
Email: lukas.scherer@unibas.ch

Personal Details

Marital Status:	Single
Place of Birth:	Kilchberg ZH, Switzerland
Date of Birth:	11/11/1976
Citizenship:	Swiss, Spanish
Languages:	German, English, Spanish, French (all fluent, spoken and written)

Education

07/1996	**Matura (Science)**, Kantonsschule Alpenquai, Lucerne, Switzerland.
10/2000	**Lic. Phil. II (Chemistry) (equivalent to a BSc)**, Uni Basel, Switzerland.
11/2000–03/2001	**Diploma Work (equivalent to an MSc)**, Supervisor: Prof. E. C. Constable, University of Birmingham, UK.
10/2001–03/2003	**Post-Graduate Research**, *Organometallic Chemistry, Total Synthesis, Ligand synthesis,* Supervisor : Prof. E. M. Carreira, ETH, Zürich, Switzerland.
04/2003–present	**PhD studies,** *Octyl-Decorated Fréchet-Type Dendrons: A General Motif for Visualisation of Static and Dynamic Behaviour Using Scanning Tunnelling Microscopy,* Supervisor : Prof. E. C. Constable, Uni Basel, Switzerland.

Employment

03/2000–06/2000	**Research**, *Synthesis of Drug Libraries*, Oncology, Novartis Pharma AG, Basel, Switzerland.
05/2001–08/2001	**Development**, *Total Synthesis*, Novartis Pharma AG, Basel, Switzerland.

Teaching

03/2002–07/2002	**Organic Chemistry Tutorial II**, ETH Zürich, Switzerland.
10/2002–02/2003	**Organic Chemistry Tutorial I**, ETH Zürich, Switzerland.
10/2004–02/2005	**General Chemistry Tutorial I**, Uni Basel, Switzerland.
03/2005–07/2005	**Demonstrator of Organometallic and Inorganic Chemistry**, Uni Basel, Switzerland.
10/2005–02/2006	**General Chemistry Tutorial I**, Uni Basel, Switzerland.
04/2003–present	**Supervising 2 master students and 2 undergraduate researchers**, Uni Basel, Switzerland.

Oral Presentations

07/2004	International Conference on Coordination Chemistry 36, Merida, Mexico.
11/2004	National Center of Competence in Research (NCCR) Colloquia, Institute of Physics, Uni Basel, Switzerland.
11/2004	Seminar in the Department of Organic Chemistry, Uni Basel, Switzerland.
06/2005	Final Symposium of NRP 47 “Supramolecular Functional Materials”, Murten, Switzerland.
11/2005	Seminar in the Department of Inorganic Chemistry, University of Cambridge, UK.

Poster Presentations

06/2003	Kick off-Meeting of NRP 47 “Supramolecular Functional Materials”, Berne, Switzerland.
10/2004	Fall Meeting of the Swiss Chemical Society, Zurich, Switzerland.
03/2005	Leopoldina Meeting, Heidelberg, Germany.
06/2005	Final Symposium of NRP 47 “Supramolecular Functional Materials”, Murten, Switzerland.
10/2005	NCCR Nanoscale Science Annual Meeting, Gwatt, Switzerland.
10/2005	Fall Meeting of the Swiss Chemical Society, Lausanne, Switzerland.

Awards and Memberships

- Awarded a Poster Prize at the Kick off-Meeting of NRP 47 “Supramolecular Functional Materials”, Berne, Switzerland, **06/2003.**

- Member of the Swiss Chemical Society.